INFORMATION TO USERS

This reproduction was made from a copy of a manuscript sent to us for publication and microfilming. While the most advanced technology has been used to photograph and reproduce this manuscript, the quality of the reproduction is heavily dependent upon the quality of the material submitted. Pages in any manuscript may have indistinct print. In all cases the best available copy has been filmed.

The following explanation of techniques is provided to help clarify notations which may appear on this reproduction.

1. Manuscripts may not always be complete. When it is not possible to obtain missing pages, a note appears to indicate this.

2. When copyrighted materials are removed from the manuscript, a note appears to indicate this.

3. Oversize materials (maps, drawings, and charts) are photographed by sectioning the original, beginning at the upper left hand corner and continuing from left to right in equal sections with small overlaps. Each oversize page is also filmed as one exposure and is available, for an additional charge, as a standard 35mm slide or in black and white paper format.*

4. Most photographs reproduce acceptably on positive microfilm or microfiche but lack clarity on xerographic copies made from the microfilm. For an additional charge, all photographs are available in black and white standard 35mm slide format.*

***For more information about black and white slides or enlarged paper reproductions, please contact the Dissertations Customer Services Department.**

Qiu, Shen Li

INCOMMENSURATE PHASE TRANSITION IN SODIUM-NITRITE

City University of New York PH.D. 1985

PLEASE NOTE:

In all cases this material has been filmed in the best possible way from the available copy. Problems encountered with this document have been identified here with a check mark __✓__.

1. Glossy photographs or pages _____
2. Colored illustrations, paper or print _____
3. Photographs with dark background _____
4. Illustrations are poor copy _____
5. Pages with black marks, not original copy _____
6. Print shows through as there is text on both sides of page _____
7. Indistinct, broken or small print on several pages __✓__
8. Print exceeds margin requirements _____
9. Tightly bound copy with print lost in spine _____
10. Computer printout pages with indistinct print _____
11. Page(s) _____ lacking when material received, and not available from school or author.
12. Page(s) _____ seem to be missing in numbering only as text follows.
13. Two pages numbered _____. Text follows.
14. Curling and wrinkled pages _____
15. Dissertation contains pages with print at a slant, filmed as received _____
16. Other _____

_____

_____

INCOMMENSURATE PHASE TRANSITION IN $NaNO_2$

BY

SHEN LI QIU

A dissertation submitted to the Graduate Faculty in Physics in Partial fulfillment of the requirements for the degree of Doctor of Philosophy, The City University of New York.

1985

This manuscript has been read and accepted for the Graduate Faculty in Physics in satisfaction of the dissertation requirement for the degree of Doctor of Philosophy.

9/9/85
date

Chairman of Examining Committee

9/9/85
date

Executive Officer

Supervisory Committee

The City University of New York

ABSTRACT

INCOMMENSURATE PHASE TRANSITION IN $NaNO_2$

by

Shen Li Qiu

Adviser: Professor Herman Z. Cummins

The incommensurate phase transition in $NaNO_2$ has been studied by the following experiments:

Dielectric constant measurements under E-field along the b-axis.

Elastic neutron scattering under E-field along the b-axis.

Elastic neutron scattering under E-field along the a-axis.

Elastic neutron scattering under E-field along the c-axis.

Brillouin scattering under E-field along the c-axis.

Inelastic neutron scattering.

Diffuse neutron scattering.

Dielectric constant measurements under hydrostatic pressure.

Brillouin scattering under hydrostatic pressure.

By numerically minimizing the Landau free energy the predictions of different Landau free energy expansions for the phase diagram and the behaviour of the modulation wave vector under E-field along the b-axis were explored. All the coefficients in the free energy have been determined from the dielectric constant measurements, the elastic neutron

scattering results and the spontaneous polarization data.

Some discussions of the free energy model are given. Comparison of the diffuse neutron scattering results with the predictions of the free energy model indicates that the η-term in the free energy cannot be neglected, and that temperature dependence of the coefficient α should be included. There is another reason why the η-term cannot be neglected: without an η-term the para $\rightarrow$ INC phase transition will be of first order. However, the observed para $\rightarrow$ INC transition is of second order.

Extension of the Lifshitz point theory to the case of a first order transition from the disordered phase to the ordered phase has for the first time been discussed in detail. By fitting our data of the elastic neutron scattering under transverse electric field to the numerically calculated results we can determine where the virtual Lifshitz point should occur and construct the whole phase transition diagram.

Using the ANNNI model, numerical calculations of dielectric constants under longitudinal electric field were carried and some discussions are presented.

The microscopic theory of Michel and coworkers is reviewed. Some of the results of the microscopic theory are cited for comparison with the results of the phenomenological theory and the Ising model.

ACKNOWLEDGEMENTS

I express my gratitude to Professor Herman Z. Cummins for his patient guidance and continued support during the course of this research.

I am grateful to Professors I. Hatta and T. Yagi for their generosity in providing $NaNO_2$ crystals. I am grateful to Professor Y. Ishibashi for his suggestion of procedures for $NaNO_2$ crystal growth.

I am grateful to Dr. S. M. Shapiro, Dr. J. P. Wicksted, Dr. M. Dutta and Professor J. C. Steiner for their collaboration and assistance. I am also grateful to Dr. Dennis Neal for his help. I thank all the members of the light scattering group, Professor G. Y. Zhang, Dr. T. Aurora, Dr. G. Livescu, Mr. H. Chou, Mr. X. Z. Lu and Miss W. Li for their cooperation and for the pleasant working atmosphere. I acknowledge the friendship and assistance of former members of this light scattering group: Dr. W. Yao, Dr. Mitsugu Matsushita, Dr. Takeshi Shigenari, Dr. B. Y. Gu, Dr. Oscar Mesquita and Dr. M. Awal.

I thank Professor X. D. Xie, Professor N. P. Chang, Professor G. J. Ni, Professor Z. Y. Wang, Professor Z. M. Zhang, Professor Q. M. Jia, Professor H. X. Cai, Professor G. Y. Zheng, Professor D. K. Tang, Professor C. Yuan and many of my colleagues in both Fudan University and CCNY, for their encouragement and help before and after I came to the United States.

I thank all the members of my thesis committee: Professor S. Williamson, Professor M. Tomkiewicz, Professor R. H. Callender and Professor F. W. Smith for their guidance and help.

With special feeling I thank Professor and Mrs. Cummins and Dr. and Mrs. Tritt for their visits and concern for my daughters whom I have not seen for more than 5 years.

I also thank Mrs. Frances Tritt and my wife De Huai Chen for proofreading this thesis.

DEDICATION

I dedicate this thesis to my parents, my wife De Huai Chen, my daughters Dong Qiu and Shuang Qiu, my relatives and friends.

CONTENTS

ABSTRACT

ACKNOWLEDGEMENTS

DEDICATION

CONTENTS

I. INTRODUCTION

A. Definition of an incommensurate phase 1

B. Crystal structure of $NaNO_2$ 2

C. Historical review 5

D. Current research 12

II. INC PHASE TRANSITION UNDER LONGITUDINAL ELECTRIC FIELD

A. Dielectric constant measurements under E-field along the b-axis 15

B. Elastic neutron scattering under E-field along the b-axis 17

C. Theoretical analysis

1. Fourth order free energy model 19

2. Sixth order free energy model 34

D. Diffuse neutron scattering and discussion of the free energy model 42

III. INC PHASE TRANSITION UNDER TRANSVERSE ELECTRIC FIELD

A. Relation of the Lifshitz point to a first order transition from the disordered to the ordered phase 46

B. Elastic neutron scattering under E-field along the a and c axes 55

C. Comparison of the experimental results with the

numerically calculated results 56

IV. BRILLOUIN SCATTERING AND INELASTIC NEUTRON SCATTERING

A. Brillouin scattering under zero E-field 59

B. Brillouin scattering under E-field along the c-axis 61

C. Inelastic neutron scattering 61

D. Discussion 62

V. INC PHASE TRANSITION UNDER HYDROSTATIC PRESSURE

A. Dielectric constant measurements under hydrostatic pressure 65

B. Brillouin scattering under hydrostatic pressure 66

C. Dependence of the Brillouin shift on pressure 67

VI. ISING MODEL

A. Ising model and mean field approximation 69

B. ANNNI model and mean field phase diagram 70

C. The calculated dielectric constant of the ANNNI model under longitudinal electric field 73

VII. MICROSCOPIC THEORY OF MICHEL AND COWORKERS

A. The microscopic model 79

B. Free energy and phase diagram 80

C. Susceptibility and wavevector 83

D. Lattice instability 85

E. Connection between microscopic and phenomenological theories 85

VIII. CONCLUSIONS 87

APPENDICES

A. Units 91

B. Crystal growth of $NaNO_2$ 100

C. Dielectric constant measurement apparatus 103

D. Brillouin scattering apparatus 105

E. Neutron scattering apparatus 108

F. Hydrostatic pressure system 111

G. Computer program listing (TAUROS) 112

TABLE CAPTIONS 120

TABLES 121

FIGURE CAPTIONS 128

FIGURES 138

REFERENCES 201

LIST OF TABLES

Table	Page
1.1	121
4.1	121
A.1	122
A.2	123
A.3	124
E.1	125
E.2	126
H.1	127

LIST OF FIGURES

Figure	Page
1.1	138
1.2	138
1.3	139
1.4	139
2.1	140
2.2	141
2.3	142
2.4	143
2.5	144
2.6	145
2.7	146
2.8	147
2.9	148
2.10	149
2.11	150
2.12	151
2.13	152
2.14	153
2.15	154
2.16	155
2.17	156
2.18	157
2.19	158

Figure	Page
2.20	159
2.21	160
2.22	161
2.23	162
3.1	163
3.2	164
3.3	165
3.4	166
3.5	167
3.6	168
3.7	169
3.8	170
3.9	171
3.10	172
3.11	173
3.12	174
4.1	175
4.2	176
4.3	177
4.4	178
4.5	179
4.6	180
4.7 (a), (b)	181
4.7 (c), (d)	182
4.8	183
5.1	184

Figure	Page
5.2	185
6.1	186
6.2	186
6.3	187
6.4	187
6.5	188
6.6	189
7.1	190
7.2	190
C.1	191
C.2	192
C.3	193
C.4	194
D.1	195
E.1	196
E.2	197
E.3	198
E.4	199
F.1	200

CHAPTER I

INTRODUCTION

A. Definition of an incommensurate phase

In the past two decades incommensurate (abbreviated INC) phases have been observed in many materials and have attracted considerable interest. The INC phase in insulating nonmagnetic crystals is defined as a phase in which the lattice period is modulated with a modulation wavelength which is not a simple multiple of the lattice spacing in the prototypic phase from which it is derived. Usually the INC phase is stable only in a limited temperature range, and there its lattice modulation wavelength generally becomes longer with decreasing temperature. At some temperature a commensurate structure becomes more stable than the INC-structure, and the INC→commensurate "lock-in" phase transition takes place. Thus we have a sequence of prototypic→INC→commensurate phases[1].

The most characteristic features of INC-structures are their diffraction patterns, which consist of primary or parent Bragg reflections in a regular array in reciprocal space, but with each of these reciprocal lattice points acting as an origin for a secondary set of satellite reflections with their own characteristic spacing. In spite of the discrete crystal-like diffraction pattern, INC-structures are not crystalline in the generally accepted sense because they lack periodic translational symmetry. INC-structures do not belong to any of the normal three dimensional space groups[2]. However, de Wolff[3] has discussed a classification for the three-dimensional structures as a cross-section of a hypothetical four-dimensional structure where the added dimension represents the evolution of the actual structure under a continuous change in

the phase of the modulation. The diffraction pattern can be viewed as the projection onto the three "physical" dimensions of a net of four-dimensional reciprocal lattice points.

The possibility of a phase transition leading to a modulated INC phase is implicitly contained in the theory of structural phase transitions developed long ago by Landau and Lifshitz[4]. Crystals where the Lifshitz invariant (composed of terms bilinear in the order parameter components and their spatial first derivatives) is allowed by symmetry represent type I INC systems. INC phases may under certain circumstances occur also in systems where the Lifshitz invariant is forbidden by symmetry (i.e. in type II INC systems such as $NaNO_2$, $Sc(NH_2)_2$ or Cs_2HgBr_4).

INC crystals are interesting from the point of view of basic physics since the breaking of the three-dimensional lattice periodicity destroys one of the most fundamental assumptions of solid state theory. they show a number of new phenomena which are not found in translationally periodic crystals. Since they possess three-dimensional long range order but lack translational periodicity INC systems are intermediate between classical periodic crystals and aperiodic biological systems. The study of INC systems may thus lead to an improved understanding of aperiodic materials and perhaps even living matter[5].

B. Crystal structure of $NaNO_2$

Sodium nitrite ($NaNO_2$) was the first dielectric crystal discovered to exist in an INC phase. It has a simple crystal structure. The crystal structure at room temperature was first determined by Ziegler[6] in 1931. According to his study, $NaNO_2$ has a body centered orthorhombic lattice. Each NO_2^- ion is surrounded by six Na^+ ions in nearest neighbour posi-

tions. Its space group is C_{2v}^{20}--Im2m, i.e. there are two mirror planes perpendicular to the a and c axes and the two fold axis is along the intersection of these planes (parallel to the b-axis). The body-centered orthorhombic unit cell in the low temperature phase is depicted in Fig. 1.1.

Strijk and MacGillavry[7,8] found a phase transition at about 158°C from an abrupt change in the temperature coefficients of the unit cell constants, and found that the low temperature strong piezoelectric effect disappears above this temperature. According to their structure analysis, a third mirror plane perpendicular to the b-axis appears in the high temperature phase, and the space group changes to D_{2h}^{25}--Immm.

The symmetry of the INC-phase of $NaNO_2$ has been discussed by various authors[9-15]. According to Heine[14] the INC phase may be written as:

$$\text{(INC structure)} = \text{(average structure)} + C_1\cos\mathbf{Q}\cdot\mathbf{r} + C_2\sin\mathbf{Q}\cdot\mathbf{r} \qquad (1.1)$$

Where C_1, C_2 are two pure component difference structures with the periodicity of the underlying lattice. The symmetries of C_1, C_2 are two related irreducible representations of the space group Immm of the average structure (equal to the disordered structure at high temperature) associated with the point $\mathbf{q}=0$ of reciprocal space. The C_1 component is the pure ferroelectric alignment of the NO_2^- ions, with the irreducible representation B_{1u} and the symmetry of C_2 is B_{2g}. The symmetry description based on the above formula is fully consistent with the discussion in terms of a four-dimensional space group by Janssen et al[13]. Recently Yamamoto[15] carried out the structure analysis of the INC phase based on the super-space-group $P^{Immm}_{\bar{1}s1}$ to clarify the discrepancy between the super-space-groups deduced from theory and experiment and compare the result with that of the model based on P^{I2mm}_{ss1}. He concluded that the

super-space-group of the INC-phase of $NaNO_2$ is P^{Immm}_{1s1} .

The structure analysis of $NaNO_2$ has been refined by many researchers[16-21]. In each primitive unit cell there is one formula unit both above and below the transition temperature[22,23]. Lattice parameters averaged over several determinations are listed in Table 1.1.

$NaNO_2$ was first shown to be ferroelectric by Sawada et al.[24] in 1958. The ferroelectric axis is the b-axis. It was pointed out that the main contribution to the spontaneous polarization comes from the relative displacement between Na^+ and NO_2^- ions[25]. The contribution of NO_2^- groups to the spontaneous polarization is not larger than 15% of the total, owing to its covalent character[26]. The spontaneous polarization was measured by many reseachers[24-29]. The latest result[29] is shown in Fig. 1.2. The result in Fig. 1.2 demonstrates that there is a discontinouus step of P_s at the Curie temperature of about 6 $\mu c\ cm^{-2}$. A saturation value of P_s = 11.7 $\mu c\ cm^{-2}$ is estimated.

The fact that above the Curie temperature there is no measurable polarization indicates that the ordered arrangement of NO_2^- groups at low temperature become disordered at the transition temperature. The random reorientation of NO_2^- ions along either +b or -b causes the spontaneous polarization to be zero. Sawada and Nomura[25,26] claimed that the transition in $NaNO_2$ is essentially of the displacive type even if it is classified as of the order-disorder type. By microscopic analysis of $NaNO_2$, Michel et al.[30] also concluded that we have in $NaNO_2$ a phase transition of both order-disorder and displacive character.

At the transition temperature, the reorientation of NO_2^- groups can be realized in one of the following two ways: (1) By rotation around the a-axis, or (2) By rotation around the c-axis. Sato et al.[31], and Chisler

et al.[32] supported mechanism (1) from their I.R. absorption and Raman experiments. A sudden change in the frequency ω_2 (153 cm^{-1}) near the Curie temperature was observed. This sudden change near the Curie temperature implies that reorientation of NO_2^- ions is around the a-axis. On the other hand, Betsuyaku[33] from NMR studies of Na in $NaNO_2$, Suzuki et al.[34-37] from their x-ray topographic studies of domain wall growth, Iwaizumi et al.[38] from their ESR experiment on NO_2 radicals, Singh et al.[39] from their ^{14}N nuclear quadrupole resonance experiments, Shibuya et al.[40] from a discussion of x-ray structural results, and Kay[20] and Harada et al.[41] from neutron diffraction results arrived at the same conclusion: the reorientation occurs by rotation around the c-axis. The steric hindrance potential of an NO_2 group in the cage of the six surrounding Na-atoms was calculated numerically by Ehrhadt and Michel[23] and is illustrated in Fig. 1.3, where ψ denotes a rotation around the a-axis and ϕ a rotation around the c-axis. From Fig. 1.3 one comes to the conclusion that the reorientations of NO_2^- groups take place essentially through rotations around the c-axis. Rotations around the a-axis are energetically much less probable. Since the duration of reorientation of a single NO_2^- group in the strong crystallines field is negligibly small in comparison with the lifetime of ferroelectric fluctuations, the angle ψ can be taken equal to zero.

C. Historical review

The existence of an INC-phase of $NaNO_2$ just above the ferroelectric Curie temperature was first suggested by Tanisaki[42] in 1961. His x-ray scattering measurements showed that just above the Curie temperature some of the Bragg reflections developed symmetrical sharp satellites

along the a-axis. The satellites correspond to a periodic modulation of the crystal structure along the a-axis, and the period calculated from the separation between satellite and normal peaks is about 8.4a where a is the lattice constant along the a-axis. The schematic structure of the modulated phase of $NaNO_2$ is depicted in Fig. 1.4.

In 1963, Yamada[43] investigated the temperature dependence of the satellite intensity. He found that with increasing temperature, the integrated intensity of the Bragg reflection decreases quite abruptly and at 163°C distinct satellites peaks appear which are observed in a very narrow temperature range and which become diffuse with increasing temperature. It was concluded that the phase transitions in $NaNO_2$ should be considered in two stages. At 163°C, ferroelectricity disappears at a first order transition and the system becomes antiferroelectric. At about 164°C, the system undergoes another phase transition of second order, becoming paraelectric. Yamada proposed a sinusoidal antiferroelectric structural model in which the successive a-planes have a sinusoidally modulated magnitude of dipoles. According to this model, higher-order satellites should not be observed. Both x-ray diffraction and neutron scattering results support this prediction[43-47].

In 1964, Hamano[48] showed that the dielectric constant ε_b exhibits two peaks (at T_I and T_L) which move together under an applied biasing electric field E_b, merging into a single peak at E_b~3kv/cm. He also found that the piezoelectric coefficient d_{22} exhibits two peaks at low bias field which merge into a single peak at E_b~4kv/cm. Extensive dielectric studies by Hatta[49] and his coworkers revealed that the dielectric constant is strongly frequency dependent, exhibiting Debye-type dispersion with a single relaxation time above T_I. Yamada et al.[50] analyzed the die-

lectric relaxation in terms of an Ising model in which the polar NO_2 groups can flip between two stable (+b, -b) orientations and it was found that the relaxation time of the flipping motion of each NO_2^- group at high temperatures is of the order of 10^{-11} seconds.

Two anomalies, at T_I and T_L were also found in the thermal expansion coefficient by Ema et al.[51] as well as in the specific heat by Hoshino[52] and Sakiyama[53]. With increasing temperature the crystal expands in the a and b direction ,while it contracts in the c direction. The coefficient of thermal expansion in the a direction is larger than that in the b direction. The linear compressibilities of $NaNO_2$ were determined from x-ray diffraction by Hazen et al.[54] and the axial compression ratios in $NaNO_2$ were determined as a : b : c = 1.0 : 0.46 : 0.28 .

In 1965, Gesi et al.[55] investigated the T dependence of the dielectric constant ε_{22} of $NaNO_2$ under hydrostatic pressure. Both T_I and T_L increase with increasing pressure, and the temperature range of the INC-phase broadens with increasing pressure from 1°C at 14.5 psi to about 8°C at 145,000 psi.

Neutron scattering studies of $NaNO_2$ were first reported by Sakurai et al.[56] who investigated the lattice dynamics of both the C_{2v} orthorhombic Im2m ferroelectric structure below T_I and the D_{2h} orthorhombic paraelectric Immm structure above T_I. No soft mode was observed. Neutron and x-ray diffraction experiments on $NaNO_2$ were reported by Durand et al. who also extended their investigation to the effects of applied electric fields[46,57,58].

Diffuse x-ray scattering and diffuse neutron scattering were studied by many researchers[107,108,57]. As temperature is decreased, the intensity of the diffuse scattering becomes stronger and its breadth narrower

and finally it grows into a satellite peak at T_I. The peak position of diffuse scattering is obout 0.12 a* at T_I and increases with increasing temperature to about 0.20 a* at ~ 185°C[108].

Ultrasonic velocity and absorption measurements on $NaNO_2$ were reported by Ota et al.[59], Hatta et al.[60,61], Hatta[62,63] and Esayan et al.[64,65] Distinct anomalies in the elastic constants and absorption coefficients were observed, particularly for C_{11} and C_{22}. Hatta has applied mode coupling theory in analyzing the ultrasonic data to extract the temperature dependent relaxation time of order parameter fluctuations which couple to the acoustic modes in third order. Brillouin scattering in $NaNO_2$ has been investigated by Shimizu et al.[66] and Yagi et al.[67,68]. Anomalies were seen in the Brillouin shifts at T_L and T_I, but they are much weaker than those seen at ultrasonic frequencies because of dispersion. These experiments confirm that the relaxation rates for orientational fluctuations near the transition lie below the hypersonic frequencies relevant to right angle Brillouin scattering. $NaNO_2$ has been investigated by Raman scattering[69,70], infrared absorption[31,37,71,72], infrared reflectivity measurement[22], nuclear magnetic resonance (NMR)[5,33,73,74,75], nuclear quadruple resonance (NQR)[39,76-82], optical second harmonic generation[83-85], D.C. conductivity[86], molecular dynamics calculations[87], and dynamical structure analysis (time resolved x-ray diffractometry) which reveals the nonequilibrium response to a pulsed biasing field[88].

Many theoretical discussions of the phase transition in $NaNO_2$ have been presented over the years. The principal theories can be roughly divided into three categories:

1. Phenomenological theory

A phenomenological theory of the INC transition in $NaNO_2$ has been proposed by Levanyuk et al.[9,10]. They considered the situation where a one-component order parameter η couples with a generalized coordinate ξ which has transformation properties different from η. Although a Lifshitz invariant[4] is absent in the case of a one-component order parameter, the existence of gradient invariants of type $\eta\delta\xi/\delta z$ and $\xi\delta\eta/\delta z$ leads to a phase transition with an INC structure.

Heine et al.[11,89] have developed a macroscopic approach for the description of the INC transition in $NaNO_2$. The theory is based on the existence of a subsidiary mode which can only have an interaction with the main mode at nonzero wave vector. In case of $NaNO_2$, the lattice shear is the subsidiary mode.

Another Landau free energy expansion was developed for the INC phase transition of $NaNO_2$ by Ishibashi et al.[1,90,91]. Ishibashi and Shiba proposed a simple model in which the instability of the prototypic phase occurs for a given wavenumber k_o quite close to the Γ point ($k=0$) and the representation at the Γ point is one dimensional. The INC state of the model and its dielectric properties were analysed by taking harmonics into account. Ishibashi pointed out that the η-term in their free energy which is of fourth power in the polarization P and of second power in the modulation wavevector k plays an important role for the successive phase transitions in $NaNO_2$.

In a recent paper by Ema et al.[92] the role of the different terms in the free energy has been estimated on the basis of the smalless of the temperature width in which the INC-phase exists. A consistent phenomenological theory for dielectric anomalies near type-II lock-in transition

has been developed. The effect of the gap between homogeneous and inhomogeneous values of the coefficients of the fourth power of the order parameter due to the long-range elastic force is considered. The possibility of applying this theory to the case of $NaNO_2$ was also discussed.

2. Ising model

The reversal of electric dipoles, each of which is composed of a NO_2^- ion and the nearest neighbouring Na^+ ion is capable of being treated theoretically as a motion of Ising spins. The INC phase transition in $NaNO_2$ was first discussed on the basis of the Ising model by Yamada et al.[43]. The successive appearance of three phases, the order of transitions , and the temperature dependence of the order parameter were satisfactorily explained by their calculations. Yamada and Hatta[50] applied a random phase approximation to an Ising variable system to explain the susceptibility and to calculate the relaxation time of the flipping motion of each NO_2^- ion.

Bak and von Boehm[93] developed a computational procedure for analyzing INC→commensurate phase transition in ANNNI system (Ising system with competitive interactions, nearest and next nearest neighbour interactions). Within the mean field approximation, they calculated the global ANNNI phase diagram. Yamada[94] proposed an "EXAFII" model, i.e. Extended Antiferroelectric Interaction Ising model which extends the ANNNI model to third nearest neighbours. Within this model, each substance is characterized by a point in a two-dimensional interaction parameter space. This model gave a unified view of INC→commensurate phase transition in A_2BX_4 type crystals.

Recently Selke et al.[95] have studied the mean field equations of the simple cubic ANNNI model in a field and compared their results to experinments on $NaNO_2$ in an electric field. The gross features of the phase diagram of $NaNO_2$ can be reproduced, but the value of $T_I - T_L$ is much larger than the experimental result.

3. Microscopic theory

Starting from a sterical hindrance potential for the motion of the NO_2^- molecular group in the deformable cage of neighbouring Na^+ ions, Ehrhardt and Michel[23], Michel[30,96,97], and Fivez and Michel[98] derived a microscopic model for the $NaNO_2$ crystal. The model leads to a Hamiltonian with bilinear coupling between translation and rotation with a wavevector-dependent coupling constant. At finite wave vector, molecular reorietations of NO_2^- groups around the crystallographic c-axis are coupled to acoustic lattice displacements. A modulation along the a-axis of nonequilibium expectation values of the orientational order produces a modulation of expectation values of acoustic displacements with polarization in the b direction. The INC transition corresponds to a freezing-in of both types of motion.

Recently Heine et al.[14] have extended Michel's theory to include the short range electrostatic forces due to the distribution of charge in the nitrite together with the repulsive parts of the interionic potential as well as steric hindrance with both the nearest six sodium ions and the neighbouring eight NO_2^- ions to explain what they believe is the correct sign of the displacement modulation, namely a displacement in the positive b direction where the nitrogen of the NO_2^- is oriented along the positive b-axis.

Lynden-Bell et al.[99] have noted the following connection between the work of Michel and coworkers and that of Heine and McConnell: Michel and coworkers have shown that the inclusion of a phonon-reorientation coupling term in the microscopic Hamiltonian of the system can account for the paraelectric→INC transition. Heine and McConnell, on the other hand, have discussed the conditions for the formation of INC-phase in terms of the parameters that appear in the expression for the macroscopic free energy. Although these two theories emphasized different aspects of the problem, the Michel Hamiltonian also leads to the Heine-McConnell form for the free energy.

D. Current research

Despite this wealth of experimental and theoretical research on $NaNO_2$, several fundamental questions remain unanswered. Among them are:

1. How do the phase transition diagram and the modulation wave vector change with both longitudinal and transverse electric field as well as with hydrostatic pressure?

2. Does a Lifshitz point or another new critical point exist in $NaNO_2$?

3. How well do the phenomenological theory, the Ising model and the microscopic theory describe the INC-phase transition in $NaNO_2$? What is the connection between them?

In order to investigate these and related questions I have carried out the following experiments and theoretical analysis on $NaNO_2$:

a. Experiments

1) Dielectric constant measurements under E-field along the b-axis.

2) Elastic neutron scattering under E-field along the b-axis.

3) Elastic neutron scattering under E-field along the a-axis.

4) Elastic neutron scattering under E-field along the c-axis.

5) Brillouin scattering under E-field along the c-axis.

6) Inelastic neutron scattering.

7) Diffuse neutron scattering.

8) Dielectric constant measurements under hydrostatic pressure.

9) Brillouin scattering under hydrostatic pressure.

Experiments 3), 4), 5) were first done by us. In experiment 2) some important new results were first obtained by us. We performed experiment 2) independently of Durand et al[46]. at almost the same time. Durand et al. put the temperature sensor quite far away from the sample; therefore, they corrected the phase transition temperature for different fields; the maximum correction was about 0.5°C while the whole temperature range of the INC-phase under that E-field is less than 0.5°C. For this reason, it was impossible for them to obtain the correct behavior of the modulation wavevector under the longitudinal electric field. We performed the same experiment with the thermister touching the sample so that both the phase transition diagram and the E-field dependence of the wave vector were obtained without temperature correction for different fields.

b. Theoretical analysis

1) By numerically minimizing the Landau free energy, the complete predictions of different Landau free energy expansions for the phase

diagram and the behaviour of the modulation wave vector under E-field along the b-axis were explored. All the coefficients in the free energy have been determined from the dielectric constant measurements, the neutron scattering results and the spontaneous polarization data.

2) Several analyses of the free energy models proposed by Ishibashi et al.[90,91] were made. Comparison of our diffuse neutron scattering results with the predictions of the free energy model indicates that the η-term in the free energy cannot be neglected, and that the temperature dependence of the coefficient α should also be included. We found another reason that the η-term cannot be neglected: without the η-term the phase transition from the para-phase to the INC-phase will be of first order while the observed para→INC transition is of second order.

3) The relation of the Lifshitz point to a system exhibiting a first-order transition from the disordered phase to the ordered phase has been analyzed in detail. By fitting our data of elastic neutron scattering under transverse electric field to the numerically calculated results we can determine where the virtual Lifshitz point should occur and construct the whole phase transition diagram.

4) Using the ANNNI model, numerical calculations of dielectric constants under longitudinal electric field were carried.

5) The microscopic theory of Michel and coworkers[23,30,96,97,98] was reviewed. Some of the results of the microscopic theory are cited for comparison with the results of the phenomenological theory and the Ising model.

CHAPTER II

INC PHASE TRANSITION UNDER LONGITUDINAL ELECTRIC FIELD

In this chapter we present our experimental results of dielectric constant measurements and elastic neutron scattering performed on $NaNO_2$ under an electric field applied along the b-axis. Then we present our theoretical analysis based on the Landau free energy.

A. Dielectric constant measurements under E-field along the b-axis

We began our experimental study of $NaNO_2$ by measuring the temperature-dependent dielectric constant as a function of electric field along the b-axis. $NaNO_2$ crystals were grown from the melt in our laboratory following procedures suggested by Professor Y. Ishibashi (see Appendix B). The size of a b-cut sample was typically 0.2 cm^2 by 0.14 cm thick. Selection of samples used for the dielectric constant measurements was determined by the mosaic observed in neutron diffraction at Brookhaven National Laborotory (BNL). A gold thin film was deposited by vacuum evaporation on the surfaces of the sample perpendicular to the b-axis. Capacitance measurements were carried out with a general radio 716C capacitance bridge excited at 1kHz with a one volt per centimeter sine wave. The capacitance measurements are described in Appendix C. The sample holder and the oven are also shown in Appendix C. The oven was designed and built at BNL for the neutron scattering experiment and was also used for the dielectric constant measurements. The temperature was measured by a thermistor mounted inside the oven touching the sample. The relative accuracy of the temperature determination was better than 0.01°C.

The rate of temperature change was reduced to about 0.2°C/hour near the transition temperatures of $NaNO_2$. The oven was evacuated to about $5x10^{-3}$ Torr to minimize the water vapor attacking the sample, as $NaNO_2$ is hygroscopic.

Fig. 2.1 shows the zero-field ε versus T curve which was measured during cooling of the sample. The peak on the right is at the INC transition temperature T_I = 163.86°C from the paraelectric to the INC-phase while the peak on the left is at the lock-in transition temperature T_L = 162.50°C from the INC to the ferroelectric phase. A comparison between measurements performed during cooling and heating is shown in Fig. 2.2. At T_L, thermal hysteresis of about 0.2°C was observed, which is in agreement with those observed by Buchheit and Petersson[29]. Therefore, the lock-in transition is of first order while the INC transition is of secod order. A series of ε versus T curves at increasing bias field E_b is shown in Fig. 2.3. The two peaks of the dielectric constant move towards each other under an applied biasing electric field E_b, merging into a single peak at E_b~3 kv/cm. Plotting T_I and T_L versus E_b leads to the phase diagram shown in Fig. 2.4. The point at which the two transition lines meet is called a triple point. At this triple point the three phases, para, INC and ferro coexist. Let E_t be the electric field at the triple point. The value of E_t has been determined by several authors as follows:

E_t = 2 kV/cm, dielectric constant meassurements, by Hamano[48].

E_t = 2.6 kV/cm, dielectric constant meassurements, by Gesi[109].

E_t = 3.4 kV/cm, neutron scattering, by Durand et al[46].

E_t = 4.0 kV/cm, x-ray diffraction, by Yamada[110].

One possible origin of such disagreement is the finite electrical conductivity of the sample which may cause uncertainties in the actual value of the applied field.

B. Elastic neutron scattering under E-field along the b-axis

During August of 1982 we initiated a study of the temperature and electric field dependence of the satellite structure in the INC-phase of $NaNO_2$ at the high flux beam reactor at BNL in collaboration with Dr. S. Shapiro. For this experiment a sample (typically 0.45 x 0.15 x 0.45 cm^3) with gold electrodes evaporated on the b-faces was mounted on a triple-axis spectrometer with the c-axis vertical in a temperature controlled oven which is the same one as used in the dielectric constant measurements. The temperature of the oven was controlled by an Omega proportional temperature controller and by constantly monitoring the temperature readout. The temperature was maintained constant to better than 0.01°C, and our measurements were completely reproducible. This is an important consideration since there is a current through the sample when a field is applied, producing an ohmic heating of the sample. The oven was evacuated to about 5×10^{-3} Torr. All scans were performed during cooling. The incident neutrons were fixed at an energy of 14.7 meV and were collimated to yield a FWHM resolution of $0.006a^*$ (0.01Å^{-1}) and $a^* = 2\pi/a$ is the reciprocal lattice vector. Scans of elastic scattering were taken through the (020) Bragg peak. A typical scan shows the main (020) Bragg peak flanked by two satellites as illustrated in Fig. 2.5. The scan is along the a-axis with δ (the position of the satellite peak in units of a^*) ranging over $\pm 0.25a^*$. Similar scans were taken over extended ranges ($\pm 0.5a^*$) to see if second or third harmonics could be observed.

None were seen, indicating that the INC modulation remains strictly sinusoidal throughout the INC range This was also true with applied field.

From scans like that of Fig. 2.5 we found the satellite intensity and the modulation wavevector δ (the position of the satellite peak in units of a^*) as a function of temperature at different bias fields. The results of these measurements are shown in Fig. 2.6 and 2.7. Fig. 2.6 shows that the satellite intensity increases as T is lowered through T_I and, after reaching a maximum, decreases again near T_L, and that the satellite intensity decreases with increasing bias field E_b. Fig. 2.7 shows that δ decreases monotonically for decreasing T between T_I and T_L and is essentially independent of E_b. Plotting the transition temperatures T_I and T_L versus E_b leads a phase diagram which is similar to that shown in Fig. 2.4.

We note that our results are in disagreement with those of Durand et al. who found that the satellite intensity increases monotonically as T is lowered from T_I to T_L, decreasing discontinuously to zero at T_L[58]. In order to determine the reason for this discrepancy we performed a special experiment on a sample generously provided by Professor T. Yagi. The full half-width of the (020) Bragg peak was 0.12 degrees which indicates that the mosaic of this sample is quite small. The sample was wrapped in aluminum foil to insure uniform temperature throughout the sample when it was heated. Much attention was paid to the temperature control. The temperature was maintained constant to better than 0.002°C. We spent more than 5 hours to obtain the data within 0.15°C in the vicinity of T_L. The result shown in Fig. 2.8 agrees with our previous results. Note that the temperature range between the maximum value and the zero value of the intensity of the satellite in the vicinity of T_L is about

0.1°C. One possible reason for the discrepancy between our results and Durand's is that Durand et al. put the temperature sensor far away from the sample, and therefore the temperature reading in their experiment was not the real temperature of the sample. Another is that our sample contain more impurities so that the transition does not occur everywhere in the crystal simultaneously.

C. Theoretical analysis

Our theoretical analysis is based on the Landau free energy expansion proposed by Ishibashi and Shiba[90,91]. Wherever Analytic solution of the equations of minimization was not possible, we have minimized the free energy by using a nonlinear least squares computer program to vary the parameters in the free energy until a minimum is obtained, a procedure which avoids the approximations required by the algebraic method[46,58]. The program listing appears in Appendix G.

1. Fourth order free energy model

We first carry out an analysis using a free energy restricted to terms quadratic and quartic in the order parameter. This implies that the direct para→ferro transition would be second order. A more realistic free energy requiring sixth power term is analyzed in the next section.

Following Ishibashi and Shiba[90], we write the free energy density as:

$$f(x) = \frac{1}{2}AP^2 + \frac{1}{4}BP^4 + \frac{1}{2}\alpha(\nabla P)^2 + \frac{1}{4}\beta(\nabla^2 P)^2 + \frac{1}{4}\eta P^2(\nabla P)^2 - E\cdot P \qquad (2.1)$$

where P (the polarization P_b) is the order parameter

$A = A_o(T - T_o)$, $B>0$, $\alpha<0$, $\beta>0$, $\eta>0$

E is the electric field E_b applied along the b-axis.

The integrated free energy density is:

$F = \frac{1}{L} \int f(x)dx$ where x is along the a-axis

L is the length of the crystal

The first, third and fourth terms in (1) are quadratic (harmonic) with respect to the order parameter P, while the second term represents the anharmonicity in the homogeneous part of the free energy. As pointed out by Ishibashi et al.[90], the meaning of the terms $(\frac{dP}{dx})$ and $(\frac{dP^2}{dx^2})^2$ becomes clear if the differential forms are transformed into the difference forms as $(P_n - P_{n-1})^2$ and $(P_{n+1} - 2P_n + P_{n-1})^2$, respectively. The former represents interaction between the nearest neighbour planes (planes are taken to be perpendicular to the a-axis), while the term $P_{n+1} \cdot P_{n-1}$ included the second nearest neighbor planes. The η-term is required to make the modulation wavevector change with temperature as observed experimentally (Fig. 2.7).

a. Free energy in the ferroelectric phase: F^{ferro}

In the ferro-phase $P=P_o$ $\therefore \nabla P=0$

$$F^{ferro} = \frac{1}{2}AP_o^2 + \frac{1}{4}BP_o^4 - EP_o \qquad (2.2)$$

$$\frac{\partial F^{ferro}}{\partial P_o} = AP_o + BP_o^3 - E = 0$$

$$AP_o + BP_o^3 = E \qquad (2.3)$$

For given E and T, P_o can be obtained by solving Eq. (2.3); then the free energy F^{ferro} can be calculated by substituting P_o into (2.2).

In the case E=0, Eq. (2.3) gives:

$$P_0^2 = -\frac{A}{B} \tag{2.4}$$

$$\therefore F^{ferro} = -\frac{A^2}{4B} \tag{2.5}$$

For calculation of the free energy, all the coefficients in the free energy expansion must be known. The determination of the coefficients will be discussed in section f.

b. Free energy in the INC-phase: F^{inc}

The elastic neutron scattering of $NaNO_2$ indicates that the INC modulation remains strictly sinusoidal throughout the INC range. Therefore the plane wave solution can be taken in the INC-phase:

$$P = P_0 + P_k \cos kx \tag{2.6}$$

where x is along the a-axis, k is the modulation wavevector and $k = \delta \cdot a^*$. Here δ is the reduced wavevector (the separation between the Bragg peak and the satellite peak in units of a^*) and a^* is the reciprocal lattice constant. The integrated free energy density is:

$$F^{inc} = \frac{1}{2}AP_0^2 + \frac{1}{4}BP_0^4 + \frac{1}{4}A_kP_k^2 + \frac{3}{8}(B + B_k)P_0^2P_k^2 + \frac{3}{32}B_kP_k^4 - EP_0 \tag{2.7}$$

where
$$A_k = A + \alpha k^2 + \frac{1}{2}\beta k^4$$

$$B_k = B + \frac{1}{3}\eta k^2 \tag{2.8}$$

$$A = A_0(T - T_0)$$

There are two ways to calculate F^{inc}, that is to find the values of P_0, P_k and k that minimize it and evaluate it for these values:

1). By solving the equations of minimization:

$$\frac{\partial F^{inc}}{\partial P_o} = 0$$

$$AP_o + \frac{3}{4}(B + B_k)P_k^2 P_o + BP_o^3 = E \tag{2.9}$$

$$\frac{\partial F^{inc}}{\partial P_k} = 0$$

$$A_k + \frac{3}{2}(B + B_k)P_o^2 + \frac{3}{4}B_k P_k^2 = 0 \tag{2.10}$$

$$\frac{\partial F^{inc}}{\partial k} = 0$$

$$k^2 = -\frac{\alpha}{\beta} - \frac{n}{2\beta}P_o^2 - \frac{n}{8\beta}P_k^2 \tag{2.11}$$

P_o, P_k and k can be obtained by solving the simultaneous equations (2.9), (2.10) and (2.11), then the free energy F^{inc} can be calculated by substituting P_o, P_k and k into Eq. (2.7).

2). By numerically minimizing the free energy:

A computer program can vary the three parameters P_o, P_k and k to minimize the free energy F^{inc}. For given E and T, the computer program gives the minimized free energy as well as the three parameters.

c. The INC→ferro phase transition line

The lock-in transition occurs when the minimum value of F^{ferro} crosses the minimum value of F^{inc}. Therefore, for given E-field, the lock-in transition temperature $T_L(E)$ can be obtained by setting $F^{inc}(E) = F^{ferro}(E)$. The $T_L(E)$ versus E curve is just the the INC→ferro phase transition line.

In the case η=0 and E=0, P_o can be dropped in Eqs. (2.6) and (2.7). Eq. (2.7) becomes:

$$F^{inc} = \frac{1}{4}A_k P_k^2 + \frac{3}{32}BP_k^4$$

Eq. (2.10) gives: $P_k^2 = -\frac{4}{3B}A_k$

$$\therefore F^{inc}(\eta=0,E=0) = -\frac{A_k^2}{6B} \tag{2.12}$$

By setting $F^{ferro} = F^{inc}$ i.e. $-\frac{A^2}{4B} = -\frac{A_k^2}{6B}$

we have: $$T_L(0) = T_o - 2.2247\ \frac{\alpha^2}{A_o\beta} \tag{2.13}$$

$T_L(0)$ is the lock-in transition temperature with E=0, η=0.

d. The para→INC phase transition line

The para→INC phase transition line can be obtained by setting the coefficient of P_k^2 in Eq. (2.7) equal to zero i.e.

$$\frac{1}{4}A_k + \frac{3}{8}(B + B_k)P_o^2 = 0$$

or $$A_k + \frac{3}{2}(B + B_k)P_o^2 = 0 \tag{2.14}$$

Comparison of Eq. (2.14) with Eq. (2.10) leads to:

$$P_k = 0 \quad \text{at } T = T_I(E) \tag{2.15}$$

where $T_I(E)$ is the para→INC phase transition temperature under electric field E_b.

Eq. (2.15) means that for each given E-field, the para→INC phase transition temperature can be obtained as the temperature where $P_k \to 0$. The P_k versus T curve can be obtained by numerically minimizing the free energy, and therefore $T_I(E)$ can be determined numerically.

In the case E=0, P_o is equal to zero in both the para and the INC phases. According to Eq. (2.14) the para→INC transition then occurs at A_k=0

$$\text{i.e.} \quad A_o(T_I(0) - T_o) + \alpha k^2 + \frac{1}{2}\beta k^4 = 0 \tag{2.16}$$

At $T = T_I(0)$ $\quad P_k = 0$, Eq. (2.11) becomes:

$$k_I^2(0) = -\frac{\alpha}{\beta} \tag{2.17}$$

Substituting Eq. (2.17) into Eq. (2.16) we get:

$$T_I(0) = T_o + \frac{\alpha^2}{2A_o\beta} \tag{2.18}$$

Combination of Eq. (2.13) with Eq. (2.18) gives:

$$T_I(0) - T_L(0) = 2.7247\ \frac{\alpha^2}{A_o\beta} \tag{2.19}$$

$T_I(0)$ and $T_L(0)$ can be obtained from the dielectric constant measurement which gave:

$$T_I(0) = 163.86°C \quad \text{and} \quad T_L(0) = 162.50°C$$

$$\therefore \quad \frac{\alpha^2}{\beta} = 0.49914A_o$$

$$T_o = T_I(0) - \frac{\alpha^2}{2A_o\beta} = 163.61°C \tag{2.20}$$

e. Dielectric constant

In CGS units, the susceptibility $\quad \chi = (\frac{\partial P}{\partial E})_T$ (2.21)

The dielectric constant $\quad \varepsilon = 1 + 4\pi\chi$

In practice ε can be written as: $\quad \varepsilon = \varepsilon_b + 4\pi\chi$ (2.22)

where ε_b is the background value of ε. This includes the contribution to χ from degrees of freedom other than the order parameter.

1). Dielectric constant in the ferroelectric phase

$$F_{ferro} = \frac{1}{2}AP_o^2 + \frac{1}{4}BP_o^4 - EP_o \tag{2.2}$$

And P_o satisfies $\quad AP_o + BP_o^3 = E$ (2.3)

$$(\frac{\partial E}{\partial P_o})_T = A + 3BP_o^2 = (\frac{\partial^2 F ferro}{\partial P_o^2})$$

$$X = (\frac{\partial P_o}{\partial E})_T = (\frac{\partial^2 F ferro}{\partial P_o^2})^{-1} \qquad (2.23)$$

$$\therefore \chi ferro = (A + 3BP_o^2)^{-1}$$

$$\therefore \varepsilon^{ferro} = \varepsilon_b + \frac{4\pi}{A + 3BP_o^2} \qquad (2.24)$$

In the case E=0, we have from (2.4): $P_o^2 = -\frac{A}{B}$ (2.4)

$$\therefore \varepsilon^{ferro} = \varepsilon_b + \frac{2\pi}{A_o(T_o - T)}$$

$$(\varepsilon^{ferro} - \varepsilon_b)^{-1} = \frac{A_o(T_o - T)}{2\pi} = \frac{A_oT_o}{2\pi} - \frac{A_oT}{2\pi}. \qquad (2.25)$$

Eq. (2.25) indicates that in the case E=0 the inverse of the dielectric constant in the ferro-phase is a straight line which has a negative slope and extrapolates to zero at $T = T_o$.

2). Dielectric constant in the paraelectric phase

In the para-phase with an E-field along the b-axis, $P = P_o \neq 0$

$$\therefore F^{para} = \frac{1}{2}AP_o^2 + \frac{1}{4}BP_o^4 - EP_o \qquad (2.26)$$

where $A = A_o(T - T_o)$ with $T > T_o$

$$\therefore \varepsilon^{para} = \varepsilon_b' + \frac{4\pi}{A + 3BP_o^2} \qquad (2.27)$$

where ε_b' is the background value of ε^{para}.

If E=0, then $P_o = 0$

$$\therefore \varepsilon^{para} = \varepsilon_b' + \frac{4\pi}{A_o(T - T_o)} \qquad (2.28)$$

$$(\varepsilon^{para} - \varepsilon_b')^{-1} = \frac{A_o(T - T_o)}{4\pi} = \frac{A_oT}{4\pi} - \frac{A_oT_o}{4\pi} \qquad (2.29)$$

Therefore, in the case of zero E-field, the inverse dielectric constant in the para-phase is a straight line too, but the slope is pos-

itive. It also extrapolates to zero at $T = T_o$.

Comparing Eq. (2.25) with Eq. (2.29) we have:

$$\frac{(\varepsilon^{ferro} - \varepsilon_b)^{-1}}{(\varepsilon^{para} - \varepsilon_b')^{-1}} = -2 \tag{2.30}$$

Note: at $T = T_o$ both $(\varepsilon^{ferro} - \varepsilon_b)^{-1}$ and $(\varepsilon^{para} - \varepsilon_b')^{-1}$ equal zero. This means that the two staight lines meet at the point $T=T_o$.

3). Dielectric constant in the INC-phase

In the INC-phase:

$$\chi = \left(\frac{\partial^2 F^{inc}}{\partial P_o^2}\right)^{-1} = \frac{1}{A + 3BP_o^2 + \frac{3}{4}(B + B_k)P_k^2}$$

$$\therefore \quad \varepsilon^{inc} = \varepsilon_b'' + \frac{4\pi}{A + 3BP_o^2 + \frac{3}{4}(B + B_k)P_k^2} \tag{2.31}$$

where ε_b'' is the background value of ε^{inc}.

P_o, P_k and k satisfy Eqs. (2.9), (2.10) and (2.11).

f. The coefficients A_o, T_o, B, α, β and η

1). The coefficient T_o

Eq. (2.20) gives: $T_o = 163.61\,^{\circ}C$

This means that in the case of the fourth order free energy model, the coefficient T_o is fixed.

2). The coefficient A_o

Eq. (2.25) and Eq. (2.29) indicate that in both the ferro and the para phases the inverse dielectric constants are straight lines. The coefficients A_o and T_o can be calculated from the slopes and the intercepts of these straight lines. Fig. 2.9 shows the inverse of the dielec-

tric constants of $NaNO_2$ (the discrete points) of Fig. 2.1. Because the values of the dielectric constant of $NaNO_2$ are very large, their inverses are very small. Therefore in Fig. 2.9 the ordinate represents the value of $\frac{1000}{\varepsilon - \varepsilon_b}$. Eq. (2.25) and Eq. (2.29) can be rewritten as:

$$\frac{1000}{\varepsilon_{ferro} - \varepsilon_b} = \frac{1000A_oT_o}{2\pi} - \frac{1000A_oT}{2\pi} \tag{2.32}$$

$$\frac{1000}{\varepsilon_{para} - \varepsilon_b'} = -\frac{1000A_oT_o}{4\pi} + \frac{1000A_oT}{4\pi} \tag{2.33}$$

The expressions (2.32) and (2.33) can be used to fit the experimental data. The solid lines in Fig. 2.9 are the fitting results. The equations for these two straight lines are:

In the ferro-phase $\quad y = 286.12 - 1.7523x$ (2.34)

In the para-phase $\quad y = -24.476 + 0.1507x$ (2.35)

The ratio of the slopes of the two straight lines is about -12 which is in agreement with the result of Buchheit and Petersson[29], but in severe disagreement with Eq. (2.30).

In the ferro-phase the coefficients A_o and T_o can be determined from Eq. (2.32) and Eq. (2.34) as:

$A_o = 1.1010 \times 10^{-2}$ (in CGS units) (2.36)

$T_o = 163.28°C$

In the para-phase from Eq. (2.33) and Eq. (2.35) we have:

$A_o = 1.8938 \times 10^{-3}$ (in CGS units) (2.37)

$T_o = 162.42°C$

The values $\varepsilon_b = \varepsilon_b' = 880$ were chosen to give the best fit of the linear equations (2.32) and (2.33) to the experimental data.

The severe disagreement between the two values of A_o has never been explained.

We note that in the present case of the fourth order free energy model, the value of T_o given in Eq. (2.36) is much closer to the prediction of Eq. (2.20) than that given in Eq. (2.37). Therefore we have taken the value of A_o from the ferro-phase data. It should also be pointed out that the value of A_o in Eq. (2.36) was obtained from the zero E-field data; hence it is necessary to adjust this value to find a proper value of A_o which is suitable for different E-fields. We have also tried to fit the experimental data of dielectric constant under different electric field using Eq. (2.24) and treating ε_b, A_o and B as parameters. The computer program gives the fitted dielectric constant as well as the parameters. One set of the values of the coefficients A_o and B obtained in this way was used to calculate the phase diagram which is shown in Fig. 2.10. The value of A_o is:

$$A_o = 3.4407 \times 10^{-2} \quad \text{(in CGS units)}$$

3). The coefficient B

In the ferro-phase Eq. (2.4) gives:

$$P_o^2 = \frac{A_o(T_o - T)}{B}$$

$$\therefore B = \frac{A_o(T_o - T)}{P_o^2} \tag{2.38}$$

where P_o is the spontaneous polarization which can be estimated from Fig. 1.2 as:

$$P_o \approx 11 \left(\frac{\mu C}{cm^2}\right) \approx 3.300 \times 10^4 \text{ (cgs)} \quad \text{at } T = 120^\circ C$$

$$\therefore B \approx 1.3778 \times 10^{-9} \quad \text{(in CGS units)}$$

The value of B used for obtaining the theoretical phase diagram shown in Fig. 2.10 is:

$B = 1.3124 \times 10^{-9}$ (in CGS units)

This value of B was chosen in the same way as for A_o.

4). The coefficients α and β

Eq. (2.17) gives: $\frac{\alpha}{\beta} = -k_I^2(0)$ (2.39)

Eq. (2.18) gives: $\frac{\alpha^2}{\beta} = 2A_o(T_I(0) - T_o)$ (2.40)

$k_I(0)$ can be obtained from the elastic neutron scattering data as:

$$k_I^2(0) = (a^* \cdot \delta)^2 = (\frac{2\pi}{a} \cdot \delta)^2 = 4.3750 \times 10^{14} \quad (cm^{-2}) \qquad (2.41)$$

where $a = 3.6647$ Å is the lattice constant along the a-axis at $T = T_I(0)$.

Taking $A_o = 3.44070 \times 10^{-2}$ and $T_o = 163.61°C$ then:

$\alpha = -3.9255 \times 10^{-17}$ (in CGS units)

$\beta = 8.9730 \times 10^{-32}$ (in CGS units)

These values of α and β were used to obtain the phase diagram shown in Fig. 2.10. The units of these and other parameters of the free energy are discussed in Appendix A.

5). The coefficient η

The value of η can be determined by fitting the theoretical modulation wavevector curve to the experimental results as illustrated in Fig. 2.13. The value found from fits is:

$\eta = 1.9709 \times 10^{-24}$ (in CGS units)

There is another way to estimate the value of η which is described as follows.

At $T = T_I(E)$, $P_k = 0$ (see Eq. (2.15)), from Eqs. (2.11) and (2.17) we have

$$k_I^2(E) - k_I^2(0) = -\frac{\eta}{2\beta}P_0^2 \tag{2.42}$$

Eq. (2.9) gives

$$AP_0 + BP_0^3 = E \tag{2.43}$$

$$\text{where } A = A_0(T_I(E) - T_0) \tag{2.44}$$

For roughly estimating the value of η, here we assume that

$AP_0 \approx E$ or

$$P_0 \approx \frac{E}{A} = \frac{E}{A_0(T_I(0) - T_0)} \tag{2.45}$$

Substituting (2.45) into (2.43) we get

$$k_I^2(E) - k_I^2(0) = -\frac{\eta E^2}{2\beta A_0^2(T_I(0) - T_0)^2} \tag{2.46}$$

From the experimental results of elastic neutron scattering we can get the value of $k_I^2(E) - k_I^2(0)$ for given E, then we can calculate η using Eq. (2.46), since all the quantities (except η) are known. The estimated value of η is

$$\eta = 1.1709 \times 10^{-23} \quad \text{(in CGS units)}$$

Starting from this value we tried to fit the thoeretical modulation wavevector curve to the experimental results, and ajusted this value of η until the best fit was obtained.

g. The calculated phase diagram

Fig. 2.10 shows the calculated phase diagrams with different η values. The other coefficients are:

$$A_0 = 3.4407 \times 10^{-2}$$

$$B = 1.3124\times10^{-9}$$

$$\alpha = -3.9255\times10^{-17} \qquad \text{(in CGS units)} \qquad (2.47)$$

$$\beta = 8.9730\times10^{-32}$$

$$T_o = 163.61^{\circ}C$$

The procedure for obtaining the phase diagrams shown in Fiq. 2.10 was as follows:

1). Substitute the values of all the coefficients in Eq. (2.47) and η into the free energy.

2). Use the method of numerically minimizing the free energy to obtain the equilibrium free energy and the corresponding three parameters, P_o, P_k and k.

3). The transition temperature T_L was obtained by setting $F^{inc} = F^{ferro}$. Fig. 2.11 depicts the F^{inc} and the F^{ferro} at zero E-field. The intersection determines the transition temperature T_L. For different E-fields, $T_L(E)$ was determined in the same way.

4). The transition temperature T_I was taken as the temperature where $P_k \to 0$. Fig. 2.12 shows P_k versus T for zero field. The end point of the curve on the abscissa gives T_I. For different E-fields $T_I(E)$ was obtained by this procedure.

Plotting $T_I(E)$ and $T_L(E)$ versus E-field for different values of η leads to the phase diagrams shown in Fig. 2.10.

h. The modulation wavevector

Fig. 2.13 shows the calculated modulation wavevector versus temperature with different η values. The discrete points are the experimental results. If η=0, the modulation wavevector k is temperature independent (see Eq. (2.17)), while if η is not zero then the modulation wave-

vector k is temperature dependent. The value of η can be determined by fitting the theoretical curve to the experimental results as shown in this figure. The value of η for the solid line in Fig. 2.13 is: $\eta = 1.9709 \times 10^{-24}$ (in CGS units).

Note that the calculated modulation wavevector does not depend on the longitudinal E-fields. In other words, all the δ versus T curves for different E-field are coincident, which agrees with our experimental results.

Since the temperature range of the INC-phase decreases with increasing E-field, hence the length of the δ versus T curve decreases with increasing E-field. Let $\delta_I(E)$ and $\delta_L(E)$ represent the wavevector at $T_I(E)$ and $T_L(E)$ respectively. Then both the experimental and theoretical results show that $\delta_I(E)$ decreases with increasing E-field while $\delta_L(E)$ increases with increasing E-field.

Our results are in disagreement with those of Durand et al.[58] who concluded that the modulation wavevector is a decreasing function of the applied field[58] from the fact that $\delta_I(E)$ depends on E.

In contrast to the case of a longitudinal E-field, our results in Chapter III will show that in the case of a transverse E-field the modulation wavevector is E-field dependent.

i. The intensity of satellites

According to Tanisaki[42] and Yamada[43], the intensity of the satellites is propotional to P_K^2. Fig. 2.14 shows the calculated P_K^2 versus temperature for E=0. Comparison of Fig. 2.8 with Fig. 2.14 indicates that in the temperature region of $T_L < T < T_I$, the intensity distribution of the satellite can be roughly explained by the Landau free enegy expansion,

but in the region of $T \approx T_L$ the theoretical result is in disagreement with the experimental result.

j. The dielectric constant

Eq. (2.21) and Eq. (2.22) give the dielectric constant as:

$$\varepsilon = \varepsilon_b + 4\pi\frac{\delta P_o}{\delta E}$$

The procedure we used for the calculation of the dielectric constant with $E \neq 0$ was the following:

1). For a given $E = E_1$, calculate $P_o(E_1)$ by using the method of numerically minimizing the free energy.

2). For $E = E_2 = E_1 + \Delta E$, calculate $P_o(E_2)$.

3). Then the dielectric constant is:

$$\varepsilon = \varepsilon_b + 4\pi \frac{P_o(E_2) - P_o(E_1)}{E_2 - E_1} \qquad (2.48)$$

Fig. 2.15 shows the calculated dielectric constant at $E = 5$ ($\frac{\text{statvolts}}{\text{cm}}$) which decreases monotonically with decreasing temperature in the INC-phase while the experimental result has a minimum value between T_L and T_I as shown in Fig. 2.1.

In order to obtain a dielectric constant curve exhibiting a double maximum, Ishibashi introduced a "field-linear harmonic" term[90] in the expression of the polarization in the INC-phase, i.e.

$$P = P_o + P_k\cos kx + P_{2k}\cos 2kx \qquad (2.49)$$

where P_{2k} is induced from P_o and P_k. Now there are four parameters: P_o, P_k, P_{2k} and k.

The dielectric constant in the INC-phase can be calculated by using the same method used above. Note that the "field-linear harmonic" term

does not affect the dielectric constant in the para and ferro phases.

Fig. 2.16 shows the dielectric constant at E = 9 ($\frac{\text{statvolts}}{\text{cm}}$). It is clear that a curve of dielectric constant versus temperature with minimum in the INC-phase can be obtained by introducing the "field-linear harmonic" term, but we still have some problems:

1). Fig. 2.3 shows that at $T_L(E)$ the experimental peak decreases with increasing E-field while the theoretical result is just the opposite.

2). The temperature range of the INC-phase is narrowed by introducing the "field-linear harmonic" term. In the case of E = 5 ($\frac{\text{statvolts}}{\text{cm}}$) and $\eta = 0$:

Without the $P_{2k}\cos 2kx$ term

$$T_I - T_L = 1.36°C \tag{2.50}$$

With the $P_{2k}\cos 2kx$ term

$$T_I - T_L = 0.40°C. \tag{2.51}$$

2. Sixth order free energy model

Fig. 2.9 shows that the two lines of $\frac{1}{\varepsilon^{ferro} - \varepsilon_b}$ and $\frac{1}{\varepsilon^{para} - \varepsilon_b'}$ go to zero at different temperature. The crossing of these two lines implies that the direct para → ferro transition is of first order. But the fourth order free energy model gives a second order transition from the para-phase to the ferro-phase. Comparison of Fig. 2.10 with Fig. 2.4 indicates that the triple point on the calculated phase diagram of the fourth order free energy model is not coincident with the experimental result. For the above reasons we next consider a free energy model which

contains a sixth order term. The sixth order free energy model can be written as[91]:

$$f(x) = \frac{1}{2}AP^2 + \frac{1}{4}BP^4 + \frac{1}{6}CP^6 + \frac{1}{2}\alpha(\nabla P)^2 + \frac{1}{4}\beta(\nabla^2 P)^2 + \frac{1}{4}\eta P^2(\nabla P)^2 - EP \quad (2.52)$$

where $A = A_o(T - T_o)$, $B<0$, $C>0$, $\alpha<0$, $\beta>0$, $\eta>0$

E is the applied electric field along the b-axis.

The integrated free energy density is:

$$F = \frac{1}{L}\int f(x)dx$$ x is along the a-axis.

a. Free energy in the ferroelectric phase: F^{ferro}

In the ferro-phase $P = P_o$

$$\therefore \quad F^{ferro} = \frac{1}{2}AP_o^2 + \frac{1}{4}BP_o^4 + \frac{1}{6}CP_o^6 - EP_o \quad (2.53)$$

$$\therefore \quad \frac{\partial F^{ferro}}{\partial P_o} = AP_o + BP_o^3 + CP_o^5 - E = 0$$

$$\therefore \quad AP_o + BP_o^3 + CP_o^5 = E \quad (2.54)$$

In the case E=0 Eq. (2.54) becomes:

$$A + BP_o^2 + CP_o^4 = 0 \quad (2.55)$$

b. Free energy in the INC-phase: F^{inc}

In the INC-phase: $P = P_o + P_k \cos kx$

$$\therefore F^{inc} = \frac{1}{2}AP_o^2 + \frac{1}{4}BP_o^4 + \frac{1}{6}P_o^6 - EP_o$$

$$+ \frac{1}{4}A_kP_k^2 + \frac{3}{8}(B + B_k)P_o^2P_k^2 + \frac{3}{32}B_kP_k^4$$

$$+ \frac{5}{4}CP_o^4P_k^2 + \frac{15}{16}CP_o^2P_k^4 + \frac{5}{96}CP_k^6 \quad (2.56)$$

where $A_k = A + \alpha k^2 + \frac{1}{2}\beta k^4$

$$B_k = B + \frac{1}{3}\eta k^2 \quad (2.57)$$

In the case $E = 0$, $P_o = 0$

$$F^{inc} = \frac{1}{4}A_k P_k^2 + \frac{3}{32}B_k P_k^4 + \frac{5}{96}CP_k^6 \tag{2.58}$$

Since the para → INC transition at T_I is experimentally second order, the coefficient B_k must be positive although B is negative.

$$\frac{\partial F^{inc}}{\partial P_k} = 0$$

$$\left[A_k + \frac{3}{2}(B + B_k)P_o^2 + 5CP_o^4\right] + \left(\frac{3}{4}B_k + \frac{15}{2}CP_o^2\right)P_k^2 + \frac{5}{8}CP_k^4 = 0 \tag{2.59}$$

$$\frac{\partial F^{inc}}{\partial P_o} = 0$$

$$\left[A + \frac{3}{4}(B + B_k)P_k^2 + \frac{15}{8}CP_k^4\right]P_o + (B + 5CP_k^2)P_o^3 + CP_o^5 = E \tag{2.60}$$

$$\frac{\partial F^{inc}}{\partial k} = 0$$

$$k^2 = -\frac{\alpha}{\beta} - \frac{\eta}{2\beta}P_o^2 - \frac{\eta}{8\beta}P_k^2 \tag{2.61}$$

c. The INC→ferro phase transition line

The free energies of F^{inc} and F^{ferro} were obtained by using the method of numerically minimizing the free energy. The transition temperature $T_L(E)$ from the INC to the ferro phase was then determined by setting $F^{inc} = F^{ferro}$. Plotting $T_L(E)$ versus E gives the INC→ferro transition line.

d. The para→INC phase transition line

The para→INC phase transition temperature can be obtained by setting the coefficient of P_k^2 to zero in (2.56), i.e.:

$$A_k + \frac{3}{2}(B + B_k)P_o^2 + 5CP_o^4 = 0 \tag{2.62}$$

Comparing (2.62) with (2.59) we get

$$(\frac{3}{4}B_k + \frac{15}{2}CP_0^2)P_k^2 + \frac{5}{8}CP_k^4 = 0 \qquad (2.63)$$

This equation has two possible solutions:

$$P_k^2 = 0$$

$$\text{or} \quad (\frac{3}{4}B_k + \frac{15}{2}CP_0^2) + \frac{5}{8}CP_k^2 = 0 \qquad (2.64)$$

Since $B_k > 0$ and $C > 0$, Eq. (2.64) cannot be satisfied. The only solution is therefore

$$P_k = 0 \qquad \text{at } T=T_I \qquad (2.65)$$

Eq. (2.65) means that the transition temperature $T_I(E)$ can be obtained as the temperature where $P_k \to 0$.

In the case E=0, P_o is equal to zero in both the para and the INC phases. $\therefore$ According to Eq. (2.62) the transition occurs at $A_k = 0$, i.e.

$$A_o(T_I(0) - T_o) + \alpha k^2 + \frac{1}{2}\beta k^4 = 0 \qquad (2.66)$$

$$\text{At } T = T_I\,, \; P_k = 0 \quad \therefore \quad k_I(0) = -\frac{\alpha}{\beta} \qquad (2.67)$$

Substituting Eq. (2.67) into Eq. (2.66) gives:

$$T_I(0) = T_o + \frac{\alpha^2}{2A_o\beta} \qquad (2.68)$$

which is the same result found in Eq. (2.18) for the fourth power free energy. (the symbol "(0)" indicates the case of zero E-field).

Combining Eqs. (2.67), (2.65) and (2.61) we have

$$K_I^2(E) - k_I^2(0) = -\frac{\eta}{2\beta}P_o^2 \qquad (2.69)$$

where k_I represents the wavevector k at T_I, and P_o represents $P_o(E)$.

e. The dielectric constant

In the para and the ferro phases for nonzero E-field

$$x^{-1} = \frac{\partial^2 F}{\partial P_o^2} = A + 3BP_o^2 + 5CP_o^4$$

$$\varepsilon = \varepsilon_b + \frac{4\pi}{A_o(T - T_o) + 3BP_o^2 + 5CP_o^4} \tag{2.70}$$

In the case E=0, in the para-phase $P_o = 0$

$$\therefore \quad \varepsilon^{para} = \varepsilon_b' + \frac{4\pi}{A_o(T - T_o)}$$

$$\text{or} \quad \frac{1}{\varepsilon^{para} - \varepsilon_b'} = \frac{A_o(T - T_o)}{4\pi} \tag{2.71}$$

At $T = T_o$

$$\frac{1}{\varepsilon^{para} - \varepsilon_b'} = 0$$

In the ferro-phase :

$$\frac{1}{\varepsilon^{ferro} - \varepsilon_b} = \frac{1}{4\pi}[A_o(T - T_o) + 3BP_o^2 + 5CP_o^4] \tag{2.72}$$

$$\therefore \text{ At } T = T_o + \frac{1}{A_o}[3BP_o^2 + 5CP_o^4]$$

$$\frac{1}{\varepsilon^{ferro} - \varepsilon_b} = 0 \qquad \text{we represent this T as } T_f.$$

$$\therefore \quad \Delta T = T_o - T_f = -\frac{1}{A_o}[3BP_o^2 + 5CP_o^4] \tag{2.73}$$

where P_o represents $P_o(T_f)$.

Eq. (2.72) gives: $A_o(T - T_o) + 3BP_o^2 + 5CP_o^4 = 0$ (2.74)

Combining Eq. (2.73) with Eq. (2.55) leads to:

$$P_o^2 = -\frac{B}{2C} \quad \text{at } T = T_f \tag{2.75}$$

Substituting (2.75) into (2.73) we have

$$\Delta T = \frac{B^2}{4A_oC} \tag{2.76}$$

Note that in the fourth order free energy model the two lines

$\frac{1}{\varepsilon^{ferro} - \varepsilon_b}$ and $\frac{1}{\varepsilon^{para} - \varepsilon_b'}$ go to zero at the same point $T = T_o$, but in the sixth order model the two lines go to zero at different temperatures. This is consistent with the experimental result, (see Fiq. 2.9), and is the principal reason that the sixth power free energy was introduced. (see refs. (29), (91), (46)).

f. The coefficients A_o, T_o, B, C, α, β, and η

1). The coefficients A_o and T_o

In the case of the fourth order free energy model the coefficient T_o is fixed as given in Eq. (2.20), while in the sixth order model there is no such restriction. It was found that for obtaining a phase diagram which is closer to the experimental result than that of the fourth order free energy model the coefficients A_o and T_o should be taken from the para-phase data. Since both models predict the same ε^{para} (Eq. (2.29) and (2.71)) we used the values in Eq. (2.37) which were obtained from the para-phase data.

Because the values of A_o and T_o in (2.37) were obtained from zero-field data, it is necessary to adjust them to obtain proper values which are suitable for different E-fields. The values of A_o and T_o used for obtaining the phase diagram shown in Fig. 2.17 are:

$$A_o = 1.8938 \times 10^{-3} \text{ (in CGS units)}, \quad T_o = 162.30^{\circ}C \qquad (2.77)$$

These values were found in the same way described in the previous section for the fourth order free energy model.

2). The coefficients B and C

Eq. (2.76) can be rewritten as:

$$C = \frac{B^2}{4A_o\Delta T} \tag{2.78}$$

Substituting Eq. (2.78) into Eq. (2.55) we get:

$$B = -\frac{1}{2}\left[\frac{4A_o\Delta T}{P_o^2} + \left[\left(\frac{4A_o\Delta T}{P_o^2}\right)^2 + \frac{16A_o^2(T_o - T)\Delta T}{P_o^4}\right]^{\frac{1}{2}}\right] \tag{2.79}$$

The value of ΔT can be obtained from Fig. 2.9 as:

$$\Delta T \approx 0.80^\circ C$$

The spontaneous polarization at T = 162.00°C can be estimated from Fig. 1.2 as:

$$P_o \approx 2.04\times10^{4}$$

$$\therefore \quad B = -1.5819\times10^{-11} \qquad \text{(in CGS units)} \tag{2.80}$$

$$C = 4.1292\times10^{-20}$$

3). The coefficients α, β, η

Eq. (2.68) gives: $$\frac{\alpha^2}{\beta} = 2A_o(T_I(0) - T_o) \tag{2.81}$$

Eq. (2.67) gives: $$\frac{\alpha}{\beta} = -k_I^2(0) \tag{2.82}$$

From the dielectric constant data we have

$$T_I(0) = 163.86^\circ C \tag{2.83}$$

The neutron scattering data give:

$$k_I^2(0) = 4.3750\times10^{-14} \quad cm^{-2} \tag{2.84}$$

Substituting Eqs. (2.77), (2.83) and (2.84) into Eqs. (2.81) and (2.82) we obtain

$$\alpha = -1.3506\times10^{-17}$$

$$\beta = 3.0870\times10^{-32} \quad \text{(in CGS uints)} \tag{2.85}$$

The value of η can be determined from fitting the theoretical wavevector curve to the experimental wavevector data as illustrated in Fig. 2.19. The determined value of η is

$$\eta = 4.1520 \times 10^{-24} \quad \text{(in CGS units)}.$$

The value of η can also be estimated by the same formula as given in Eq. (2.46), it was obtained as: $\eta = 4.7520 \times 10^{-25}$ (in CGS units). Then we can use this value to fit the theoretical modulation curve to the experimental results, and adjust it until the best fit is obtained.

g. The calculated phase diagram

Fig. 2.17 depicts the calculated phase diagram of the sixth order model (the dashed curve) obtained by using the same procedure which was used for the fourth order model. For comparison, the phase diagrams of the fourth order model (the solid curve) and the experimental result (the discrete points) are also plotted in the same figure. All the coefficients used for this diagram are listed in Table A.3. The data of W. Buchheit and J. Petersson[29] and of Durand et al[46]. are also listed in this table for comparison. The conversion of the free energy from MKS units into CGS units is discussed in Appendix A. It is clear that the triple point of the sixth order model is coincident with the experimental result and the phase diagram is closer to the experimental one than that of the fourth order model.

$T_I(E)$ and $T_L(E)$ can be plotted in another way. Fig. 2.18 shows $T_I - T_L$ versus electric field E_b. The discrete points are the experimental results and the solid curve is the calculated result of the sixth order free energy model. The agreement between experiment and theory is quite good.

h. The calculated modulation wavevector

The calculated modulation wavevector versus T curve (the solid line) is shown in Fig. 2.19 where the discrete points are the experimental results. The agreement between theoretical and experimental results is better than that of the fourth order model (Fig. 2.13).

Fig. 2.20 shows δ_I and δ_L versus electric field E_b. The upper and lower solid curves are respectively the calculated $\delta_I(E)$ and $\delta_L(E)$ of the sixth order free energy model. The discrete points are the experimental results. Fig. 2.18 and Fig. 2.20 are plotted together for comparison in Fig. 2.21.

The P_K^2 versus T curve and the dielectric constant curve are similar to those of the fourth order free energy model. Without the "field-linear harmonic" term the dielectric constant in the INC-phase is still a monotonic function of temperature.

D. Diffuse neutron scattering and discussion of the free energy model

A diffuse neutron scattering experiment was performed at BNL using the same apparatus and the same sample described in section B.

Fig. 2.22 shows the experimental results of the peak positions of the diffuse neutron scattering in the para-phase and the satellite positions in the INC-phase, both plotted as functions of temperature. The ratio of the slope of the peak positions of the diffuse scattering to that of the satellite positions is about 1 : 4.

In a recent paper by Ema et al[92]. the role of the different terms in the free energy has been estimated on the basis of the smallness of the

temperature width in which the INC-phase exists. According to this paper, in a consistent phenomenological theory it may be possible to neglect the $\eta(\nabla P)^2P^2$ term, but it may not be possible to neglect the temperature dependence of the coeficient α in the free energy. We can estimate the relative importance of these two terms experimentally by comparing our diffuse neutron scattering results with the predictions of the free energy model. We present here the result of an analysis suggested by Professor A. P. Levanyuk.

Again, we take the free energy density as

$$f(x) = \frac{1}{2}AP^2 + \frac{1}{4}BP^4 + \frac{1}{6}CP^6 + \frac{1}{2}\alpha(\nabla P)^2 + \frac{1}{4}\beta(\nabla^2 P)^2 + \frac{1}{4}\eta P^2(\nabla P)^2 \qquad (2.86)$$

where $A = A_o(T - T_o)$, $B < 0$, $C > 0$, $\alpha < 0$, $\beta > 0$, $\eta > 0$

In the INC-phase, for the case of zero E-field, Eq. (2.61) gives

$$k^2 = -\frac{\alpha}{\beta} = \frac{\eta}{8\beta}P_k^2 \qquad (2.87)$$

This means that in the INC-phase the satellite positions are governed by α, β and η.

In the para-phase, the response fuction (i.e. the susceptibility χ) can be obtained by taking the second derivative of the Fourier transform of the free energy with respect to the order parameter. Thus we have

$$\chi(k) = A_k^{-1} = (A + \alpha k^2 + \frac{1}{2}\beta k^4)^{-1} \qquad (2.88)$$

The intensity of the diffuse scattering is proportional to the square of the fluctuation in P_k, while from the fluctuation-dissipation theorem the mean square fluctuation is proportional to the susceptibility. Therefore the temperature dependence of the peak positions of the diffuse scattering is governed by the temperature-dependent susceptibility $\chi(k)$ in Eq. (2.88). In other words, the peak position of the diffuse scattering does not depend on the coefficient η.

If all the temperature dependence of k comes from the η-term (i.e. $\eta \neq 0$ and α = constant), the plot of the satellite positions below T_I and the peak positions of the diffuse scattering above T_I would be of the form shown in Fig. 2.23 (a), where the positions of satellite varies with temperature while the peak positions of the diffuse scattering are constant.

If all the temperature dependence comes from temperature dependence of the α-term, on the other hand, and the η-term is neglected (i.e. $\eta = 0$ and $\alpha = \alpha(T)$), then there would be no change in the slope at T_I as shown in Fig. 2.23 (b).

If we keep the η-term and also assume that the coefficient α is temperature dependent (i.e. $\eta \neq 0$ and $\alpha = \alpha(T)$), then we can obtain a plot of the form shown in Fig. 2.23 (c), which is in agreement with our experimental results.

Therefore our diffuse neutron scattering results shown in Fig. 2.22 indicate that the η-term in the free energy cannot be neglected, and the temperature dependence of α should be also assumed.

There is another fact which also leads to the conclusion that the η-term cannot be neglected.

Eq. (2.58) gives the free energy in the INC-phase in the case of zero E-field as

$$F^{inc} = \frac{1}{4}A_k P_k^2 + \frac{3}{32}B_k P_k^4 + \frac{5}{96}C P_k^6 \qquad (2.58)$$

where $B_k = B + \frac{1}{3}\eta k^2$

It is clear that if $\eta = 0$, then $B_k = B < 0$, and the phase transition from the para-phase to the INC-phase is always of first order. But the observed para → INC transition in $NaNO_2$ is of second order. Therefore the

η-term must be included in order to make $B_k > 0$.

CHAPTER III

INC PHASE TRANSITION UNDER TRANSVERSE ELECTRIC FIELD

The Lifshitz point (LP) was initially proposed by Hornreich, Luban and Shtrikman[100] in 1975, and many theoretical studies have been done since then[101]. There have been, to date, only three systems[102,103,104] in which there is positive experimental evidence for the existence of a Lifshitz point. To introduce the Lifshitz point Hornreich et al. considered the expansion of the free energy functional F(M) in terms of the order parameter M and its spatial derivatives, concentrating their attention on the term $\alpha(\nabla M)^2$. The coefficient α is assumed to depend on some perturbation which can change it continuosly from negative to positive. In the region where α is positive, second order phase transition from the disordered phase leads to the ordered phase directly. In the region where α is negative, second order phase transition from the disordered phase leads not to the ordered phase but to a modulated phase characterized by a modulation wavevector k. The point at which α vanishes is called the Lifshitz point (LP). A characteristic feature of the LP is that the wavevector k in the modulated phase approaches zero continuously as the LP is approached. At the LP, k equals zero, and the three phases, disordered, modulated and ordered, meet in a prescribed fasion. In Hornriech's theory, a second order transition from the disordered phase to the ordered phase is required. However, in the case of $NaNO_2$, the direct transition from the para-phase to the ferro-phase is of first order. To our knowledge, no theoretical treatment of the LP which is related to a first order transition from the disordered phase to the ordered phase based on a Landautype free energy expasion has been con-

sidered in detail. Therefore in this chapter we will first discuss what happens in general to the whole phase diagram and in particular to the Lifshitz point when the direct transition from the disordered phase to the ordered phase is of first order starting from the free energy expresion (2.52). We then present our data of elastic neutron scattering experiments in $NaNO_2$ with an electric field applied transverse to the ferroelectric axis. Finally we compare these experimental results with the theoretical phase diagram.

Note that previous neutron scattering experiments have explored the effect of a longitudinal field E_b which leads to a triple point at E_b~3 kv/cm. This is not a LP however, since the modulation wavevector does not decreases to zero near this point (Fig. 2.20).

A. Relation of the Lifshitz point to a first order transition from the disordered phase to the ordered phase

Under applied transverse electric field the free energy density for $NaNO_2$ can be written as:

$$f(x) = \frac{1}{2} AP^2 + \frac{1}{4} BP^4 + \frac{1}{6} CP^6 + \frac{1}{2} \alpha(\nabla P)^2 + \frac{1}{4} \beta(\nabla^2 P)^2 + \frac{1}{4} \eta P^2(\nabla P)^2 \quad (3.1)$$

with $A = A_o(T - T_o)$, $B < 0$, $C > 0$, $\beta > 0$, $\eta > 0$

here the E·P term is taken to be zero as there is no field component along the b-axis. We assume that α and T_o are monotonic functions of the transverse electric field E. The simplest E-dependent equations for $\alpha(E)$ and $T_o(E)$ allowed by symmetry are

$$\alpha = \alpha_o + \alpha_1 E^2$$

$$T_o = T_{oo} + T_{o1} E^2 \quad (3.2)$$

This T_o versus E curve is plotted in Fig. 3.1.

The integrated free energy density is

$$F = \frac{1}{L} \int f(x)\, dx \tag{3.3}$$

where x is along the a-axis, and L is the length of the crystal.

1. The para → INC phase transition line T_I

In the INC-phase $P = P_k \cos kx$ (3.4)

where k is the modulation wavevector.

The free energy in the INC-phase is

$$F^{inc} = \frac{1}{4} A_k P_k^2 + \frac{3}{32} B_k P_k^4 + \frac{5}{96} C P_k^6 \tag{3.5}$$

with $A_k = A + \alpha k^2 + \frac{1}{2} \beta k^4$

$$B_k = B + \frac{1}{3} \eta k^2 \tag{3.6}$$

if $B_k > 0$, the para → INC phase transition occurs at

$A_k \to 0$ or,

$$A + \alpha k^2 + \frac{1}{2} \beta k^4 = 0 \tag{3.7}$$

$\frac{\partial F^{inc}}{\partial P_k} = 0$ gives

$$A_k + \frac{3}{4} B_k P_k^2 + \frac{5}{8} C P_k^4 = 0 \tag{3.8}$$

$\frac{\partial F^{inc}}{\partial k} = 0$ gives

$$k^2 = - \frac{\alpha}{\beta} - \frac{\eta}{8\beta} P_k^2 \tag{3.9}$$

Comparing Eq. (3.8) with Eq. (3.7) gives

$$3 B_k P_k^2 + \frac{5}{2} C P_k^4 = 0 \tag{3.10}$$

Eq. (3.10) has two solutions:

$$P_k^2 = 0 \tag{3.11}$$

$$\text{or} \quad P_k^2 = -\frac{6B_k}{5C} \tag{3.12}$$

The first solution holds for both cases of $B_k > 0$ and $B_k < 0$, while the second solution only holds for the case of $B_k < 0$.

If we take the first solution, assuming $B_k > 0$, we have

$$k^2 = -\frac{\alpha}{\beta} \tag{3.13}$$

From eq. (3.7) we get

$$T_I - T_o = \frac{\alpha^2}{2A_o\beta} \tag{3.14}$$

Eq. (3.14) means that the second-order T_I line meets the T_o line at $\alpha = 0$, which is the LP shown in Fig. 3.1, while Eq. (3.13) indicates that the wavevector k approaches zero continuously as α approaches zero, and becomes zero at $\alpha = 0$.

2. The direct first-order para → ferro transition line T_1

In the para-phase, $P = 0$

$\therefore F^{para} = 0$

In the ferro-phase $P = P_o$

$$\therefore F^{ferro} = \frac{1}{2} AP_o^2 + \frac{1}{4} BP_o^4 + \frac{1}{6} CP_o^6 \tag{3.15}$$

Since $B < 0$, the direct para → ferro transition is of first order. The transition line can be obtained by setting

$$F^{para} = F^{ferro} = 0$$

$$\text{i.e.} \quad \frac{1}{2} AP_o^2 + \frac{1}{4} BP_o^4 + \frac{1}{6} CP_o^6 = 0 \tag{3.16}$$

$$\frac{\partial F^{ferro}}{\partial P_o} = 0 = P_o(A + BP_o^2 + CP_o^4)$$

$$\therefore \quad P_o = 0 \tag{3.17}$$

or $\quad A + BP_o^2 + CP_o^4 = 0$

i.e. $$P_o^2 = -\frac{B}{2C} + \frac{1}{2C}\sqrt{B^2 - 4AC} \tag{3.18}$$

$$F^{ferro} = \frac{1}{24C^2}\left[-6ABC + B^3 - (B^2 - 4AC)^{\frac{3}{2}}\right] \tag{3.19}$$

Setting $F^{ferro} = 0$ gives

$$64AC - 12B^2 = 0$$

$$\therefore \quad A = \frac{3B^2}{16C} \tag{3.20}$$

or $$A_o(T_1 - T_o) = \frac{3B^2}{16C}$$

or $$T_1 - T_o = \frac{3B^2}{16A_oC} \tag{3.21}$$

At any given value of the E-field (or α) the difference between T_1 and T_o is a constant. The first-order transition line $T_1(E)$ is shown in Fig. 3.1 (the dashed line).

Since we have assumed that

$$T_o = T_{oo} + T_{o1}E^2 \tag{3.2}$$

The T_o versus E line is parabolic, and so is the T_1 versus E line.

3. The crossing point CP of the T_I line and the T_1 line

$$T_I - T_o = \frac{\alpha^2}{2A_o\beta} \tag{3.14}$$

$$T_1 - T_o = \frac{3B^2}{16A_oC} \tag{3.21}$$

Setting Eq. (3.21) equal Eq. (3.14) gives

$$\alpha^2 = \frac{3\beta B^2}{8C} \tag{3.22}$$

This means that at $\alpha^2 = \frac{3\beta B^2}{8C}$, $T_I = T_1$, which is the point CP in Fig. 3.1. Thus the T_I line crosses the T_1 line before it meets the T_o line. At

this point the direct first order transition intervenes and the INC transition becomes virtual before the LP is reached.

4. The INC → ferro transition line T_L and the Lifshitz point LP

The INC → ferro transition is of first order. The transition line can be obtained by setting $F^{inc} = F^{ferro}$.

At the point where the T_L line meets the T_I line, the INC-phase disappears, and the free energy at this point equals zero, i.e.

$$F^{ferro} = F^{inc} = F^{para} = 0 \tag{3.23}$$

From eq. (3.23) and eq. (3.19) we have

$$F^{ferro} = \frac{1}{24C^2}\left[-6ABC + B^3 - (B^2 - 4AC)^{\frac{3}{2}}\right] = 0 \tag{3.24}$$

Eq. (3.24) has two solutions:

one is given by eq. (3.20) i.e.

$$A = \frac{3B^2}{16C} \quad \text{or}$$

$$T_{L1} - T_o = \frac{3B^2}{16A_oC} \tag{3.25}$$

the other solution is

$$A = 0 \quad \text{or}$$

$$T_{L2} = T_o \tag{3.26}$$

where T_{L1} and T_{L2} denote the two solutions at the critical point at which the T_L line meets the T_I line.

The T_L line can meet the T_I line in two different ways: one is that at the point P, where $\alpha^2 = \frac{3\beta B^2}{8C}$, the T_L line jumps to the point CP, where the T_L line meets the T_I line. The physical transition is then along the T_I line. The other way is that the T_L line meets the T_I line at T_o (the dotted line in Fig. 3.1), where $\alpha = 0$ and $k = 0$. Therefore this

point is the Lifshitz point (i.e. the point LP in Fig. 3.1).

In principle, the T_L line could be either below or above the T_0 line. For $NaNO_2$, our numerical calculations show that the T_L line is above the T_0 line, which is in agreement with Durand et al[46].

Now we can conclude that: mathematically we obtained the Lifshitz point in the phase diagram exhibiting a first order transition from the disordered phase to the ordered phase, but it is physically inaccessible. The phase diagram which can physically occur is shown in Fig. 3.1 by the heavy solid and dashed lines and is described as follows: the para → INC transition is along the T_I line (solid line). At the point CP the T_I line meets the T_1 line and the INC-phase disappears. The INC → ferro transition is along the T_L line (solid line with dots on it). At the point P the T_L line jumps to the point CP where it meets the T_I line, for E fields greater than E_{CP} the physical transition is a direct first-order para → ferro one along the T_1 line (heavy dashed line).

Let T_{LP} be the transition temperature at the LP point and T_{1LP} be the transition temperature on the T_1 line at $\alpha = 0$. Then

$$T_{1LP} - T_{LP} = \frac{3B^2}{16A_0C} \tag{3.27}$$

Therefore the physically accessible point closest to LP (i.e. the difference between T_{1LP} and T_{LP}) depends on the coefficients A_0, B and C.

5. The tricritical point TP

From eq. (3.5) we can see that if $B_K > 0$, the para → INC transition will be of second order; if $B_K < 0$, it will be of first order. The point at which $B_K = 0$ is a tricritical point[4].

$$B_k = B + \frac{1}{3}\eta k^2 = 0$$

$$\therefore k^2 = -\frac{3B}{\eta} \tag{3.28}$$

Substituting eq. (3.13) into eq. (3.28) gives

$$\alpha = \frac{3B\beta}{\eta} \tag{3.29}$$

Eq. (3.29) means that the transition changes from second order to first order at point TP in Fig. 3.1 where $\alpha = \frac{3B\beta}{\eta}$. In principle, the tricritical point TP could be on either high or low temperature side of the critical point CP. In other words, the tricritical point could be physically accessible for some value of the three coefficients B, β and η. It would be interesting to find such systems for which the tricritical point is physically accessible.

The above argument also leads to a conclusion that the η-term in the free energy cannot be neglected, otherwise the para → INC transition will be of first order, however, the observed para → INC transition at zero E-field is of second order in the case of $NaNO_2$.

6. The para → INC transition line T_I'

As mentioned above, in the region of $B_k < 0$, Eq. (3.10) has two solutions which are given in Eqs. (3.11) and (3.12) corresponding to a second order and a first order transition respectively. If we take the solution in Eq. (3.12) then we can obtain a transition line T_I'. The derivation is given as follows:

Rewrite Eq. (3.5) as

$$F_{inc} = \frac{1}{2}\left(\frac{A_k}{2}\right)P_k^2 + \frac{1}{4}\left(\frac{3}{8}B_k\right)P_k^4 + \frac{1}{6}\left(\frac{5C}{16}\right)P_k^6$$

$$= \frac{1}{2}A_k'P_k^2 + \frac{1}{4}B_k'P_k^4 + \frac{1}{6}C'P_k^6 \tag{3.30}$$

$$\frac{\partial F^{inc}}{\partial P_k} = 0 = P_k\,(A_k' + B_k'P_k^2 + C'P_k^4)$$

$\therefore$ $P_k = 0$ or

$$A_k' + B_k'P_k^2 + C'P_k^4 = 0 \tag{3.31}$$

$$\therefore\ P_k^2 = -\frac{B_k'}{2C'} + \frac{1}{2C'}\sqrt{B_k'^2 - 4A_k'C'} \tag{3.32}$$

$$\therefore\ F^{inc} = \frac{1}{24C'^2}\left[-6A_k'B_k'C' + B_k'^3 - (B_k'^2 - 4A_k'C')^{\frac{3}{2}}\right] \tag{3.33}$$

Since when $B_k < 0$, the para $\rightarrow$ INC transition is of first order, the trasition line T_I' can be obtained by setting $F^{para} = F^{inc}$.

$F^{para} = 0$

$\therefore$ at $T = T_I'$, $F^{inc} = 0$ (3.34)

The solution of Eq. (3.34) is:

$$A_k' = \frac{3B_k'^2}{16C'} \tag{3.35}$$

$$\text{i.e.}\quad A_k = \frac{3B_k'^2}{8c'} \tag{3.36}$$

$$\text{or}\quad A_o(T_I' - T_o) + \alpha k^2 + \frac{1}{2}\beta k^4 = \frac{3B_k'^2}{8C'} \tag{3.37}$$

On the T_I line, $A_k = 0$, hence

$$A_o(T_I - T_o) = -\alpha k^2 - \frac{1}{2}\beta k^4 \tag{3.38}$$

Substituting Eq. (3.38) into Eq. (3.37) gives

$$A_o(T_I' - T_I) = \frac{3B_k'^2}{8C'} \tag{3.39}$$

Eq. (3.39) indicates that at the tricritical point TP where $B_k = 0$ (or $B_k' = 0$), we have:

$$T_I' = T_I \tag{3.40}$$

Beyond the point TP, From Eq. (3.39), we have:

$$T_I' > T_I \tag{3.41}$$

Eqs. (3.40) and (3.41) mean that the T_I' line starts from the tricritical point TP, then moves above the T_I line. This is shown in Fig. 3.1 (the dashed-dotted line).

If the tricritical point TP is on the high temperature side of the critical point CP, then not only the tricritical point TP but also the T_I' line are physically accessible.

B. Elastic neutron scattering under E-field along the a and c axes

The elastic neutron scattering experiments were performed at the High Flux Beam Reactor at Brookhaven National Laboratory in collaboration with Dr. S. Shapiro and Dr. J. Wicksted. The samples were typically 0.34 x 0.62 x 0.42cm^3, and had gold film evaporated on the a-face and c-face respectively, for the application of the electric field parallel to the a-axis and tha c-axis. The experimental apparatus was the same as described in Chapter II. The scans were along the a-axis with δ ranging from 0.09 to 0.13 a^* on either side of the (020) Bragg peak, to measure the wavevector and intensity of the satellites that appear in the INC-phase. The field were applied to a maximum of 1.36 kV/cm in the case of the field parallel to the a-axis and to 2.21 kV/cm for E-field parallel to the c-axis, before electrical breakdown of the sample occurred.

Figs. 3.2 and 3.3 show the intensity of the satellite versus temperature, while Figs. 3.4 and 3.5 show the wavevector versus temperature for different transverse fields parallel to the a-axis (Figs. 3.2 and 3.4) and the c-axis (Figs. 3.3 and 3.5) respectively. The range of the INC

region clearly decreases with increasing E-field, while the end points (T_I and T_L) both move towards lower temperatures, the effect being more pronounced for E parallel to the a-axis. The end points of the wavevector of the satellites (δ_I and δ_L) also decrease, with the decrease being more significant for E parallel to the a-axis. The width of the satellites was resolution limited and no broadening was observed.

C. Comparison of the experimental results with the numerically calculated results

We calculated the phase transition temperature and the modulation wavevector with applied transverse field by the same procedure of minimization of the free energy described in Chapter II, and with the same set of coeficients listed in Table A.3. The application of the transverse field is equivalent to varying α and T_o as shown by Eq. (3.2). The effect of varying α is to reduce the INC region, while that of varying T_o is to move the INC region to lower temperature, thus reproducing two features of our observed results. We can fit the experimental data of δ versus temperature shown in Fig. 3.4 and Fig. 3.5. Although the limiting modulation wavevector obtained agreed with experimental data, the calculated wavevector versus temperature is essentially a continuous curve and does not reproduce the bend seen in the data of Fig. 3.4 and Fig. 3.5. In Fig. 3.6 the dashed line is the calculated $T_I - T_L$ while the upper and lower solid lines are respectively the calculated limiting modulation wavevectors δ_I and δ_L as a function of α. When α goes to zero, the INC region $T_I - T_L$ vanishes and the wavevector δ goes to zero continously. At the point at which $\alpha=0$ and the three lines meet, the conditions for a LP are satisfied. This point is, however, a virtual one as described above. The

experimentally obtained points are shown with the theoretical curve in Figs. 3.7 and 3.8 for E parallel to the a-axis and c-axis respectively. We find that the experimental points lie consistently on the theoretical curves as shown in Fig. 3.9 and Fig. 3.10, where the data are plotted on an expanded scale to determine the accuracy of our results. We can calculate α_1 and T_{o1} from our fits to the data and determine where the virtual LP should occur. We find that the LP should occur at E^a_{LP} = 7.32 kv/cm and T^a_{LP} = 122.15°C for E parallel to the a-axis and E^c_{LP} = 16.37 kv/cm and T^c_{LP} = 142.73°C for E parallel to the c-axis.

We can now plot the phase diagrams for $NaNO_2$ in a form similar to the schematic phase diagram in Fig. 3.1. These are shown in Figs. 3.11 and 3.12 for the E-field parallel to the c-axis and the a-axis respectively, where the upper solid line is the T_I line, the lower solid line is the T_L line, the dashed line (between T_I line and T_L line) is the T_1 line and the dot-dashed line is the T_o line. In both Figures the point LP denotes the Lifshitz point. The LP is virtual and the INC-phase ceases to exist for a field of 4.59 kV/cm for the E-field parallel to the a-axis and 10.24 kV/cm for the E-field parallel to the c-axis. The tricritical point TP is at $\alpha = -3.5\times10^{-19}$ (CGS units). Substituting the values of A_o, B and C into Eq. (3.27) gives the difference between the physically accessible transition temperature T_{1LP} and the virtual transition temperature T_{LP} about 0.6°C. For the case of the E-field parallel to the a-axis, T^a_{LP} = 122.15°C and T^a_{1LP} = 122.75°C; for the case of the E-field parallel to the c-axis, T^c_{LP} = 142.73°C and T^c_{1LP} = 143.33°C.

Thus our experimental data implies that the application of a transverse field to $NaNO_2$ causes a decrease of both the range of the INC-phase and the value of the modulation wavevector, both effects sug-

gesting the onset of an LP, and that our data fit the calculated results very well in the range of our experiments. However, this LP cannot be achieved not only because the samples break down electricly, but also because the first order direct transition intervenes and the LP is virtual.

CHAPTER IV

BRILLOUIN SCATTERING AND INELASTIC NEUTRON SCATTERING

We began our Brillouin scattering in $NaNO_2$ by reproducing the 90° scattering experiments under zero E-field reported in references (66)-(68) and extended these measurements in exploring the modifications of the spectrum under applied electric field along the c-axis.

For comparison of sound velocities in different frequency regions an inelastic neutron scattering experiment was also performed at BNL.

A. Brillouin scattering under zero E-field

Our measurements were performed with a high-resolution computer-controlled interferometer (Tropel model 350) in either single-or triple-pass, and a single-mode argon laser (Spectra-Physics model 165) operating at 5145Å. Data were collected in a Digital Equipment Corporation PDP8E minicomputer, which also maintained interferometer alignment, and transferred to a central VAX/UNIX system for subsequent analysis by a nonlinear least squares fitting program. (The apparatus will be described in Appendix D)

Large single crystals of good quality were grown from the melt. A cube-shaped sample with the c-axis vertical and the a and b axes along the two diagonals of the c-face was finely polished using a piece of wet paper (BSWP 090 25 MILLIPORE CORP) and had gold films evaporated on the c-faces for application of the electric field parallel to the c-axis. The sample was then placed in a light scattering cell designed especially for precise temperature regulation from room temperature to about 300°C. The temperature was measured by a thermistor mounted inside the cell

touching the sample and the temperature of the oven was controlled by a Fisher proportional temperature controller. The temperature was maintained constant to better than 0.01°C. All spectra were taken during cooling. The oven was evacuated to about 5×10^{-3} Torr to minimize the water vapor attacking the sample.

Fig. 4.1 shows a typical Brillouin scattering spectrum of $NaNO_2$ under zero E-field at 198.0°C with the acoustic phonon propagating along the [010] direction. The discrete points are the experimental data while the solid curves are the fit obtained with a nonlinear least squares fitting program. As the output of this fitting program, the computer gives the center frequency, the halfwidth and the peak height for the Rayleigh line and each of the Brillouin components.

In Fig. 4.1 the two Brillouin components observed were assigned as a L-mode and a T_1 mode according to the selection rule in Table 4.1 by using the four possible combinations of the incident and scattered polarizations $\hat{e}_o$ and $\hat{e}_s$ and the three Brillouin tensors (for crystal class mm2) to compute the quantities $[\hat{e}_s\cdot T^j\cdot\hat{e}_o]^{105}$.

A series of Brillouin spectra under zero E-field from 50°C up to 240°C is shown in Fig. 4.2, and the corresponding Brillouin shift of the L-mode propagating along the [010] direction is shown in Fig. 4.3. The longitudinal acoustic mode propagating along the [010] direction becomes soft gradually when the temperature approaches the melting point.

We paid special attention to the INC-phase of $NaNO_2$. Fig. 4.4 shows the temperature dependence of the Brillouin shift of the longitudinal acoustic mode propagating along the [010] direction in the vicinity of the phase transition temperatures T_L and T_I. The solid lines are drawn as a guide to the eye. A small but discontinuous change appears at T_L as

a result of the first order phase transition at T_L and a bend is observed at T_I. In the INC-phase the $\Delta\nu$ curve shows a linear decrease with increasing temperature. Our results agree with the previous results reported by Yagi et al.[67,68].

B. Brillouin scattering under E-field along the c-axis

Fig. 4.5 shows the Brillouin shift versus temperature of the L-mode propagating along the [010] direction under an E-field along the c-axis: (a) E_c = 0.5 kv/cm, and (b) E_c = 1.0 kv/cm. The main features of Fig. 4.5 are:

1. Both T_I and T_L move towards lower temperatures and T_I-T_L decreases with increasing E-field which agrees with our neutron scattering results presented in Chapter III.

2. The difference of the Brillouin shift between the para and the ferro phases decreases with increasing E-field. It is easy to imagine that at the Lifshitz point the Brillouin shift curve would become smooth, since at this point there is no difference among the three phases.

Two serious problems restrict the application of high E-field to the sample of $NaNO_2$. One is that the surface of the sample becomes opaque very fast when a higher E-field is applied. The other is that the sample exhibits electrical breakdown at high E-field, as discussed in Chapter III.

C. Inelastic neutron scattering

The inelastic neutron scattering experiments were performed at the High Flux Reactor at BNL in collaboration with Dr. S. Shapiro and Dr. J.

Wicksted. The apparatus, the incident neutron energy and the δ-resolution were the same as in Chapter III. The scans were taken over the phonon energy range: -1.0 → +5.0 meV. For each fixed temperature three values of the wavevector were taken: $0.080a^*$, $0.145a^*$ and $0.200a^*$.

Fig. 4.6 shows the acoustic mode energies in $NaNO_2$ from inelastic neutron scattering experiments with q parallel to the a-axis. There are two sets of data, one was taken at 165.41°C, the other was taken at 180.72°C. All the data lie on the same straight line.

D. Discussion

1. Sound velocity along the [010] direction

The hypersonic velocity v of the scattering phonons can be calculated from the Brillouin frequency shift by using the following formula:

$$v = \frac{\Delta\nu\lambda_o}{(n_o^2 + n_s^2)^{\frac{1}{2}}} \qquad (4.1)$$

where $\Delta\nu$ is the Brillouin shift, λ_o is the incident laser wavelength, n_o and n_s are the refractive indices in the incident and scattered light polarization directions respectively.

The temperature dependence of n_o and n_s should be taken into consideration, but as pointed out by Yagi et al.[68], n_o and n_s have no anomalous feature near T_L and T_I and their change with temperature in the range considered here is estimated to be smaller than one percent. Thus, in the calculation of v, the refractive indices can be taken as constants: $n_a = 1.349$ and $n_c = 1.650$ at 165°C for $\lambda = 5145\text{Å}$[67].

The calculated hypersonic velocities along the [010] direction under diferent E-fields are shown in Fig. 4.7: (a) & (b) E=0, (c) E=0.5 kv/cm (d) E=1.0 kv/cm. For comparison, the ultrasonic velocity reported

by Hatta et al[60,61]. is shown in Fig. 4.8. It is clear that there is a pronounced continuous minimum in the ultrasonic velocity just below T_I but there is no minimum in the hypersonic velocity. It was pointed out by Hatta et al. that the ultrasonic anomalies result from coupling between strain and the staggered polarization[60,61]. Comparison of Fig. 4.7 with Fig. 4.8 indicates that this coupling does not affect the hypersonic wave.

Figs. 4.7 (c) and (d) show that the transverse E-field does not dramatically change the propagation of the hypersonic wave, but it does reduce the difference of the sound velocities between the para and the ferro phases. Let v_L and v_I be the sound velocities along the [010] direction at T_L and T_I respectively, and $\Delta v = v_L - v_I$. Then, at $E = 0$ kV/cm, $\Delta v = 1 \times 10^3$ cm/s, at $E = 0.5$ kV/cm, $\Delta v = 0.4 \times 10^3$ cm/s, and at $E =$ 1.0 kV/cm $\Delta v = 0.26 \times 10^3$ cm/s.

2. Sound velocity along the [100] direction

The acoustic phonons observed in inelastic neutron scattering have frequencies in the terahertz region. The hypersonic phonons observed in Brillouin scattering are in the gigahertz region. Ultrasonic phonons are in the megahertz region.

The sound velocity in the terahertz region can be deduced from Fig. 4.6 by using the formula:

$$v = \frac{1}{h}\frac{dE}{dk} \tag{4.2}$$

this is just the slope of the line in Fig. 4.6.

In the temperature region from 165.41°C to 180.71°C the value of a^* is almost constant (The change is less than 0.5 percent) which was obta-

ined from our experiment as: $a^* = 1.71 \times 10^8$ cm^{-1}.

$\therefore v \approx 1.45 \times 10^5$ cm/s (in the terahertz region) (4.3)

This result is in agreement with the result obtained by Durand et al.[46,58].

The sound velocity in the megahertz region shown in Fig. 4.8 is:

$v \approx 3.4 \times 10^5$ cm/s (4.4)

The hypersonic sound velocity along the [100] direction is[68] :

$v = 3.5 \times 10^5$ cm/s (4.5)

It is clear that the hypersonic and ultrasonic sound velocities along the [100] direction are almost the same, while the sound velocity in the terahertz region is smaller, by a factor of 2.4.

CHAPTER V

INC PHASE TRANSITION UNDER HYDROSTATIC PRESSURE

In this chapter the results of dielectric constant and Brillouin scattering measurements under hydrostatic pressure (in the low pressure region) are presented, and a neutron scattering experiment under hydrostatic pressure is proposed.

A. Dielectric constant measurements under hydrostatic pressure

We measured the pressure dependence of T_I and T_L in collaboration with Professor J. Steiner using a temperature controlled hydrostatic pressure system pressurized with argon gas. The high pressure system is described in Appendix F. The samples were typically 0.3 x 0.4 cm^2 in area and 0.03 cm thick, and had gold films evaporated on the surfaces of the sample perpendicular to the b-axis. The capacitance measurement apparatus is the same as described in Chapter II. The temperature was measured by a thermocouple and the temperature was maitained constant to within $\pm$ 0.01°C. All the measurements were carried out in the cooling process. The rate of the temperature decrease was about 0.2°C/hour near the transition temperatures of $NaNO_2$.

Fig. 5.1 shows both T_I and T_L, taken as the temperatures of the peaks in the dielectric constant, versus hydrostatic pressure. The solid lines are for guiding the eye. The two sets of data were obtained with two different methods of temperature measurements. The data indicated by circles were taken with the thermocouple mounted outside the high pressure vessel, while the triangle data were taken with the thermocouple mounted inside the high pressure vessel. The two sets of experimen-

tal results show the same behavior: in the range of pressure from 14.5 psi (1 atm.) to 1000 psi, both T_I and T_L decrease while ΔT ($\Delta T = T_I - T_L$) decreases slightly. Above 1000 psi, however, T_I, T_L and ΔT all increase with increasing pressure.

In 1965, Gesi et al.[55] investigated the temperature dependence of the dielectric constant ε_{22} of $NaNO_2$ under hydrostatic pressure. They concluded that T_I, T_L and ΔT increase with increasing pressure. But they did not give any data between 1 atm (14.5 psi) and 8,000 psi. We paid much attention to this low pressure region.

B. Brillouin scattering under hydrostatic pressure

Brillouin scattering under hydrostatic pressure was performed with the same apparatus described in Chapter IV and Appendix D. The 15 x 12 x 10 cm^3 steel high-pressure optical cell (41-11552, Newport Scientific, Inc.) was wrapped by two heavy insulated heating tapes (11-463 50B, Fisher Scientific Comp.), and the temperature was controlled by a Fisher proportional temperature controller. The thermocouple was mounted outside the high-pressure optical cell, but was inserted 4 cm deep in the steel block. The temperature was maintained constant to within 0.01°C. The sample was typically 5 x 5 x 6 mm^3. A standard Helium gas cylinder equipped with a special pressure regulator (Model No. 3-580, Matheson gas products Inc.) was used to pressurize the system.

Fig. 5.2 shows the Brillouin shift versus temperature as a function of hydrostatic pressure, at (Δ) 14.5 psi (1atm), (o) 900 psi, (□) 1500 psi. The data in Fig. 5.2 show that there is a jump in the Brillouin shift at the lock-in transition temperature T_L for all three pressures, but the phase transition temperature does not change with pressure. These res-

ults are in disagreement with those of the dielectric constant measurements which were presented in section A. To explain this disagreement we performed dielectric constant measurements again under the same conditions as for Brillouin scattering. The sample was 0.4 x 0.4 cm^2 and 0.03 cm thick, and had gold films evaporated on the surfaces of the sample perpendicular to the b-axis. The capacitance measurement apparatus was the same as described in section A. The results of the dielectric constant measurements were in agreement with those of the Brillouin scattering, i.e. the transition temperatures do not change with pressure.

In order to resolve this conflict a new neutron scattering experiment under hydrostatic pressure is necessary. The preparation of this experiment is in progress.

C. Dependence of the Brillouin shift on pressure

From Fig. 5.2 we can calculate the quantity:

$$\Gamma = \frac{\Delta\omega}{\omega P} \tag{5.1}$$

where ω is the Brillouin shift at pressure P and $\Delta\omega$ is the change in frequency due to the change in pressure.

Using the data at 900 psi in Fig. 5.2 we obtained

$$\Gamma = 1.06\times10^{-5}\ (psi^{-1}) \tag{5.2}$$

For comparison we give the values of Γ for two other materials:

For Polymethylmethacrylate (Ref. 113)

$$\Gamma = 4.5\times10^{-6}\ (psi^{-1}) \tag{5.3}$$

For GaS (Ref. 114)

$$\Gamma = 4.17\times10^{-7}\ (psi^{-1}) \tag{5.4}$$

Γ is a linear function of P for Polymethymethacrylate from zero to 20 kpsi, and for GaS from zero to 720 kpsi. But for $NaNO_2$, Γ saturates at very low pressure (about 1.5 kpsi, see Fig. 5.2).

CHAPTER VI

ISING MODEL

Using the ANNNI model we performed numerical calculations of dielectric constants under a longitudinal electric field.

A. Ising model and mean field approximation

Consider a spin-$\frac{1}{2}$ Ising model with

$$H = - \sum_i \sum_j J_{ij} S_i S_j \tag{6.1}$$

where $S_i = \pm 1$

The partition function

$$Z = \sum_{(S_i)} \exp(- \beta H(S_i)) \tag{6.2}$$

The free energy

$$F = - K_B T \ln Z \tag{6.3}$$

F determines all equilibrium thermodynamic properties.

The statistical average (or expectation value) of a variable V is

$$\langle V \rangle = \frac{1}{Z} \sum_{(S_i)} V \exp(- \beta H(S_i)) \tag{6.4}$$

In the mean field approximation Eq. (6.1) becomes

$$\begin{aligned} H &= - \sum_i S_i \left(\sum_j J_{ij} S_j \right) \\ &= - \sum_i S_i \left(\sum_j \langle S_j \rangle \right) = - \sum_i S_i H_i \end{aligned} \tag{6.5}$$

where $H_i = \sum_j J_{ij} \langle S_j \rangle$ (6.6)

The Hamiltonian H is now a sum of single particle Hamiltonian H_i.

The expectation value of S_i is

$$\begin{aligned} \langle S_i \rangle &= \frac{1}{Z} \sum_{(S_i)} S_i \exp(- \beta H(S_i)) \\ &= \sum_{S_i = -1}^{1} S_i \exp(- \beta H_i) \; / \; \Sigma \exp(- \beta H_i) \end{aligned} \tag{6.7}$$

We therefore have

$$\langle S_i \rangle = \text{Tanh} (\beta H_i)$$

$$= \text{Tanh } \beta \left(\sum_j J_{ij} \langle S_j \rangle\right) \tag{6.8}$$

In the polarized (ferro) state, all $\langle S_i \rangle$ are equal

$$\therefore \quad \langle S_i \rangle = \text{Tanh} [\beta \langle S_i \rangle J] \tag{6.9}$$

with $J = \sum_j J_{ij}$

The graphical solution of Eq. (6.9) is shown in Fig. 6.1.

The phase transition occurs when the initial slope of Tanh $\beta J \langle S \rangle$ equals 1.

$$\beta J = 1 \rightarrow T_C = \frac{J}{K_B} = \frac{1}{K} \sum_j J_{ij} \tag{6.10}$$

Next, suppose there is a sinusoidal modulation

$$S_i = S_o \exp (ik r_i)$$

The mean field result is

$$\langle S_o \rangle \exp (ik r_i) = \text{Tanh } \beta\left(\sum_j J_{ij} \exp (ik r_j \langle S_o \rangle) \right)$$

$$\therefore \quad \langle S_o \rangle = \text{Tanh } \beta \langle S_o \rangle \left(\sum_j J_{ij} \exp (ik (r_j - r_i)) \right)$$

$$= \text{Tanh } (\beta \langle S_o \rangle J_k) \tag{6.12}$$

Again, the phase transition occurs when

$$T_C = \frac{J_k}{K_B} \tag{6.13}$$

$$\text{where } J_k = \sum_j J_{ij} \exp (ik (r_j - r_i)) \tag{6.14}$$

If we take $K_B = 1$, then

$$T_C = J_k \tag{6.15}$$

B. ANNNI model and mean field phase diagram

The anisotropic Ising model with competing nearest and next nearest neighbor interaction (the ANNNI model) is depicted in Fig. 6.2. The model

was invented by Elliott[111] in 1961 in order to describe the modulated magnetic structure of erbium. Following Elliott, the spins within the xy planes interact through a ferroelectric nearest neighbor coupling, $J_o > 0$; the nearest neighbor interaction between planes is J_1. For reasons of simplicity we assume $J_1 = J_o$. The interaction between spins in next-nearest-neighbor layers is antiferroelectric, $J_2 < 0$. The competing interactions stablize the modulated phase.

The ANNNI Hamiltonian is

$$H = -J_o \sum_{ij}^{xy(NN)} S_iS_j - J_1 \sum_{ij}^{z(NN)} S_iS_j - J_2 \sum_{ij}^{z(NNN)} S_iS_j$$

In mean field theory

$$H = -\sum_i S_i \left[4J_1\langle S_i\rangle + J_1(\langle S_{i+1}\rangle + \langle S_{i-1}\rangle) + J_2(\langle S_{i+2}\rangle + \langle S_{i-2}\rangle)\right] \tag{6.16}$$

The expectation value of the energy is

$$\langle H\rangle = -\sum_i \left[4J_1\langle S_i\rangle^2 + J_1(\langle S_i\rangle\langle S_{i+1}\rangle + \langle S_i\rangle\langle S_{i-1}\rangle) + (\langle s_i\rangle\langle S_{i+2}\rangle + \langle S_{i-2}\rangle)\right]$$

Assuming, again, a sinusoidal modulation, after some algebra we obtain

$$\frac{\langle H\rangle}{N} = \langle S_o\rangle^2 \left[-2J_1 - J_1 \cos ka - J_2 \cos 2ka\right] \tag{6.17}$$

Minimizing $\langle H\rangle$ to find the ground state

$$\frac{\partial\langle H\rangle}{\partial\theta} = 0$$

where $\theta = ka$

$$\therefore \quad J_1 \sin\theta + 4J_2 \sin\theta \cos\theta = 0 \tag{6.18}$$

The solutions of Eq. (6.18) are

$$\begin{array}{llll} \text{(a)} & \sin\theta = 0 \quad \theta = 0 & k = 0 & \text{ferro-phase} \\ \text{(b)} & \sin\theta = 0 \quad \theta = \pi & k = \frac{\pi}{a} & \text{antiferro-phase} \end{array} \tag{6.19}$$

(c) $\cos\theta = -\frac{J_1}{4J_2}$ $\theta = \cos^{-1}(-\frac{J_1}{4J_2})$ modulated-phase

Eqs. (6.14) and (6.15) give

$$T_C = 4J_1 + 2J_1\cos\theta + 2J_2\cos 2\theta \tag{6.20}$$

with $\theta = \cos^{-1}(-\frac{J_1}{4J_2})$ (6.21)

Eq. (6.20) can be rewritten as

$$\frac{T_C}{J_1} = 4 + 2\cos\theta + \frac{2J_2}{J_1}\cos\theta \tag{6.22}$$

Let $-\frac{J_2}{J_1} = \phi$ then

$$\frac{T_C(\phi)}{J_1} = 4 + 2\cos\theta - 2\phi\cos 2\theta \tag{6.23}$$

with $\theta = \cos^{-1}(\frac{1}{4\phi})$ (6.24)

Eq. (6.23) gives the transition line $T_C(\phi)$

$\phi = 0 \rightarrow J_2 = 0 \rightarrow \frac{T_C}{J_1} = 6$

$\phi = \frac{1}{4} \rightarrow J_1 = -4J_2 \rightarrow \frac{T_C}{J_1} = 5.5$

$\phi = 1 \rightarrow J_1 = -J_2 \rightarrow \frac{T_C}{J_1} = 6.25$

This transition line is shown in Fig. 6.3 (the upper solid line)

Eq. (6.20) gives

$\cos\theta = \frac{1}{4\phi}$ $\therefore$ $\phi \geq \frac{1}{4}$

Hence the modulated phase only exists in the region: $\phi \geq \frac{1}{4}$

The point of $\phi = \frac{1}{4}$ separates the three phases. This point corresponds to the Lifshitz point[93] (the point P in Fig. 6.3).

At T = 0 when $-\frac{J_2}{J_1}$ is small, the ground state is ferroelectric which is shown in Fig. 6.4 (a). The cost of creating a domain wall as shown in Fig. 6.4 (b) is $2J_2 + J_1$. When $-J_2 = \frac{1}{2}J_1$, the ferroelectric phase becomes marginally stable. Therefore at T = 0 the point of $\phi = 0.5$ is the transition point. In Fig. 6.3 the line from point P to the point of $\phi = 0.5$ separates the ferroelectric and the sinusoidal phase.

C. The calculated dielectric constant and the phase transition diagram of the ANNNI model

In $NaNO_2$, the dipole moment of the i-th ionic group $\mathbf{p}_i$ can be written as

$$\mathbf{p}_i = p\, s_i \frac{\mathbf{b}}{|\mathbf{b}|} \tag{6.25}$$

where p is the magnitude of a single moment.

In a longitudinal electric field the hamiltonian can be expressed as

$$\begin{aligned} H &= -\sum_{ij} J_{ij} S_i S_j - pE_{ext} \sum_i S_i \\ &= -\sum_{ij} J_{ij} S_i S_j - E \sum_i S_i \end{aligned} \tag{6.26}$$

where $E = p\, E_{ext}$, E_{ext} denotes the external electric field.

In the mean field approximation

$$\begin{aligned} H &= -\sum_i S_i \left[\sum_j J_{ij} \langle S_j \rangle + E \right] \\ &= -\sum_i S_i H_i \end{aligned} \tag{6.27}$$

where $H_i = \sum_j J_{ij} \langle S_j \rangle + E$ (6.28)

Similar to Eq. (6.8) the expectation value of S_i is

$$\langle S_i \rangle = \mathrm{Tanh}\, \beta \left[\sum_j J_{ij} \langle S_j \rangle + E \right] \tag{6.29}$$

The free energy per spin is given as[93,106]:

$$F(m,T) = \frac{1}{m} \sum_{i=0}^{m-1} [- T \ln(2 \cosh \beta (\sum_j J_{ij} < S_j > + E)) + < S_i > \sum_j J_{ij} < S_j >] \quad (6.30)$$

where m is the number of planes.

In the ANNNI model the expectation value of S_i under electric field E becomes

$$<S_i>_E = \text{Tanh } \beta [4J_1<S_i> + J_1(<S_{i+1}> + <S_{i-1}>) + J_2(<S_{i+2}> + <S_{i-2}>) + E] \quad (6.31)$$

The susceptibility is defined as

$$\chi = \frac{\delta P}{\delta E_{ext}} \quad (6.32)$$

where P is the polarization

$$P = \sum_i p_i$$

$$\therefore \quad P = p \sum_i <S_i> \quad (6.33)$$

$$\therefore \quad \chi = \frac{\delta P}{\delta E_{ext}} = \frac{p \delta P}{\delta E}$$

$$= p^2 \frac{\sum_i^m <S_i>_{E+\Delta E} - (\sum_i^m <S_i>_E)}{\Delta E} \quad (6.34)$$

where m is the number of planes.

The procedure we used for calculating χ was as follows:

Given J_1, J_2 and E (all in units of K_B), choose T, and start with a set of initial $<S_i>$ to compute the $<S_i>$ according to Eq. (6.31) using an iterative method. For N spins, there are N equations (i = 1, 2, ··· N). The boundary condition $<S_{N+1}> = <S_1>$ is used.

We note that in this approch the INC plane wave approximation has not been made, and that the modulated wave can develop higher harmonics naturally. Caculations by Bak and von Boehm[93] and those repeated by us, show that near the temperature T_I the spin arrangement, seen to be

stable, is almost sinusoidal, while higher harmonics develop as the temperature is lowered towards the lock-in temperature T_L. The only restraint in this approch is that the spin configuration repeats itself after a certain number of planes, m.

In order to determine the value of the parameters J_1 and J_2, we use the IPW (INC plane wave) approximation near T_I. This is justified further in the case of $NaNO_2$ as the modulated wavevector is purely sinusoidal throughout the INC-phase.

The value of J_1 can be determined as follows.

In $NaNO_2$, $T_I = 437^{\circ}K$

From Eq. (6.20) we have

$$T_I = 4J_1 + 2J_1\cos\theta + 2J_2\cos 2\theta \tag{6.35}$$

with $\theta = \cos^{-1}(-\frac{J_1}{4J_2})$

Elastic neutron scattering at zero electric field gives

$\delta = 0.122$ where δ is the reduced wavevector in units of a^*.

$$k = \delta a^* = \delta \frac{2\pi}{a}$$

$\therefore$ $ka = 2\pi \cdot 0.122 = 0.77$ (radians)

$= 43.9^{\circ}$

$\therefore$ $\cos ka = 0.72$, $\cos 2ka = 0.037$

$$\therefore -\frac{J_2}{J_1} = \phi = 0.347 \tag{6.36}$$

From Eq. (6.35) we obtain

$J_2 = -28.0$

$J_1 = 80.7$ (in units of K_B) (6.37)

Using these values for the iteration coefficients, with two different starting spin configurations, we obtained the dielectric constant

vesurs temperature curves with m = 25. For zero electric field, there are two peaks in the dielectric constant curve, qualitatively similar to the experimental results. The starting spin configurations used for the iteration for the curves shown in Fig. 6.5 and Fig. 6.6 were (-,+,-,+.....) and (-,-,+,+.....) respectively. While there were differences in some details when starting from the two different configurations, the qualitative features were essentially the same. In the former case (-,+, starting configuration), the two peaks at zero field are seperated by a temperature difference of ~ 200°C, while in the latter case of (-,-,+,+), the temperature difference was ~ 40°C. Both these values however, are much larger than the 1.4°C experimental value in the case of $NaNO_2$. We also calculated the free energiy per spin (Eq. (6.30)) for the final spin configuration at each temperature and found that for the case of the (-,-,+,+) starting spin configuration, the free energy calculated from the final spin configuration was lower than in the case where the starting spin configuration was (-,+). In both cases the application of an electric field, causes the two peaks to move further apart, that is, it increases the range of the INC region, rather than producing the experimentally observed result of the INC region becoming gradually narrower and eventually disappearing for a field of ~ 3 kV/cm. This behaviour of the INC region becoming larger with the application of field was consistently observed for a large range of the parameters J_1 and J_2 and for different starting spin configurations. Furthermore, the application of the field caused the first peak, (i.e. INC → ferro), to decrease in magnitude (absolute value), and the second peak (i.e. para → INC) to decrease in magnitude and also to broaden. The fields applied were larger than the experimental values.

We observed, from these calculations, that the dielectric constant curves versus temperature obtained were consistent with the mean field phase diagram, Fig. 6.3, given by Bak et al.[93] For values of $-J_2/J_1 < 0.5$, we obtained, for zero field, two peaks in the dielectric constant curve, reflecting the two transitions for positive temperatures, while for $-J_2/J_1 > 0.5$ we only obtained one peak, equivalent to the one transition, as predicted by the phase diagram.

Another variation we tried was as follows. After we obtained the self-consistent solution to Eq. (6.31), the solution was used to calculate the free energy per spin (Eq. (6.30)) for that value of m, the number of planes. This was done for a range of m ($3 \rightarrow 25$) and the m with the minimum free energy per spin is the stable phase at that temperature and for the given interaction coefficients. Again we found the qualitative behaviour for the dielectric constants calculated to be similar although the details were different. There were two peaks in the χ vs T curves and with the application of electric field, the two peaks moved further apart.

Recently, there has been an ANNNI model calculaton by Selke et al.[95] in which a mean field phase diagram (E vs T) was calculated which qualitatively models the behaviour in $NaNO_2$. Quantitatively, the values for the E-field and temperature range of the INC-phase are much larger than the experimental values. The range of the INC-phase at zero field is ~ 40°C, while the field at the triple point is ~ 60 statvolts/cm. The values of J_1 and J_2 that Selke et al. have used are similar to ours; the reason for the differences between their results and ours, with the application of electric field is not yet clear.

There has also been an ANNNI model calculation and an extended-ANNNI model calculation in external fields by Randa[106]. Here T/J_1 vs J_2/J_1 mean-field-phase diagram have been determined. According to this calculation, for a field of $E = 0.1$, there is no INC region for the parameters that either we or Selke at al. have used. The results of Selke et al. indicated that an INC-phase should exist for those parameters of J_0, J_1 and J_2 until a value of $E \sim 0.8$. Again the lack of agreement between the results of Randa and Selke et al., and between Randa and ours, is not yet understood.

CHAPTER VII

MICROSCOPIC THEORY OF MICHEL AND COWORKERS

In this chapter the microscopic theory of $NaNO_2$ of Michel and coworkers[23,30,96,97,98] is reviewed. Some of the results of the microscopic theory are cited for comparison with the results of the Landau free energy and the Ising model.

A. The microscopic model

As shown in Fig. 1.1, each NO_2^- ion is surrounded by six nearest-neighbor Na^+ ions. The single particle (one NO_2^- ion) potential which represents a crystal field term can be calculated numerically as shown in Fig. 1.3. The energetically most favorable path of reorientation is along the valley in Fig. 1.3, i.e. the reorientations take place essentially through rotations around the c-axis.

As a nitrite ion reorients, it interacts with neighboring sodium ions, pushing them out of the way. This leads to a coupling of translations and rotations. The Hamiltonian can be written as:

$$H = T + V_{TT} + V_{TR} + V_{RR} \tag{7.1}$$

where T is the kinetic energy of translations

$$T = \frac{1}{2} \sum_{\mathbf{k}} \mathbf{P}(\mathbf{k})\cdot\mathbf{P}(\mathbf{k}) \tag{7.2}$$

V_{TT} is the corresponding harmonic interactions

$$V_{TT} = \frac{1}{2} \sum_{\mathbf{k}} \mathbf{u}(\mathbf{k})\bar{\bar{M}}(\mathbf{k})\mathbf{u}(\mathbf{k}) \tag{7.3}$$

The variables **u** and **p** respectively are the Fourier transforms (**k** is the wavevector) of the center of mass lattice displacements and their conjugate momenta. The total mass $m = m_{Na} + m_{NO_2}$ is taken equal to 1.

$\bar{M}(\mathbf{k})$ is the corresponding 3x3 dynamical matrix.

The tranlation-rotation interactions V_{TR} is given by the bilinear interaction

$$V_{TR} = \sum_{\mathbf{k}} V(\mathbf{k})\cdot\mathbf{u}(\mathbf{k})\,\sigma(-\mathbf{k}) \tag{7.4}$$

The coupling matrix $V(\mathbf{k})$ is an even function of $\mathbf{k}$ and is quadratic in $\mathbf{k}$ in the long-wavelength limit.

The direct orientational interaction is written as:

$$V_{RR} = \frac{1}{2}\sum_{\mathbf{k}} J(\mathbf{k})\,\sigma(\mathbf{k})\,\sigma(-\mathbf{k}) \tag{7.5}$$

$J(\mathbf{k})$ accounts for the electric dipole-diple interaction, $\sigma(\mathbf{k})$ denotes an Ising pseudospin order parameter.

B. Free energy and phase diagram

The Helmhotz free energy is given by

$$\mathcal{N} = \mathrm{Tr}(\rho H + T\rho\ln\rho) \tag{7.6}$$

where ρ is the density matrix and T is the temperature in units of K_B. The density matrix satisfies the condition $\mathrm{Tr}(\rho) = 1$.

The non-equilibrium free energy depends on the instantaneous expectation values of the slow dynamic variables given by:

$$\begin{aligned} s_i(\mathbf{k},t) &= T_r\rho u_i(\mathbf{k}) \\ \dot{s}_i(\mathbf{k},t) &= T_r\rho P_i(\mathbf{k}) \\ m(\mathbf{k},t) &= T_r\rho\,\sigma(\mathbf{k}) \end{aligned} \tag{7.7}$$

where m is the orientational order parameter, s is the displacement parameter.

After some algebra, the non-equilibrium free energy of the dynamic variable in Eq. (7.7) and in a mean-field approximation to fourth order in the order parameter can be written as:

$$F = \frac{1}{2}\sum_{k}\dot{s}\cdot\dot{s}(-k) + \frac{1}{2}\sum_{k}\bar{\bar{M}}(k)s(k)s(-k)$$

$$+ \sum_{k} v(k)m(k)s(-k) + \frac{1}{2}\sum_{k}(J(k) + C^{S} + T)m(k)m(-k)$$

$$+ \frac{T}{12}\sum_{k,p,q} m(-k)m(-p)m(-q)m(k + p + q) + o(m^{6}) \tag{7.8}$$

here, C^{S} is given by

$$C^{S} = \frac{1}{N}\sum_{k} C(k) \tag{7.9}$$

$$C(k) = v(k)\bar{\bar{M}}^{-1}(k)v^{\tau}(k) \tag{7.10}$$

where τ represents transposition. C^{S} takes into account that the effective self interaction mediated by the lattice must be subtracted in a mean-field calculation.

The equilibrium free energy can be simply obtained from Eq. (7.8) by minimization with respect to the expectation values $s(k)$, $\dot{s}(k)$, and $m(k)$.

From $\frac{\partial F}{\partial s(k)} = 0$ yields

$$s(k) = - v(k)\bar{\bar{M}}^{-1}(k)m(k) \tag{7.11}$$

From $\frac{\partial F}{\partial \dot{s}(k)} = 0$ follows

$$\dot{s}(k) = 0 \tag{7.12}$$

Substituting Eq. (7.11) and (7.12) into Eq. (7.8), we have

$$F = -\frac{1}{2}\sum_{k}(K(k)-T)m(k)m(-k)$$

$$+\frac{T}{12}\sum_{k,p,q} m(-k)m(-p)m(-q)m(k + p + q) \tag{7.13}$$

where the orientational interaction $K(k)$ is defined by

$$K(k) = C(k) - J(k) - C^{S} \tag{7.14}$$

From $\frac{\partial F}{\partial m(k)} = 0$ we obtain:

If $k=0$ then $F(0) = -\frac{1}{2}(K(0) - T)|m(0)|^{2} + \frac{T}{12}|m(0)|^{4}$ (7.15)

If $k \neq 0$ then

$$F(\mathbf{k}) = -(K(\mathbf{k}) - T)|m(\mathbf{k})|^2 + \frac{T}{2}|m(\mathbf{k})|^4 \tag{7.16}$$

A necessary condition to have an INC-phase is that $K(k)$ has an extremum at $\mathbf{k}_o \neq 0$. Since $K(\mathbf{k})$ is even in $\mathbf{k}$, we have an extremum at $\mathbf{k}=0$.

Equation $\frac{\partial F}{\partial m(\mathbf{k})} = 0$ has three solutions:

$$m(k)=0; \quad F=0 \quad \text{(all T)} \tag{7.17}$$

$$m(\mathbf{k}) = m(\mathbf{k}_o)\ \delta_{k,k_o} + m(-\mathbf{k}_o)\ \delta_{k,-k_o};$$

$$|m(\mathbf{k}_o)|^2 = \beta\ K(\mathbf{k}_o) - 1;$$

$$F(\mathbf{k}_o) = -\frac{T}{2}(\beta\ K(\mathbf{k}_o) - 1)^2 \qquad (T < K(\mathbf{k}_o)) \tag{7.18}$$

$$m(\mathbf{k}_o) = m(0)\ \delta_{k,o}; \quad m(0)^2 = 3\ (\beta K(0) - 1)$$

$$F(0) = -\frac{3}{4}(\beta K(0) - 1)^2 \tag{7.19}$$

Fig. 7.1 depicts the temperature behavior of the three solutions of the free energy. Here we assumed

$$0 < K(0) < K(\mathbf{k}_o) \tag{7.20}$$

Fig. 7.1 is very similar to Fig. 2.11 which was obtained from the phenomenological free energy.

The transition from the para-phase to the INC-phase is of second order, since the free energy has a continuous derivative, with transition temperature

$$T_I = K(\mathbf{k}_o) \tag{7.21}$$

On the other hand the transition from the INC to the ferro-phase is of first order because the free energies $F(0)$ and $F(\mathbf{k}_o)$ cross each other. The intersection determines the transition temperature

$$T_L = K(\mathbf{k}_o) \cdot \frac{\alpha - \sqrt{\frac{2}{3}}}{1 - \sqrt{\frac{2}{3}}} \tag{7.22}$$

where $\alpha = \frac{K(0)}{K(\mathbf{k}_o)}$ and $0 < \alpha < 1$

The resulting phase diagram is shown in Fig. 7.2.

C. Susceptibility and modulation wavevector

The static orientational susceptibilities can be obtained by using the relation

$$\chi^{-1}(\mathbf{k}) = \frac{\partial^2 F}{\partial m(\mathbf{k}) \partial m(-\mathbf{k})} \Big| m(\mathbf{q}) = <o(\mathbf{q})> \tag{7.23}$$

It is found in the para-phase

$$\chi^{-1}(\mathbf{k}) = T - K(\mathbf{k}) \tag{7.24}$$

and in the INC-phase

$$\chi^{-1}(\mathbf{k}) = T - K(\mathbf{k}) + 2Tm^2 \tag{7.25}$$

Eq. (7.10) gives $C(\mathbf{k}) = v(\mathbf{k}) \bar{\bar{M}}^{-1} v^T(\mathbf{k})$

Due to the simple structure of $v(\mathbf{k})$, the matrix C has only one single element:

$$C_{11} = v_1 (M^{-1})_{11} v_1 \tag{7.26}$$

The Eq. (7.24) can be rewritten as

$$\chi^{-1} = T - C_{11}(\mathbf{k}) + C^S + J(\mathbf{k}) \tag{27}$$

For $\mathbf{k} = (k,0,0)$ and in the long wavelength case the coefficients in Eq. (7.26) can be specified as

$$M_{11}(k) = \alpha' k^2 \tag{7.28}$$

where $\alpha' = C_{66}^o \rho^{-1}$, C_{66}^o is the bare elastic constant

ρ is the material density

$$v_1(k) = 2\sigma k^2$$

where $\sigma = -\frac{Ca^2}{4}$, C is a coupling parameter

a is the lattice constant

σ is a microscopic model constant

For the dipolar interaction J(k), we use an expansion:

$$J(k) = -d + \sigma k^2 + \gamma k^4 \tag{7.29}$$

where $d > 0, \quad \gamma > 0, \quad \delta \lesssim 0$

Eq. (7.27) becomes

$$\chi^{-1} = uk^4 + vk^2 + w \tag{7.30}$$

where $u = \gamma, \quad v = \delta - \frac{4\sigma^2}{\alpha'}, \quad w = T + C_o - d$

In the para-phase, for a given temperature T, the susceptibility $\chi(k)$ has a maximum at

$$k_m = \pm\sqrt{-\frac{v}{2u}} = \pm\sqrt{\frac{4\sigma^2 - \delta\alpha'}{2\alpha'\gamma}} \tag{7.31}$$

With decreasing temperature, $\chi(k)$ increases and becomes infinite at a temperature T_I obtained from the solution of

$$v^2 - 4uw = 0$$

i.e. $$T_I = d - C_o + \frac{(\frac{4\sigma^2}{\alpha'} - \delta)^2}{4\gamma} \tag{7.32}$$

The corresponding value of k is given by

$$k_o = k_m \tag{7.33}$$

Experiment shows that the position of the maximum of $\chi(k)$ in the para-phase shifts to lower values k_m with decreasing temperature. In Michel's opinion the temperature dependence of k_m arises from a tempera-

ture dependence of the bilinear coupling $\sigma \propto C$. The coupling is a function of lattice parameters. The thermal fluctuations lead to an increase of coupling C with increasing temperature. Since $C \propto \sigma$, it follows from Eq. (7.31) that k_m decreases with decreasing temperature until it reaches the value k_o at T_I. The decrease of the INC wavevector k_o with decreasing temperature which is observed by experiment should also result from a decrease of the amplitude of fluctuations with decreasing temperature. Michel pointed out that since we expect that the decrease of the amplitude of fluctuations has a different slope in the disordered and in the INC-phase, we expect a different slope in the temperature variations of $k_m(T)$ and $k_o(T)$.

D. Lattice instability

Fivez and Michel[98] have investigated the dynamical consequences of the translation-rotation coupling mechanism. They concluded that the dynamics is dominated by the slow relaxation behavior of orientational fluctuations. Therefore the lattice dynamics of the para-phase is characterized by phonon side bands which are not sensibly influenced by the coupling to the orientational order parameter. There is no phonon softening. The phonon side bands in the INC-phase are also unaffected by the translation-rotation coupling and again there is no phonon softening.

E. Connection between microscopic theory and phenomenological theory

Fivez and Michel[98] pointed out that the expression (7.13) for the free energy, based on the microscopic model, has the same mathematical structure as the phenomenological potential used by Ishibashi and

Shiba[90].

In order to establish more closely a connection with the macroscopic approaches used by Levanyuk et al.[9] and Heine et al.[11], Michel[30] related the center-of-mass displacements to the strain field $\varepsilon(\mathbf{k})$ by writing

$$\varepsilon_{ij}(\mathbf{k}) = ik_i \, s_j(\mathbf{k})$$

In the long-wavelength limit and $\mathbf{k} = (k,0,0)$, Eq. (7.11) reads:

$$s_y(k) = - M_{11}^{-1} \, v_1(k) \, m(k) \tag{7.34}$$

$$\therefore \varepsilon_{xy}(k) = ik \, m(k) \cdot \frac{aC}{bcC_{66}^0} \tag{7.35}$$

where a, b, c are the lattice constants.

The correspondence of the axes is $\mathbf{a}, \mathbf{b}, \mathbf{c} \rightarrow x, y, z$

Consequently the strain field is proportional to the gradient of the orientational order parameter. The bilinear coupling term in Eq. (7.8) now reads in the long-wavelength limit

$$\sum_k v_1(k) \, s_y(k) \, m^*(k) = - \frac{Ca^2}{4} \sum_k [\varepsilon_{xy}(ikm)^* + ikm \varepsilon_{xy}^*] \tag{7.36}$$

where ε_{xy} and m depend on k.

Expression (7.36) has the same form as the gradient terms which are introduced in the phenomenological theories[9,11].

CHAPTER VIII

CONCLUSIONS

Dielectric constant measurements and Elastic neutron scattering in the presence of a longitudinal electric field revealed that the temperature range of the INC-phase of $NaNO_2$ decreases with increasing electric field. At 3 kV/cm the three phases, para, INC and ferro, meet at a point which is called a triple point. At the triple point the modulation wavevector is not equal to zero. In the INC-phase the modulation wavevector decreases with decreasing temperature but does not depend on the longitudinal electric field.

The phase diagram and the behavior of the modulation wavevector can be reproduced fairly well by numerical calculations with the Landau-type free energy model proposed by Ishibashi et al.[90,91]. Comparison of our diffuse neutron scattering results with the predictions of the free energy model indicates that the η-term in the free energy cannot be neglected, while the temperature dependence of the coefficient α should also be retained. There is another fact which also leads to the conclusion that the η-term cannot be neglected: without the η-term the phase transition from the para-phase to the INC-phase will be of first order. However, the observed para → INC transition is of second order.

All the coefficients in the free energy model have been determined from the dielectric constant measurements, the elastic neutron scattering results and the spotaneous polarization data.

The extension of the Lifshitz point concept to systems with a first order transition from the disordered phase to the ordered phase has been discussed in detail. The phase diagram is as follows: the para → INC

transition occurs along the T_I line. At the crossing point CP the T_I line meets the first-order para→ferro T_1 line; the INC → ferro transition occurs along the T_L line. At the point P ($\alpha^2 = 3\beta B^2/8C$) the T_L line jumps to the point CP where it meets the T_I line; beyond this point the direct para → ferro transition occurs along the T_1 line. Fitting our data of elastic neutron scattering under transverse electric field to the numerically calculated results of δ_I, δ_L and $T_I - T_L$ indicates that in $NaNO_2$ the virtual Lifshitz point is at (7.32 kV/cm, 122.15°C) for the E-field parallel to the a-axis, and at (16.37 kV/cm, 142.73°C) for the E-field parallel to the c-axis. The INC-phase ceases to exist at E_a = 4.59 kV/cm or E_c = 10.24 kV/cm. The tricritical point TP is at 3.5×10^{-19} (CGS units). The difference between the physically accessible transition temperature T_{1LP} and the virtual transition temperature T_{LP} is about 0.6°C. This LP point is inaccessible, however, not only because the samples break down electrically at electric fields above 1.36 kV/cm for the E-field parallel to the a-axis, and at electric fields above 2.21 kV/cm for the E-field parallel to the c-axis, but also because the first order direct transition intervenes and the LP is virtual.

It should be pointed out that the position of the tricritical point TP on the phase diagram depends on the coefficients B, β and η (see Eq. (3.29)). Therefore, in principle, the tricritical point TP could be on the high temperature side of the critical point CP; in other words, the tricritical point could be physically accessible for some values of the above three coefficients. As a result, the T_I' line would also be physically accessible. It would be interesting to find such systems for which the tricritical point and the T_I' line are physically accessible.

The results of Brillouin scattering with an E-field along the c-axis confirmed the results of neutron scattering under transverse E-field and also revealed that the transverse electric field does not dramatically change the propagation of hypersonic waves, but it does reduce the difference of the sound velocities between the para and the ferro phases. Let v_L and v_I be the sound velocities along the [010] direction at T_L and T_I respectively, and $\Delta v = v_L - v_I$. Then, at E = 0 kV/cm, $\Delta v = 1 \times 10^3$ cm/s, at E = 0.5 kV/cm, $\Delta v = 0.4 \times 10^3$ cm/s, and at E = 1.0 kV/cm, $\Delta v = 0.26 \times 10^3$ cm/s. The sound velocity along the [100] direction deduced from the inelastic neutron scattering experiments is about 1.45×10^5 cm/s, which is in agreement with the result obtained by Durand et al.[46,58].

The results of the dielectric constant measurements performed in 1983 show that in the range of pressure from 14.5 psi to 1000 psi, both T_I and T_L decrease while ΔT ($\Delta T = T_I - T_L$) decreases slightly. Above 1000 psi, however, T_I, T_L and ΔT all increase with increasing pressure. The results of Brillouin scattering under hydrostatic pressure show that the transition temperatures do not depend on the pressure. To explain this disagreement the dielectric constant measurements were performed again under the same coditions as for Brillouin scattering, and results identical to those of the Brillouin scattering experiment were obtained. In order to resolve this contradiction, a new neutron scattering experiment under hydrostatic pressure is necessary.

Using the ANNNI model, a preliminary calculation of the dielectric constants under longitudinal electric field was performed in mean-field approximation. For zero electric field, there are two peaks in the dielectric constant curve, somewhat similar qualitatively to the experimental results, and consistent with the mean field phase diagram in Fig.

6.3. But the application of an electric field causes the two peaks to move apart rather than reproducing the experimentally observed result of the INC region becoming gradually narrower with increasing field. This behaviour of the INC region becoming larger with the application of field, is consistently observed with a large range of the parameters and different starting spin configurations.

The microscopic theory of Michel and coworkers[23,30,96-98] can explain many important experimental results such as the reorientations of NO_2^- groups which take place essentially through rotations around the c-axis, and the fact that there are no soft modes in either the para or INC phases, etc.. But the phase diagram and the behavior of the modulation wavevector under electric field are not yet explained quantitatively by the microscopic thoery.

APPENDIX A

UNITS

It is well known that the Coulomb's law has different forms in different systems of units.

In MKS units: $f = \frac{kq_1q_2}{r^2}$ where f is in Newtons (N)

q is in Coulombs (C)

r is in meters (m)

$k = 9.0\times10^9 \frac{Nm^2}{C^2}$

In CGS units: $f = \frac{q_1q_2}{r^2}$ where f is in dynes

q is in esu

r is in cm

The units of the terms in the free energy and their conversion from MKS to CGS units are derived below. The results are given in Tables A.1 and A.2.

1. Conversion of the Landau free energy from MKS to CGS units

We take the Landau free energy as:

$$F = \frac{1}{2}AP_o^2 + \frac{1}{4}BP_o^4 + \frac{1}{6}CP_o^6 - EP_o + \frac{1}{4}(A + \alpha k^2 + \frac{1}{2}\beta k^4)P_K^2$$

$$+ \frac{3}{8}(2B + \frac{1}{3}\eta k^2)P_o^2P_K^2 + \frac{3}{32}(B + \frac{1}{3}\eta k^2)P_K^4$$

Now we convert F from MKS units to CGS units term by term.

a. Conversion of the first term $\frac{1}{2}AP^2$ in F:

In MKS units we write $F_M=\frac{1}{2}A_M P_M$ (1)

where the subscript M denotes MKS units.

The dimension of energy F is:

$$1\ (\frac{J}{m^3}) = \frac{10^7}{10^6}\ (\frac{erg}{cm^3}) = 10\ (\frac{erg}{cm^3})$$

The dimension of polarization P is:

$$1\ (\frac{C}{m^2}) = \frac{3x10^9}{10^4}\ (\frac{esu}{cm^2}) = 3x10^5\ (\frac{esu}{cm^2})$$

Therefore the dimension of coefficient A is:

$$1\ (\frac{Vm}{C}) = \frac{1}{300}\frac{100}{3x10^9}\ (\frac{statevolt\cdot cm}{esu})$$

$$= \frac{1}{9x10^9}\ (\frac{statevolt\cdot cm}{esu})$$

$$\therefore \quad F_M = \frac{1}{10}F_C$$

$$P_M = \frac{1}{3x10^5}P_C \qquad (2)$$

$$A_M = 9x10^9 A_C$$

where the subscript C denotes CGS units.

Substituting (2) into (1) we get:

$$\frac{1}{10}F_C = \frac{1}{2}x9x10^9 A_C\cdot(\frac{1}{3x10^5}P_C)^2$$

$$\therefore \quad F_C = \frac{1}{2}A_C P_C^2 \qquad (3)$$

b. Conversion of the second term $\frac{1}{4}BP^4$ in F:

In MKS units $F = \frac{1}{4}B_M P_M$ (4)

$\because$ For F $1\ (\frac{J}{m^3}) = 10\cdot\ (\frac{erg}{cm^3})$

For P $1\ (\frac{C}{m^2}) = 3x10^5\ (\frac{esu}{cm^2})$

For B $\quad 1\ (\frac{Vm^5}{C^3}) = \frac{1}{300}\frac{10^{10}}{3^3x10^{27}}\ (\frac{statvolt\cdot cm^5}{esu^3})$

$$= \frac{1}{3^4x10^{19}}\ (\frac{statvolt\cdot cm^5}{esu^3})$$

$\therefore \quad F_M = \frac{1}{10}F_C$

$$P_M^4 = (\frac{1}{3x10^5}P_C)^4 \tag{5}$$

$$B_M = \frac{1}{3^4x10^{19}}B_C$$

Substituting (5) to (4) we get

$$\frac{1}{10}F_C = \frac{1}{4}\frac{1}{3x10^{19}}B_C\cdot(\frac{1}{3x10^5}P_C)$$

$$\therefore \quad F_C = \frac{1}{4}B_C\cdot P_C^4 \tag{6}$$

c. Conversion of the third term $\frac{1}{6}P^6$ in F:

In MKS units $\quad F_M = \frac{1}{6}C_M P_M^6$ (7)

$\because$ For C $\quad 1\ (\frac{Vm^9}{C^5}) = \frac{1}{300}\frac{10^{18}}{3^5x10^{45}}\ (\frac{statvolt\cdot cm^9}{esu^5})$

$$= \frac{1}{3x10^{29}}\ (\frac{statvolt\cdot cm^9}{esu^5})$$

$\therefore \quad F_M = \frac{1}{10}F_C$

$$P_M^6 = (\frac{1}{3x10^5}P_C)^6 \tag{8}$$

$$C_M = \frac{1}{3^6x10^{29}}C_C$$

Substituting (8) into (7) we get:

$$\frac{1}{10}F_C = \frac{1}{6}\frac{1}{3^6x10^{29}}C_C\cdot\ (\frac{1}{3x10^5}P_C)^6$$

$$\therefore \quad F_C = \frac{1}{6}C_C P_C^6 \tag{9}$$

d. Conversion of the term of $\frac{1}{4}\alpha k^2 P_K^2$ in F:

In MKS units $$F_M = \frac{1}{4}\alpha_M k_M^2 P_{KM}^2 \tag{10}$$

$\because$ For α: $$1\ (\frac{Vm^3}{C}) = \frac{1}{300}\frac{10^6}{3x10^9}\ (\frac{statvolt\cdot cm^3}{esu})$$

$$= \frac{1}{3^2x10^5}\ (\frac{statvolt\cdot cm^3}{esu})$$

For k: $$1\ (\frac{1}{m}) = \frac{1}{10^2}\ (\frac{1}{cm})$$

$\therefore$ $$F_M = \frac{1}{10}F_C$$

$$P_{KM}^2 = (\frac{1}{3x10^5}P_{kC})^2 \tag{11}$$

$$\alpha_M = (\frac{1}{3^2x10^5})^{-1}\cdot\alpha_C = 3^2x10^5\alpha_C$$

$$k_M^2 = 10^4\cdot k_C^2$$

Substituting (11) into (10) we get:

$$\frac{1}{10}F_C = \frac{3^2x10^5}{4}\alpha_C x10^4 k_C^2\cdot(\frac{1}{3x10^5}P_{kC})^2$$

$\therefore$ $$F_C = \frac{1}{4}\alpha_C k_C^2 P_{KC}^2 \tag{12}$$

e. Conversion of the term of $\beta k^4 P_K^2$ in F:

In MKS units $$F_M = \beta_M k_M^4 P_{KM}^2 \tag{13}$$

For β: $$1\ (\frac{Vm^5}{C}) = \frac{1}{300}\frac{10^{10}}{3x10^9}\ (\frac{statvolt\cdot cm^5}{esu})$$

$$= \frac{1}{3^2x10}\ (\frac{statvolt\cdot cm^5}{esu})$$

$\therefore$ $$F_M = \frac{1}{10}F_C$$

$$P_{KM}^2 = (\frac{1}{3x10^5}P_{kC})^2 \tag{14}$$

$$\beta_M = 3^2x10\beta_C$$

$$k_M^4 = (10^2 k_C)^4$$

Substituting (14) into (13) we get:

$$\frac{1}{10}F_C = 3^2 \times 10 \beta_C \cdot (10^2 k_C)^4 \cdot \left(\frac{1}{3\times10^5} P_{kC}\right)^2$$

$$\therefore \quad F_C = \beta_C k_C^4 P_{kC}^4 \tag{15}$$

f. Conversion of the term of $\eta k^2 P_o^2 P_k^2$ in F:

In MKS units $\quad F_M = \eta_M k_M^2 P_{oM}^2 P_{kM}^2 \tag{16}$

For η: $\quad 1 \left(\frac{Vm^7}{C^3}\right) = \frac{1}{300} \frac{10^{14}}{3^3 \times 10^{27}} (CGS)$

$$= \frac{1}{3^4 \times 10^{15}} (CGS)$$

$$\therefore \quad F_M = \frac{1}{10} G_C$$

$$\eta_M = 3^4 \times 10^{15} \eta_C \tag{17}$$

$$k_M^2 = (10^2 k_C^2)^2$$

$$P_{oM}^2 P_{kM}^2 = \left(\frac{1}{3\times10^5}\right)^4 P_{oC}^2 P_{kC}^2$$

Substituting (17) into (16) we get

$$\frac{1}{10}F_C = 3\times10^{15} \eta_C k_C^2 (10^2 k_C)^2 \cdot \left(\frac{1}{3\times10^5}\right)^4 P_{oC}^2 P_{kC}^2 \tag{18}$$

$$\therefore \quad F_C = \eta_C k_C^2 P_{oC}^2 P^2$$

g. Conversion of the term of EP in F:

In MKS units $\quad F_M = E_M P_M \tag{19}$

For E: $\quad 1 \left(\frac{V}{m}\right) = \frac{\frac{1}{300}}{10^2} (CGS)$

$$= \frac{1}{3\times10^4} (CGS)$$

$$\therefore \quad F_M = \frac{1}{10} F_C$$

$$P_M = \frac{1}{3\times10^5} P_C \tag{20}$$

$$E_M = 3\times10^4 E_C$$

Substituting (20) into (19) we get

$$\frac{1}{10} F_C = 3\times10^4 E_C \frac{1}{3\times10^5} P_C$$

$$\therefore \quad F_C = E_C P_C \tag{21}$$

The above conversions show that the Landau free energy has the same form in both MKS and CGS units.

Next we are going to determine the dimension of each coefficient of the Landau free energy in MKS and CGS units respectively.

2. Dimensions of the coefficients of the Landau free energy in CGS units

a. Dimensions of the coefficients A and A_0

Take $F = \frac{1}{2}AP^2$

Dimension of F is: $[F] = (\frac{erg}{cm^3})$

Dimension of P is: $[P] = (\frac{esu\cdot cm}{cm^3}) = (\frac{esu}{cm^2})$

Coulomb's law in vacuum is $f=\frac{q_1q_2}{r^2}$

$$[f] = (\frac{esu^2}{cm^2})$$

$$f\cdot r = \frac{q_1q_2}{r^2\cdot r} \quad \therefore \quad [f\cdot r] = (\frac{esu^2}{cm}) = erg$$

$$(\frac{erg}{cm^3}) = (\frac{esu^2}{cm^4})$$

$$\therefore \quad [F] = (\frac{erg}{cm^3}) = (\frac{esu^2}{cm^4}) \tag{23}$$

$$\because \quad [P] = (\frac{esu}{cm^2}) \quad \therefore \quad [P^2] = (\frac{esu^2}{cm^4})$$

Therefore F and P^2 have the same dimension, from $F = \frac{1}{2}AP^2$ it is found that in CGS units A is dimensionless.

$\therefore$ $A = A_o(T - T_o)$

$\therefore$ $[A_o] = (\frac{1}{T})$ (24)

where T is temperature.

b. Dimensions of the coefficients B and C

(1). Take $F \sim BP^4$

$$[F] = (\frac{esu^2}{cm^4}), \quad [P^4] = (\frac{esu^4}{cm^8})$$

$\therefore$ $[B] = (\frac{esu^2}{cm^4})\cdot(\frac{cm^8}{esu^2}) = (\frac{cm^4}{esu^2})$ (25)

(2). Take $F \sim CP^6$

$$[F] = (\frac{esu^2}{cm^4}), \quad [P^6] = (\frac{esu^6}{cm^{12}})$$

$\therefore$ $[C] = (\frac{esu^2}{cm^4})\cdot(\frac{cm^{12}}{esu^6}) = (\frac{cm^8}{esu^4})$ (26)

c. Dimensions of the coefficients α, β and η

(1). Take $F \sim \alpha k^2 P_k^2$

$$[k^2] = (\frac{1}{cm^2}), \qquad [P^2{}_k] = (\frac{esu^2}{cm^4})$$

$$[\alpha] = (\frac{esu^2}{cm^4})\cdot(cm^2)\cdot(\frac{cm^4}{esu^2}) = (cm^2)$$ (27)

(2). Take $F \sim \beta k^4 P_k^2$

$$[k^4] = (\frac{1}{cm^4}), \qquad [P_k^2] = (\frac{esu^2}{cm^4})$$

$\therefore$ $[\beta] = (\frac{esu^2}{cm^4})\cdot(cm^4)\cdot(\frac{cm^4}{esu^2}) = (cm^4)$ (28)

(3) Take $F \sim \eta k^2 P_o^2 P_k^2$

$$[P_o^2 P_k^2] = (\frac{esu^4}{cm^8})$$

$\therefore$ $[\eta] = (\frac{esu^2}{cm^4})\cdot(cm^2)\cdot(\frac{cm^8}{esu^4}) = (\frac{cm^6}{esu^2})$ (29)

3. Dimensions of the coefficients of the Landau free energy in MKS units

a. Dimensions of the coefficients A and A_o

Take $F \sim AP^2$

In MKS units F has dimension: $[F] = (\frac{J}{m^3})$,

P has dimension: $[P] = (\frac{C \cdot m}{m^3}) = (\frac{C}{m^2})$ (30)

where J denotes joule and C denotes coulomb.

According to Coulomb's law: $f = k \frac{q_1 q_2}{r^2}$

where k is determined by experiment to be $\sim 9.0 \times 10^9$ $(\frac{Nm^2}{C^2})$

$[f] = (\frac{Nm^2}{C^2}) \cdot (\frac{C^2}{m^2}) = N$, and $[f \cdot r] = (N \cdot m) = J$

$(\frac{J}{m^3}) = (\frac{N}{m^2})$

$\therefore [F] = (\frac{J}{m^3}) = (\frac{N}{m^2})$

On the other hand $F = Eq = -\nabla V q$

$\therefore [F] = (\frac{VC}{m^3}) = (\frac{J}{m^3}) = (\frac{N}{m^2})$ (31)

Eq. (29) gives $[P^2] = (\frac{C^2}{m^4})$

$\therefore [A] = (\frac{VC}{m^3}) \cdot (\frac{m^4}{C^2}) = (\frac{Vm}{C}) = (\frac{Jm}{C^2})$ (32)

$A = A_o(T - T_o)$

$\therefore [A_o] = (\frac{Vm}{TC}) = (\frac{Jm}{C^2T})$ (33)

b. Dimensions of the coefficients B and C

(1) Take $F \sim BP^4$

$[F] = (\frac{VC}{m^3})$, $[P^4] = (\frac{C^4}{m^8})$

$$\therefore [B] = \left(\frac{VC}{m^3}\right)\cdot\left(\frac{C^4}{m^8}\right) = \left(\frac{Vm^5}{C^3}\right) = \left(\frac{Jm^5}{C^4}\right) \tag{34}$$

(2) Take $F \sim CP^6$

$$[F] = \left(\frac{VC}{m^3}\right), \quad [P^6] = \left(\frac{C^6}{m^{12}}\right)$$

$$\therefore [C] = \left(\frac{VC}{m^3}\right)\cdot\left(\frac{m^{12}}{C^6}\right) = \left(\frac{Vm^9}{C^5}\right) = \left(\frac{Jm^9}{C^6}\right) \tag{35}$$

c. Dimensions of the coefficients α, β and η

(1) Take $F \sim \alpha k^2 P_K^2$

$$[F] = \left(\frac{VC}{m^3}\right), \quad [P_K^2] = \left(\frac{C^2}{m^4}\right), \quad [k^2] = \left(\frac{1}{m^2}\right)$$

$$\therefore [\alpha] = \left(\frac{VC}{m^3}\right)\cdot\left(\frac{m^4}{C^2}\right)\cdot(m^2) = \left(\frac{Vm^3}{C}\right) = \left(\frac{Jm^3}{C^2}\right) \tag{36}$$

(2) Take $F \sim \beta k^4 P_K^2$

$$[k^4] = \left(\frac{1}{m^4}\right)$$

$$\therefore [\beta] = \left(\frac{VC}{m^3}\right)\cdot\left(\frac{m^4}{C^2}\right)\cdot(m^4) = \left(\frac{Vm^5}{C}\right) = \left(\frac{Jm^5}{C^2}\right) \tag{37}$$

(3) Take $F \sim \eta k^2 P_0^2 P_K^2$

$$[P_0^2] = \left(\frac{C^4}{m^8}\right)$$

$$\therefore [\eta] = \left(\frac{VC}{m^3}\right)\cdot(m^2)\cdot\left(\frac{m^8}{C^4}\right) = \left(\frac{Vm^7}{C^3}\right) = \left(\frac{Jm^7}{C^4}\right) \tag{38}$$

4. Summary

a. The dimensions of the coefficients of the Landau free energy in both MKS and CGS units are listed in Table A.1.

b. The conversions of each coefficient in the Landau free energy from MKS to CGS units is listed in Table A.2.

c. The values of the coefficients in the sixth order free energy model determined by three authors are listed in Table A.3.

APPENDIX B

CRYSTAL GROWTH OF $NaNO_2$

$NaNO_2$ single crystals were grown from the melt in our laboratory following procedures suggested by Professor Y. Ishibashi which are described as follows:

1. Use purest reagent

We used S-347 $NaNO_2$ powder ordered from Fisher Scientific Company (purity is 97%). The material can be further purified by recrystallization.

2. Dry the $NaNO_2$ powder for several days (~5 days) at a temperature higher than 100°C in a vacuum of 10^{-2} Torr. This is very important since $NaNO_2$ is hygroscopic.

3. Charge the dried $NaNO_2$ powder in a glazed alumina-crucible (Cat. No. 12-220B from Fisher Scientific Company). Set the crucible in a vertical electric furnace. Melt the powder, but do not raise the temperature higher than the melting temperature (277°C) + 20°C, because the NO_2 may be oxidized.

4. Hold a seed with b-axis vertical 1 cm above the surface of the melt. Keep the temperature just a little bit above the melting point for several (~5) hours in order to obtain a stable temperature distribution and let the air be released from the crucible wall.

The quality of the seed is very important. The seeds can be selected by cleaving a big crystal. The cleavage surfaces of the seeds

should be very smooth and shining. The size of the seed is typically 5 mm^2 by 5~10 mm long.

5. Put the seed in the melt 1~3 mm, and keep it in for several (~2) hours. Since there is a temperature gradient along the seed, the bottom end of the seed may melt but the seed still contacts the melt.

6. Lower the temperature of the melt surface a little below the melting point. A crystal is first nucleated around the seed on the melt surface and then develops towards the wall of the crucible. When the diameter of the crystal is about half of the diameter of the crucible we start pulling up the crystal with the aid of a servomotor. Since $NaNO_2$ is plastic, the crystal is not constantly pulled up during growth. We made a special switch to turn the servomotor on and off alternately. The intermittent pulling process we used is: turn on the motor for 5 seconds then turn off it for 25 seconds and repeat.

In the crystallization process, some stress is applied to the growing crystal when it reaches the wall of the crucible. Therefore the speed of the servomotor and the intermittent process should match the horizontal growth rate. The vertical growth rate of the crystal which we used is about 2 mm/hour.

7. Separate the crystal from the melt when the size of the crystal is acceptible. Keep it in situ for one hour before cooling down to room temperature.

The cooling rate we used was about ~8°C/hour, but was reduced to ~3°C/hour around 210°C and 163°C.

8. Keep the crystal in a desiccator to guard against humidity.

APPENDIX C

DIELECTRIC CONSTANT MEASUREMENT APPARATUS

1. The schematic diagram of capacitance measurement

Fig. C.1 shows the schematic diagram of the General Radio Type 716-C Capacitance Bridge.

Fig. C.2 shows a simplified schematic diagram of the bridge. C_N is a precision variable capacitor calibrated from 100 pF to 1150 pF. This capacitor is used to balance the unknown capacitance, C_{XS}, when the unknown is connected to the UNKNOWN-DIRECT terminals of the bridge for a direct measurement. The resistance R_{XS} of the unknown is balanced by a variable capacitor, C_A, and since R_{XS} depends onpon the variable capacitor C_N, as well as upon C_A, the capacitor cannot be made to read directly the resistance, R_{XS}. Capacitor C_A is calibrated to read directly the dissipation factor, D_X, of the unknown.

The elementary balance equations of the bridge for direct measurement are:

$$C_{XS} = (R_A / R_B)*C_N$$

$$R_{XS} = (C_A / C_N)*R_B$$

$$D_X = \omega C_{XS} R_{XS} = \omega C_A R_A$$

The bridge is at balance when no voltage exists at the detector input. This condition is called a null. To obtain the balance, the CAPACITANCE CONTROL (C_N) and the DISSIPATION FACTOR control (C_A) are adjusted until the detector output is zero or a minimum.

2. The simplified schematic diagram of capacitance measurement

under D.C. electric field

Fig. C.3 shows the simplified circuit of the capacitance measurement under D.C. field, where DCP is the high voltage D.C. power supply (MODEL 410B, JOHN FLUKE MFG. CO. INC.); μA is the microampere meter (KEITHIEY 169 MULTMETER); and DET is the Lock-in Amplifier (model HR-8, PRINCETON APPLIED RESEARCH) and GEN is a sine wave generator (HEATHKIT SINE-SQUARE AUDIO GENERATOR) operated typically at 1000 Hz, 1 V/cm.

3. The furnace and the sample holder

Fig. C.4 shows the furnace and the sample holder which were designed and built at BNL for the neutron scattering experiments and was also used for the dielectric constant measurements.

A: thermistor for measuring temperature.

B: $NaNO_2$ sample.

C: electrodes which were made of soft aluminum foil.

D: sample holder made of boron.

E: aluminum cover #1.

F: aluminum cover #2.

G: aluminum cover #3.

H: heater

I: thermocouple used for the temperature control.

APPENDIX D

BRILLOUIN SCATTERING APPARATUS

The Brillouin scattering apparatus is illustrated schematically in Fig. D.1. The Spectra-Physics Model 165 argon-ion laser (either at 4880Å or 5145Å) was run in single mode operation by the use of an intracavity etalon. A check on the stability and quality of the single-mode laser output was performed from time to time with a small spherical Fabry-Perot (FPS) (Model 760, COHERENT OPTICS, INC.) with a free spectral range ν_{FSR} of 8 GHz (the free spectral range FSR is determined by the spacing d (cm) between the Fabry-Perot mirrors and is given by the expression $\nu_{FSR} = 1/2d$ in units of wavenumber), whose output was monitored on an oscilloscope. The oscilloscope's sawtooth ramp output was used to scan the small FPS. By simultaneous use of a photodiode power meter, one can also maximize the single mode output by careful manipulation of the intracavity air etalon.

The laser beam was focused into sample contained in a sample cell inside a furnace by a lens (FL = 17.2 cm, f/4.5 ACH.) so that the beam focuses at the center of the crystal. With the help of a polarization rotator, the incident beam could be made either vertically or horizontally polarized (with respect to the plane containing the wavevectors of the incident and scattered light). Light scattered at 90° was collected by a lens (8.25 inch f/4.5 XEROX, made in England by Rank Taylor Hobson). The polarization of the scattered light was selected by a polaroid analyser, and its aperture was determined by an adjustable iris diaphragm. The scattered light was collimated and passed through a spatial filter which served to define the scattering volume and to improve the effec-

tive instrumental finesse. The size of the pinhole in the spatial filter (usually 0.1 mm) was chosen to match the image of the scattering column in the focal plane.

The scattered light from the region of the crystal defined by the spatial filter was then analysed by a piezoelectrically scanned (single pass or triple pass) plane Fabry-Perot Interferometer (Tropel Model 360) which is controlled by a PDP-8E minicomputer. The Fabry-Perot scan is driven by an associated linear ramp generator (Tropel, Fairport, N.Y.) which also provides a trigger signal to the minicomputer for multi-scaling data collection. During the scan, a fast shutter closes automatically whenever the count rate exceeds a preset maximum, and remains closed during a preset number of channels in order to protect the photomultiplier from excessive light. After a preset number of scans, the computer jumps to an alignment routine. With the shutter open and a neutral density filter inserted in the optical path, the bias voltages to two of the three piezoelectric stacks are alternately stepped via two programmable power supplies (0-500V, 0-40mA, OPS-500 KEPCO Digital Programmer) until the peak height of the central Rayleigh line is maximized. The position of the central Rayleigh line is then recorded and used to reset a delay in the triggered multi-scaling routine to compensate for interferometer and laser drifts. Before returning to the regular data acquisition mode, one scan is added to the memory with the ND filter in place in order to provide reduced Rayleigh peaks in the spectrum for subsequent computer analysis of the data. The output of the Fabry-Perot was focused on another pinhole of appropriate diameter that compromised between instrumental width and signal output, before being imaged onto a photomultiplier tube (I.T.T Startracker, FW-130) operated at a cathode voltage of

1750 volts d.c.. For reducing the background (dark-current) emission from the phototube, the phototube is cooled by a refrigerated chamber (model Te-104, Products for Research Inc.). A narrowband laser filter was placed in front of the phototube to eliminate the Raman scattering intensity.

Photon counting was used in the detection system. The electrical pulses emitted by the photomultiplier were processed by a preamplifier-discriminator (model 10145, Uniphoto System Inc.). The rate at which photo-electrons are emitted (proportional to the intensity of scattered light) from the PMT was measured either by a rate meter, whose output was then recorded on a strip chart recorder, or by the Digital Equipment Corporation PDP-8 minicomputer which also maintained interferometer alignment. A total of 512 24-bit memory channels were used in the Brillouin scattering experiment. The counting time per channel was set so that the 512 channels covered slightly more than two free spectral ranges. Sequential scans were taken to build up the Brillouin components until a satisfactory signal to noise ratio was obtained. Data were subsequently transferred to a central VAX/UNIX system for subsequent analysis by a nonlinear least squares fitting program. To keep a record of all necessary experimental conditions during the collection of a particular spectrum, a raw x-y plot of the data in the PDP-8 was recorded by a HP 7040A x-y plotter interfaced to the PDP-8 computer.

APPENDIX E

NEUTRON SCATTERING APPARATUS

1. The High Flux Beam Research Reactor

The High Flux Beam Research Reactor (HFBR) at Brookhaven National Laboratory was designed to provide a total flux of 2.4×10^{15} neutrons/cm^2-sec at a power of 60 megawatts[114].

Fig. E.1 is a plan view of the reactor vessel showing the location of the experimental beam tubes and irradiation facilities.

The HFBR statistics are listed in the Table E.1.

2. The triple-axis spectrometer

Most of our neutron scattering experiments were performed at the triple-axis spectrometer H7 which is illustrated schematically in Fig. E.2.

The H7 station parameters are listed in the Table E.2.

3. Determination of the geometry of the sample

In our elastic neutron scattering experiments the scans were taken through the (020) Bragg peak along the a-axis. The question is : how to set the sample in respect to the incident neutron beam? The following calculation is necessary for the determination of the geometry of the sample.

a. Definition of angles C_1, C_2, C_3, A_1, A_2, A_3

The angles C_1, C_2, C_3, A_1, A_2, A_3 are defined in Fig. E.3. Here we are only interested in the angles A_2 and C_2 where A_2 is the acute angle

between the initial and final wavevectors K_I and K_F, C_2 is the angle between the unit vector of the a-axis and the direction perpendicular to K_I.

b. Calculations of A_2 and C_2

For elastic neutron scattering $|K_I| = |K_F|$

Fig. E.4 shows the vector diagram of the elastic neutron scattering with the modulation wavevector **k** along the $\mathbf{a}^*$ direction.

From Fig. E.4 we have:

$$|Q| = |G + k| = \sqrt{|G|^2 + |k|^2} = 2|k| \sin \frac{A_2}{2}$$

where **G** is the reciprocal lattice vector and $\mathbf{G} = 2\mathbf{b}^*$ (for (020) Bragg reflection).

$$\therefore \quad A_2 = 2 \sin^{-1}\left(\frac{\sqrt{|G|^2 + |k|^2}}{2|K_I|}\right)$$

$$= 2 \sin^{-1}\left(\frac{\sqrt{4|b^*|^2 + |k|^2}}{2|K_I|}\right)$$

When **k**=0 i.e. for (020) Bragg reflection

$$A_2 = 2 \sin^{-1}\left(\frac{|b^*|}{|K_I|}\right)$$

In our experiment $|K_I| = 2.6700\ cm^{-1}$, and

at room temperature $|b^*| = 1.1259\ cm^{-1}$

$$\therefore \quad A_2 = 49.88^\circ$$

$$\therefore \quad \sin \gamma = \frac{|k|}{|Q|} = \frac{|k|}{\sqrt{|G|^2 + |k|^2}}, \quad \text{and}$$

$$\alpha = \frac{\pi - A_2}{2}, \quad \beta = \frac{\pi}{2} - \alpha = \frac{A_2}{2}$$

$$\therefore \quad C_2 = \frac{\pi}{2} + (\gamma + \beta) = \frac{\pi}{2} + \frac{A_2}{2} + \sin^{-1}\left(\frac{|k|}{\sqrt{|G|^2 + |k|^2}}\right)$$

For $k = 0$, then

$$C_2 = \frac{\pi}{2} + \frac{A_2}{2} = 114.94^\circ$$

Therfore the geometry of the sample with respect to the incident neutron beam is: the a-axis of the sample should be horizontal, the c-axis should be vertical, and the acute angle between K_I and **a** should be equal to $\gamma + \beta = 24.94^\circ$.

APPENDIX F

HYDROSTATIC PRESSURE SYSTEM

The hydrostatic pressure system which we used for the dielectric measurements described in Chapter V, section A was installed in the Earth and Planetary Sciences Department of CCNY by Professor J. Steiner. Pressure was generated by a Harwood Engineering 0-50,000 psi one-to-one hydraulic intensifier, and measured using a 0-50,000 psi bourdon tube Heise gauge. Pressure readings are accurate to within 0.1%, based on dead weight calibrations. Experiments were performed in a high pressure cold-seal vessel modified from the design of Tuttle (Tuttle. O. F., 1949, Two pressure vessels for silicate-water studies, Geol. Soc. Am. Bull. 60, 1727-1729). The high pressure seal vessel and the sample holder are shown in Fig. F.1 where:

A: $NaNO_2$ sample.

B: Thermocouple with ground junction which is recommended for high pressure application (SCAIN-010G-40 chromel-alumel subminiature thermocouple, Omega Engineering, Inc.).

C & D: Shielded wire used as electrodes.

E: Ceramic cylinder. There are three parallel holes through the cylinder, for the two electrode wires and the thermocouple. At the top end of the cylinder there are two special screws for fixing the two wires and the thermocouple.

F: The seal vessel.

G: 100,000 psi pressure AMINCO lines.

H: A special seal.

APPENDIX G

COMPUTER PROGRAM LISTING (TAUROS)

TAUROS: A minimizing subroutine based on the Rosenbrock stepping method: Revised 1984 for double precision by S. L. Qiu

```
      implicit double precision (a-h,o-z)
      character*40 blank,p0fil,pkfil,fefil,vkfil
      common /parint/x(15),xt(15),dirin(15),maxint,npar
      common/qiu1/tp,ef,fmin,p0,pk,vk
      data blank/'                    '/
1     continue
      write(6,2)
2     format(/' enter p0 file name')
      read(5,3) p0fil
3     format(a10)
      if(p0fil.eq.blank) stop
      write(6,4)
4     format(/' enter pk file name')
      read(5,3) pkfil
      write(6,10)
10    format(/' enter vk file name')
      read(5,3) vkfil
      write(6,5)
5     format(/' enter fe file name')
      read(5,3) fefil
      open(4,file=p0fil)
      open(7,file=pkfil)
      open(9,file=fefil)
      open(12,file=vkfil)
      write(6,6)
6     format(/' enter e-field in cgs unit')
      read(5,7) ef
7     format(e15.0)
      do 2000 n=1,200
      tp=162.00+0.010*n
      call minnew
      write(4,8) tp,p0
8     format(e15.5,1x,e15.5)
      write(7,8) tp,pk
      write(9,8) tp,fmin
      write(12,8) tp,vk
2000  continue
      close (4)
      close (7)
      close (9)
      close (12)
      go to 1
      end
      subroutine minnew
        implicit double precision (a-h,o-z)
      common
     2/parint/ x(15)       ,xt(15)      ,dirin(15)  ,maxint      ,npar
     3/parext/ u(30)       ,w(30)       ,werr(30)   ,maxext      ,nu
     6/unit  / isysrd      ,isyswr
     8/title / title(20)                ,isw(7)     ,nblock
     9/conver/ epsi, apsi  ,vtest       ,nstepq     ,nfcn        ,nfcnmx
     b/minima/ amin        ,up          ,newmin     ,itaur       ,lmi(30)
     c/deriva/ g(30)
        common/qiu1/tp,ef,fmin,p0,pk,vk
      maxint=15
      maxext=30
      isysrd=5
      isyswr=6
      nblock=0
  110 continue
      nfcn=1
      call midata
      call intoex(x)
      write(isyswr,120)
  120 format(' first entry to fcn')
      call fcn(npar,g,amin,u,1)
      call fcn(npar,g,amin,u,4)
      call mprint(1,amin)
      call fcn(npar,g,f,u,4)
      nfcn=3
      call comand
```

```
      return
      end
      subroutine midata
        implicit double precision (a-h,o-z)
      common
     1/names / nam1(30)     ,nam2(30)
     2/parint/ x(15)        ,xt(15)      ,dirin(15)   ,maxint      ,npar
     3/parext/ u(30)        ,w(30)       ,werr(30)    ,maxext      ,nu
     4/limits/ alim(30)     ,blim(30)    ,lcode(30)   ,lcorsp(30)  ,limset
     6/unit  / isysrd       ,isyswr
     8/title / title(20)                 ,isw(7)      ,nblock
     9/conver/ epsi, apsi   ,vtest       ,nstepq      ,nfcn        ,nfcnmx
     b/minima/ amin         ,up          ,newmin      ,itaur       ,lmi(30)
      common
     c/deriva/ g(30)
        common/qiu1/tp,ef,fmin,p0,pk,vk
        character*40 range3
        dimension array(12)
      double precision dax,dbx
      equivalence(kp,maxext)
      nblock=nblock+1
        write(6,1004)
      do 50 i=1,7
   50 isw(i)=0
      npfix=0
      nint=0
      nu=0
      npar=0
      k2=0
      kcard=1
      do 100 i=1,kp
      u(i)=0.0
      g(i)=0.
      nam1(i)=0
      lcode(i)=0
      lcorsp(i)=0
  100 continue
      do 105 i=1,maxint
      dirin(i)=0.0
  105 continue
        range3='range3.dat'
        open(11,file=range3)
        read(11,5010) (array(i),i=1,12)
5010    format(e15.0)
        u(1)=array(1)
        w(1)=array(2)
        blim(1)=array(3)
        alim(1)=array(4)
        u(2)=array(5)
        w(2)=array(6)
        blim(2)=array(7)
        alim(2)=array(8)
        u(3)=array(9)
        w(3)=array(10)
        blim(3)=array(11)
        alim(3)=array(12)
        do 200 i=1,3
      nint=nint+1
      lcorsp(i)=nint
      nu=max0(nu,i)
      werr(i)=w(i)
      if(alim(i))140,130,140
  130 if(blim(i))140,135,140
  135 lcode(i)=1
      go to 160
  140 lcode(i)=4
  160 continue
  200 continue
        rewind (11)
  250 continue
      npar=nint
      call extoin(x)
```

```
      do 300 i=1,nu
      k=lcorsp(i)
      if(k)300,300,260
  260 sav=u(i)+w(i)
      b=pintf(sav,i)
      sav=u(i)-w(i)
      a=pintf(sav,i)
      dbx=dble(b-x(k))
      dax=dble(a-x(k))
      dirin(k)=(dabs(dax)+dabs(dbx))/2.0
      xt(k)=x(k)
  300 continue
      up=1.0
      isw(5)=1
 1004   format(1x,/,1x,'nonlinear least squares fitting prog. ')
        return
      end
      subroutine extoin(pint)
        implicit double precision (a-h,o-z)
      common
     1/names / nam1(30)     ,nam2(30)
     3/parext/ u(30)        ,w(30)       ,werr(30)   ,maxext      ,nu
     4/limits/ alim(30)     ,blim(30)    ,lcode(30)  ,lcorsp(30) ,limset
     6/unit  / isysrd       ,isyswr
        common/qiu1/tp,ef,fmin,p0,pk,vk
      dimension pint(30)
      limset=0
      do 100 i=1,nu
      j=lcorsp(i)
      if(j) 100,100,50
   50 pint(j)=pintf(u(i),i)
  100 continue
      return
      end
      subroutine intoex(pint)
        implicit double precision (a-h,o-z)
      common
     1/names / nam1(30)     ,nam2(30)
     3/parext/ u(30)        ,w(30)       ,werr(30)   ,maxext      ,nu
     4/limits/ alim(30)     ,blim(30)    ,lcode(30)  ,lcorsp(30) ,limset
     6/unit  / isysrd       ,isyswr
        common/qiu1/tp,ef,fmin,p0,pk,vk
      dimension pint(30)
      do 100 i=1,nu
      j=lcorsp(i)
      if(j) 100,100,50
   50 continue
      u(i)=pextf(pint(j),i)
  100 continue
      return
      end
      function pextf(pintj,i)
        implicit double precision (a-h,o-z)
      common
     1/names / nam1(30)     ,nam2(30)
     3/parext/ u(30)        ,w(30)       ,werr(30)   ,maxext      ,nu
     4/limits/ alim(30)     ,blim(30)    ,lcode(30)  ,lcorsp(30) ,limset
     6/unit  / isysrd       ,isyswr
        common/qiu1/tp,ef,fmin,p0,pk,vk
      double precision dpintj
      igo=lcode(i)
      go to (100,200,300,400),igo
  100 pextf=pintj
      go to 800
  200 continue
  300 continue
  400 alimi=alim(i)
      blimi=blim(i)
      dpintj=dble(pintj)
      pextf=alimi+0.5*(dsin(dpintj)+1.0)*(blimi-alimi)
  800 return
      end
```

```
      function pintf(pexti,i)
        implicit double precision (a-h,o-z)
      common
     1/names / nam1(30)     ,nam2(30)
     3/parext/ u(30)        ,w(30)       ,werr(30)    ,maxext      ,nu
     4/limits/ alim(30)     ,blim(30)    ,lcode(30)   ,lcorsp(30) ,limset
     6/unit  / isysrd       ,isyswr
        common/qiu1/tp,ef,fmin,p0,pk,vk
      double precision dy
      data big,small /1.570796326795,-1.570796326795/
      igo=lcode(i)
      go to (100,200,300,400),igo
  100 pintf=pexti
      go to 800
  200 continue
  300 continue
  400 alimi=alim(i)
      blimi=blim(i)
      if(pexti-alimi) 440,500,460
  440 a=small
  450 pintf=a
      pexti=pextf(a,i)
      limset=1
      write(isyswr,241) i
      go to 800
  460 if(blimi-pexti) 470,520,480
  470 a=big
      go to 450
  480 y=2.0*(pexti-alimi)/(blimi-alimi)-1.0
      dy=dble(1.0-y**2)
      pintf=datan(y/dsqrt(dy))
      go to 800
  500 pintf=small
      go to 800
  520 pintf=big
  800 return
  241 format(' error in pintf. variable', i3,'  not within limits'  )
      end
      function dexdin(x,int)
        implicit double precision (a-h,o-z)
      common
     3/parext/ u(30)        ,w(30)       ,werr(30)    ,maxext      ,nu
     4/limits/ alim(30)     ,blim(30)    ,lcode(30)   ,lcorsp(30) ,limset
        common/qiu1/tp,ef,fmin,p0,pk,vk
      double precision dx
      do 50 i=1,nu
      lc=lcorsp(i)
      if(lc-int) 50,100,50
   50 continue
      dexdin=0.0
      go to 200
  100 id=lcode(i)
      go to (110,120,130,140),id
  110 dexdin=1.0
      go to 200
  120 continue
  130 continue
  140 dx=dble(x)
 9140 dexdin=(blim(i)-alim(i))*0.5*dabs(dcos(dx))
  200 return
      end
      subroutine mprint(ikode,fval)
        implicit double precision (a-h,o-z)
      common
     1/names / nam1(30)     ,nam2(30)
     2/parint/ x(15)        ,xt(15)      ,dirin(15)   ,maxint      ,npar
     3/parext/ u(30)        ,w(30)       ,werr(30)    ,maxext      ,nu
     4/limits/ alim(30)     ,blim(30)    ,lcode(30)   ,lcorsp(30) ,limset
     5/varian/ v(15,15)
     6/unit  / isysrd       ,isyswr
     8/title / title(20)                 ,isw(7)      ,nblock
     9/conver/ epsi, apsi   ,vtest       ,nstepq      ,nfcn        ,nfcnmx
```

```
   b/minima/ amin        ,up          ,newmin     ,itaur       ,lmi(30)
   c/deriva/ g(30)
      common/qiu1/tp,ef,fmin,p0,pk,vk
    double precision dxn,ddirin
    dimension ddirin(15)
    dimension d(15),y(15),xs(15,15),et(15,15)
 10 np=npar
    iswtr=isw(5)-itaur
    npfn=nfcn
    al=3.
    be=-.4
    gam=-2./(al*be)
    nk=20
    neq=0
    do 30 i=1,npar
    do 20 j=1,npar
 20 xs(i,j)=0.0
    ddirin(i)=dble(dirin(i))
    if(dabs(ddirin(i)).lt.1.0d-20) dirin(i)=1.0e-20
 30 xs(i,i)=1.0
    iflag=4
    ovr=amin
    nst=0
    write(isyswr,470) epsi,nstepq
    call mprint(1,amin)
    write(isyswr,480)
 40 ast=amin
    do 270 j=1,np
    y1=1.
    ne=0
    ns=0
    d(j)=0.
    kont=0
 50 do 60 i=1,npar
 60 y(i)=x(i)+dirin(j)*xs(j,i)
    call intoex(y)
    iflag=4
    call fcn(npar,g,a,u,iflag)
    nfcn=nfcn+1
    y2=amin-a
    if(y2) 110,70,80
 70 if(y1) 90,210,110
 80 ne=0
    amin=a
 90 y1=y2
    ns=1
    do 100 i=1,npar
100 x(i)=y(i)
 95 continue
    d(j)=d(j)+dirin(j)
    kont=kont+1
    if(kont-nk) 105,105,210
105 continue
    dirin(j)=al*dirin(j)
    go to 50
110 kont=kont+1
    if(kont-nk) 115,115,95
115 dirin(j)=be*dirin(j)
    if(ns) 120,50,120
120 continue
130 if(y1) 160,140,160
140 if(ne) 150,150,210
150 dirin(j)=gam*dirin(j)
    ne=1
    go to 50
160 x2=dirin(j)/be
    x1=x2/al
    da=x2*y1
    db=x1*y2
      dpp=da-db
      if(dpp.ge.0.e00.and.dpp.le.1.e-38) dpp=1.e-38
      if(dpp.lt.0.e00.and.dpp.gt.-1.e-38) dpp=-1.e-38
```

```
      b/minima/ amin        ,up          ,newmin      ,itaur       ,lmi(30)
        common/qiu1/tp,ef,fmin,p0,pk,vk
       double precision dup,dv
       dimension dv(15,15)
       dup=dble(up)
       squp=dsqrt(dup)
       write(isyswr,1000)
       kount=0
       do 200 i=1,nu
    20 l=lcorsp(i)
       if(l.eq.0) go to 55
       if(isw(2)-1) 29,25,25
    25 if(v(l,l).lt.0.) v(l,l)=-v(l,l)
       dv(l,l)=dble(v(l,l))
       werr(i)=dexdin(x(l),l)*dsqrt(dv(l,l))*squp
    29 if(kount) 30,30,40
    30 kount=1
       write(isyswr,1001)fval,nfcn
       go to 200
    40 continue
       go to 200
    55 if(ikode.eq.0) go to 200
       if(kount) 60,60,70
    60 kount=1
       write(isyswr,1001) fval,nfcn
       go to 200
    70  continue
    200 continue
       write(isyswr,1003)
       return
   1000 format(14x,' fcn value',5x,' calls')
   1001 format(10x,e15.7,i7)
   1002 format(' ' ,55x,i6,i4,1x,2a4,2x,4e13.5)
   1003 format(' ' )
       end
       subroutine comand
         implicit double precision (a-h,o-z)
       common
      2/parint/ x(15)        ,xt(15)      ,dirin(15)   ,maxint      ,npar
      3/parext/ u(30)        ,w(30)       ,werr(30)    ,maxext      ,nu
      4/limits/ alim(30)     ,blim(30)    ,lcode(30)   ,lcorsp(30)  ,limset
      5/varian/ v(15,15)
      6/unit   / isysrd      ,isyswr
      8/title / title(20)                 ,isw(7)      ,nblock
      9/conver/ epsi, apsi   ,vtest       ,nstepq      ,nfcn        ,nfcnmx
      a/card   / cword       ,cword2      ,word7(7)
      b/minima/ amin         ,up          ,newmin      ,itaur       ,lmi(30)
      c/deriva/ g(30)
        common/qiu1/tp,ef,fmin,p0,pk,vk
       dimension word8(8)
       equivalence(word8,cword2)
       npunch=0
       itaur=0
       nfcnmx=1500
       epsi=.0000000000000001
       nstepq=2
       call touros
       iflag=3
       write(isyswr,5009)
 5009    format('0call to fcn with iflag=3'/)
       call fcn(npar,g,f,u,iflag)
         return
         end
       subroutine touros
         implicit double precision (a-h,o-z)
       common
      2/parint/ x(15)        ,xt(15)      ,dirin(15)   ,maxint      ,npar
      3/parext/ u(30)        ,w(30)       ,werr(30)    ,maxext      ,nu
      6/unit   / isysrd      ,isyswr
      8/title / title(20)                 ,isw(7)      ,nblock
      9/conver/ epsi, apsi   ,vtest       ,nstepq      ,nfcn        ,nfcnmx
      a/card   / cword       ,cword2      ,word7(7)
```

```
      stj=.5*(da*x2+db*x1)/dpp
      if(stj) 170,210,170
  170 do 180 i=1,npar
  180 y(i)=x(i)+stj*xs(j,i)
      call intoex(y)
      iflag=4
      call fcn(npar,g,a,u,iflag)
      nfcn=nfcn+1
      if(a-amin) 190,210,210
  190 amin=a
      do 200 i=1,npar
  200 x(i)=y(i)
      d(j)=d(j)+stj
  210 continue
      nst=nst+1
      if(iswtr.ge.3.or.(iswtr.eq.2.and.mod(nst,10).eq.0)) call mprint(0,
     *amin)
  260 if(nfcn-nfcnmx-npfn) 270,430,430
  270 continue
      ame=amin-ast
      if(ame) 290,280,280
  280 write(isyswr,490)
      go to 435
  290 if(epsi+ame) 300,410,410
  300 neq=0
  310 do 320 i=1,npar
  320 et(np,i)=d(np)*xs(np,i)
      if(npar.eq.1) go to 40
      do 330 j=2,np
      jj=np+1-j
      do 330 i=1,npar
  330 et(jj,i)=et(jj+1,i)+d(jj)*xs(jj,i)
      do 400 j=1,np
      do 340 k=1,npar
  340 xs(j,k)=et(j,k)
      if(j-1) 380,380,350
  350 do 370 i=2,j
      d(i)=0.
      do 360 k=1,npar
  360 d(i)=d(i)+et(j,k)*xs(i-1,k)
      do 370 k=1,npar
  370 xs(j,k)=xs(j,k)-d(i)*xs(i-1,k)
  380 xn=0.
      do 390 k=1,npar
  390 xn=xn+xs(j,k)**2
      dxn=dble(xn)
      dir=dsqrt(dxn)
      dirin(j)=dir*al
        if(dir.le.1.e-38) go to 2222
      do 400 k=1,npar
  400 xs(j,k)=xs(j,k)/dir
 2222   continue
      go to 40
  410 neq=neq+1
      if(neq-nstepq) 310,420,420
  420 continue
      write(isyswr,500)
      go to 435
  430 write(isyswr,510)
      isw(1)=1
  435 continue
      do 450 i=1,npar
      d(i)=0.
      do 450 j=1,np
  440 d(i)=d(i)+dirin(j)*xs(j,i)
  450 continue
      do 460 i=1,npar
  460 dirin(i)=d(i)
      call intoex(x)
      call mprint(1,amin)
      return
  470 format(1x,'start point for tauros min',/1x,'convergence criterion'
```

```
   1,/1x,'function change less than',e10.2,'during',i3,'full iterat'/)
480 format(' ' )
490 format(  'minimization terminated since no improvement',/1x,
   1'can be found on current minimum')
500 format(' tauros minimization has converged'/)
510 format(51h0tauros minimization terminated without convergence /)
    end
```

```
      subroutine fcn(npar,g,f,x,iflag)
      implicit double precision (a-h,o-z)
      dimension x(5)
      common/qiu1/tp,ef,fmin,p0,pk,vk
      goto(50,50,50,50)iflag
50    continue
      b1=ef
      b2=3.44070e-02
      b3=1.63610e+02
      b4=1.31238e-09
      b5=-3.92550e-17
      b6=8.97300e-32
      b7=1.97094e-24
      a=b2*(tp-b3)
      ak=a+b5*x(3)**2.0+0.5*b6*x(3)**4.0
      bk=b4+0.33333*b7*x(3)**2.0
      f=0.5*a*x(1)**2.0+0.25*b4*x(1)**4.0-b1*x(1)
      f=f+0.25*ak*x(2)**2.0
      f=f+0.09375*bk*x(2)**4.0
      f=f+0.375*(b4+bk)*x(1)**2.0*x(2)**2.0
      if(iflag.ne.3) return
      fmin=f
      p0=abs(x(1))
      pk=abs(x(2))
      vk=abs(x(3))
      return
      end
```

TABLE CAPTIONS

Table 1.1 Lattice parameters of $NaNO_2$ (in unit of Å). Standard deviations are in parentheses and refer to the least significant figures.

Table 4.1 Predicted values of $[\hat{e}_s \cdot T \cdot \hat{e}_o]$ for some acoustic modes in $NaNO_2$.

Table A.1 Dimensions of the coefficients of the Landau free energy in both MKS and CGS units.

Table A.2 Conversion of each coefficient in the Landau free energy from MKS to CGS units.

Table A.3 Comparison of the values of the coefficients in the sixth order free energy model determined by three authors.

Table E.1 HFBR statistics. (Ref. 115)

Table E.2 H7 station parameters. (Ref. 115)

Table H.1 Character tables of point groups C_{2v} and D_{2h}. (Ref. 116)

TABLE 1.1

Lattice parameters of $NaNO_2$ (in unit of Å). Standard deviations are in parentheses and refer to the least significant figures

	room T	T=150°C	T=T_I	T=185°C	T=225°C
a	3.560 (10)	3.642 (19)	3.665	3.671 (12)	3.695 (17)
b	5.563 (05)	5.653 (20)	5.670	5.670 (08)	5.701 (30)
c	5.384 (05)	5.375 (16)	5.358	5.341 (18)	5.298 (22)

TABLE 4.1

Predicted values of $[\hat{e}_S \cdot T \cdot \hat{e}_o]$ for some acoustic modes in $NaNO_2$

		Longitudinal (L)	Transverse (T_1)	Transverse (T_2)
		$\hat{u} = (0,1,0)$	$\hat{u} = (0,0,1)$	$\hat{u} = (1,0,0)$
	q	$\rho v^2 = C_{22}$	$\rho v^2 = C_{44}$	$\rho v^2 = C_{66}$
V_V	[010]	$\varepsilon_Z^2\, p_{32}$	0	0
H_V	-4.9°[010]	0	$\frac{\sqrt{2}}{2}\varepsilon_Z \varepsilon_y\, p_{44}$	0
V_h	4.9°[010]	0	$\frac{\sqrt{2}}{2}\varepsilon_y \varepsilon_Z\, p_{44}$	0
H_h	[010]	$-\frac{1}{2}\varepsilon_x^2 p_{12} + \frac{1}{2}\varepsilon_y^2 p_{22}$	0	0

4.9°[010]: A right-hand screw motion through 4.9° from [010], along $+\hat{e}_o$

TABLE A.1

Dimmensions of the coefficients of the Landau free energy in both MKS and CGS units

$$f = \frac{1}{2}AP^2 + \frac{1}{4}BP^4 + \frac{1}{6}CP^6 - EP + \frac{1}{2}\alpha(\nabla P)^2 + \frac{1}{4}\beta(\nabla^2 P)^2 + \frac{1}{4}\eta P^2(\nabla P)^2$$

$$F = \frac{1}{L}\int f(x)\,dx$$

	MKS	CGS
F	$(\frac{J}{m^3}) = (\frac{N}{m^2}) = (\frac{VC}{m^3})$	$(\frac{erg}{cm^3}) = (\frac{esu^2}{cm^4}) = (\frac{statvolt \cdot esu}{cm^3})$
P	$(\frac{C}{m^2})$	$(\frac{esu}{cm^2})$
A	$(\frac{Vm}{C}) = (\frac{Jm}{C^2})$	$(\frac{statvolt \cdot cm}{esu}) =$ dimensionless
A_o	$(\frac{Vm}{CT}) = (\frac{Jm}{C^2T})$	$(\frac{1}{T}) = (\frac{statvolt \cdot cm}{esu \cdot T})$
B	$(\frac{Vm^5}{C^3}) = (\frac{Jm^5}{C^4})$	$(\frac{cm^4}{esu^2}) = (\frac{statvolt \cdot cm^5}{esu^3})$
C	$(\frac{Vm^9}{C^5}) = (\frac{Jm^9}{C^6})$	$(\frac{cm^8}{esu^4}) = (\frac{statvolt \cdot cm^9}{esu^5})$
α	$(\frac{Vm^3}{C}) = (\frac{Jm^3}{C^2})$	$(cm^2) = (\frac{statvolt \cdot cm^3}{esu})$
β	$(\frac{Vm^5}{C}) = (\frac{Jm^5}{C^2})$	$(cm^4) = (\frac{statvolt \cdot cm^5}{esu})$
η	$(\frac{Vm^7}{C^3}) = (\frac{Jm^7}{C^4})$	$(\frac{cm^6}{esu^2}) = (\frac{statvolt \cdot cm^7}{esu^3})$

TABLE A.2

Conversion of each coefficient in the Landau free energy from MKS to CGS units

	MKS		CGS
A_o	$1\ (\frac{Vm}{CT})$	=	$\frac{1}{9\times10^9}\ (\frac{statvolt\cdot cm}{T\cdot esu})$
B	$1\ (\frac{Vm^5}{C^3})$	=	$\frac{1}{81\times10^{19}}\ (\frac{statvolt\cdot cm^5}{esu^3})$
C	$1\ (\frac{Vm^9}{C^5})$	=	$\frac{1}{3^6\times10^{29}}\ (\frac{statvolt\cdot cm^9}{esu^5})$
α	$1\ (\frac{Vm^3}{C})$	=	$\frac{1}{9\times10^5}\ (\frac{statvolt\cdot cm^3}{esu})$
β	$1\ (\frac{Vm^5}{C})$	=	$\frac{1}{90}\ (\frac{statvolt\cdot cm^5}{esu})$
η	$1\ (\frac{Vm^7}{C^3})$	=	$\frac{1}{3^4\times10^{15}}\ (\frac{statvolt\cdot cm^7}{esu^3})$
E	$1\ (\frac{V}{m})$	=	$\frac{1}{3\times10^4}\ (\frac{statvolt}{cm})$
P	$1\ (\frac{C}{m^2})$	=	$3\times10^5\ (\frac{esu}{cm^2})$
	$1\ (\frac{\mu C}{cm^2})$	=	$3\times10^3\ (\frac{esu}{cm^2})$

TABLE A.3

The values of the coefficients in the sixth order free energy model determined by three authors

$$f = \frac{1}{2}AP^2 + \frac{1}{4}BP^4 + \frac{1}{6}CP^6 - EP + \frac{1}{2}\alpha(\nabla P)^2 + \frac{1}{4}\beta(\nabla^2 P)^2 + \frac{1}{4}\eta P^2(\nabla P)^2$$

	S.L.Qiu et al.		W.Buchheit et al.[29]		D.Durand et al.[46]	
	MKS	CGS	MKS	CGS	MKS	CGS
A_0	1.7×10^{7}	1.9×10^{-3}	1.9×10^{7}	2.1×10^{-3}	2.2×10^{7}	2.4×10^{-3}
B	-1.3×10^{10}	-1.6×10^{-11}	-2.2×10^{10}	-2.7×10^{-11}	-7.0×10^{10}	-8.6×10^{-11}
C	3.0×10^{12}	4.1×10^{-20}	4.3×10^{12}	5.9×10^{-20}	4.3×10^{13}	5.9×10^{-19}
α	-1.2×10^{-11}	-1.4×10^{-17}			-2.3×10^{-11}	-2.6×10^{-17}
β	2.8×10^{-30}	3.1×10^{-32}			5.0×10^{-30}	5.5×10^{-32}
η	3.4×10^{-7}	4.2×10^{-24}			3.7×10^{-8}	4.5×10^{-25}

Note: (a). The units of the above coefficients are listed in Table A.1.

(b). The values of the coefficients α, β and η determined by D. Durand et al.[46] have been converted :

α -7.3×10^{9} MKS(r.u.)$^{-2}$ → -2.3×10^{-11} (Jm^3C^{-2})

β 4.9×10^{11} MKS(r.u.)$^{-4}$ → 5.0×10^{-30} (Jm^5C^{-2})

η 1.15×10^{13} MKS(r.u.)$^{-2}$ → 3.67×10^{-8} (Jm^3C^{-4})

TABLE E.1

HFBR Statistics (Ref. 115)	
Reactor power	60 million watts
Total fast neutron flux, fuel region	2.4×10^{15} n/cm^2-sec
Maximum thermal flux, reflector	1.05×10^{15} n/cm^2-sec
Active core volume	97 liters
Active height of core	52.7 cm
Diameter of core (equivalent cylinder)	47.8 cm
Number of fuel elements in core	28
Dimensions of fuel element	
Cross section (fuel plates)	8.113×7.163 cm
Length of 2 outer plates	58.4 cm
Length of 18 inner fuel plates	52.7 cm
Total length of fuel element	154.4 cm
Uranium-235 content of fuel element	351 g
Total uranium-235 loading	9.8 kg
Reactor coolant	heavy water (D_2O)
Total coolant flow rate	1150 liters/sec
Maximum operating coolant pressure	1.72×10^6 pascals
Maximum operating inlet coolant temperature	65° C
Maximum temperature at fuel element surface	≈175°C
Number of control rods	16
Dimensions of control rod cross section (rods are right angle shape)	$7.6 \times 7.6 \times 1.78$ cm
Length of main rods	102.9 cm
Length of auxiliary rods	31.8 cm
Neutron absorber in rods	Dy_2O_3 and Eu_2O_3
Diameter of spherical portion of reactor vessel	208.3 cm
Diameter of neck of reactor	121.9 cm
Thickness of thermal shield (lead and steel)	22.9 cm
Minimum thickness of biological shield (heavy concrete)	243.8 cm

TABLE E.2

H7 Station Parameters (Ref. 115)	
Flux at monochromator position (20′ collimation in-pile)	4.1×10^{9} n/cm^{2}-sec
Monochromator scattering angle	$10^{\circ}<2\theta_{M}<75^{\circ}$
E_0 or λ_0 (PG 002)	$4.9<E_0<240$ meV $4.1>\lambda_0>0.58$ Å
Beam size at sample	5 (h)×3.1 (w) cm^{2}
Sample scattering angle	$-45^{\circ}<2\theta_{S}<123^{\circ}$
Analyzer scattering angle	$-100^{\circ}<2\theta_{A}<100^{\circ}$
In-pile collimation	10′, 20′, 40′
External collimation	10′, 20′, 40′
Detector	BF_3

TABLE H.1

Character tables of point groups C_{2v} and D_{2h} (ref. 116)

C_{2v}	E	C_2	$\sigma_v(xy)$	$\sigma_v(yz)$		[mm2]
A_1	1	1	1	1	z	x^2, y^2, z^2
A_2	1	1	-1	-1	R_z	xy
B_1	1	-1	1	-1	x, R_y	xz
B_2	1	-1	-1	1	y, R_x	yz

D_{2h}	E	C_2	$C_2(y)$	$C_2(x)$	i	$\sigma(xy)$	$\sigma(xz)$	$\sigma(yz)$		[mmm]
A_g	1	1	1	1	1	1	1	1		x^2,y^2,z^2
B_{1g}	1	1	-1	-1	1	1	-1	-1	R_z	xy
B_{2g}	1	-1	1	-1	1	-1	1	-1	R_y	xz
B_{3g}	1	-1	-1	1	1	-1	-1	1	R_x	yz
A_u	1	1	1	1	-1	-1	-1	-1		
B_{1u}	1	1	-1	-1	-1	-1	-1	1	z	
B_{2u}	1	-1	1	-1	-1	1	-1	1	y	
B_{3u}	1	-1	-1	1	-1	1	1	-1	x	

FIGURE CAPTIONS

Fig. 1.1 Body-centered orthorhombic unit cell of $NaNO_2$ in the low temperature ferroelectric phase. The spontaneous polarization is along the b-axis. In the paraelectric phase the NO_2^- dipoles are oriented with equal probablity along $\pm$**b**.

Fig. 1.2 Temperature dependence of spontaneous polarization measured with decreasing temperature[29]. Dashed curve: results of Hamano[28].

Fig. 1.3 Single particle potential V^0 for $\Omega = (\psi, \phi)$. The points A-F correspond to the values $(\psi, \phi) = (0, 0); (0, 180); (90, 180); (90, 0); (-90, 0); (-90, 180)$ in degrees respectively[23].

Fig. 1.4 Schematic structure of the INC-phase of $NaNO_2$. Upper row: the two positions (up/down orientations) of the NO_2^- ions. Lower row: corresponding positions of the Na^+ ions. Dark, light and shaded: high, low and average probablity of the site occupation. The repeat distance shown is of length about 9a[89].

Fig. 2.1 Temperature dependence of the dielectric constant of melt-grown $NaNO_2$ in vacuum with zero bias field.

Fig. 2.2 Thermal hysteresis about 0.2°C at T_L: (Δ) the heating process and (+) the cooling process.

Fig. 2.3 Temperature dependence of the dielectric constant of $NaNO_2$ in

vacuum with increasing bias field E_b.

Fig. 2.4 Experimental phase transition diagram under the longitudinal electric field.

Fig. 2.5 Elastic scattering of neutrons from $NaNO_2$. The scan is along the a-axis through the (020) Bragg peak (The wavevector is in units of the reciprocal lattice vector a^*). T=163.5°C.

Fig. 2.6 Intensity of the (δ20) satellites in $NaNO_2$ vs T for bias fields E_b = 0 (+), 0.6 kV/cm (o), 1.2 kV/cm (Δ) and 1.8 kV/cm ($\square$).

Fig. 2.7 Modulation wavevector δ of the INC-phase of $NaNO_2$ vs T for the bias fields shown in Fig. 2.6.

Fig. 2.8 Intensity of the (δ20) satellites in $NaNO_2$ vs T for E_b = 0. Special attention was paid to the temperature control in the vicinity of T_L.

Fig. 2.9 Temperature dependence of ε_B^{-1} at 1 kHz as measured at decreasing temperature.

Fig. 2.10 Calculated phase diagrams of the fourth order free energy model with different η values: the solid curve with η = 0, the dashed curve with $\eta = 5.1709 \times 10^{-24}$ (in CGS units) and the dot curve with $\eta = 1.1709 \times 10^{-23}$ (in CGS units).

Fig. 2.11 Free energies F^{inc} and F^{ferro} at zero electric field. The intersection determines the transition temperature T_L.

Fig. 2.12 P_K versus T curve at zero electric field. The end point of the curve on the abscissa gives T_I.

Fig. 2.13 Calculated modulation wavevector of the fourth order free energy model with different η values: the horizontal line with η=0, the dashed line with $\eta = 1.1709 \times 10^{-24}$, the solid line with $\eta = 1.9709 \times 10^{-24}$, the dot dashed line with $\eta = 1.1709 \times 10^{-23}$ (all in CGS units). It is clear that without an η term in the free energy expression the modulation wavevector is temperature independent.

Fig. 2.14 P_K^2 versus T curve which gives the intensity distribution of the satellites.

Fig. 2.15 Calculated dielectric constant at E_b = 5 statvolts/cm for $P = P_o + P_K \cos kx$.

Fig. 2.16 Calculated dielectric constant at (a) E_b = 5, (b) E_b = 7, (c) E_b = 9 statvolts/cm obtained by introducing the "field-linear harmonic" term: $P_{2k} \cos 2kx$.

Fig. 2.17 Calculated phase transition diagram of the sixth order free energy model (the dashed curve). For comparison, the phase diagrams of the fourth order model (the solid curve) and the experimental results (the discrete points) are also plotted.

Fig. 2.18 $T_I - T_L$ versus longitudinal electric field E_b. The discrete points are the experimental results and the solid curve is the calculated result of the sixth order free energy model.

Fig. 2.19 Calculated modulation wavevector versus T curve of the sixth order free energy model with $\eta = 4.1520 \times 10^{-24}$ (in CGS units), the discrete points are the experimental results.

Fig. 2.20 δ_I and δ_L versus longitudinal electric field. The upper and lower solid curves are respectively the calculated $\delta_I(E)$ and $\delta_L(E)$ of the sixth order free energy model, the discrete points are the experimental results.

Fig. 2.21 $T_I - T_L$, δ_I and δ_L versus longitudinal electric field. This figure was obtained by plotting Fig. 2.18 with Fig. 2.20 together. The ordinate for the δ is on the left, while that for the $T_I - T_L$ is on the right.

Fig. 2.22 Diffuse neutron scattering. The ratio of the slope of the peak possitions of the diffuse scattering above T_I to the slope of the satellite possitions below T_I is about 1:4.

Fig. 2.23 The peak possitions of the diffuse scattering above T_I and the satellite possitions below T_I predicted qualitatively by the free energy model , where (a) $\eta \neq 0$, α = constant; (b) $\eta = 0$, $\alpha = \alpha(T)$; (c) $\eta \neq 0$, $\alpha = \alpha(T)$.

Fig. 3.1 Schematic phase transition diagram which is related to a first order transition from the disordered phase to the ordered phase, where the point LP is a virtual Lifshitz point.

Fig. 3.2 Intensity of the satellites versus temperature when the applied electric field is along the a-axis. The fields are: + = 0, Δ = 0.55, □ = 0.82, * =1.09, o =1.36 kV/cm. The solid lines are for guiding the eye.

Fig. 3.3 Intensity of the satellite versus temperature when the applied electric field is along the c-axis. The fields are: + = 0, Δ = 0.74, o = 1.47, * = 2.21 kV/cm. The solid lines are for guiding the eye.

Fig. 3.4 Modulation wavevector measured in units of a^* versus temperature, the fields along the a-axis are: + = 0, Δ = 0.55, □ = 0.82, * = 1.09, o = 1.36 kV/cm. The solid lines are to guide the eye. The horizontal line on the highest field curve represents the extrapolated zero intensity points of the respective curve of Fig. 3.2.

Fig. 3.5 Modulation wavevector measured in units of a* versus temperature, the fields along the c-axis are: + = 0, Δ = 0.74, o = 1.47, * = 2.21 kV/cm. The solid lines are to guide the eye. The horizontal line on the highest field curve represents the extrapolated zero intensity points of the respective curve of Fig. 3.3.

Fig. 3.6 Lifshitz point. The dashed line is the calculated $T_I = T_L$ while the upper and lower solid lines are respectively the calculated limiting

modulation wavevectors δ_I and δ_L as a function of α. When α goes to zero, the INC region $T_I - T_L$ vanishes and the wavevector δ goes to zero continuously. At the point at which $\alpha=0$ and the three lines meet, all the conditions for the existence of an LP are satisfied. The ordinate for the δ is on the left, while that for the $T_I - T_L$ is on the right.

Fig. 3.7 The upper solid line is the calculated value of δ_I, while the lower solid line is the calculated value of δ_L. The dashed line is a plot of the calculated value of $(T_I - T_L)$ as a function of transverse electric field. The discrete points are the experimental data for δ_I, (*), δ_L, (*), and $T_I - T_L$, (o), with the field along the a-axis. The ordinate for the δ is on the left, while that for the $T_I - T_L$ is on the right.

Fig. 3.8 Description for this figure is the same as that for Fig. 3.7, except the field is along the c-axis.

Fig. 3.9 The experimental data shown in Fig. 3.7 are now plotted on an expanded scale with error bars to show the accuracy of the results.

Fig. 3.10 The experimental data shown in Fig. 3.8 are now plotted on an expanded scale with error bars to show the accuracy of the results.

Fig. 3.11 The calculated phase transition diagram for E-field parallel to the c-axis, in a manner similar to the schematic phase diagram in Fig. 3.1.

Fig. 3.12 The calculated phase transition diagram for E-field parallel

to the a-axis, in a manner similar to the schematic phase diagram in Fig. 3.1.

Fig. 4.1 A typical Brillouin scattering spectrum of $NaNO_2$ under zero electric field at T = 198.0°C with the acoustic phonon propagating along the [010] direction, where the discrete points are the experimental data while the solid curves are the fitting results by a nonlinear least squares fitting program. The two Brillouin components were assigined experimentally as a L-mode and a T_1-mode according to the Table 5.1.

Fig. 4.2 A series of Brillouin spectra of $NaNO_2$ under zero electric field from 50°C upto 240°C.

Fig. 4.3 Brillouin frequency shift versus temperature of the L-mode propagating along the [010] direction.

Fig. 4.4 The temperature dependence of the longitudinal acoustic phonon propagating along the [010] direction in the vicinity of the phase transition temperatures T_L and T_I. The solid lines are drawn as an eye guide.

Fig. 4.5 The Brillouin frequency shifts versus temperature of the L-mode propagating along the [010] direction under E-field parallel to the c-axis: (a) E_c = 0.5 kV/cm, (b) E_c = 1.0 kV/cm.

Fig. 4.6 Acoustic mode energies in $NaNO_2$ from inelastic neutron scattering experiment with **q** parallel to the a-axis. (*) T = 165.41°C, (□) 180.72°C.

Fig. 4.7 Temperature dependence of the hypersonic velocities of the longitudinal acoustic wave propagating along the [010] direction, where: (a) and (b) E = 0, (c) E_c = 0.5 kV/cm, (d) E_c = 1.0 kV/cm.

Fig. 4.8 Temperature dependence of the ultrasonic velocities of the longitudinal acoustic wave propagating along the directions: (a) [010], at 2.74 MHz, (b) [100], at 6.60MHz, (c) [001], at 12.0Mhz. (from references (60) and (61)).

Fig. 5.1 T_I and T_L versus hydrostatic pressure, the solid line are for guiding the eye. The two sets of data were obtained in two different cases of temperature measurements: (o) the thermocouple was mounted outside the high pressure vessel; (Δ) inside the high pressure vessel.

Fig. 5.2 Brillouin frequency shift versus temperature as function of hydrostatic pressure, where (Δ) 14.5 psi (1 atm), (o) 900 psi, (□) 1500 psi. The solid lines are for guiding the eye.

Fig. 6.1 The graphical solution of the implicit mean field Eq. (6.9) with $T_c = J_K/K_B$

Fig. 6.2 Ising model with competing interactions. (Ref. 111, 112, 93)

Fig. 6.3 Mean-field phase diagram of the ANNI model. (Ref. 112, 93)

Fig. 6.4 Ground-state spin configurations (T = 0): (a) ferro-phase, (b) ferro-phase with domain wall.

Fig. 6.5 Dielectric constant calculated from the ANNNI model with an initial spin configuration of (-,+) and $-J_2/J_1 = 0.347$, $J_1 = 80.7$. For the solid curve, E = 0.0; for the dotted curve, E = 10.0; for the dot-dashed curve, E = 20.0; for the dashed curve, E = 30.0. (E = 1 corresponds to E_{ext} = 86 statvolts/cm).

Fig. 6.6 Dielectric constant calculated from the ANNNI model with an initial spin configuration of (-,-,+,+) and $-J_2/J_1 = 0.347$, $J_1 = 80.7$. For the solid curve, E = 0.0; for the dotted curve, E = 10.0; for the dot-dashed curve, E = 20.0; for the dashed curve E = 30.0.

Fig. 7.1 Schematic behavior of the free energy F of the three states extremizing F. At each temperature the lowest free energy determines the stable state.

Fig. 7.2 Phase diagram in molecular field approximation to fourth order. In the shaded region the expansion is not valid.

Fig. C.1 Schematic diagram of the General Radio Type 716-C Capacitance Bridge.

Fig. C.2 Simplified schematic diagram of the Type 716-C Capacitance Bridge.

Fig. C.3 Simplified circuit of the capacitance measurement under D.C. field, where DCP is the high voltage D.C. power supply, μA is the micro-ampere meter, DET is the Lock-in amplifier, GEN is a sine-wave generator.

Fig. C.4 Furnace and sample holder which were designed and built at BNL for both neutron scattering and dielectric constant measurements. A: thermistor, B: sample, C: electrodes, D: sample holder, E: cover #1, F: cover #2, G: cover #3, H: heater, I: thermocouple.

Fig. D.1 Brillouin scattering spectrometer consisting of an ion laser, computer controlled triple pass Fabry-Perot interferometer and digital data collection system.

Fig. E.1 Plan view of the location of the experimental beam tubes and irradiation facilities within the reactor vessel. (Ref. 115)

Fig. E.2 Schematic plan of triple-axis spectrometer installed at H7. (Ref. 115)

Fig. E.3 Definition of the angles C_1, C_2, C_3, A_1, A_2, A_3. Where K_I and K_F are the initial and final wavevector of neutrons.

Fig. E.4 Vector diagram of the elastic neutron scattering with the modulation wavevector **k** along the $\mathbf{a}^*$ direction.

Fig. F.1 High pressure seal vessel. A: sample, B: thermocouple, C & D: electrodes, E: ceramic cylinder, F: the seal vessel, G: 100,000 psi pressure AMINCO lines, H: a special seal nut.

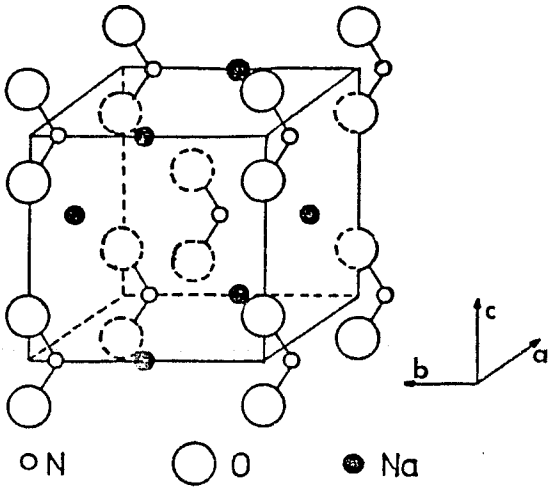

1.1

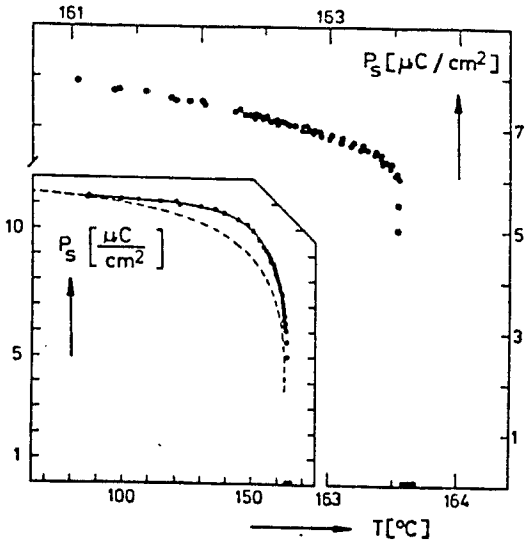

1.2

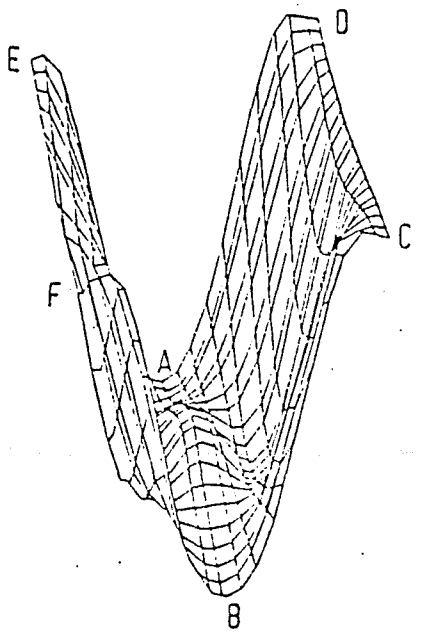

1.3

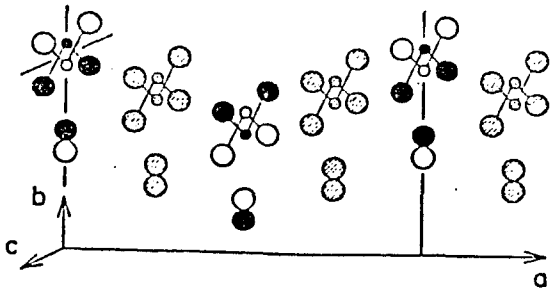

1.4

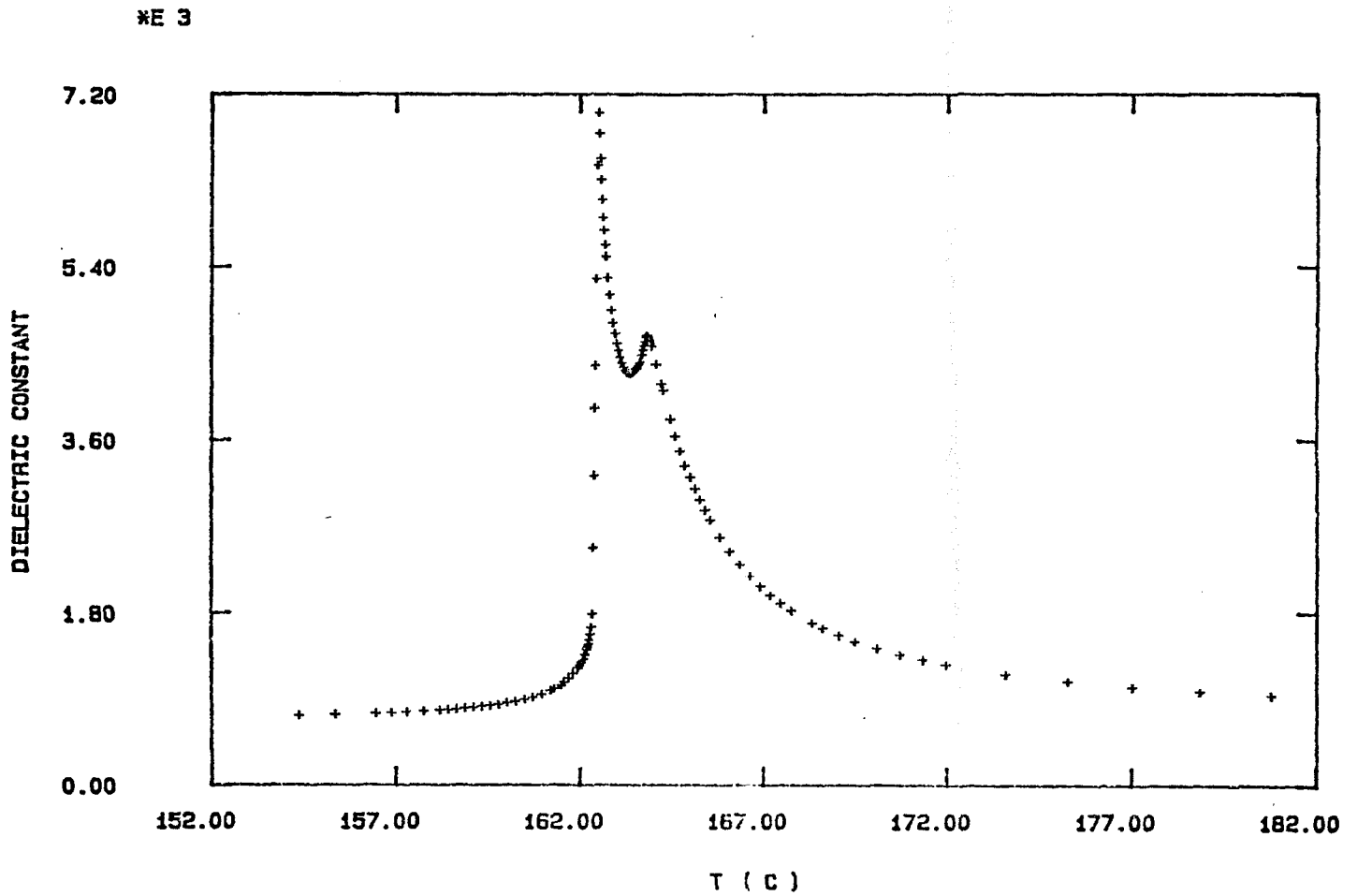
*E 3
7.20
5.40
3.60
1.80
0.00
DIELECTRIC CONSTANT
152.00
157.00
162.00
167.00
172.00
177.00
182.00
T (C)

2.1

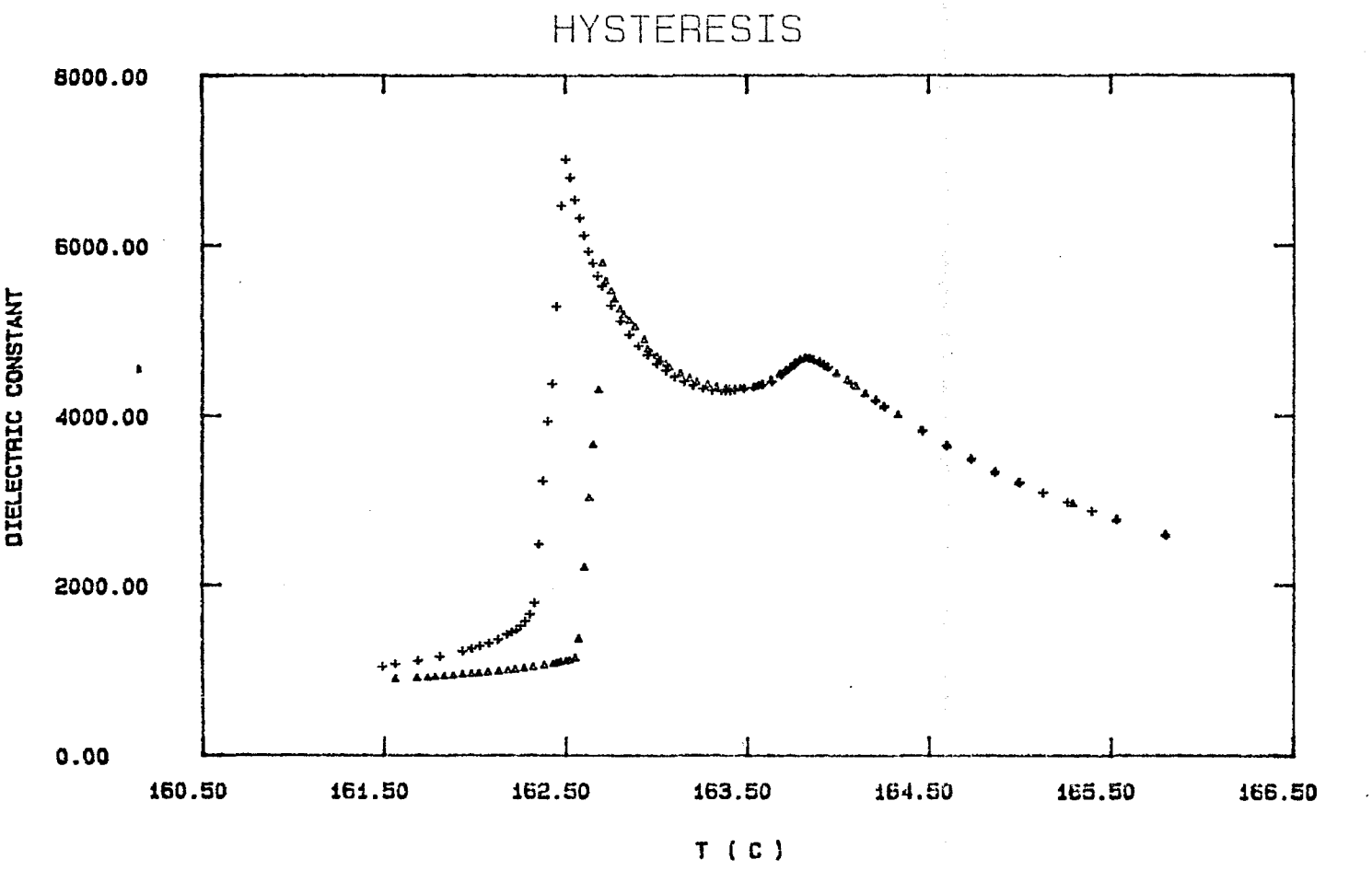

2.2

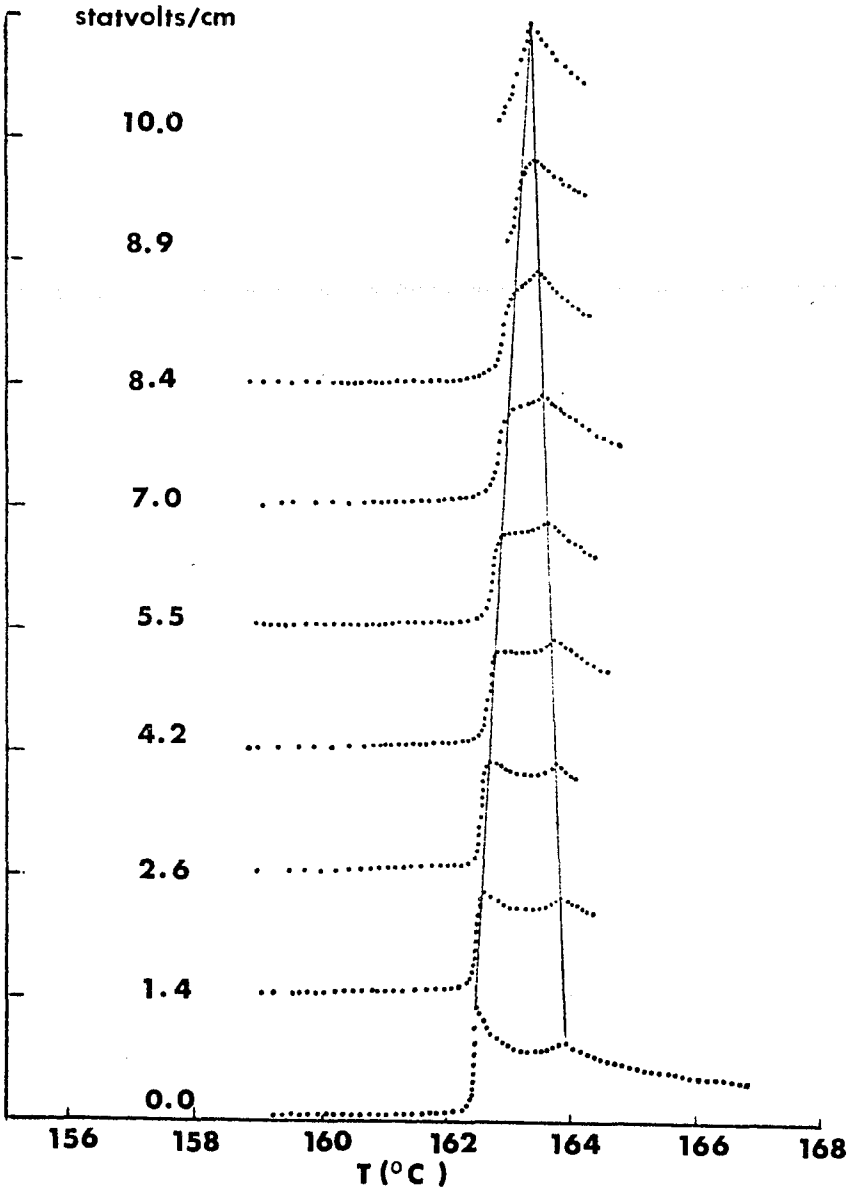
statvolts/cm
10.0
8.9
8.4
7.0
5.5
4.2
2.6
1.4
0.0
156
158
160
162
164
166
168
T (°C)

2.3

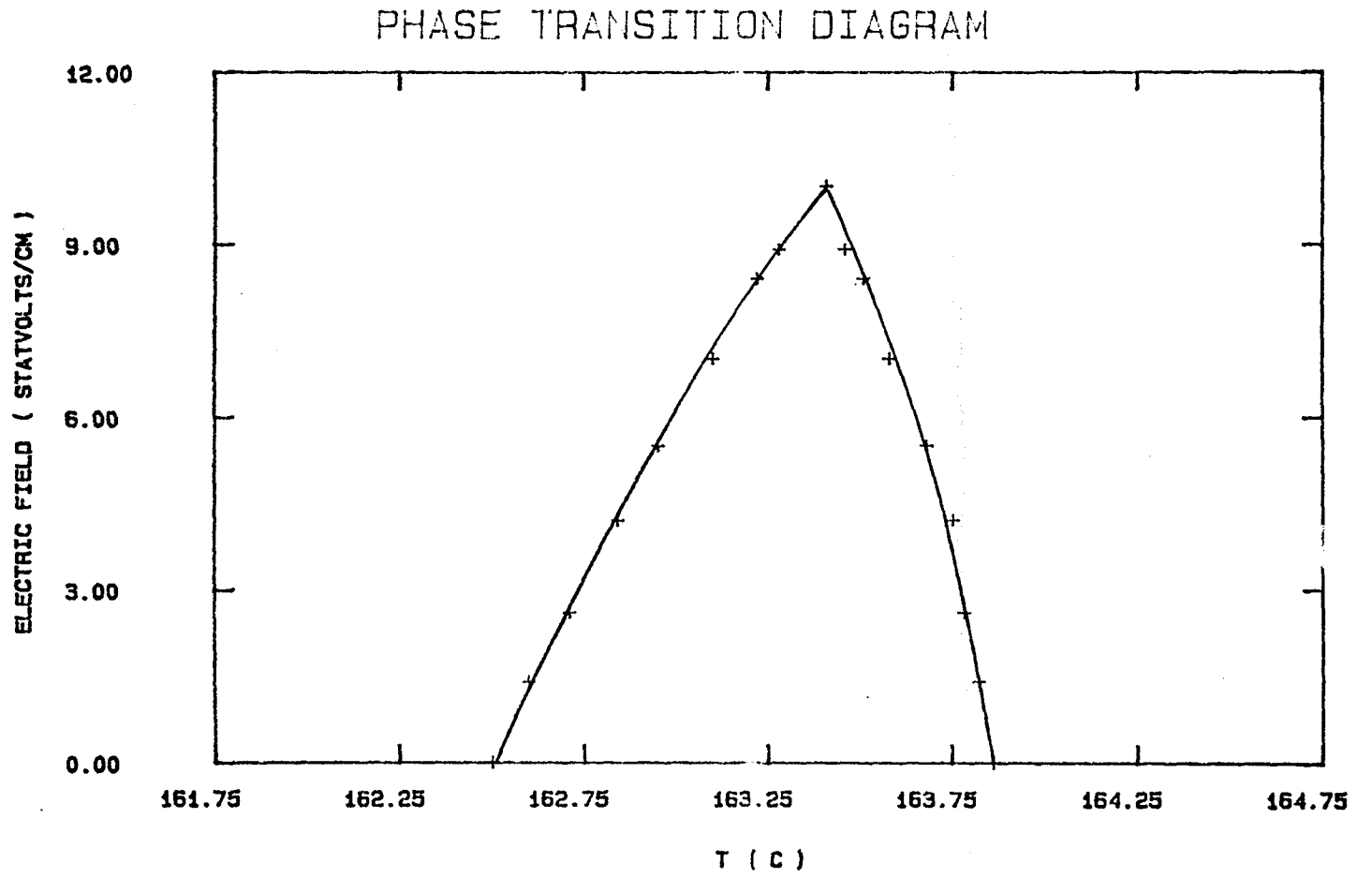

2.4

Sun Jun 30 11:[illegible] 11 EDT 1968

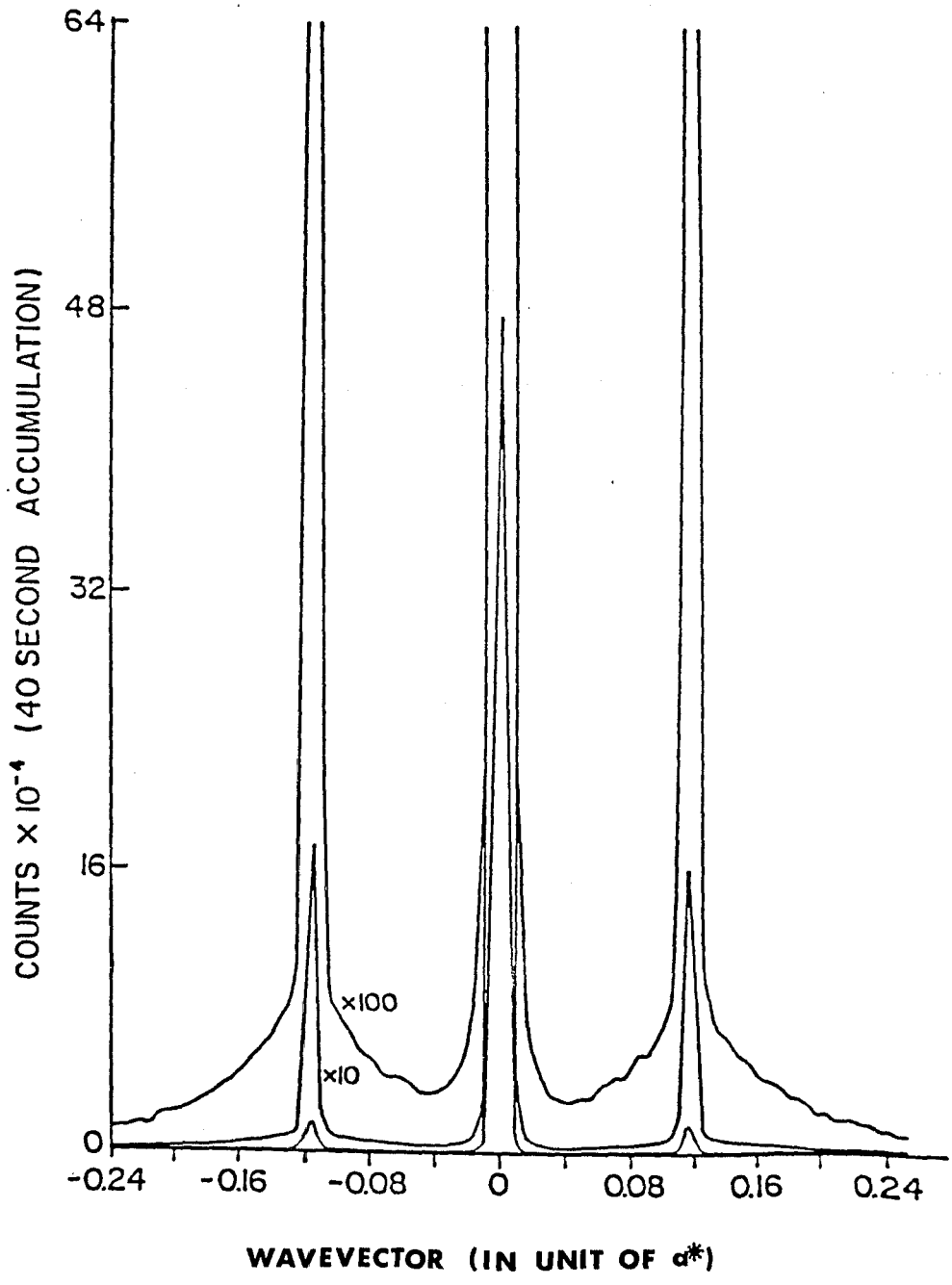
64
48
32
16
0
COUNTS X 10⁻⁴ (40 SECOND ACCUMULATION)
×100
×10
-0.24
-0.16
-0.08
0
0.08
0.16
0.24
WAVEVECTOR (IN UNIT OF a*)

2.5

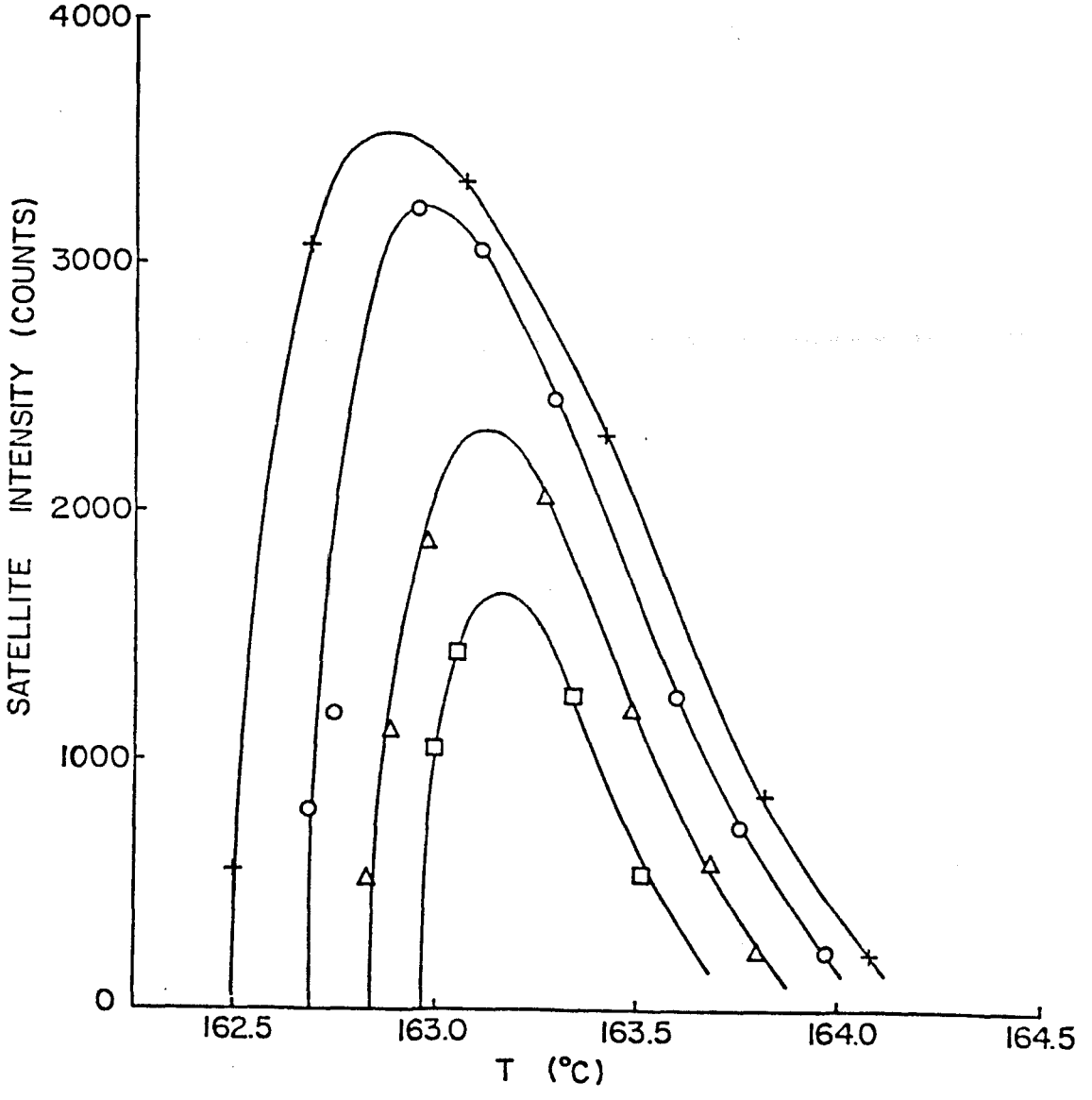
4000
3000
2000
1000
0
SATELLITE INTENSITY (COUNTS)
162.5
163.0
163.5
164.0
164.5
T (°C)

2.6

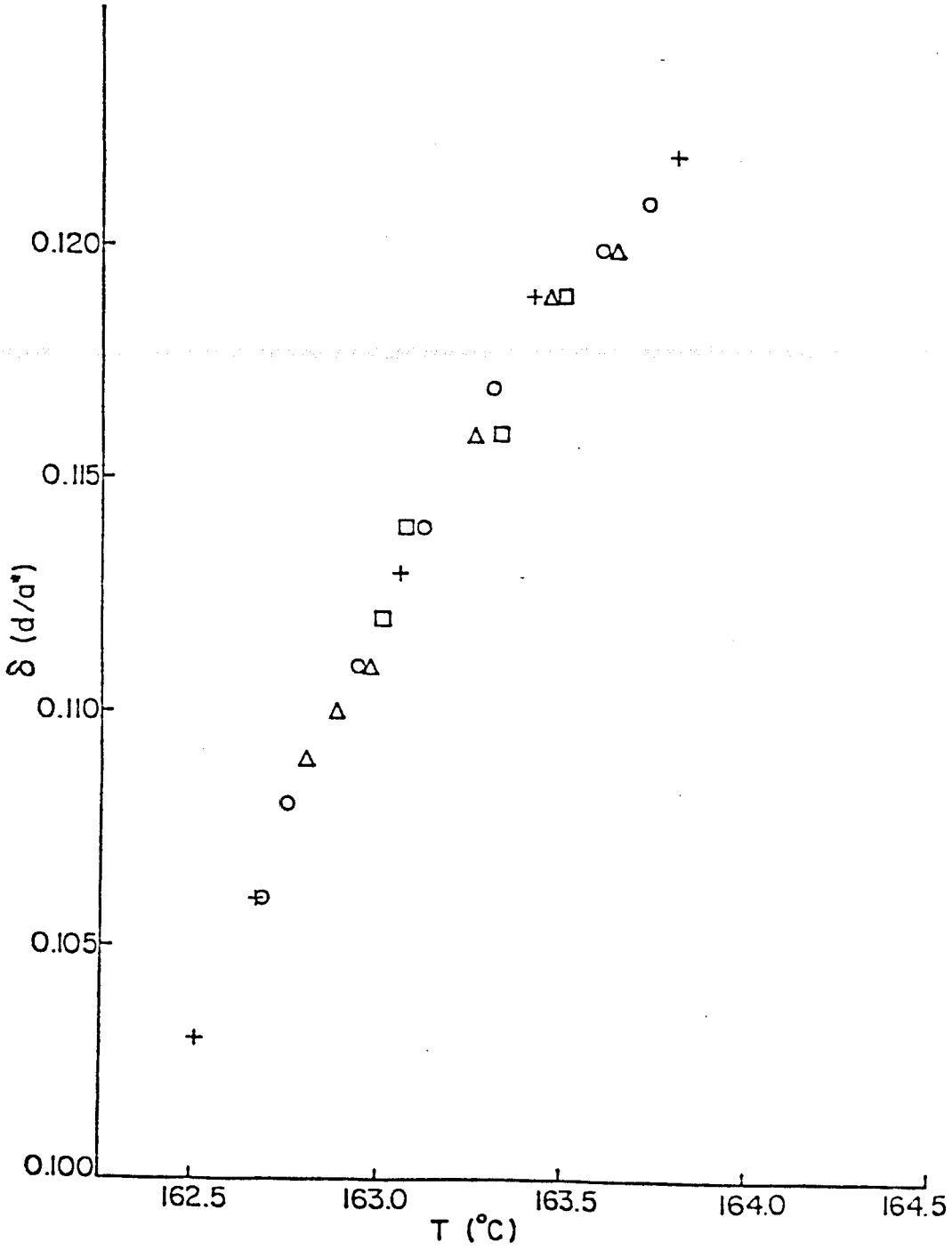

2.7

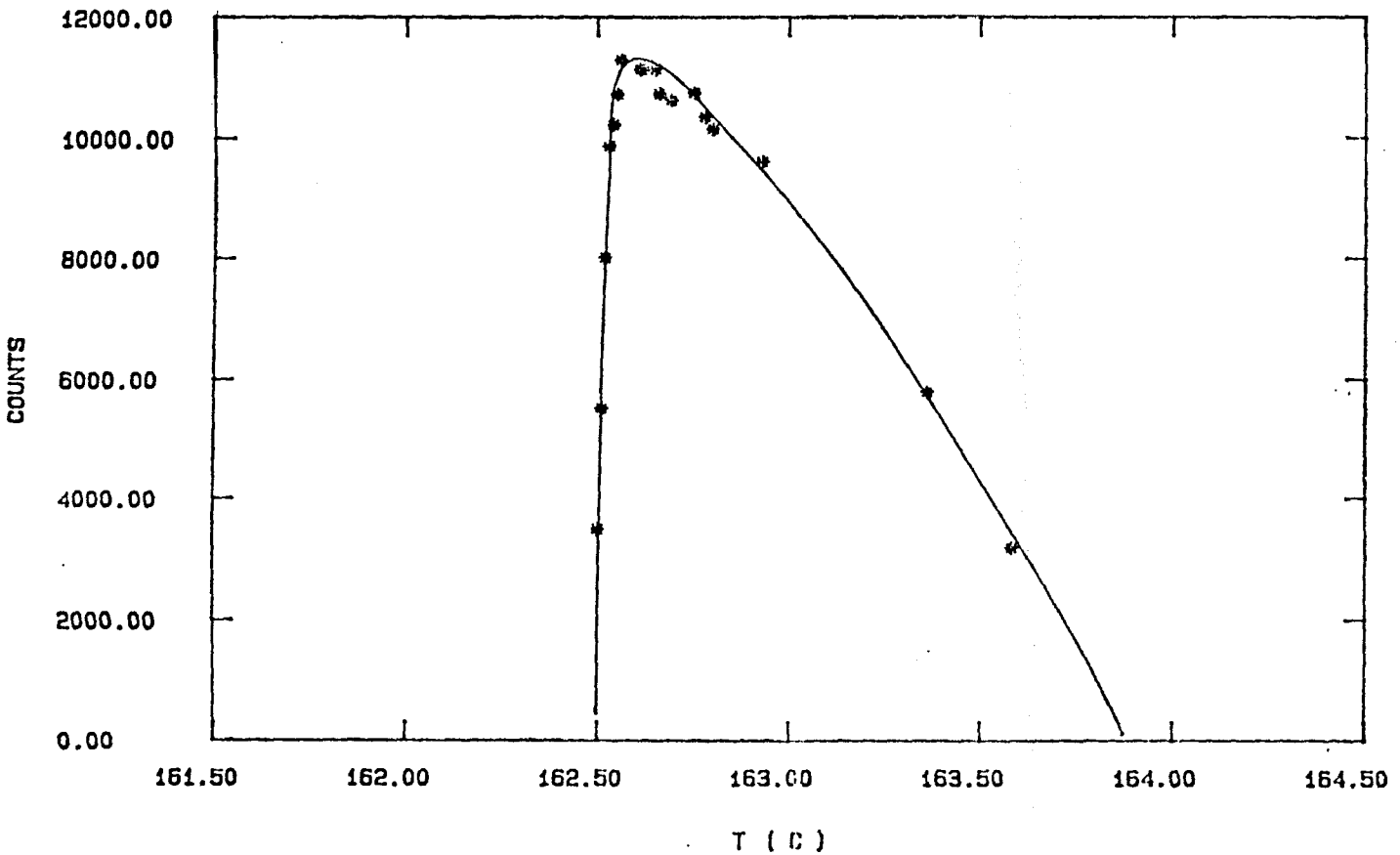
12000.00
10000.00
8000.00
6000.00
4000.00
2000.00
0.00
COUNTS
161.50
162.00
162.50
163.00
163.50
164.00
164.50
T (C)

2.8

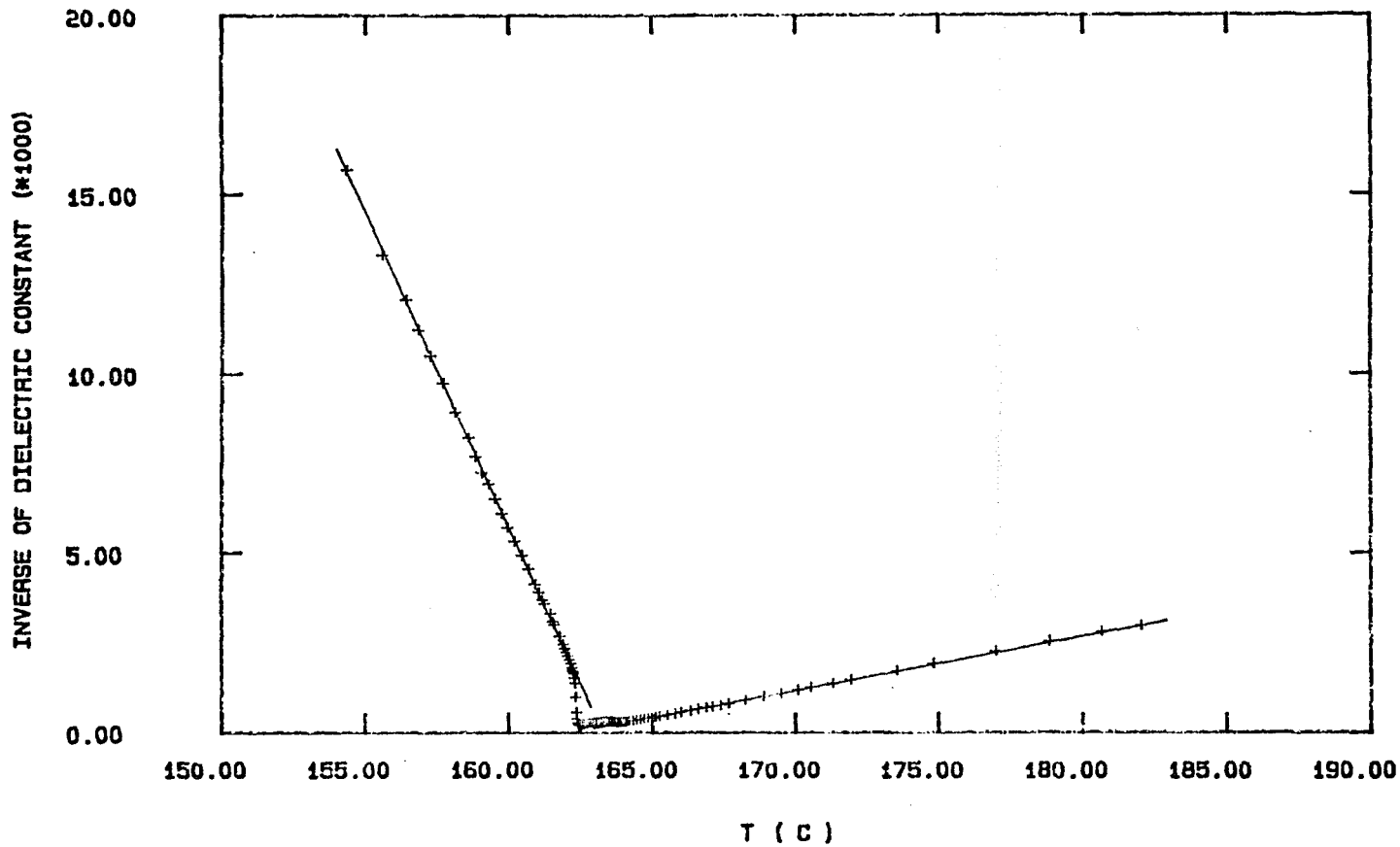

2.9

Tue Jun 4 13:48:43 EDT 1991

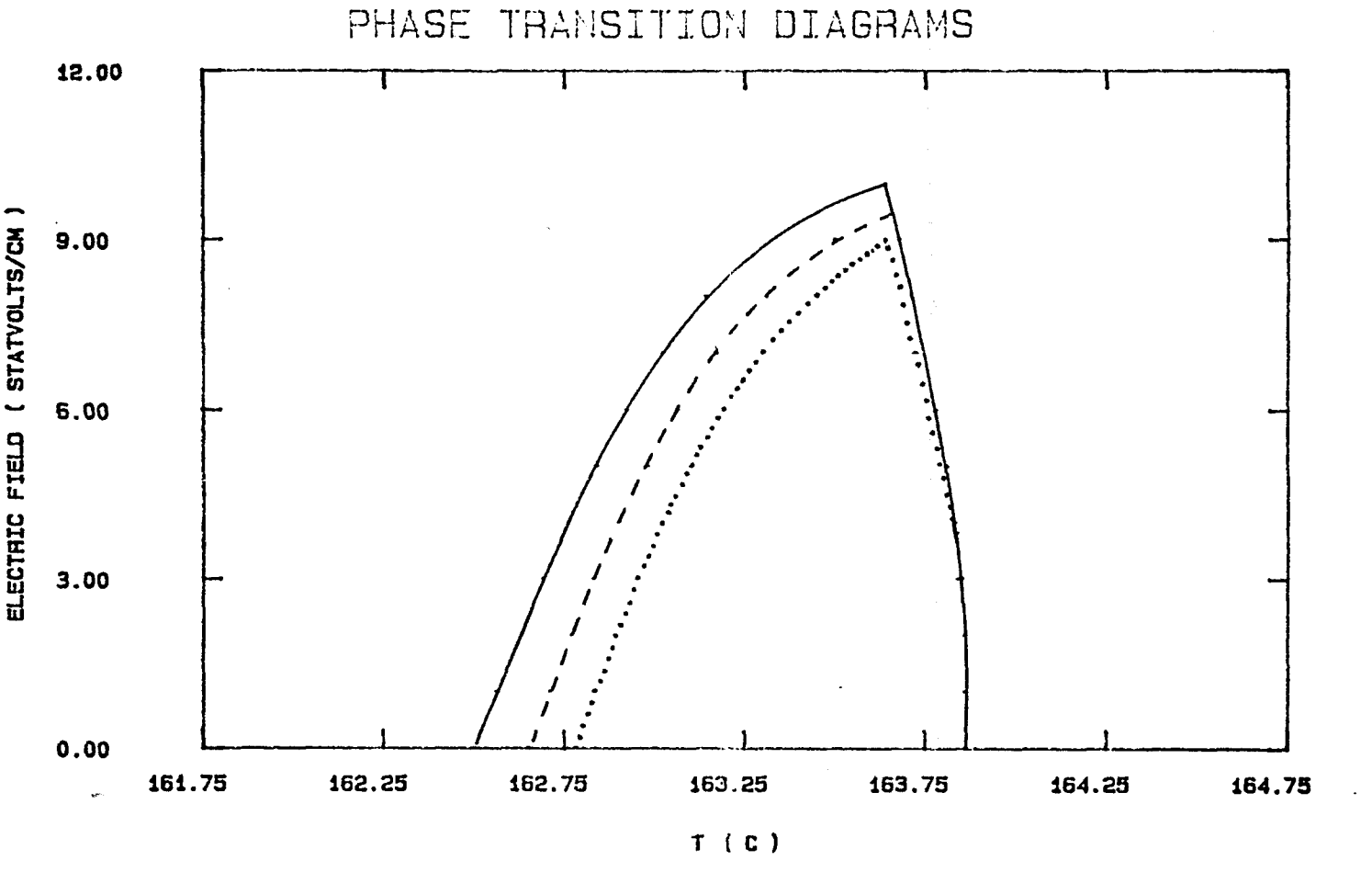

FOURTH ORDER FREE ENERGY MODEL

2.10

Sun Jun 30 11:30:48 EST 1985

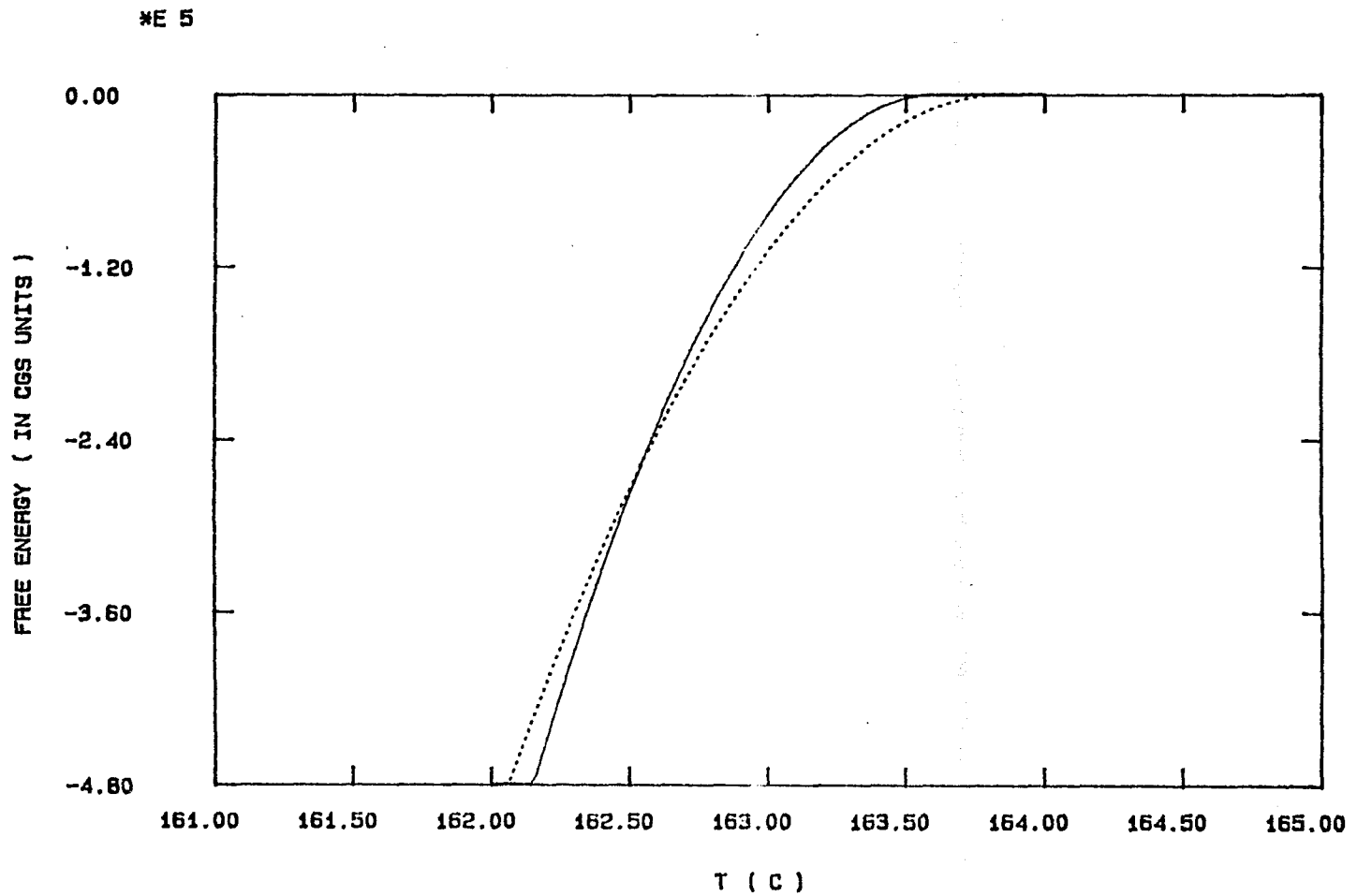

2.11

Sun Jun 30 10:02:27 EST 1963

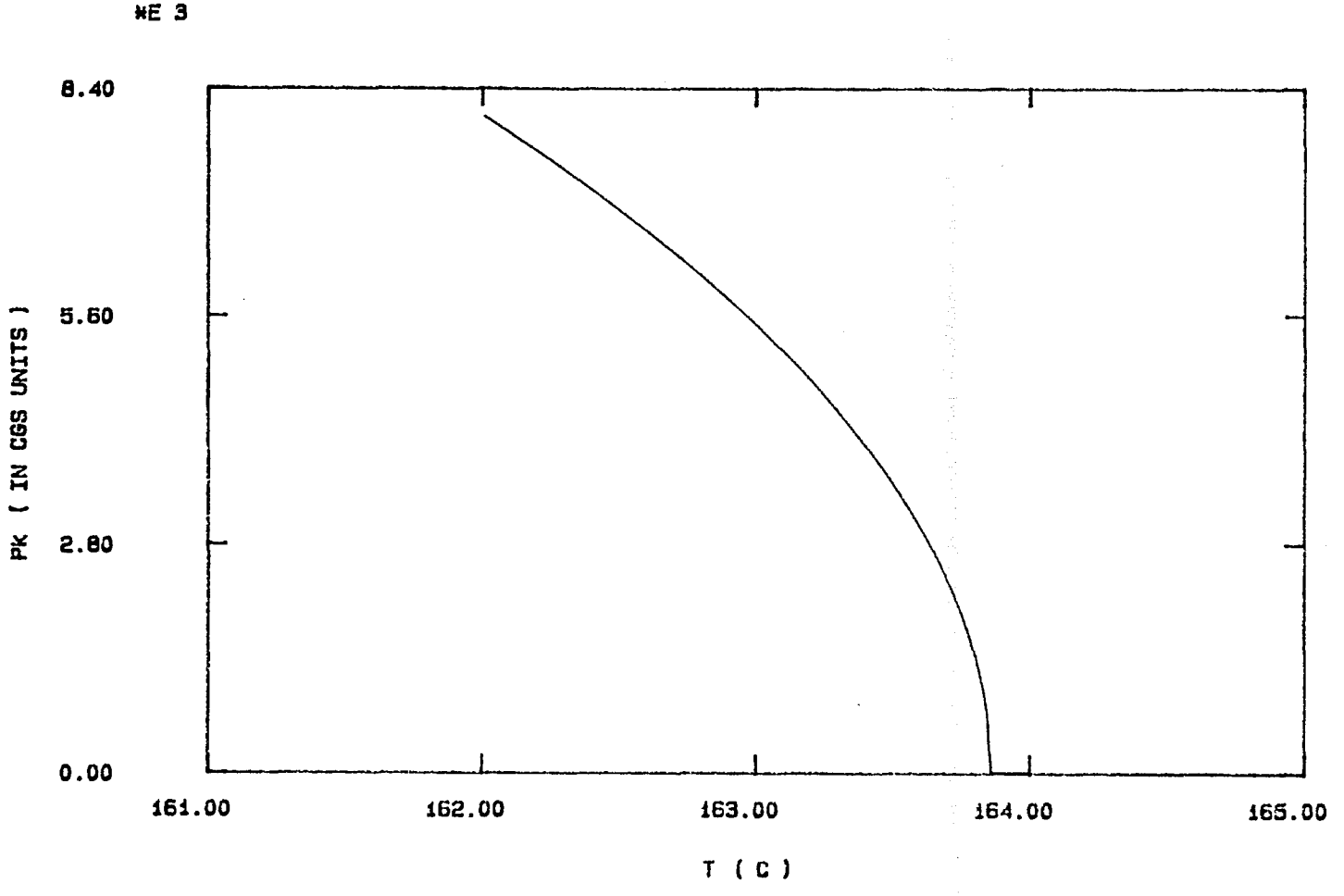

2.12

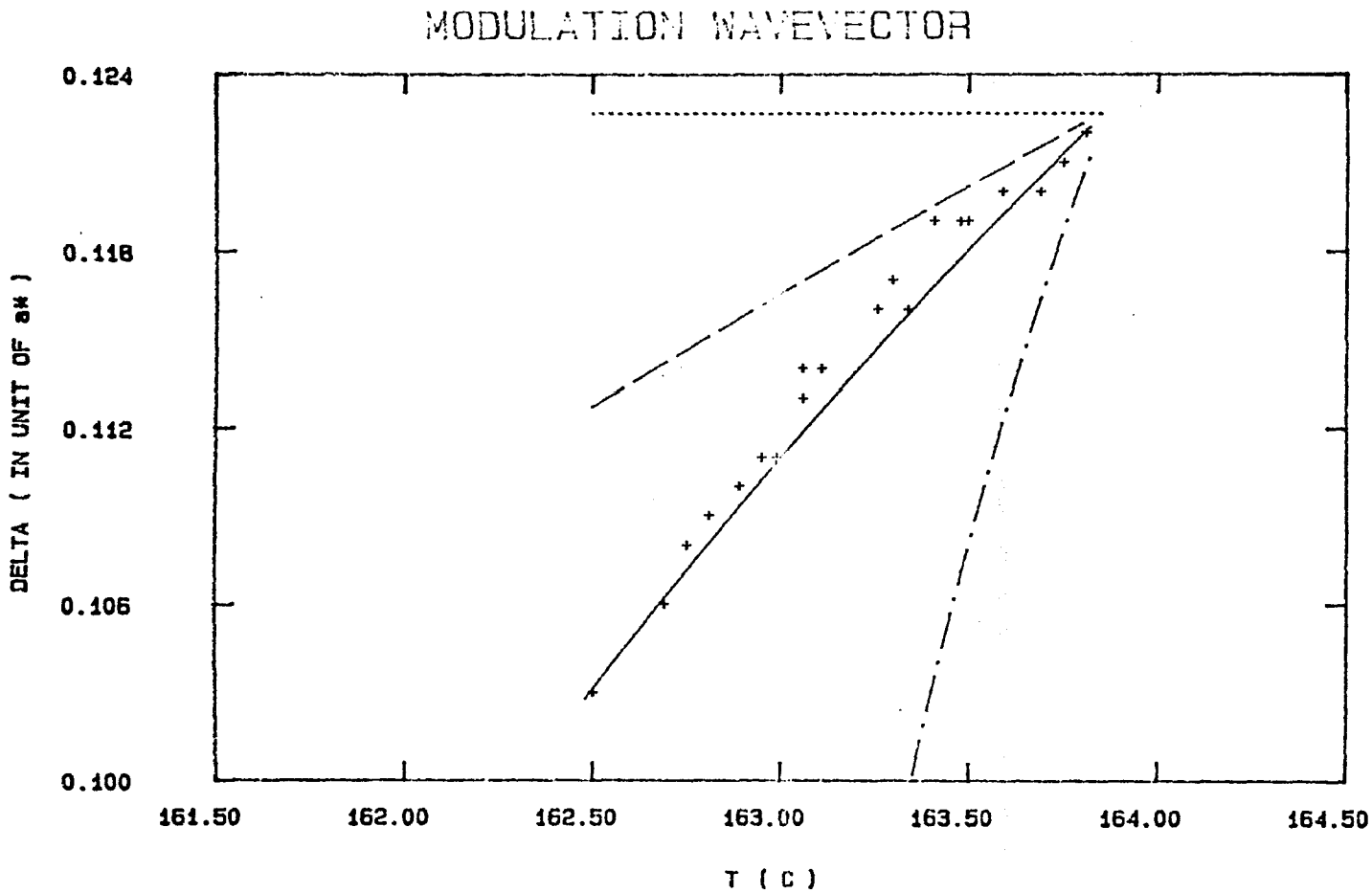
MODULATION WAVEVECTOR
0.124
0.118
0.112
0.106
0.100
DELTA (IN UNIT OF a*)
161.50
162.00
162.50
163.00
163.50
164.00
164.50
T (C)

2.13

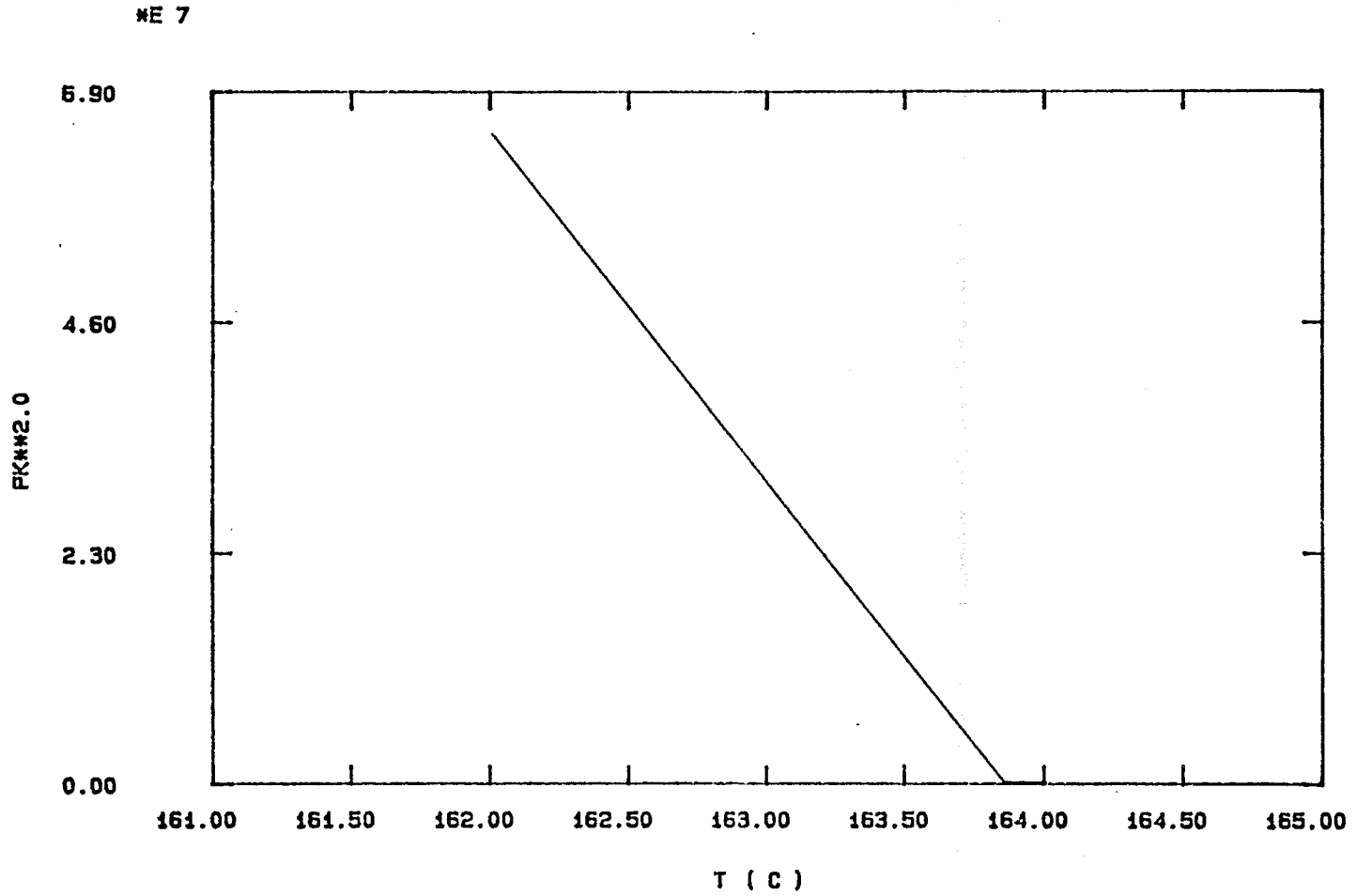

2.14

Sun Jun 30 11:08:37 EDT 1968

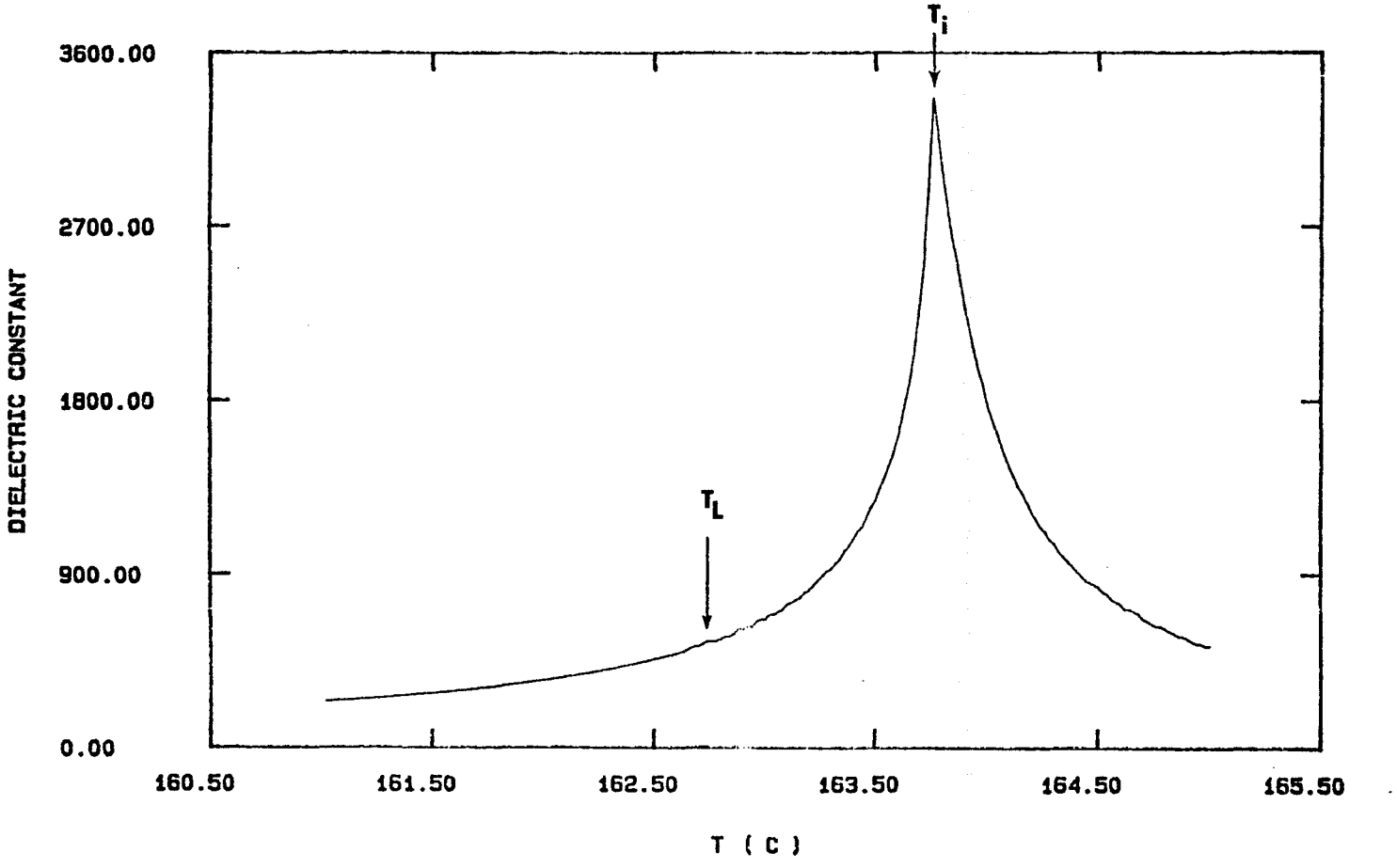
T_i
3600.00
2700.00
1800.00
900.00
0.00
DIELECTRIC CONSTANT
T_L
160.50
161.50
162.50
163.50
164.50
165.50
T (C)

2.15

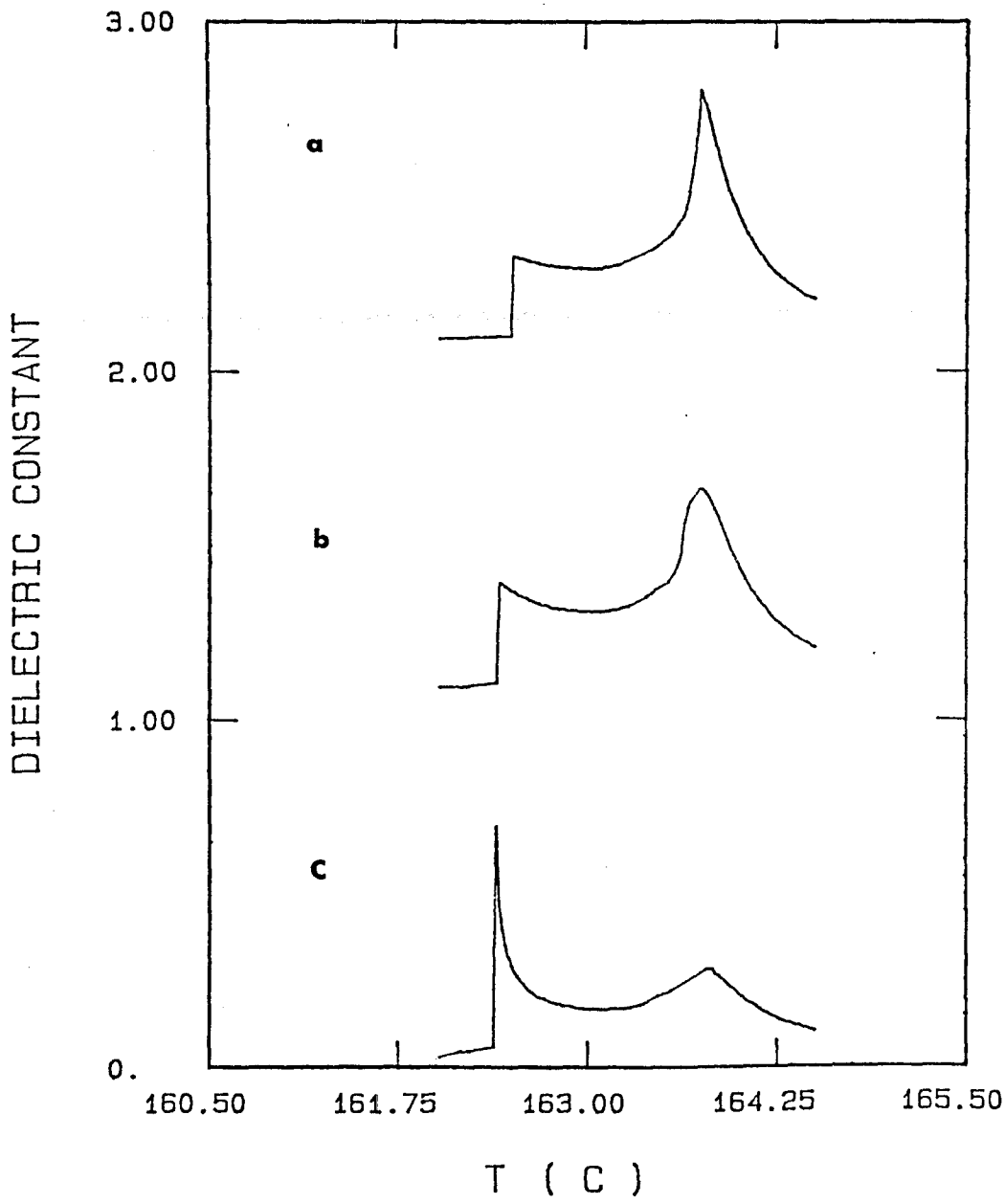
3.00
2.00
1.00
0.
DIELECTRIC CONSTANT
a
b
c
160.50
161.75
163.00
164.25
165.50
T (C)

2.16

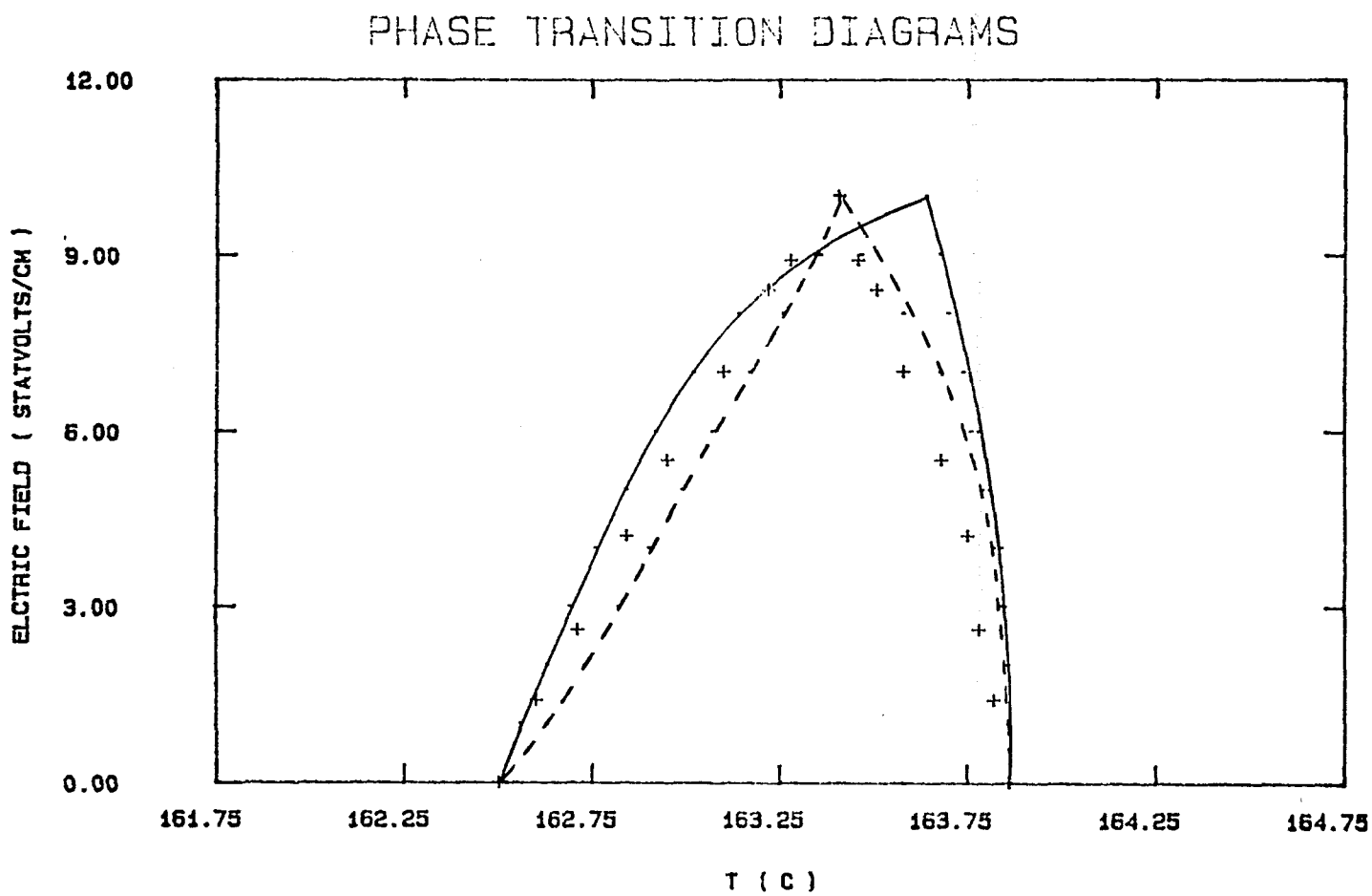

2.17

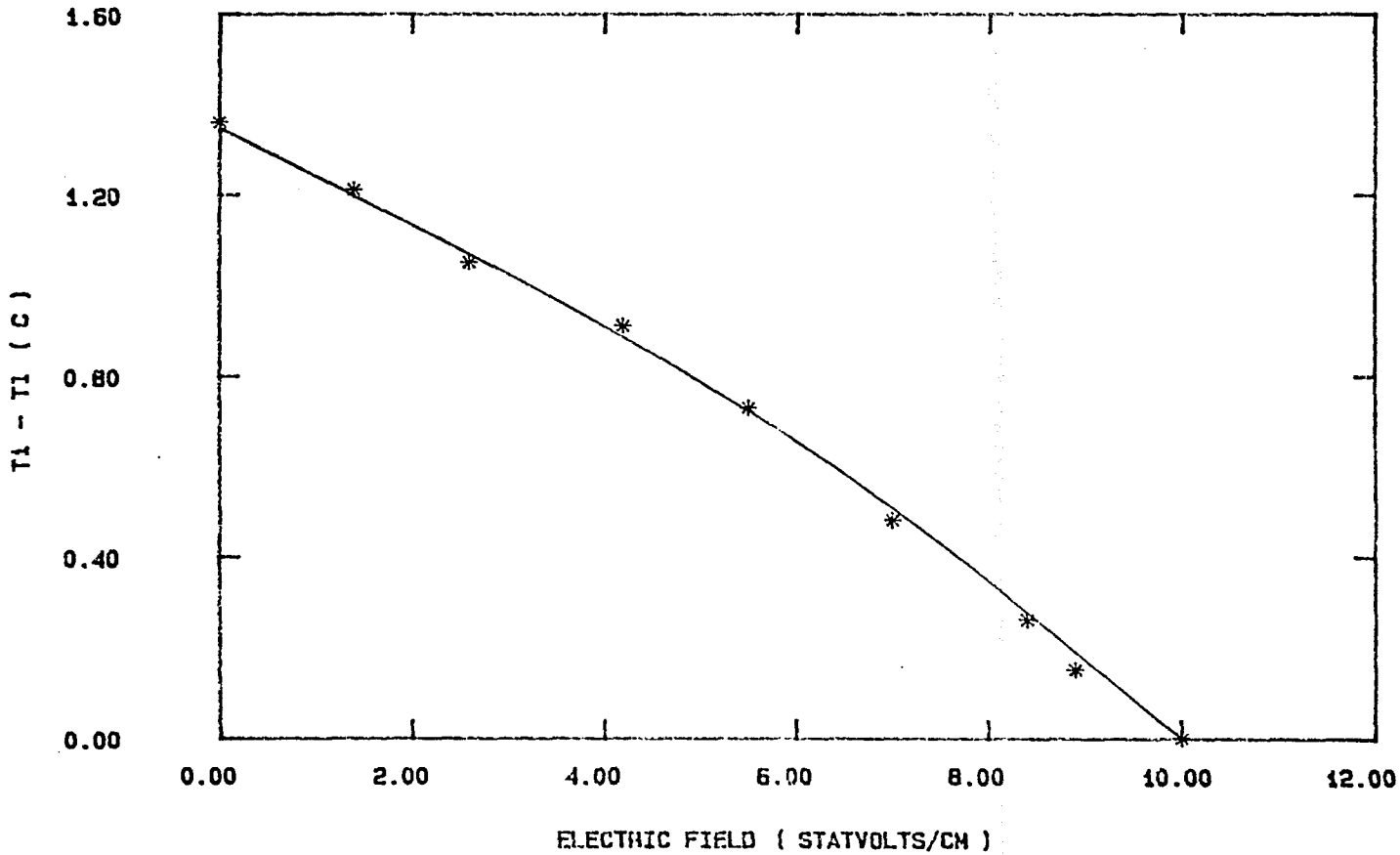

2.18

Sun Jun 30 12:XX:XX XXT 1990

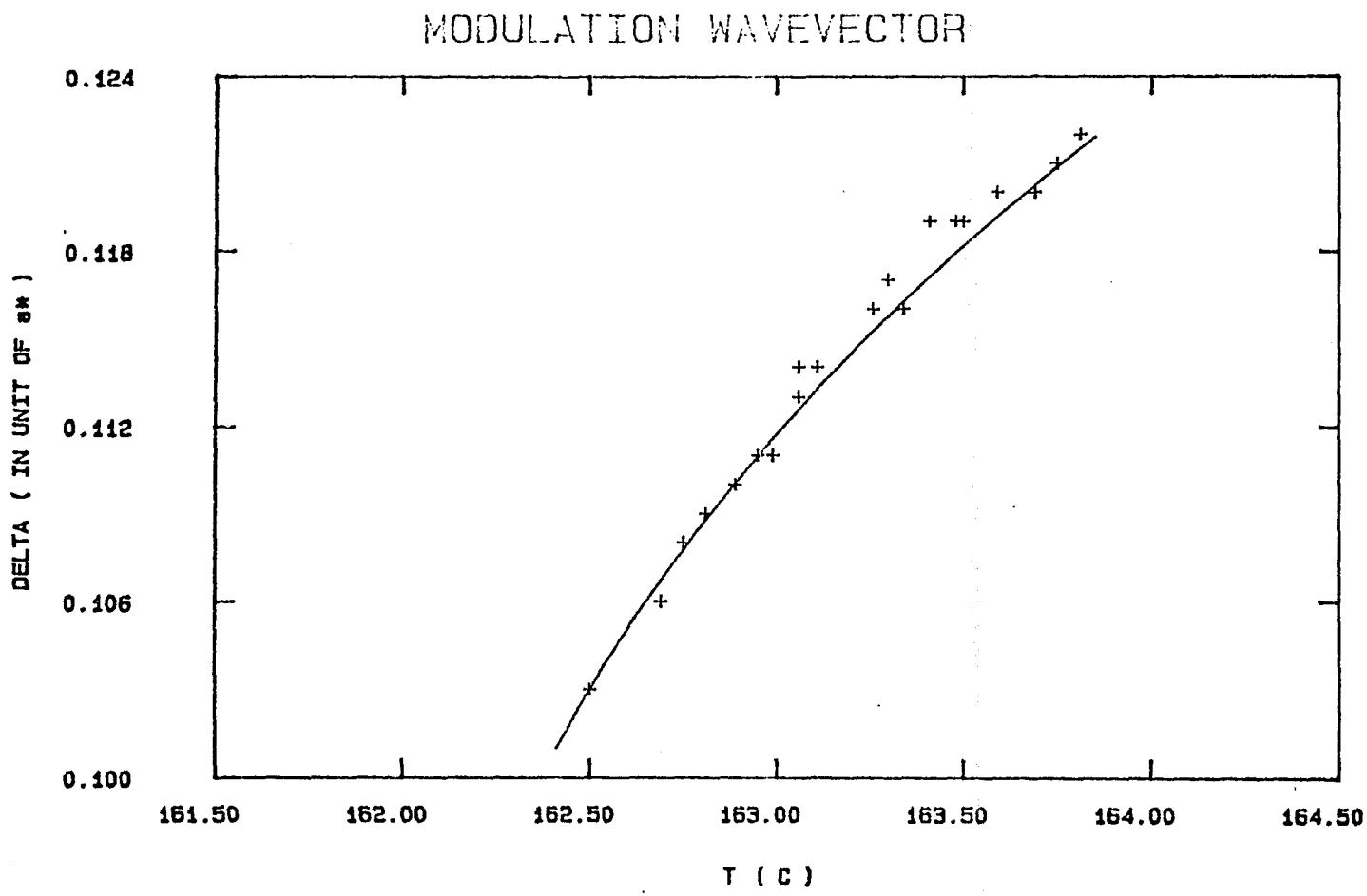

SIXTH ORDER FREE ENERGY MODEL

2.19

Sun Jun 30 10:48:57 EDT 1985

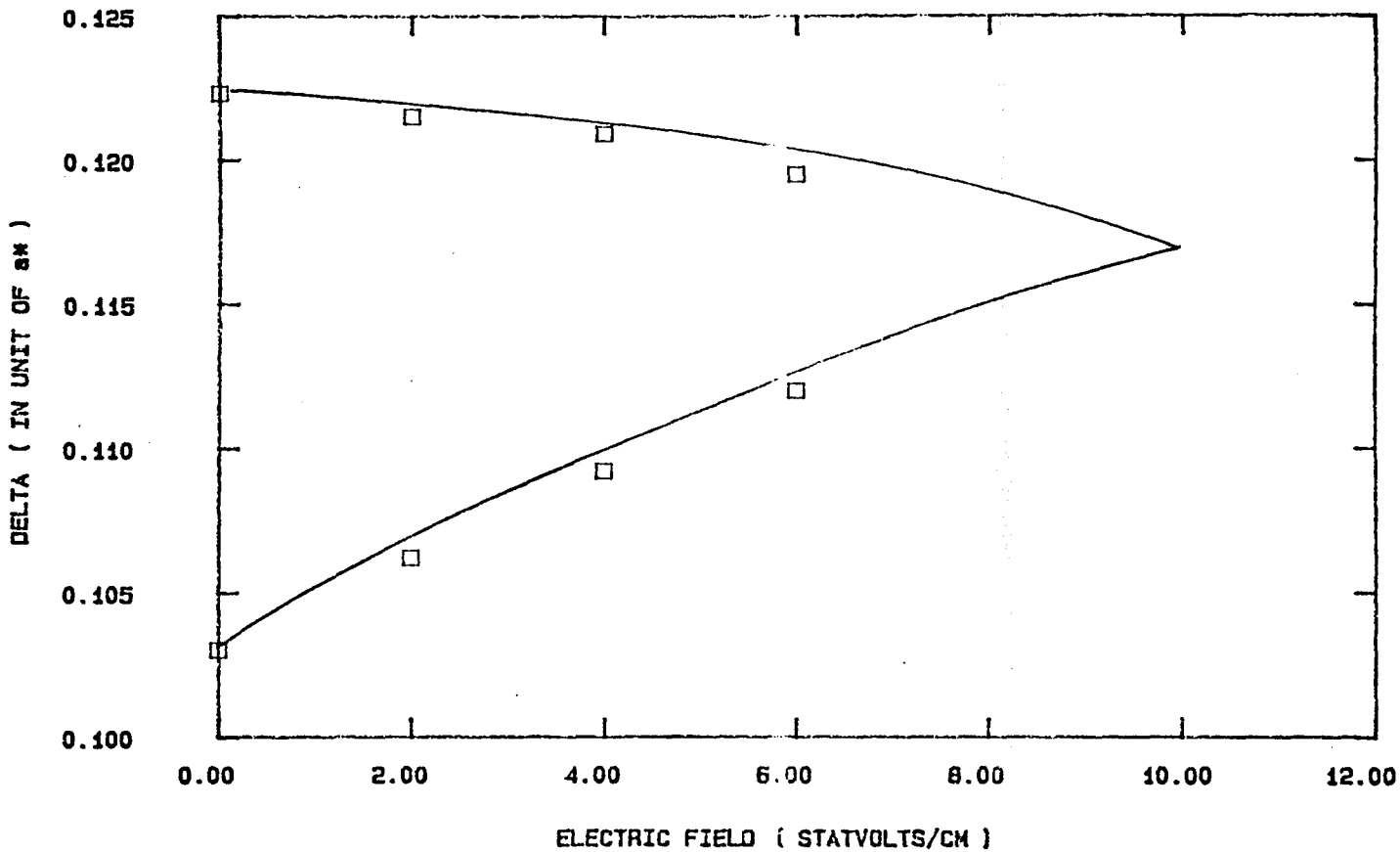

2.20

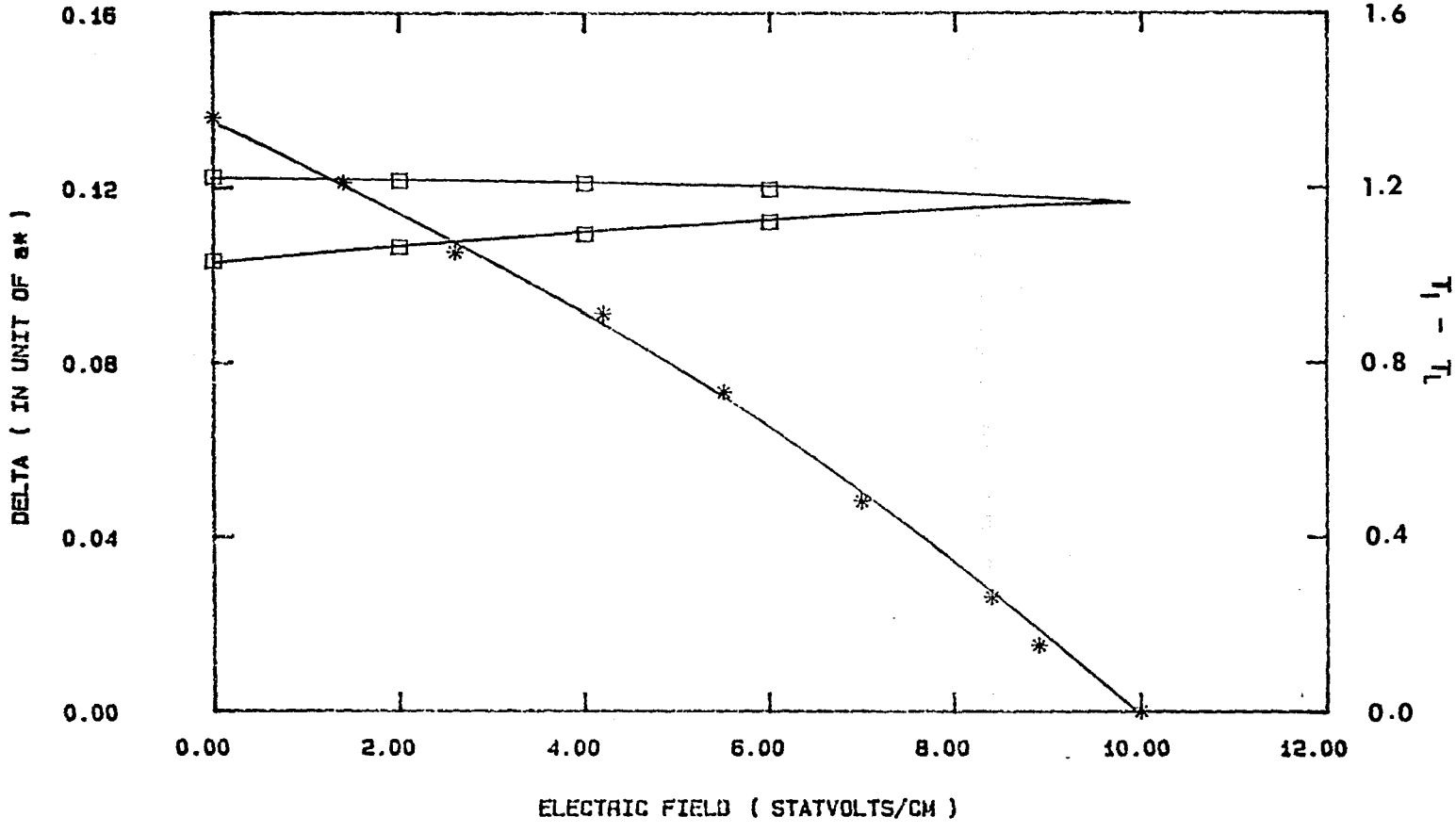
0.16
0.12
0.08
0.04
0.00
DELTA (IN UNIT OF aM)
1.6
1.2
0.8
0.4
0.0
$T_l - T_L$
0.00
2.00
4.00
6.00
8.00
10.00
12.00
ELECTRIC FIELD (STATVOLTS/CM)

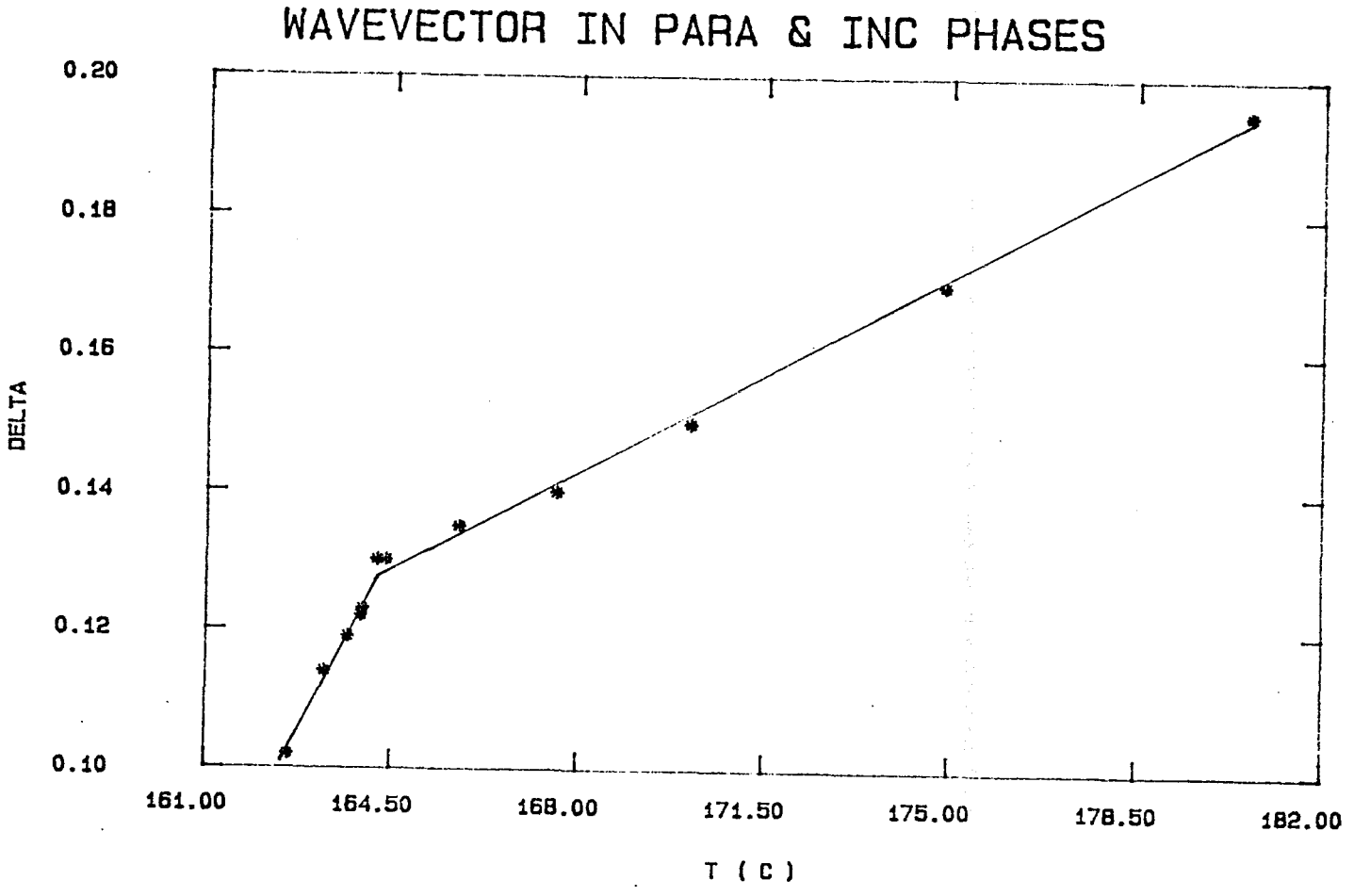

2.22

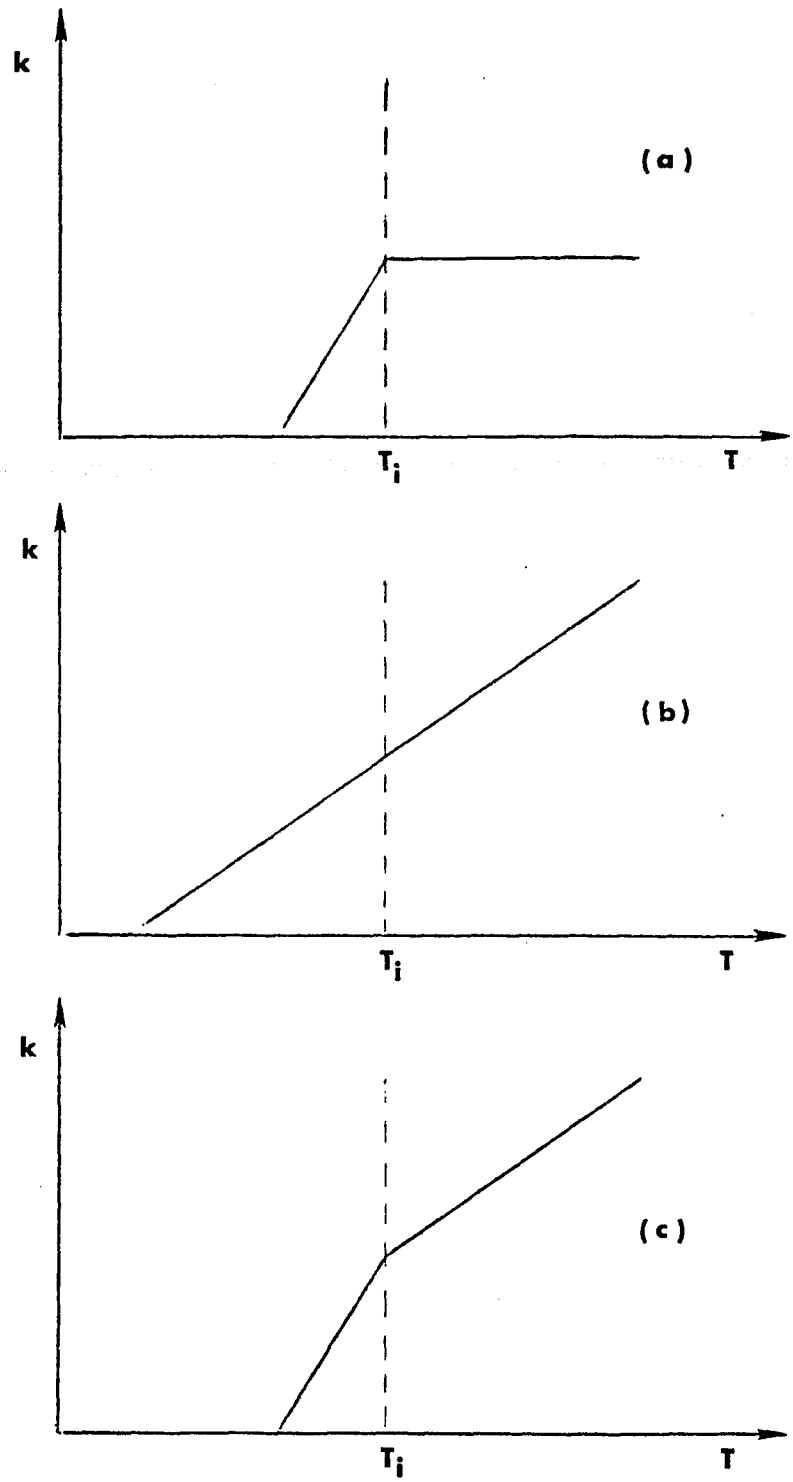

2.23

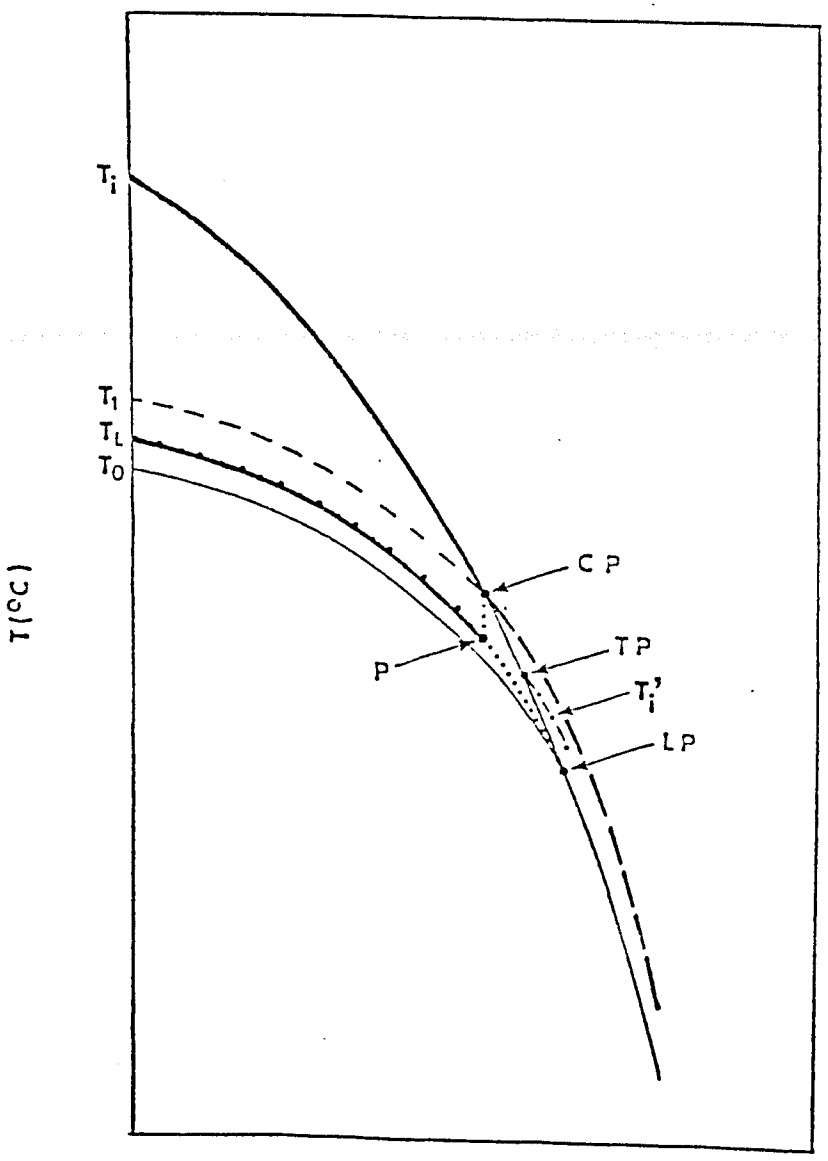

3.1

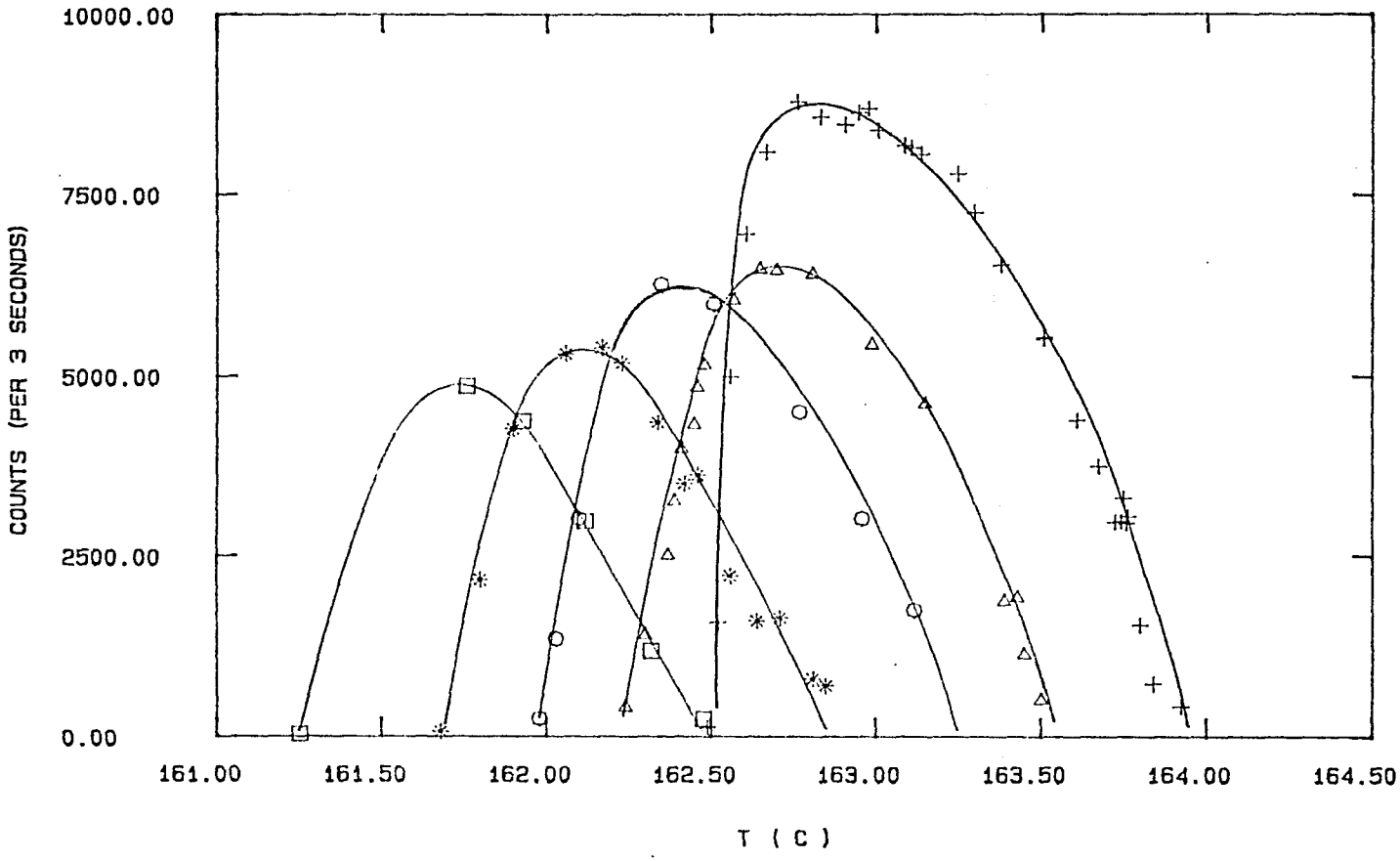

The solid lines are the eye guide

3.2

Sat Jul 30 14:02:58 EDT 1983

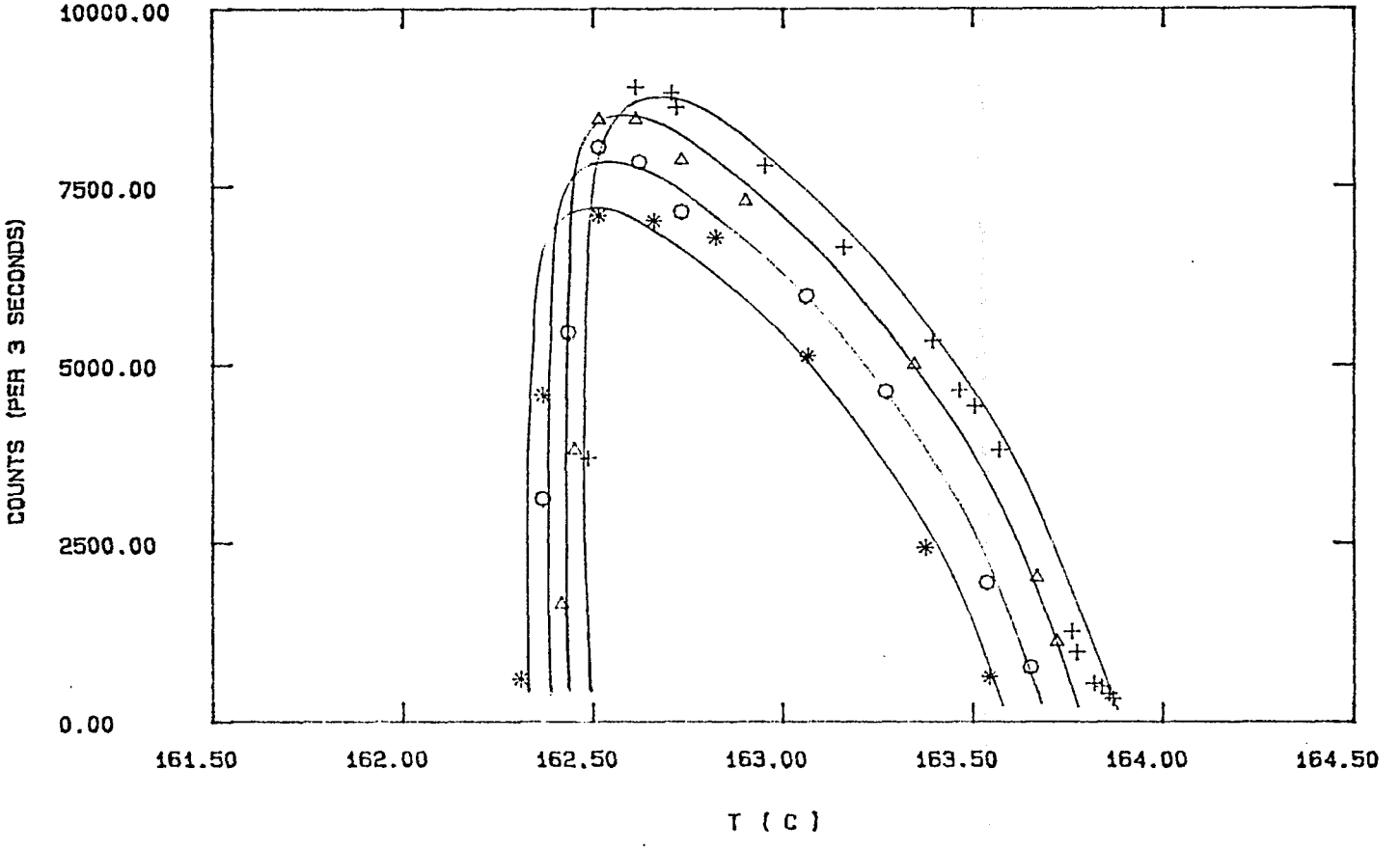

The solid lines are for eye guide

3.3

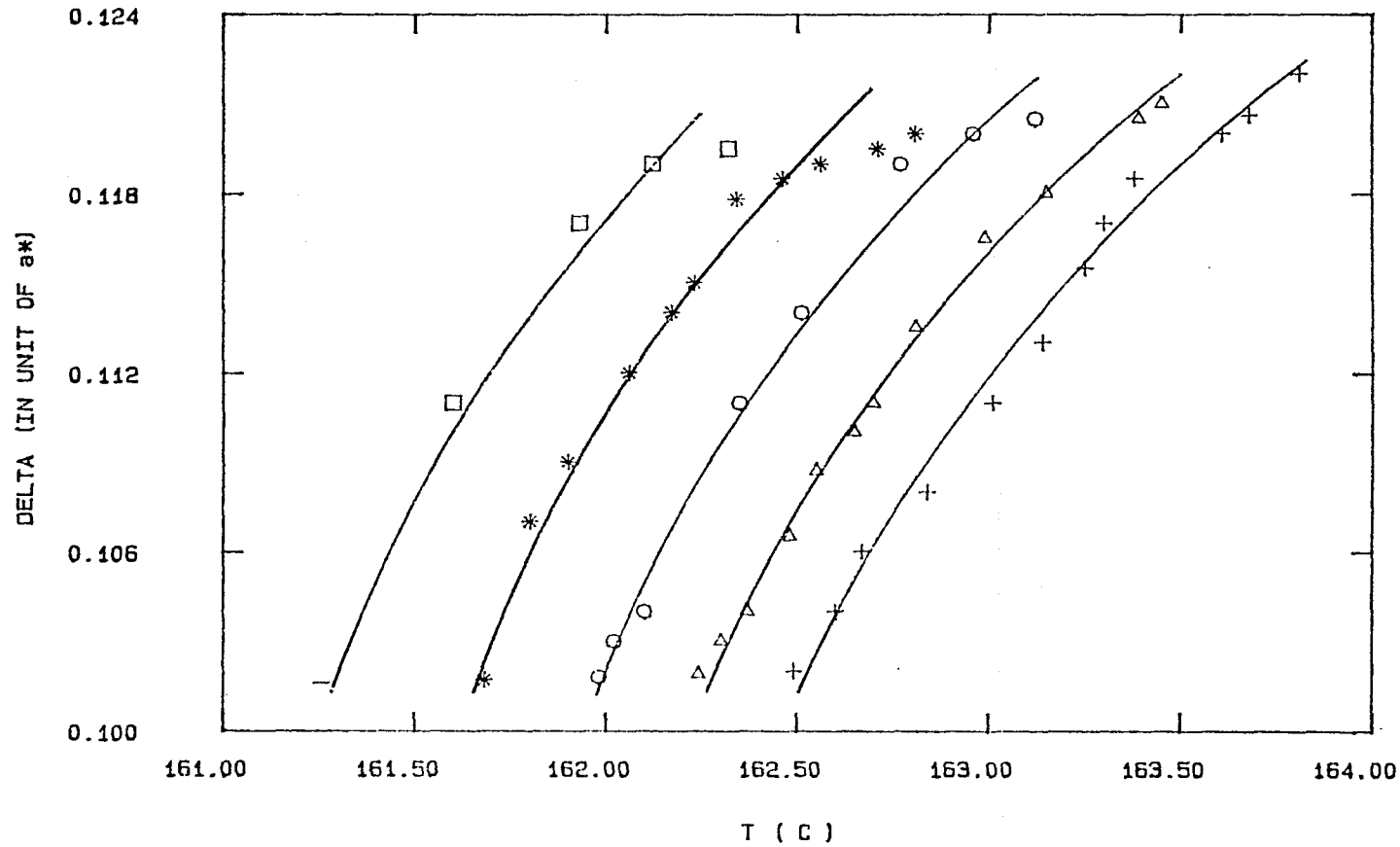

The solid lines are for eye guide

3.4

Sat Jul 20 11:23:22 EDT 1985

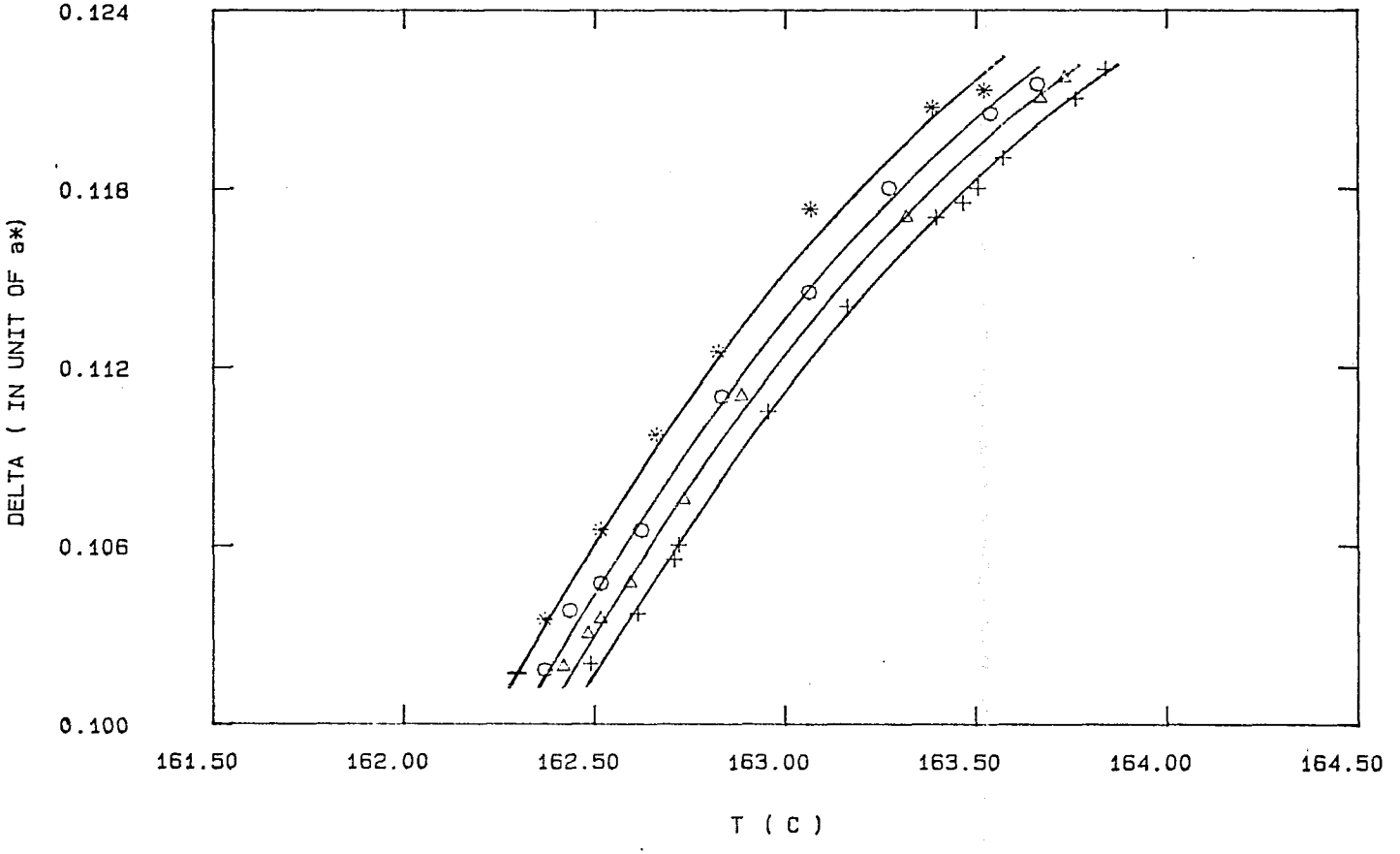

The solid lines are for eye guide

3.5

Sat Jul 20 10:50:04 EDT 1985

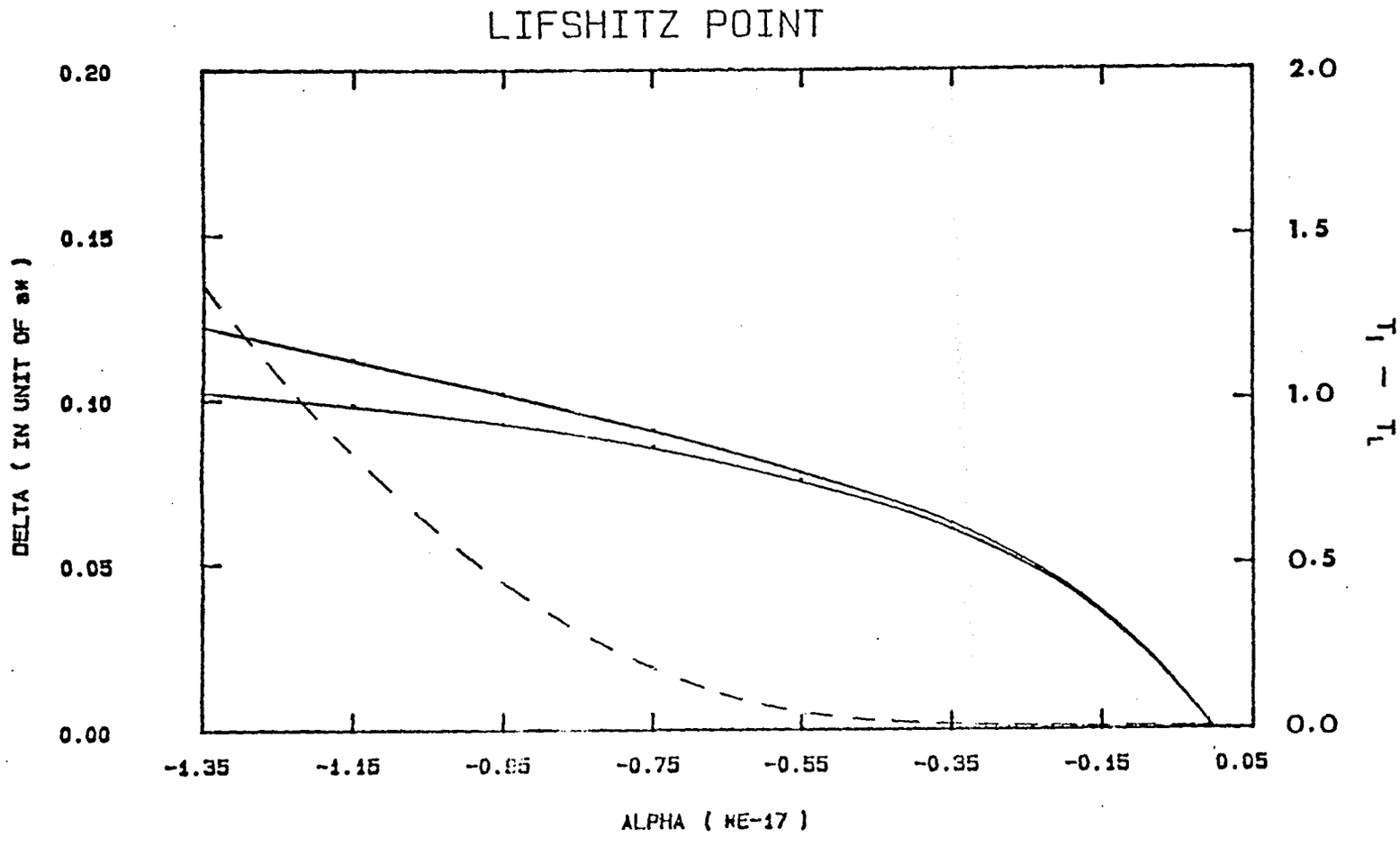
LIFSHITZ POINT
0.20
0.15
0.10
0.05
0.00
DELTA (IN UNIT OF aN)
2.0
1.5
1.0
0.5
0.0
$T_I - T_L$
-1.35
-1.15
-0.95
-0.75
-0.55
-0.35
-0.15
0.05
ALPHA (ME-17)

3.6

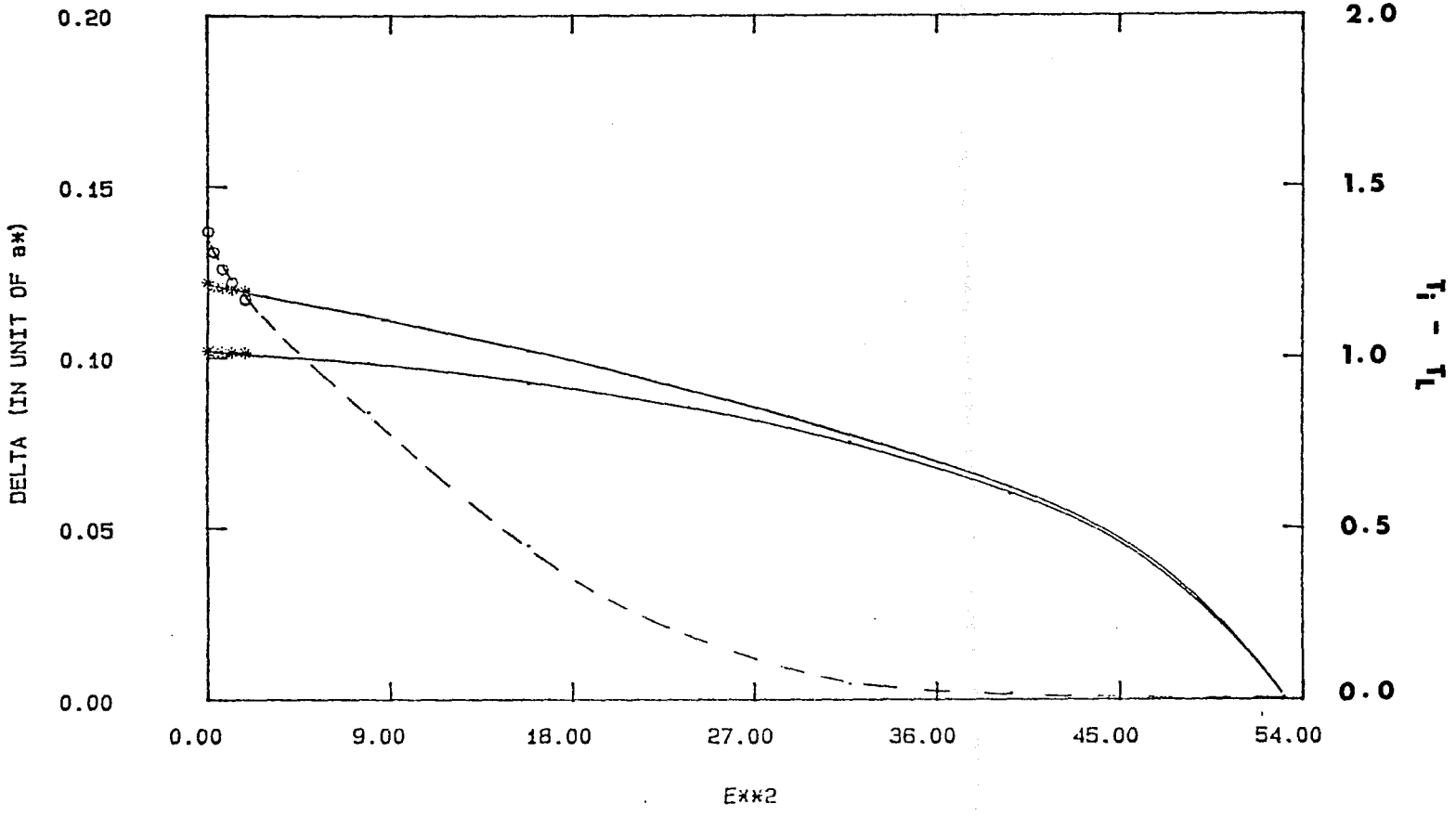

3.7

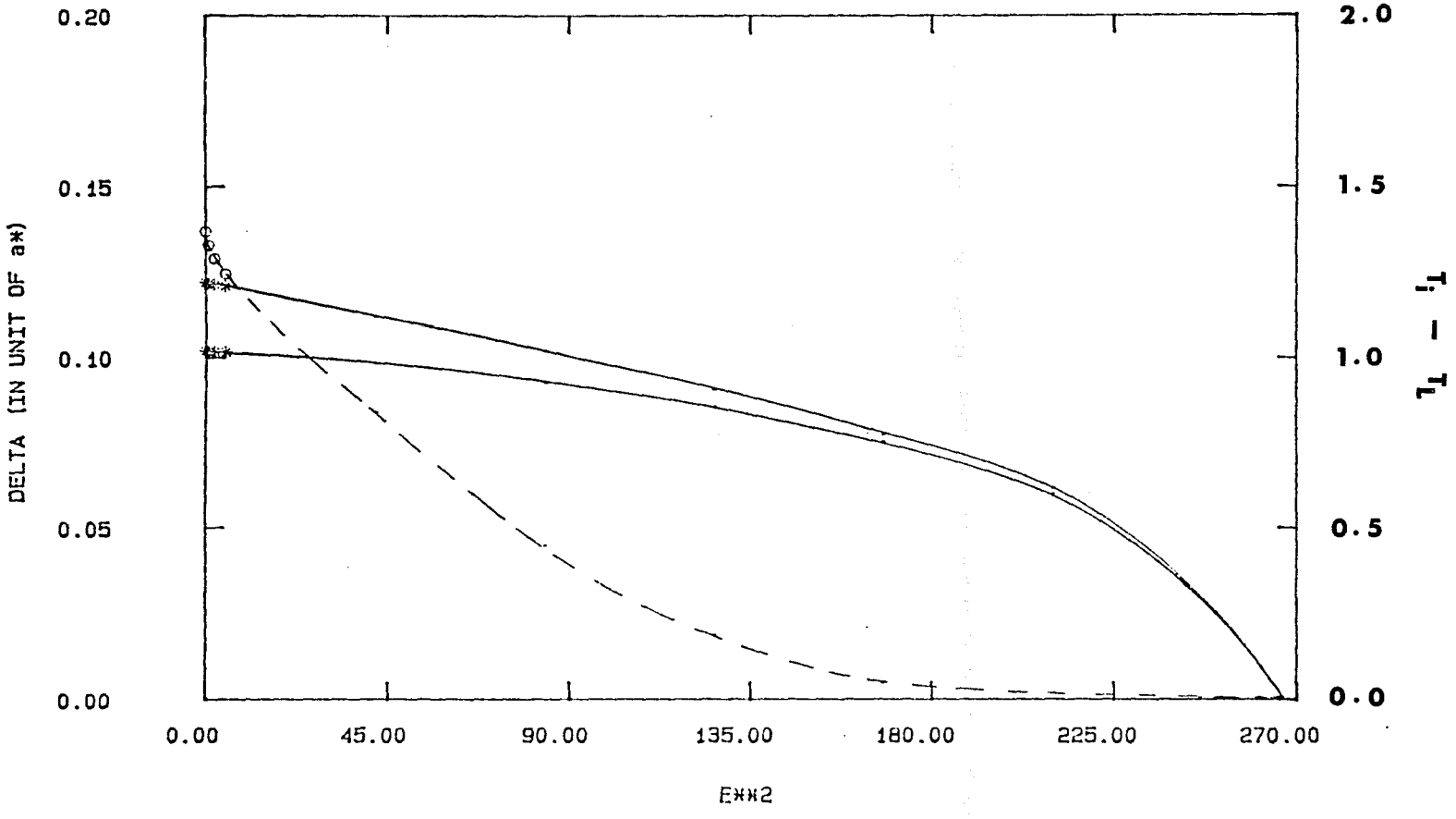

3.8

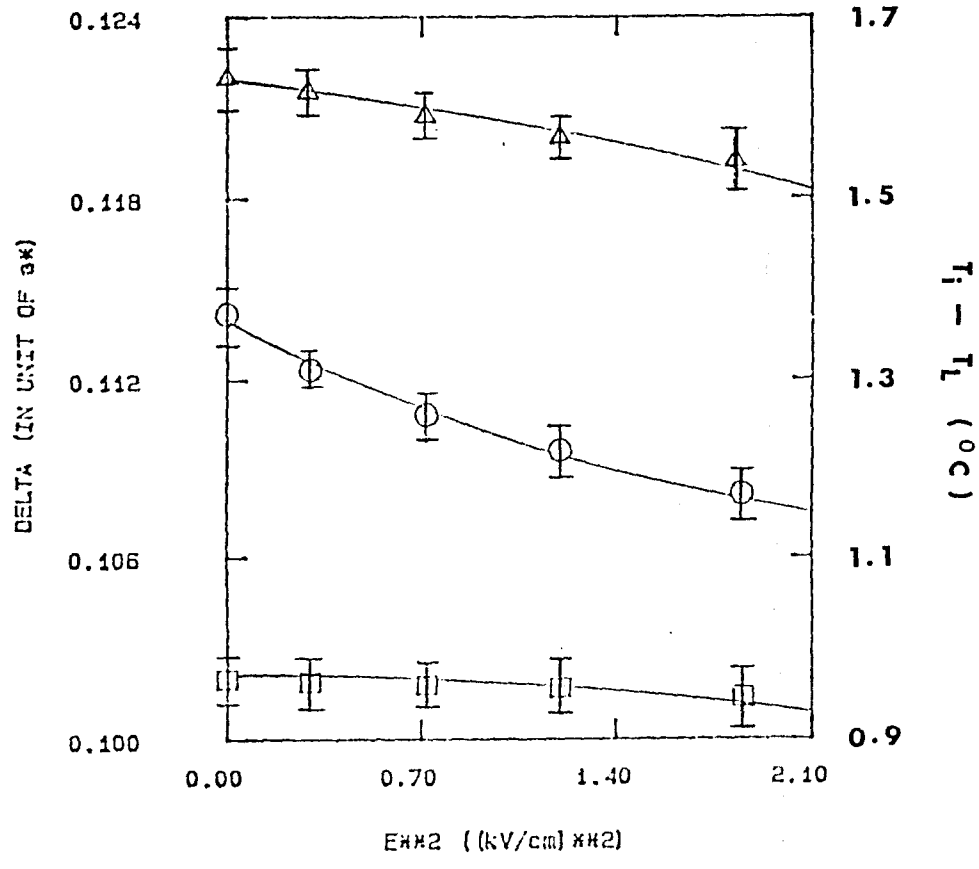
0.124
0.118
0.112
0.106
0.100
DELTA (IN UNIT OF a*)
1.7
1.5
1.3
1.1
0.9
$T_i - T_L$ (°C)
0.00
0.70
1.40
2.10
E**2 ((kV/cm)**2)

3.9

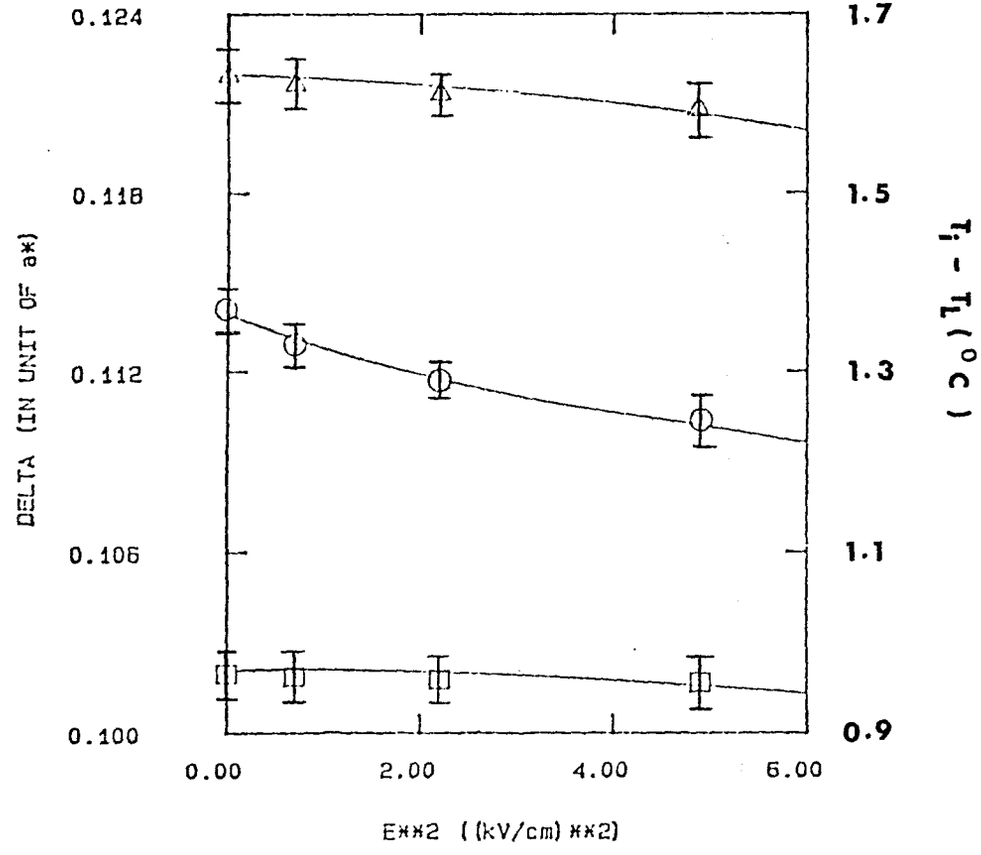

3.10

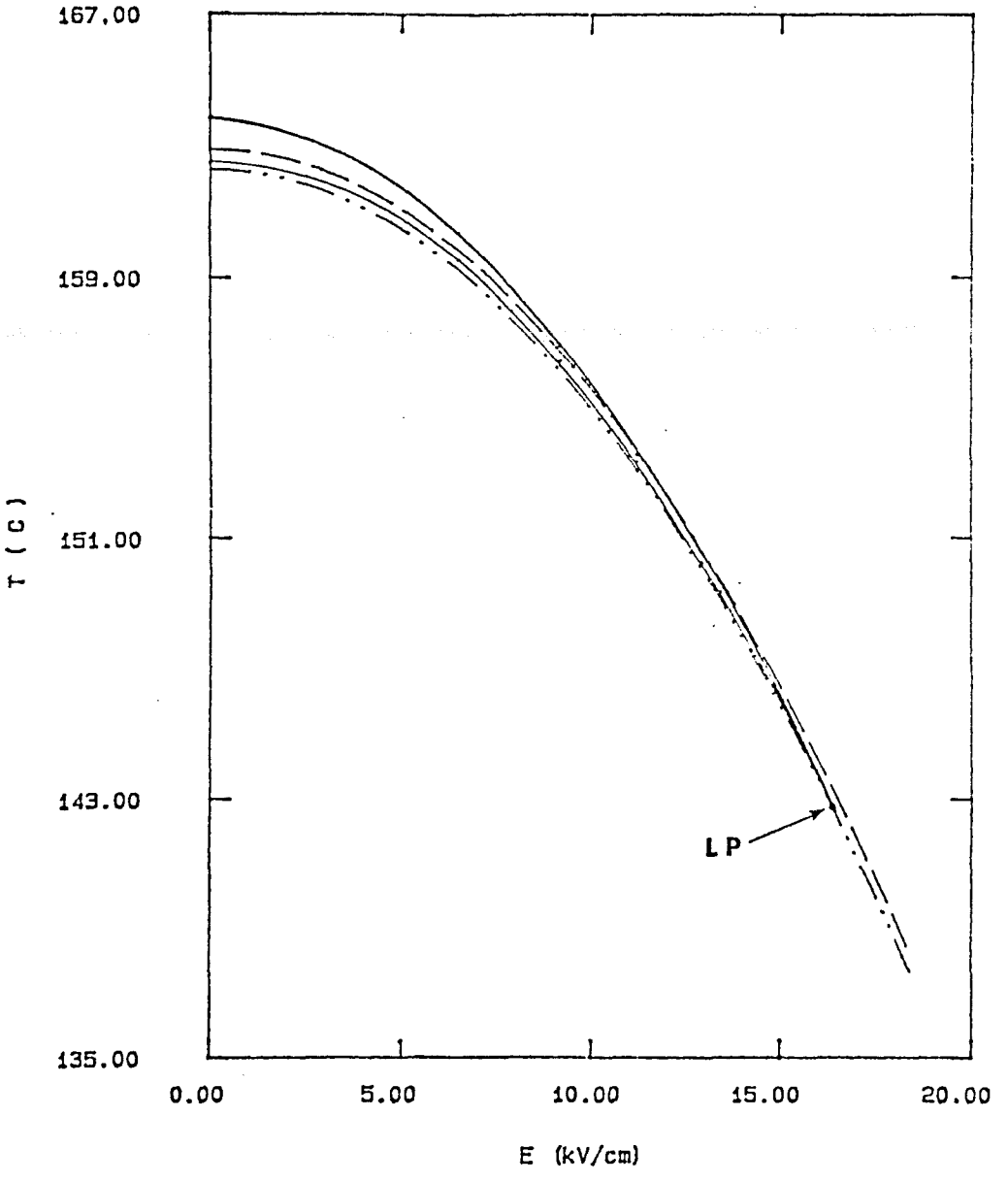

E-FIELD PARALLEL TO THE C-AXIS

3.11

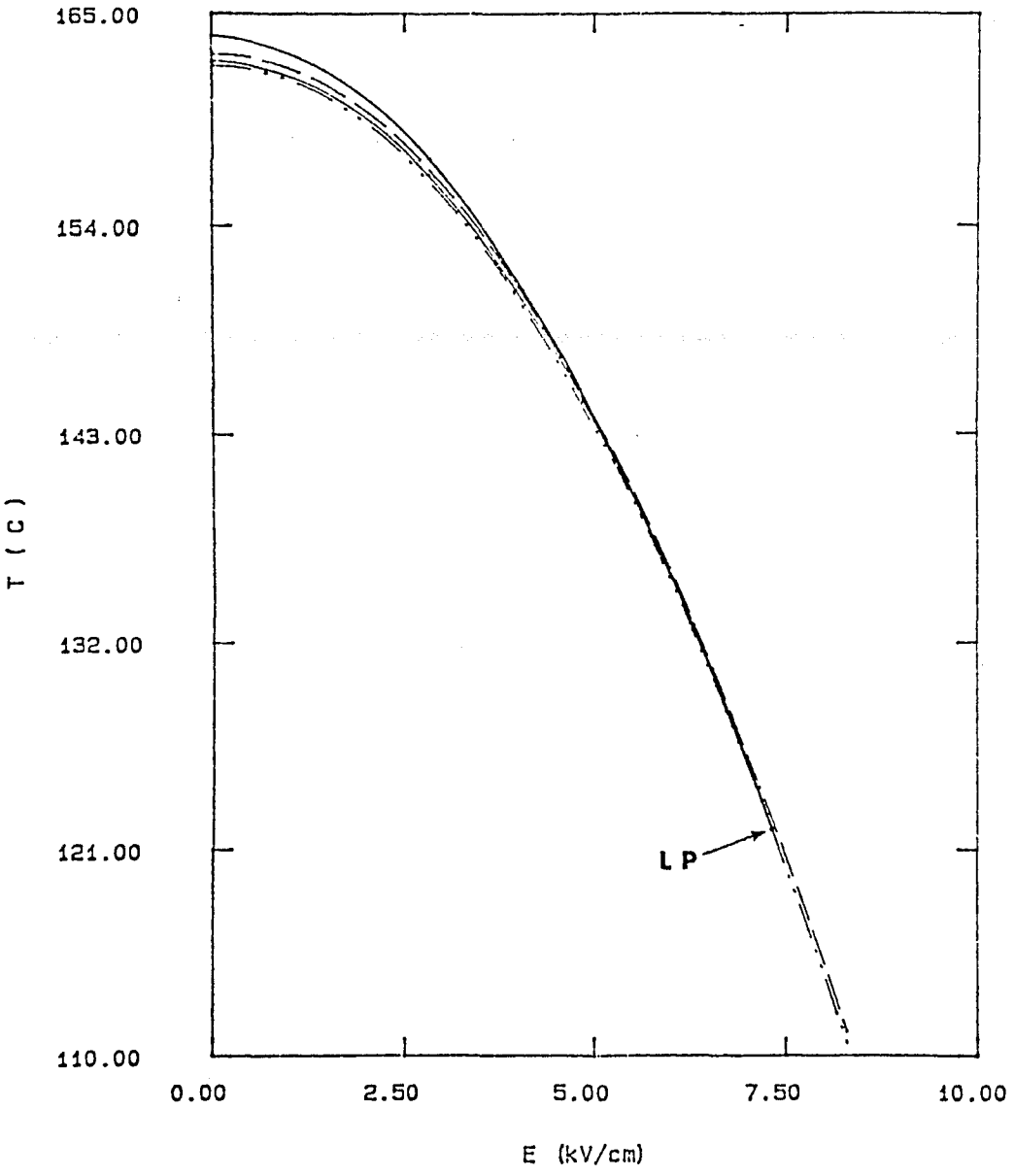

E-FIELD PARALLEL TO THE a-AXIS

3.12

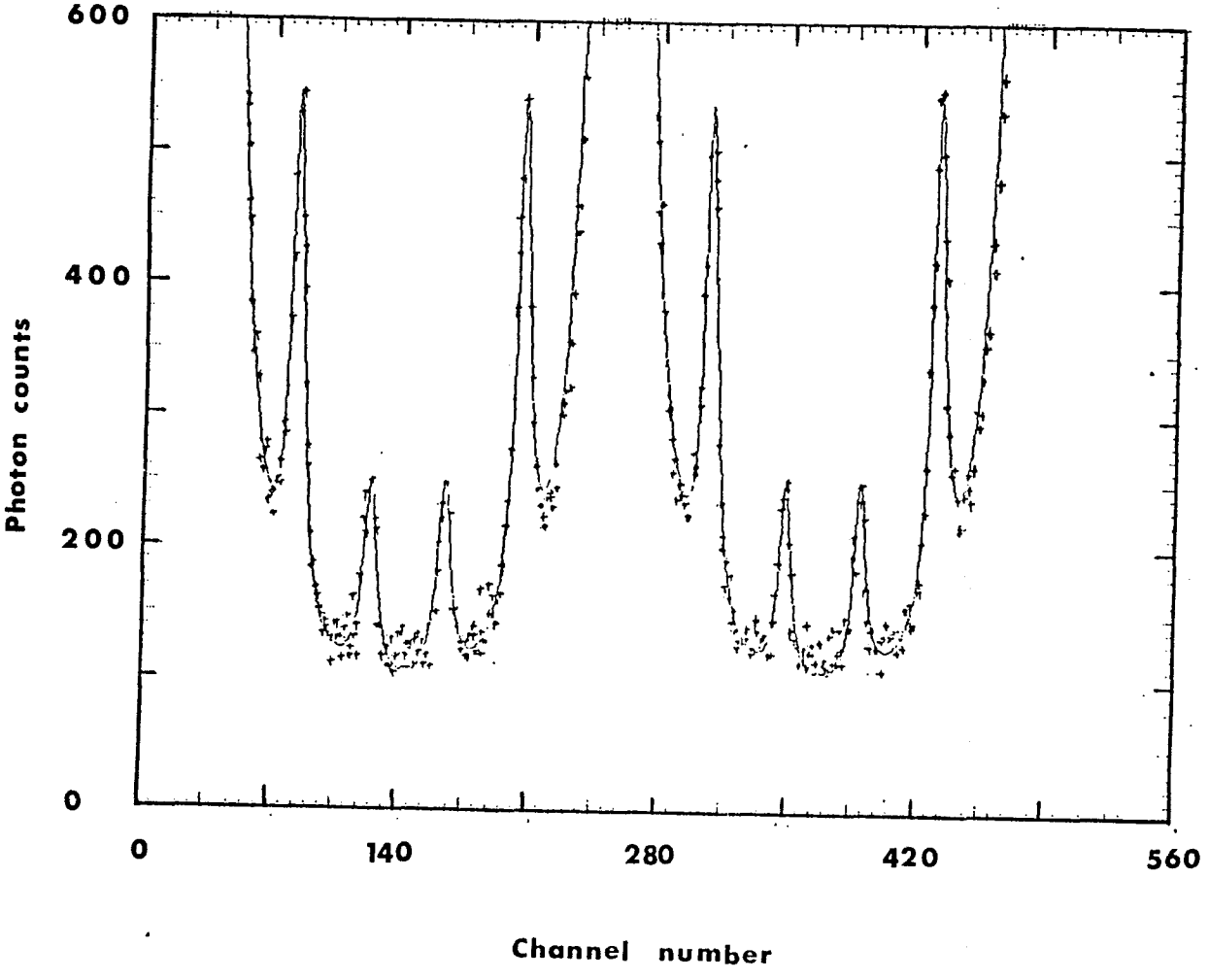

4.1

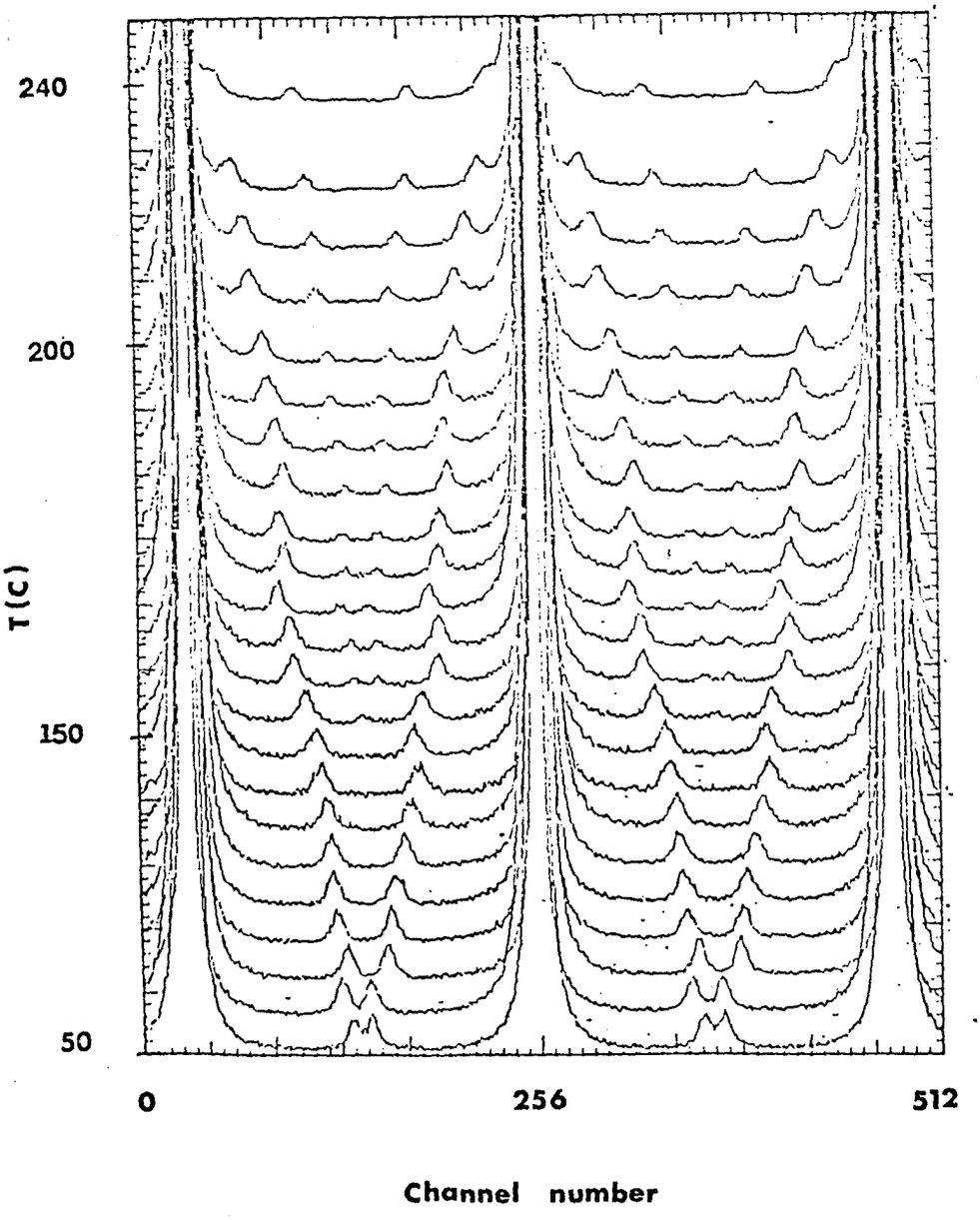

4.2

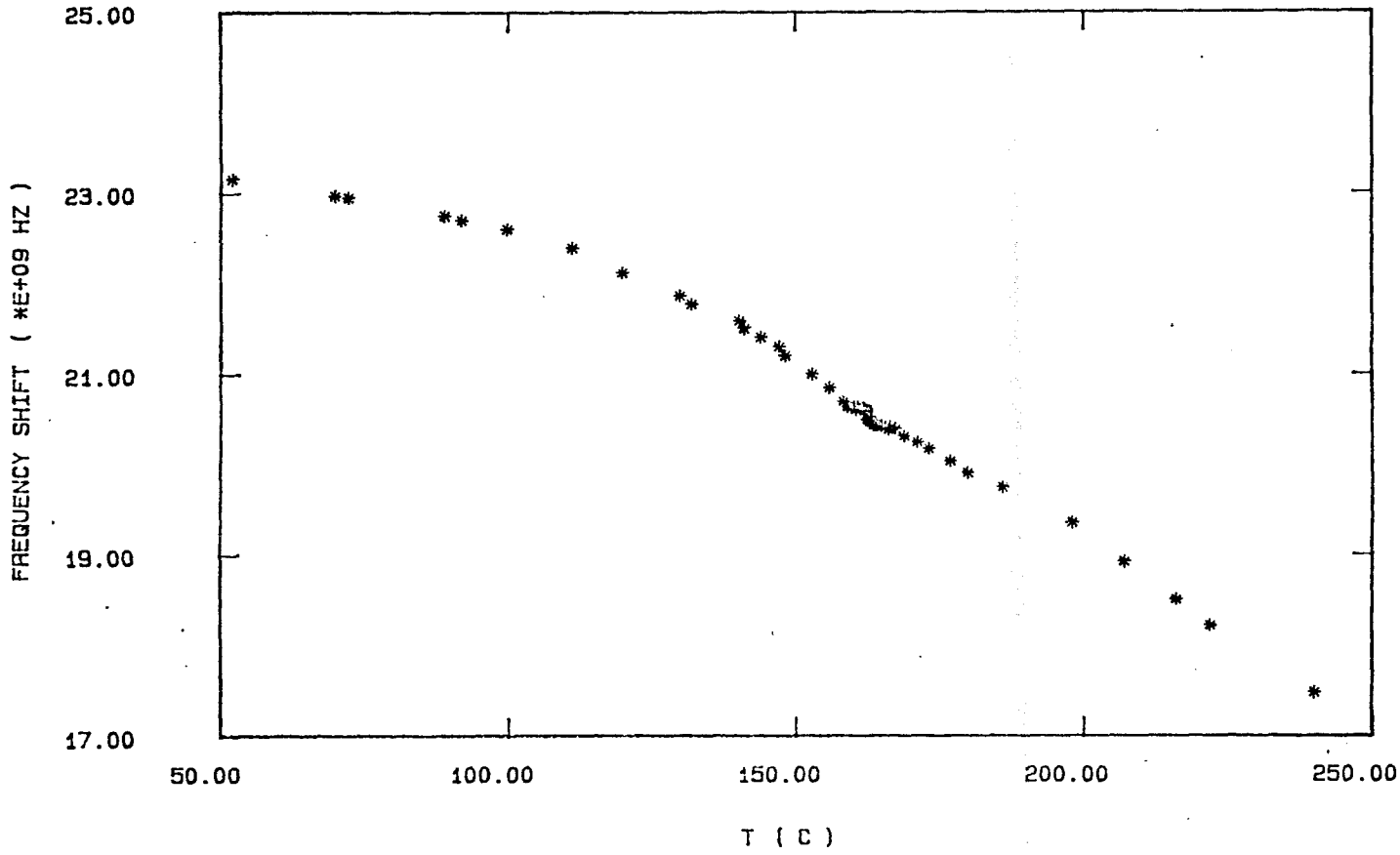

4.3

Fri May 17 08:53:24 EDT 1985

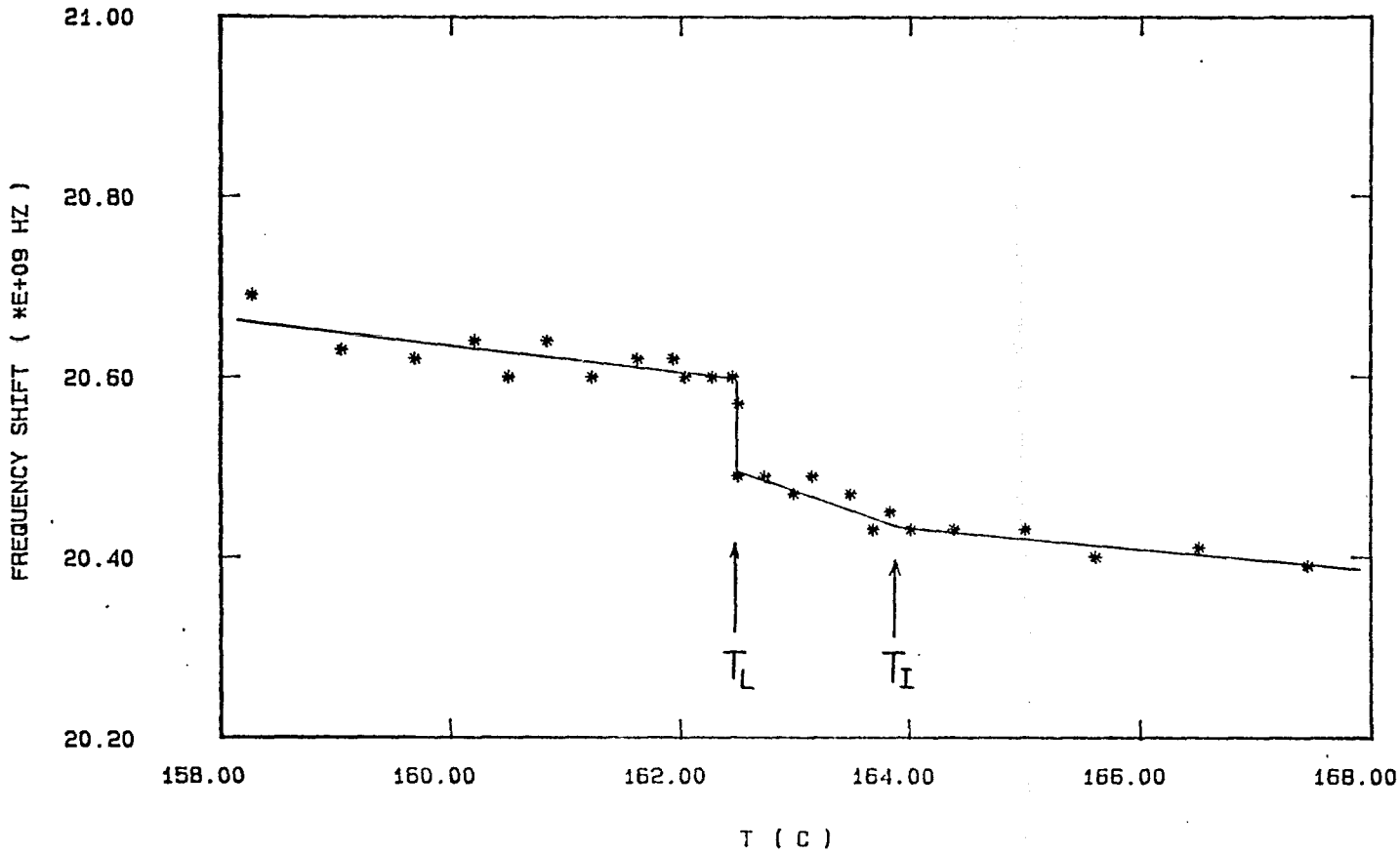

4.4

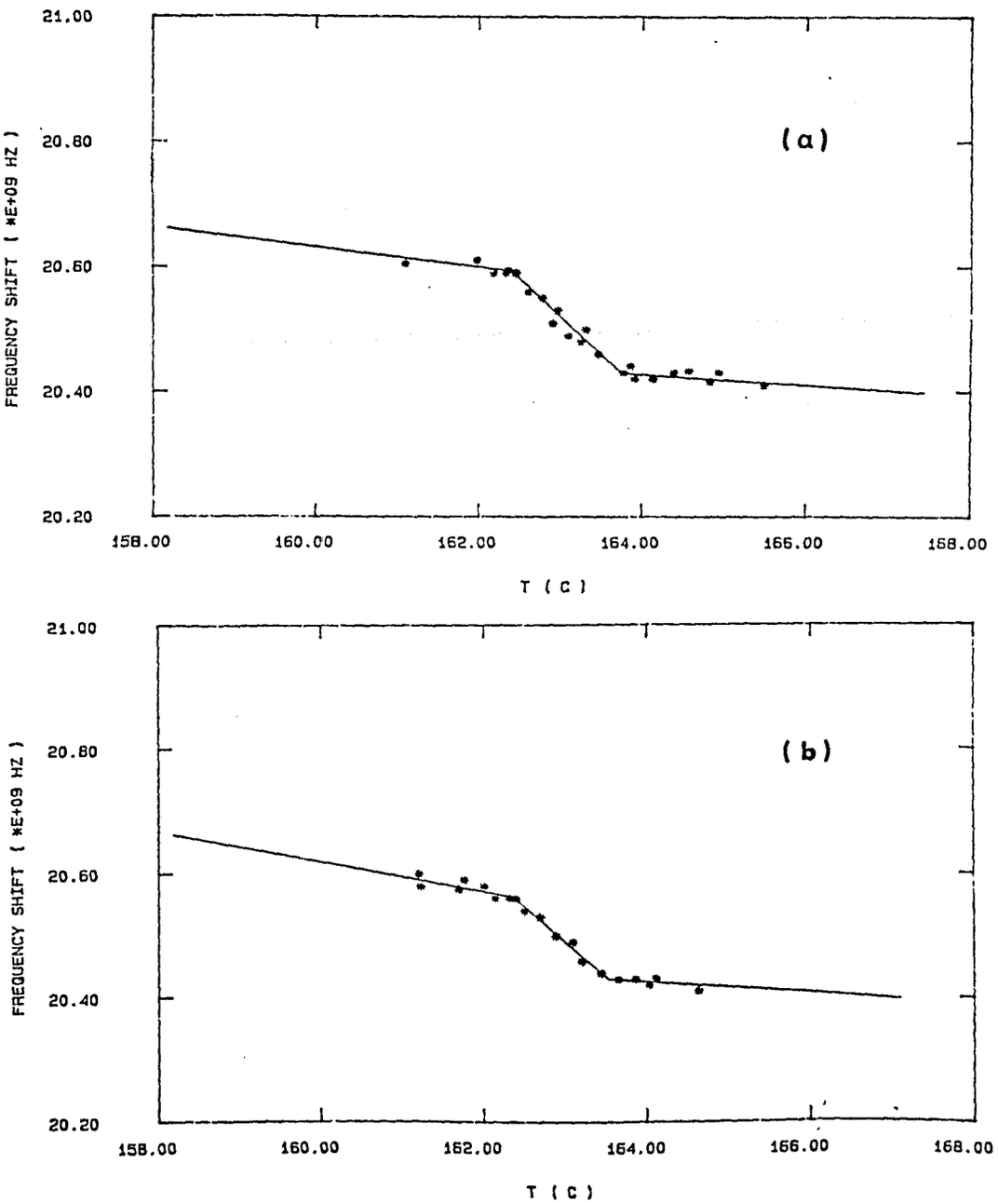
21.00
20.80
20.60
20.40
20.20
FREQUENCY SHIFT (*E+09 HZ)
(a)
158.00
160.00
162.00
164.00
166.00
168.00
T (C)
21.00
20.80
20.60
20.40
20.20
FREQUENCY SHIFT (*E+09 HZ)
(b)
158.00
160.00
162.00
164.00
166.00
168.00
T (C)

4.5

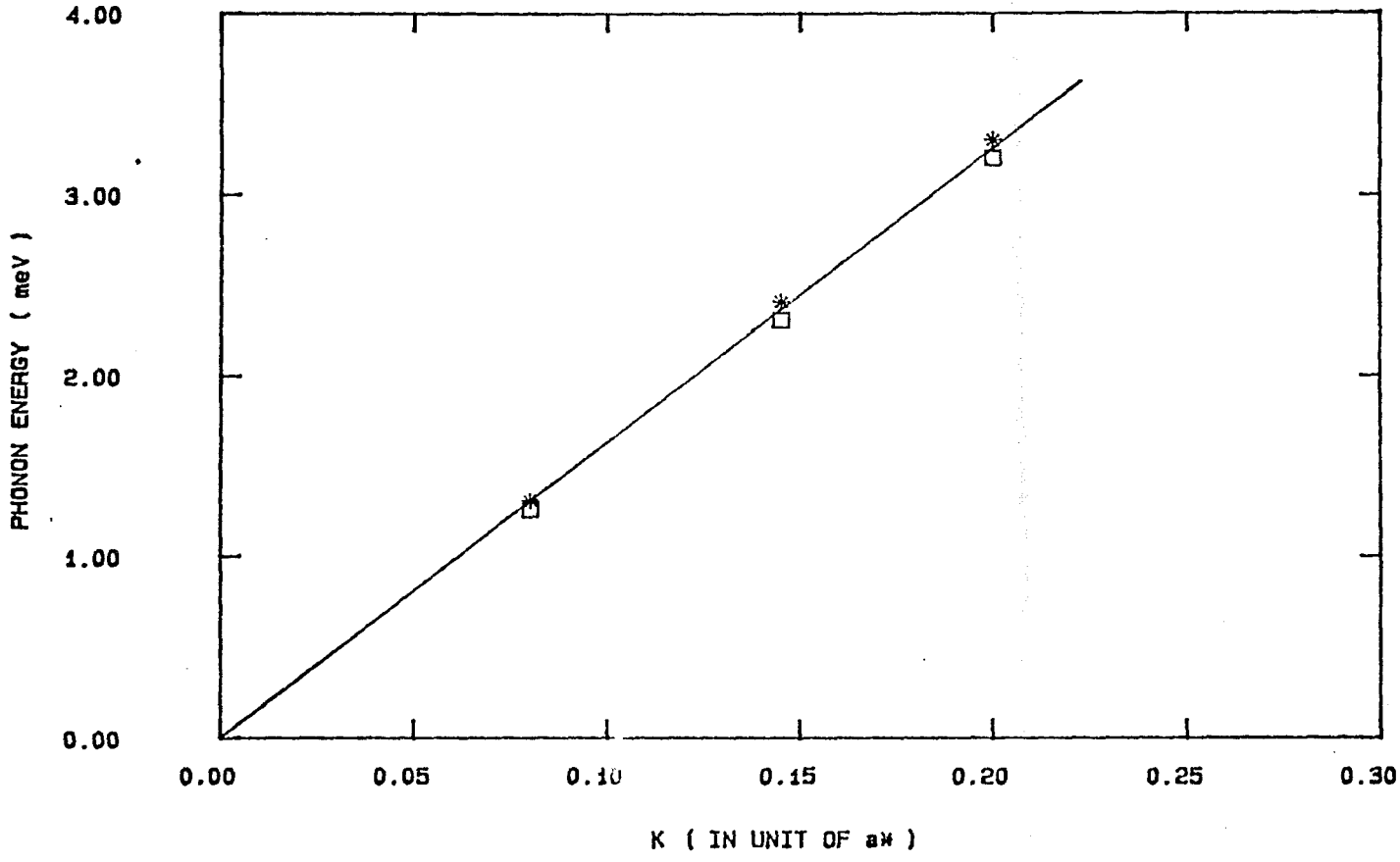

4.6

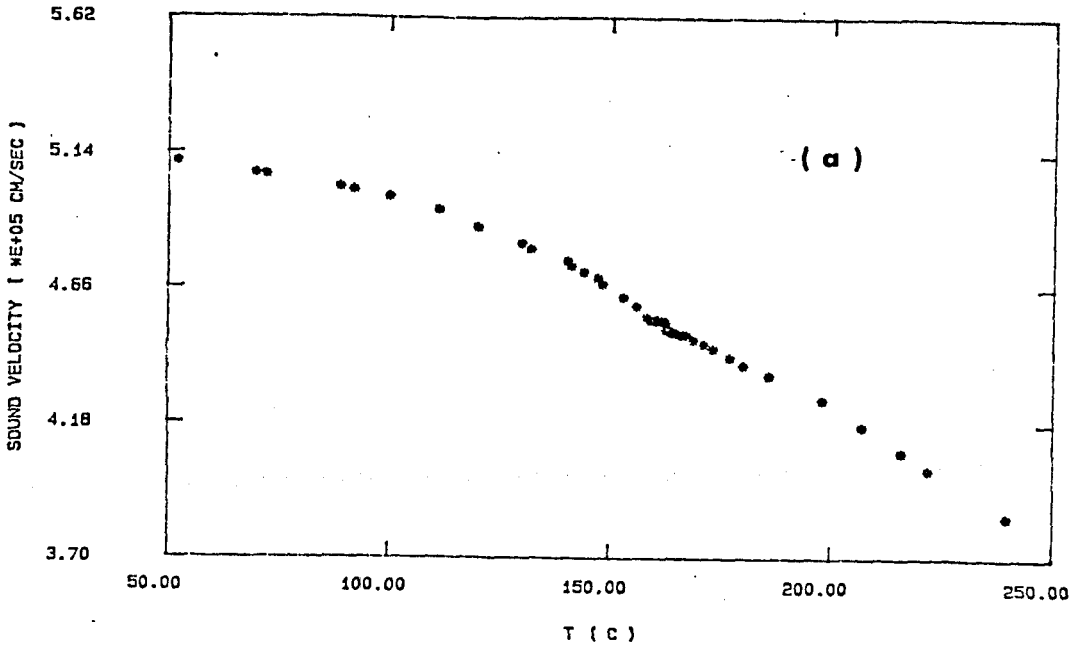

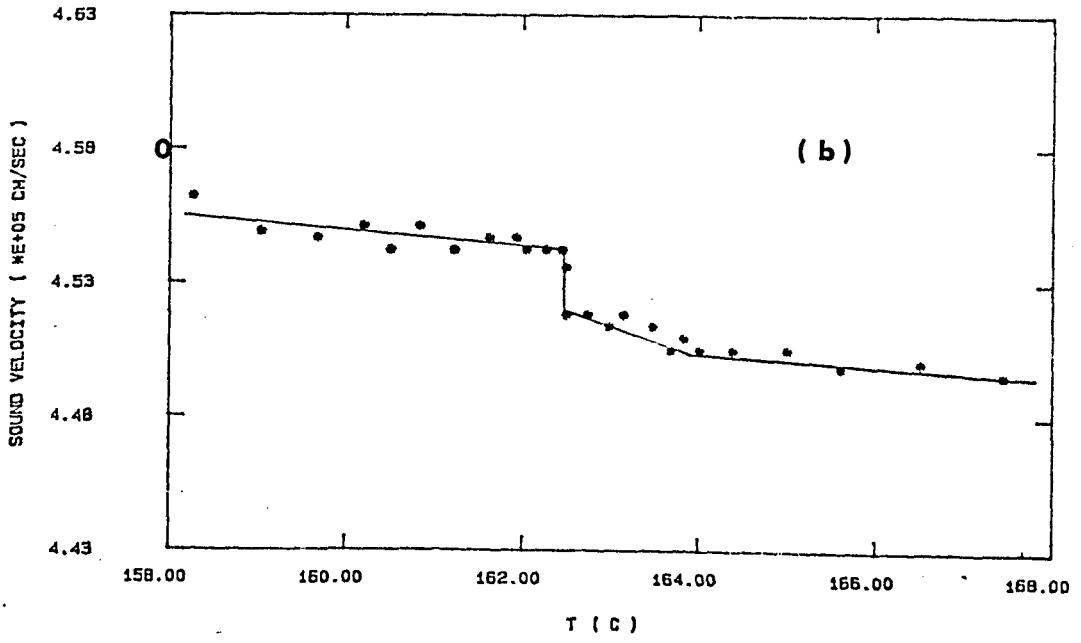

4.7

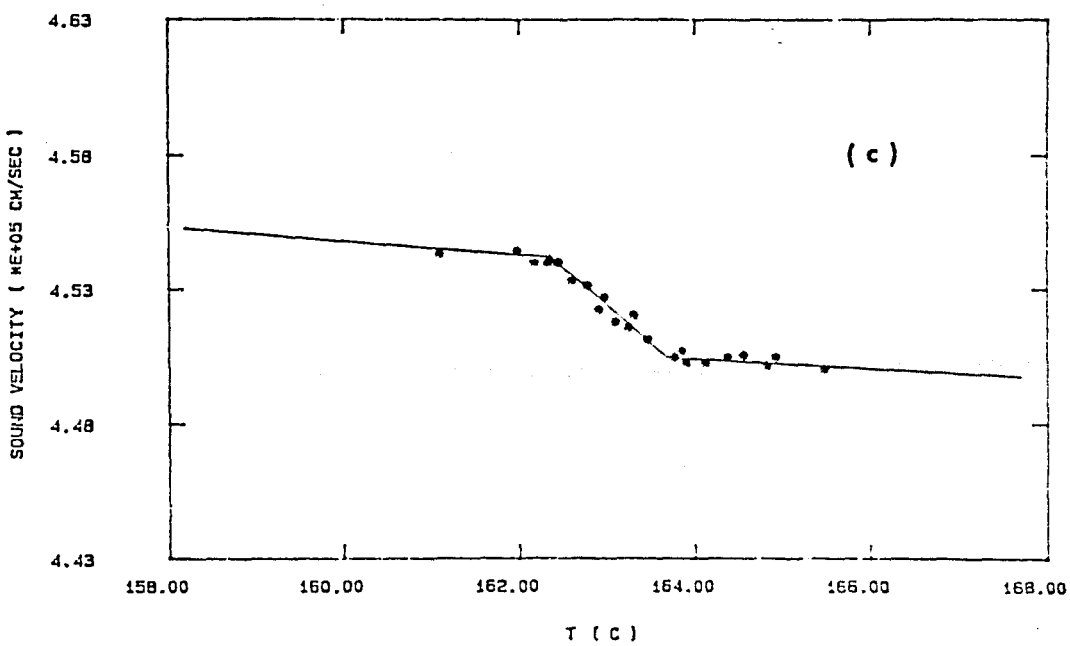
4.63
4.58
4.53
4.48
4.43
SOUND VELOCITY (ME+05 CM/SEC)
(c)
158.00
160.00
162.00
164.00
166.00
168.00
T (C)

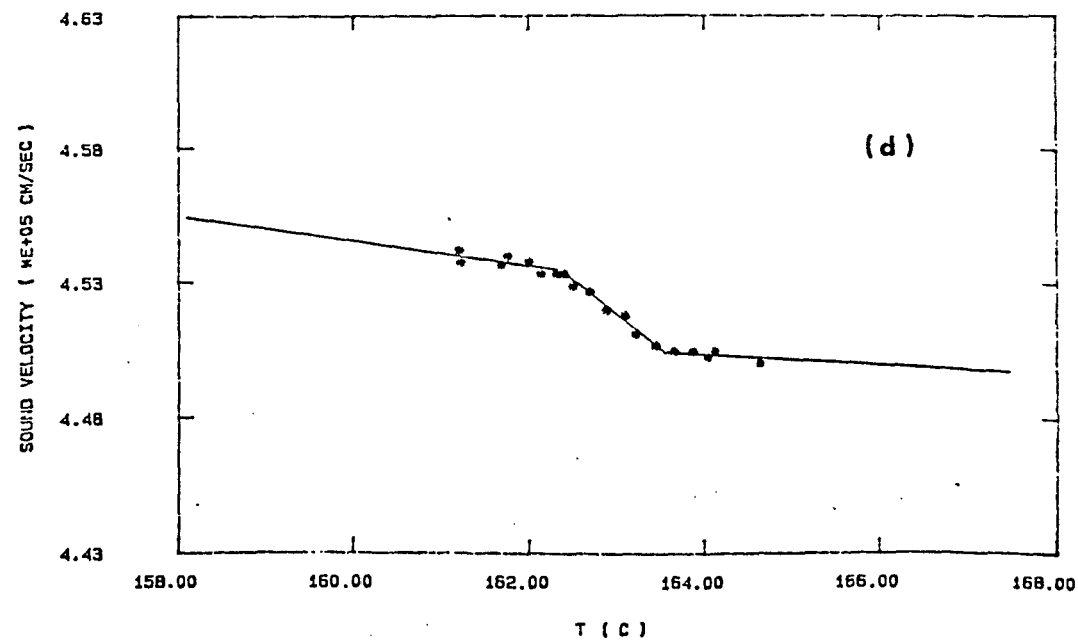
4.63
4.58
4.53
4.48
4.43
SOUND VELOCITY (ME+05 CM/SEC)
(d)
158.00
160.00
162.00
164.00
166.00
168.00
T (C)

4.7

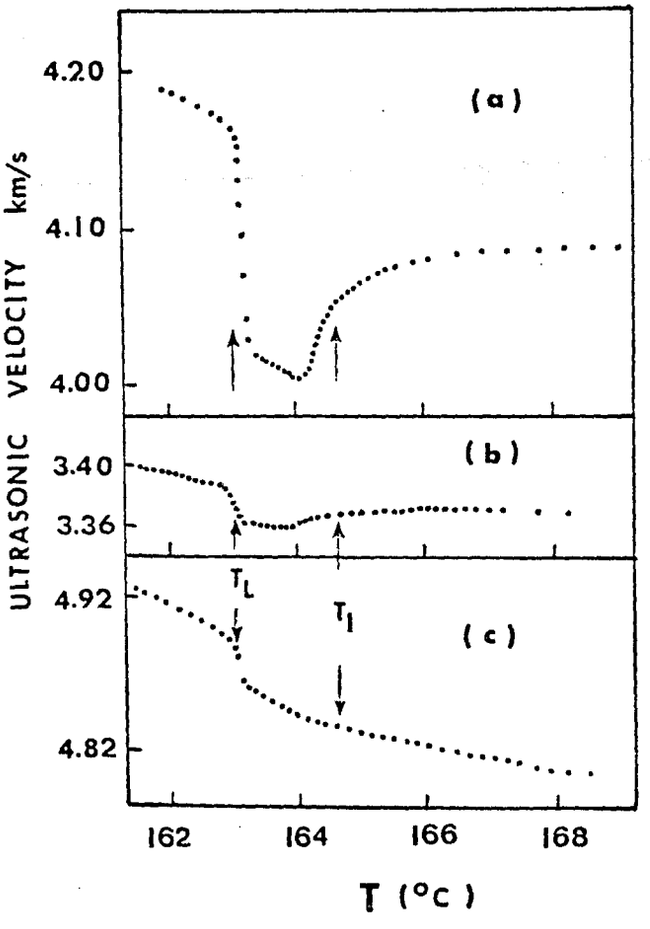
4.20
4.10
4.00
(a)
ULTRASONIC VELOCITY km/s
3.40
3.36
(b)
4.92
4.82
T_L
T_I
(c)
162
164
166
168
T (°C)

4.8

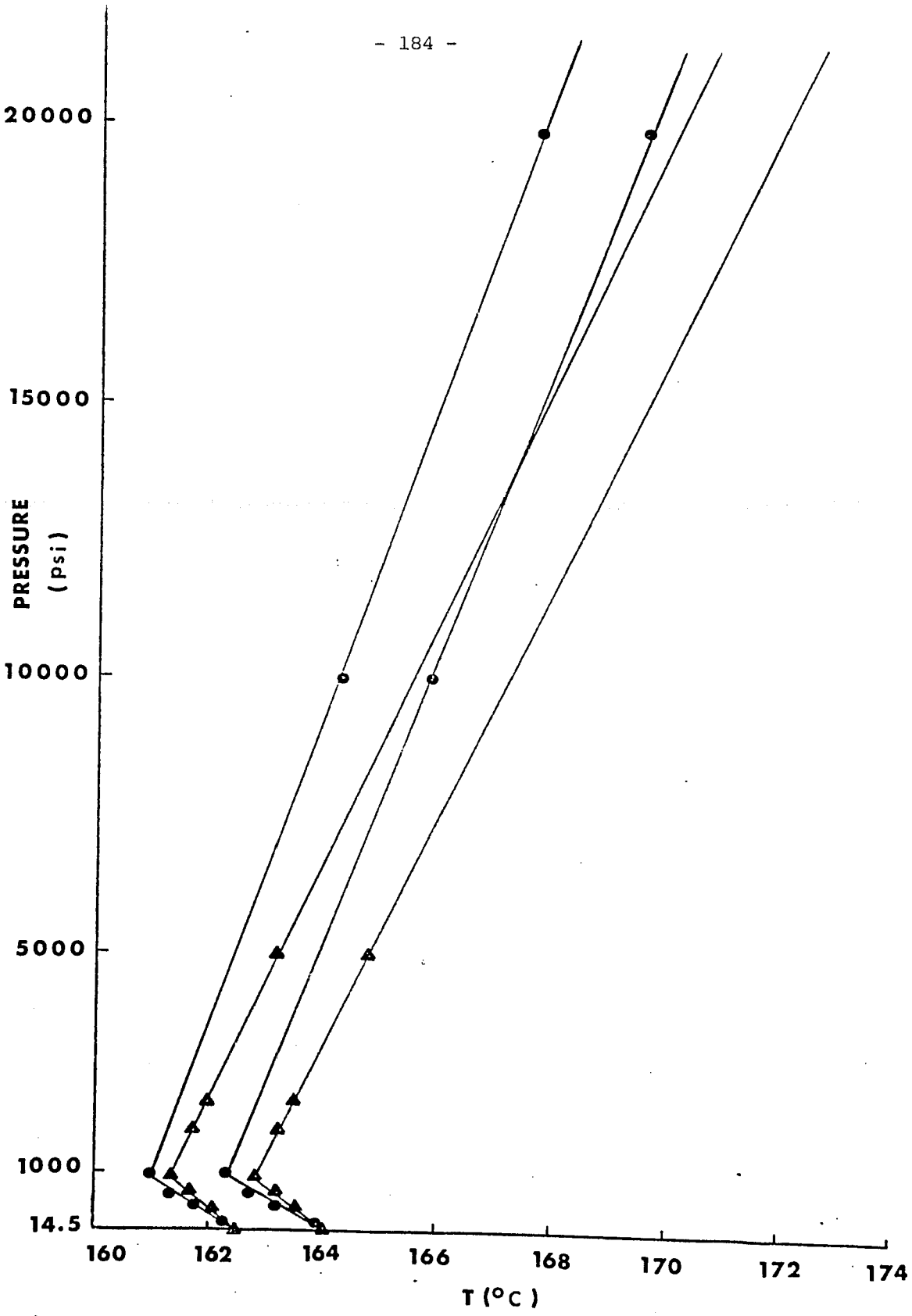
20000
15000
10000
5000
1000
14.5
PRESSURE (psi)
160
162
164
166
168
170
172
174
T (°C)

5.1

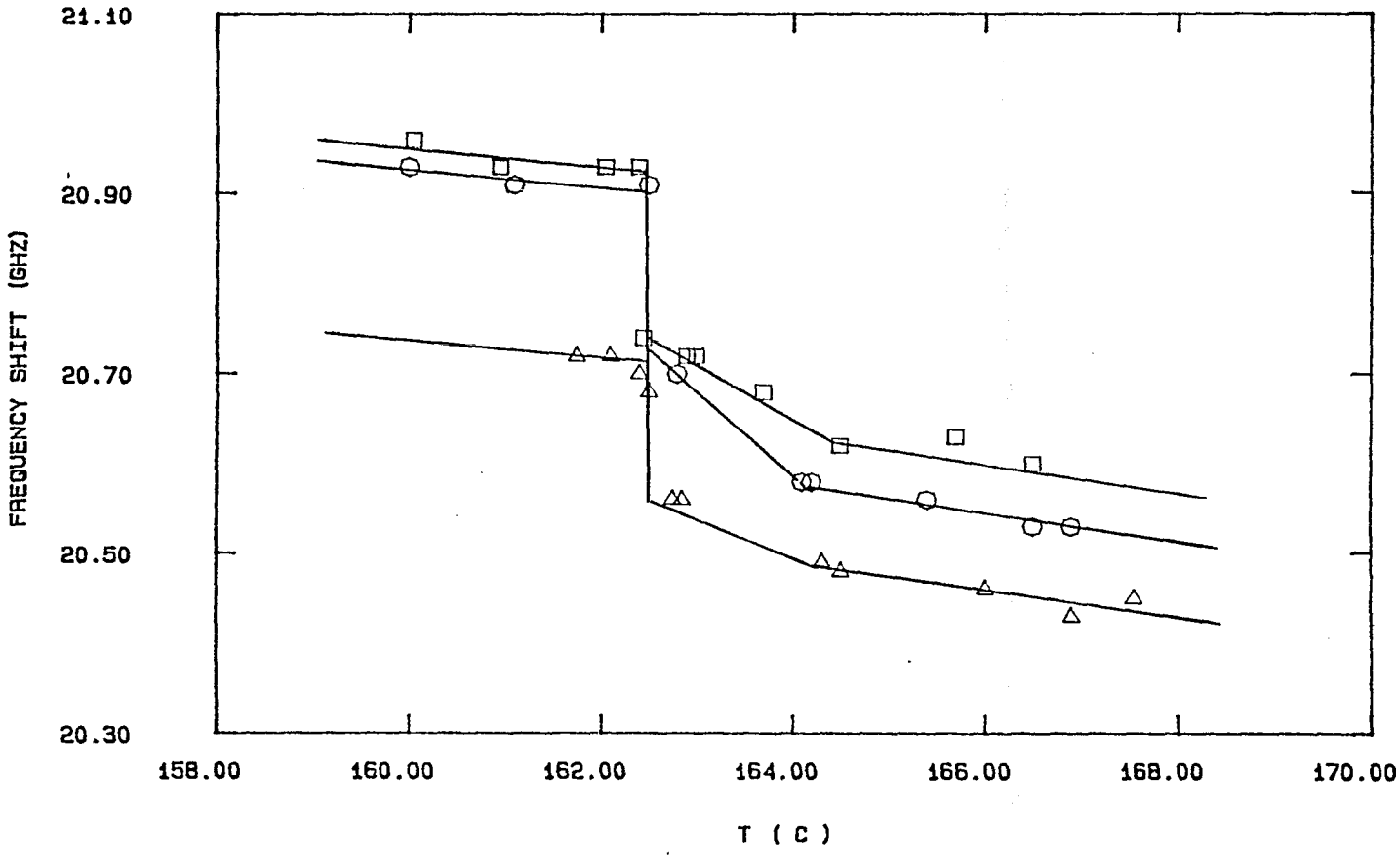

5.2

Mon Aug 8 17:11:06 EDT 1988

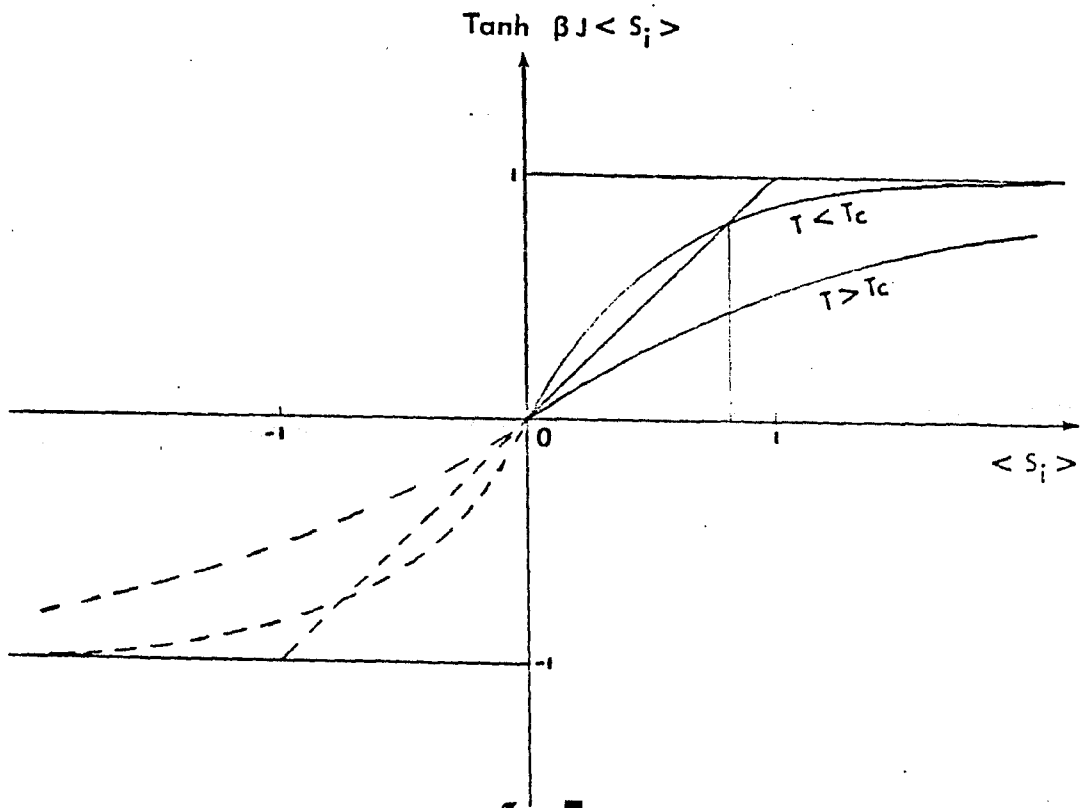

6.1

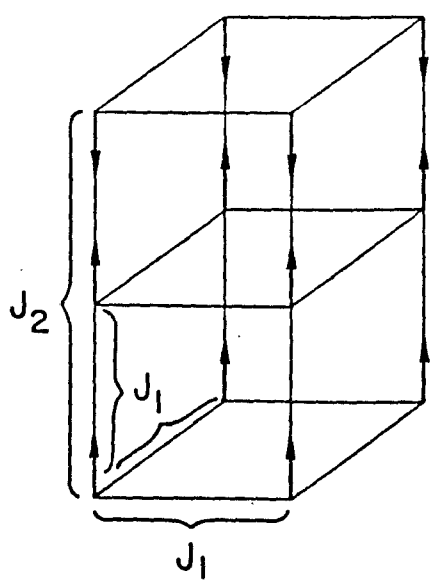

6.2

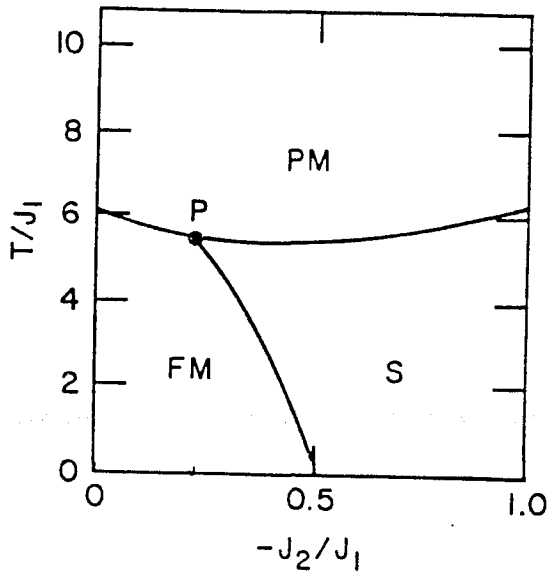

6.3

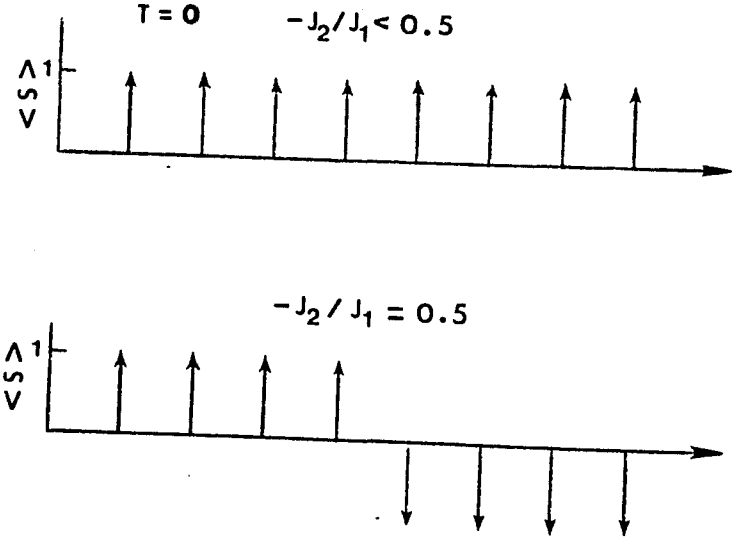

6.4

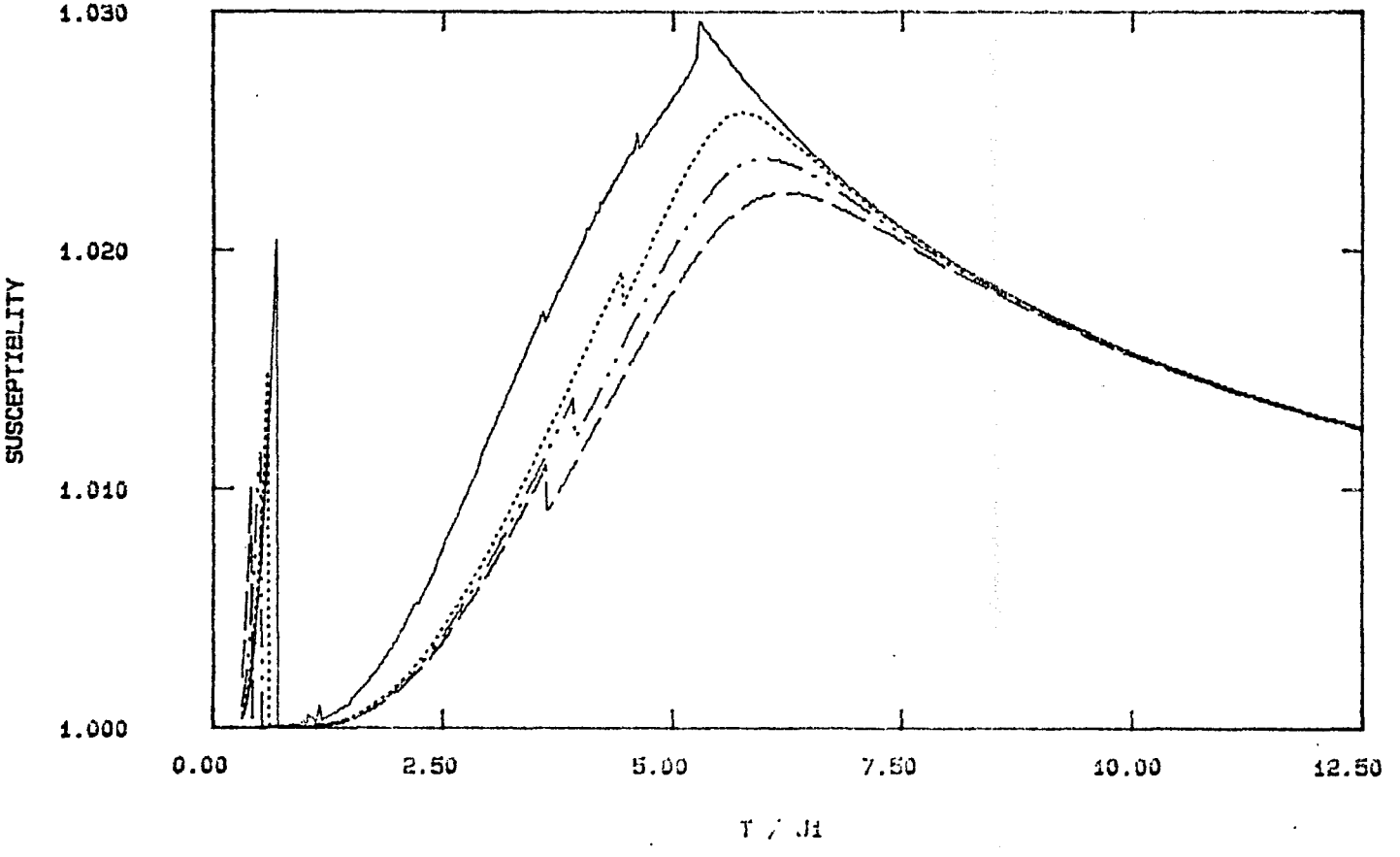
1.030
1.020
1.010
1.000
SUSCEPTIBLITY
0.00
2.50
5.00
7.50
10.00
12.50
T / J1

6.5

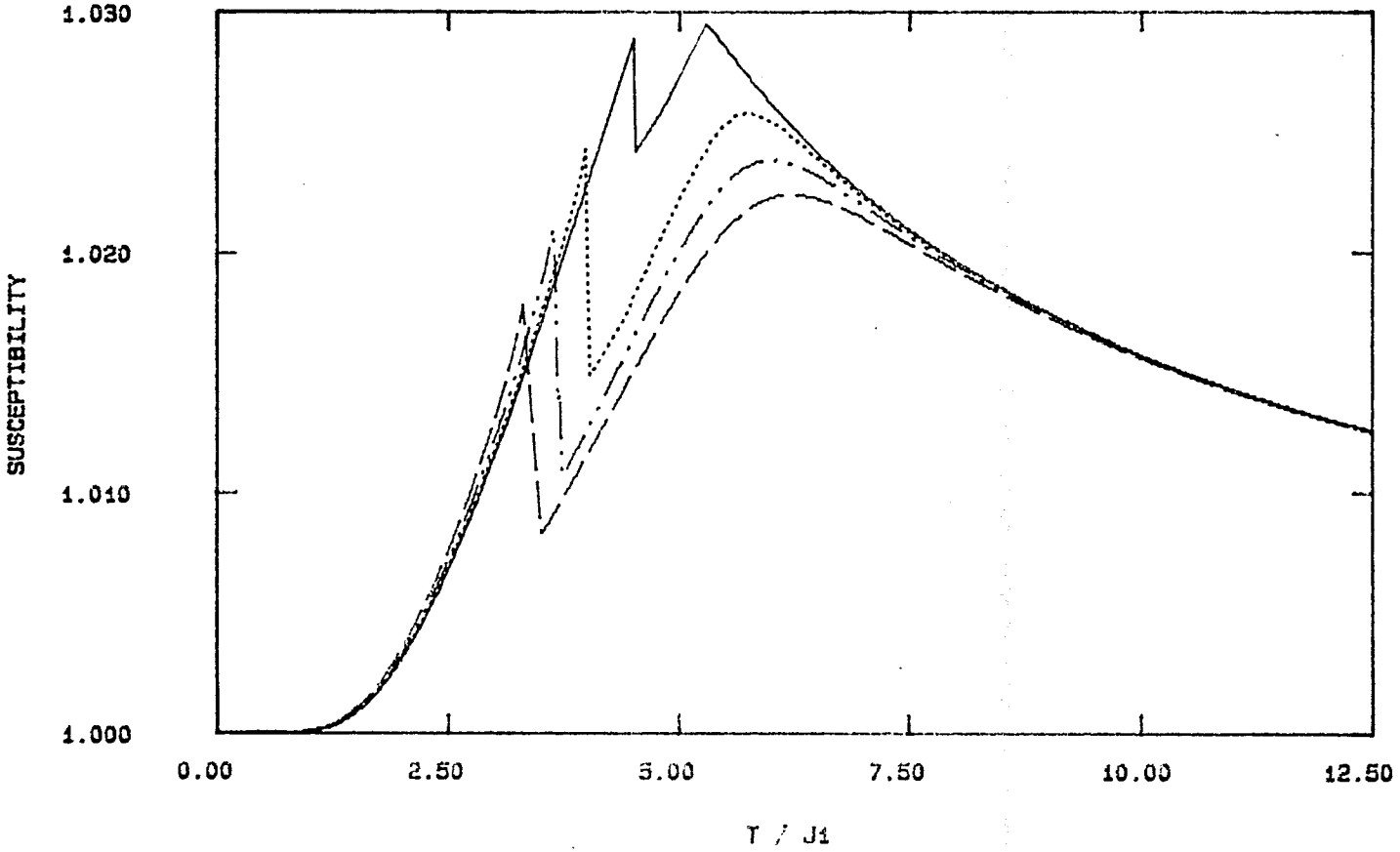

6.6

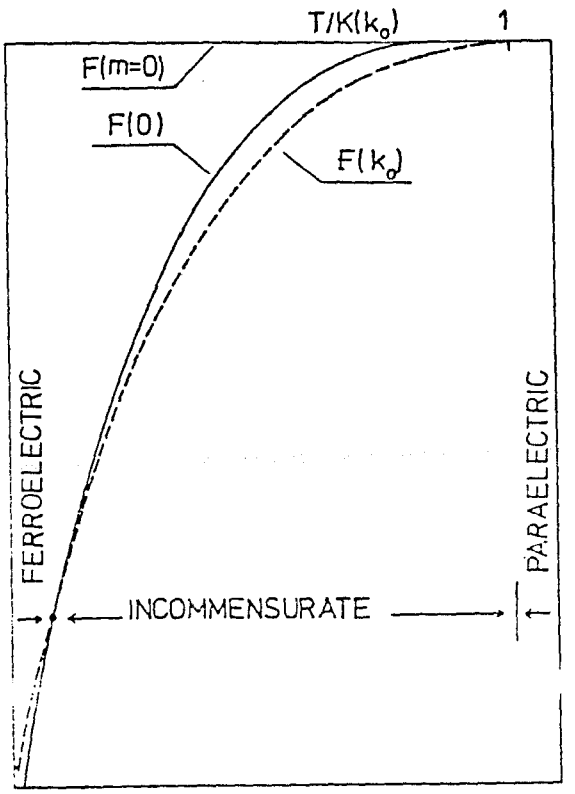
T/K(k_o)
1
F(m=0)
F(0)
F(k_o)
FERROELECTRIC
INCOMMENSURATE
PARAELECTRIC

7.1

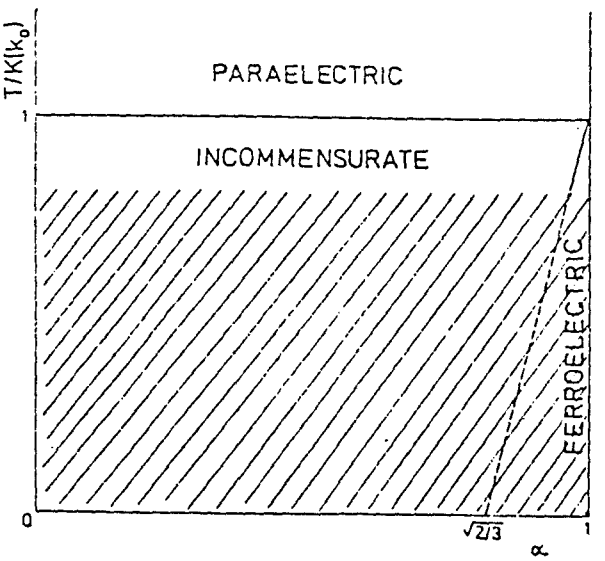
T/K(k_o)
PARAELECTRIC
1
INCOMMENSURATE
FERROELECTRIC
0
√2/3
1
α

7.2

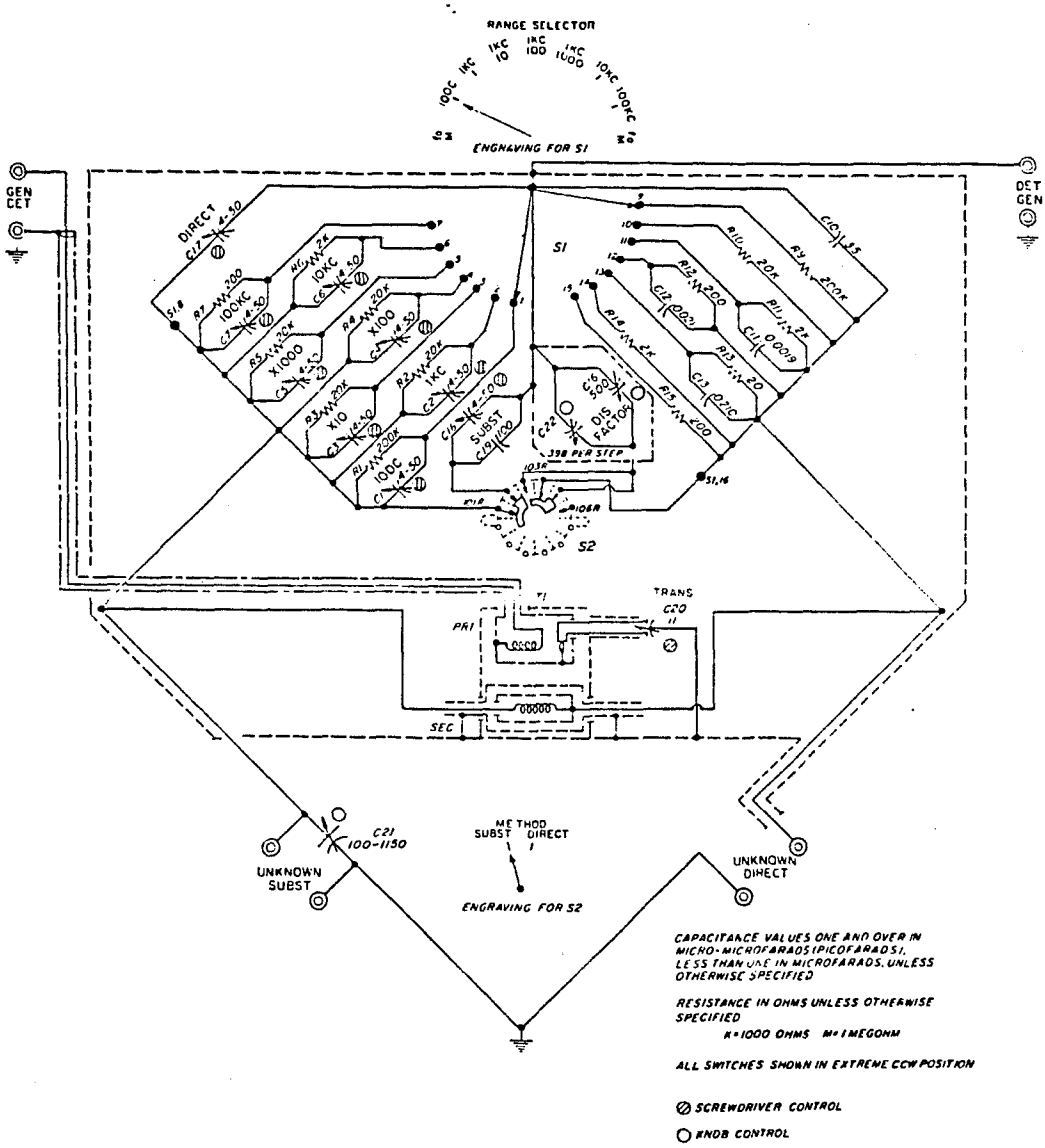

Schematic diagram of the Type 716-C Capacitance Bridge.

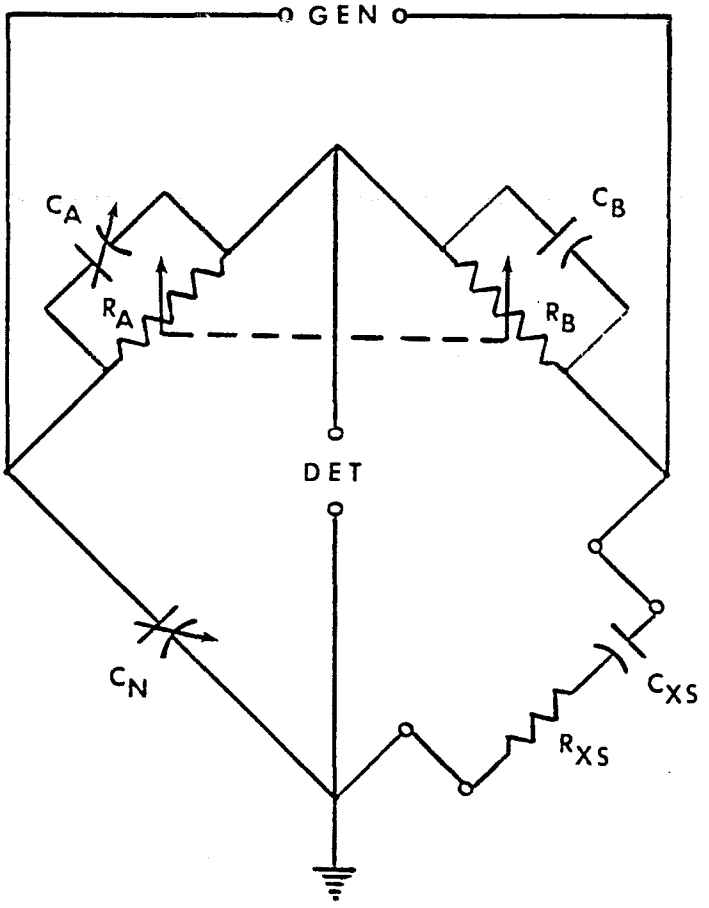

C.2

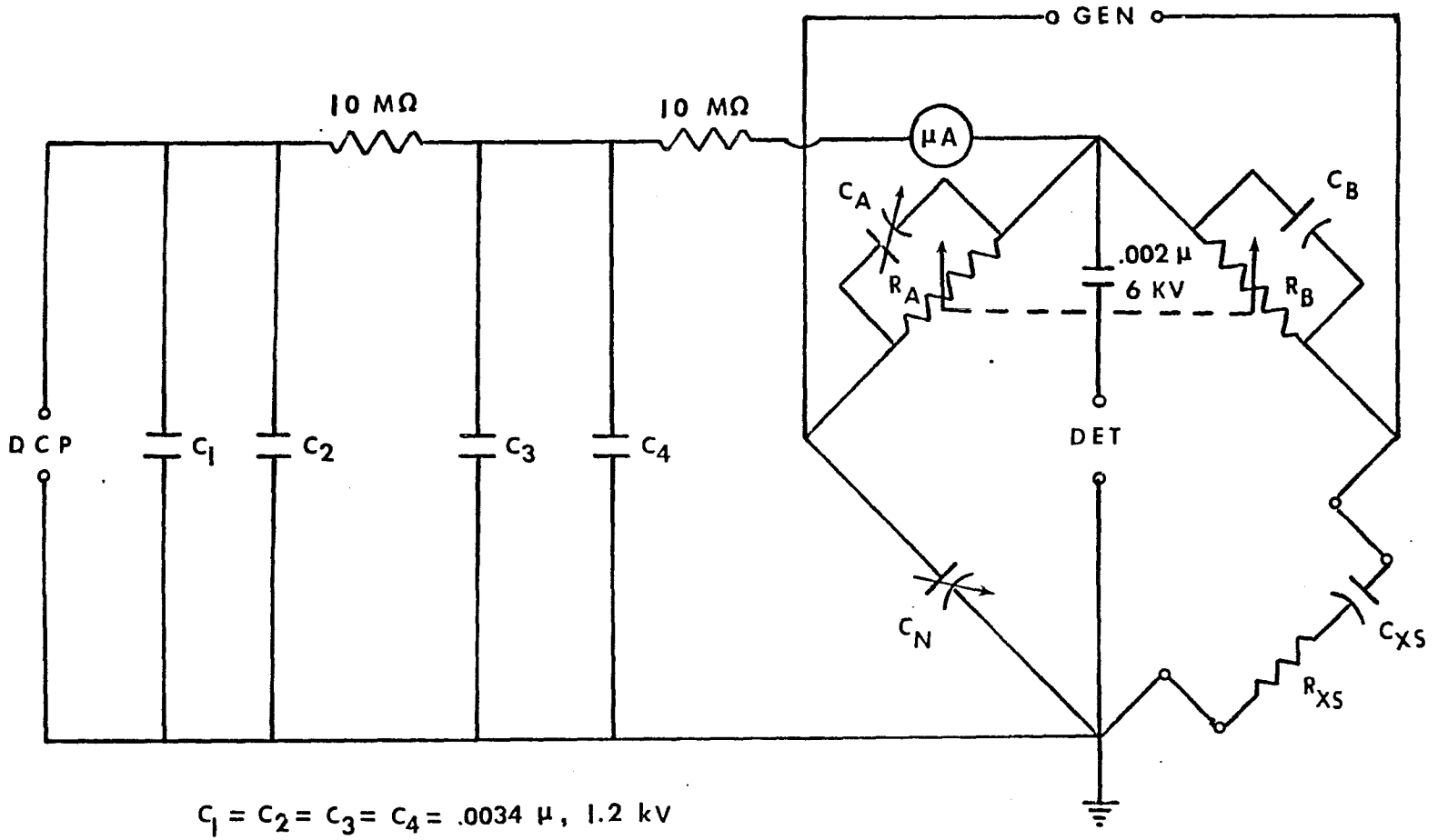

$C_1 = C_2 = C_3 = C_4 = .0034\ \mu$, 1.2 kV

C.3

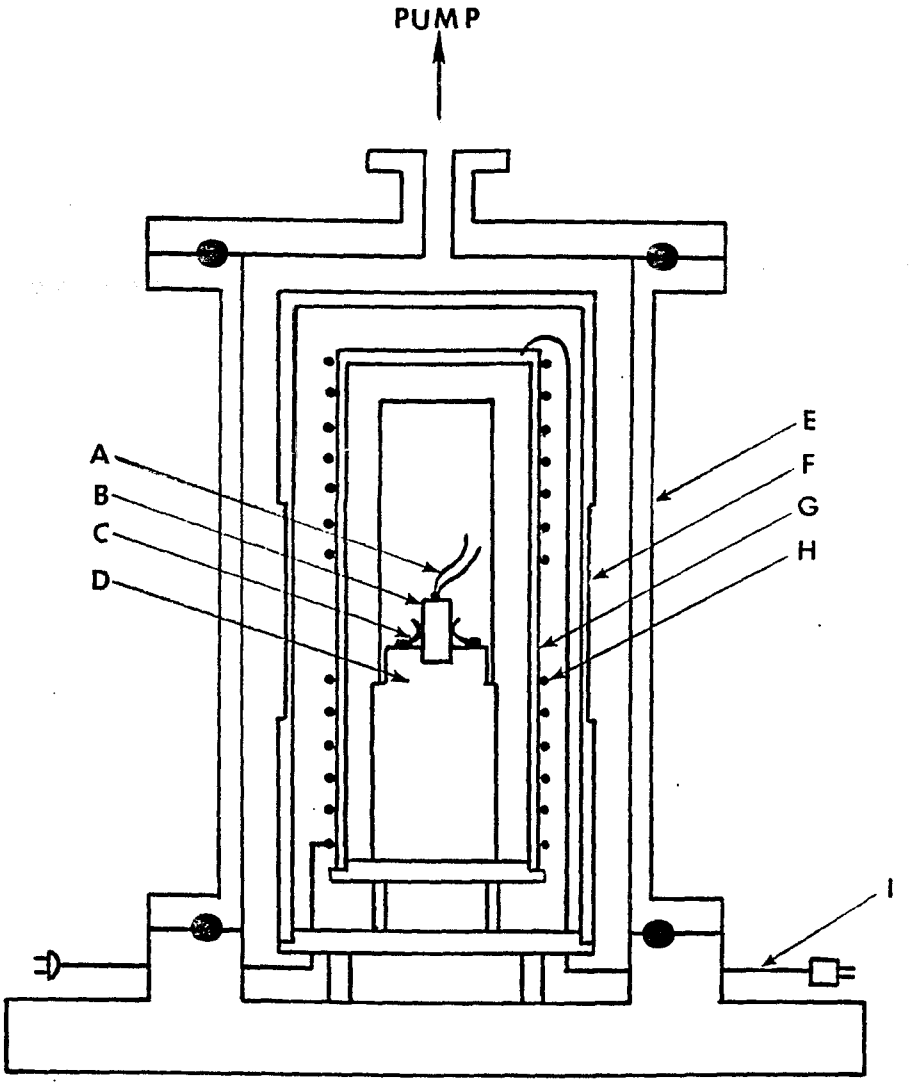

C.4

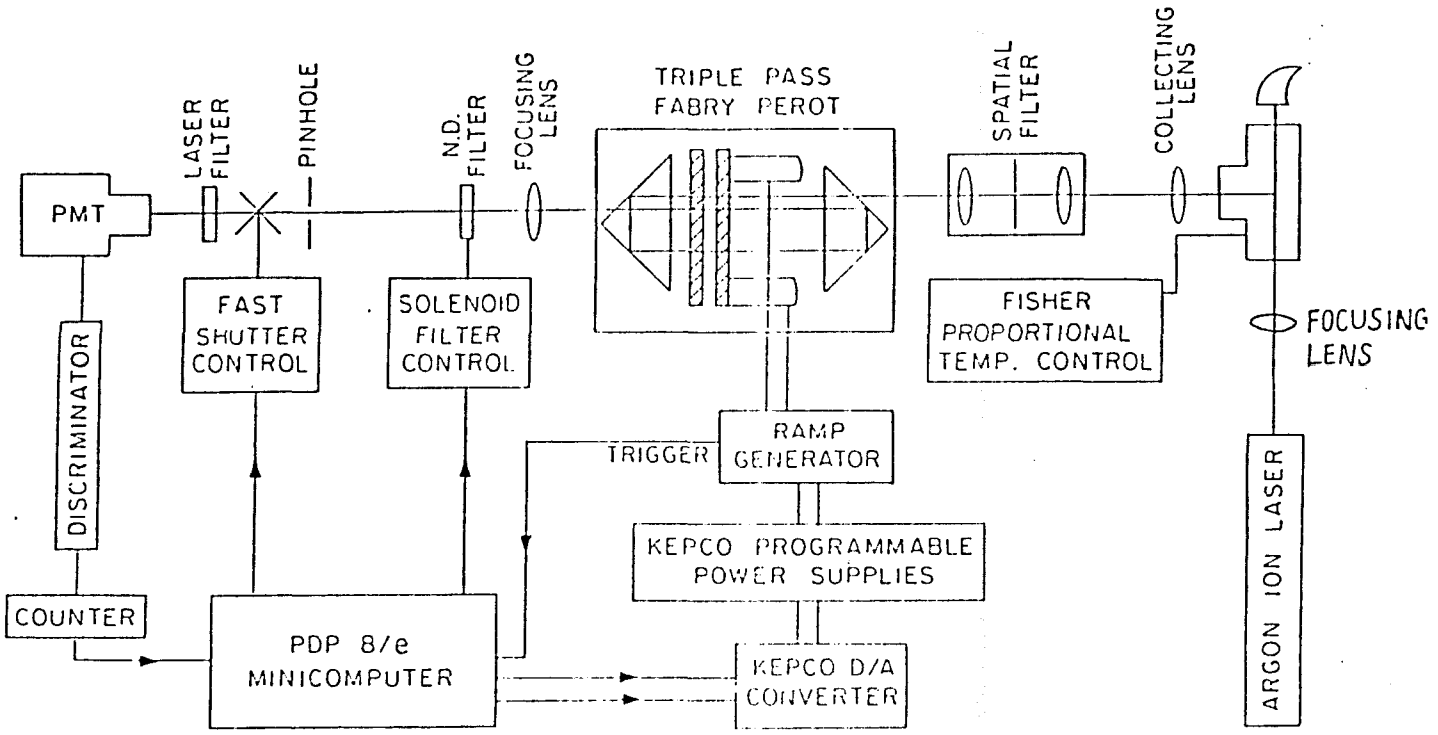

BLOCK DIAGRAM OF THE EXPERIMENTAL SETUP

D.1

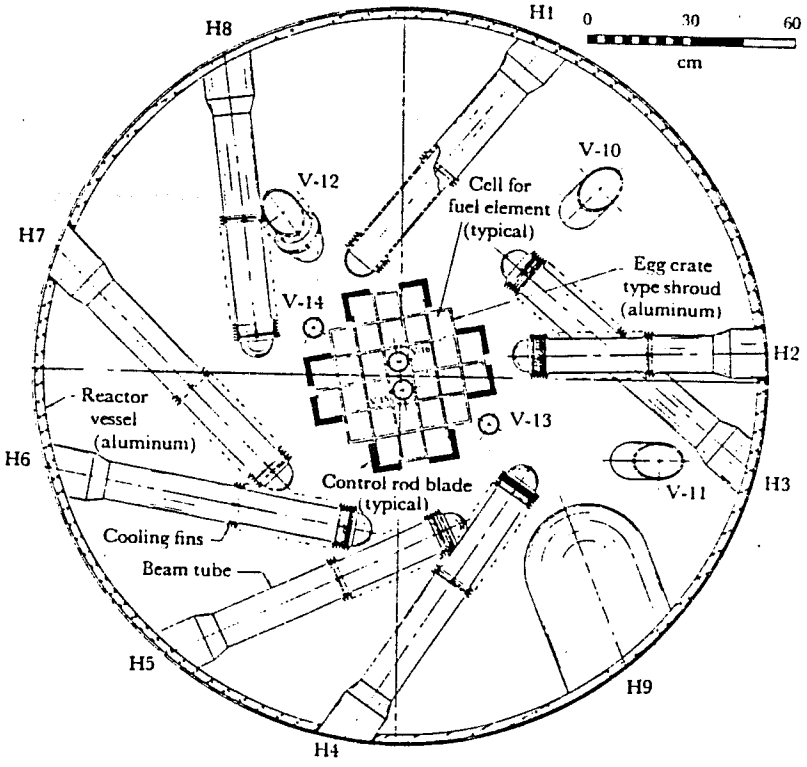
H1
H2
H3
H4
H5
H6
H7
H8
H9
0
30
60
cm
V-10
V-11
V-12
V-13
V-14
Cell for
fuel element
(typical)
Egg crate
type shroud
(aluminum)
Reactor
vessel
(aluminum)
Control rod blade
(typical)
Cooling fins
Beam tube

E.1

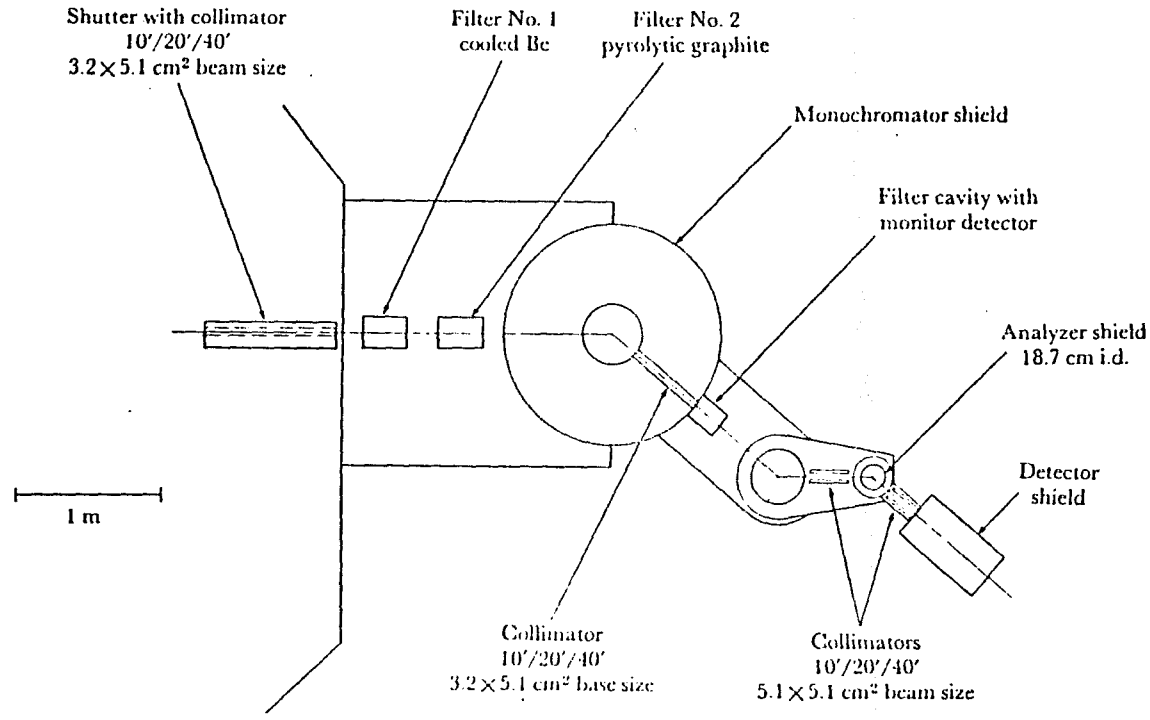

Schematic plan of triple-axis spectrometer installed at H7.

E.2

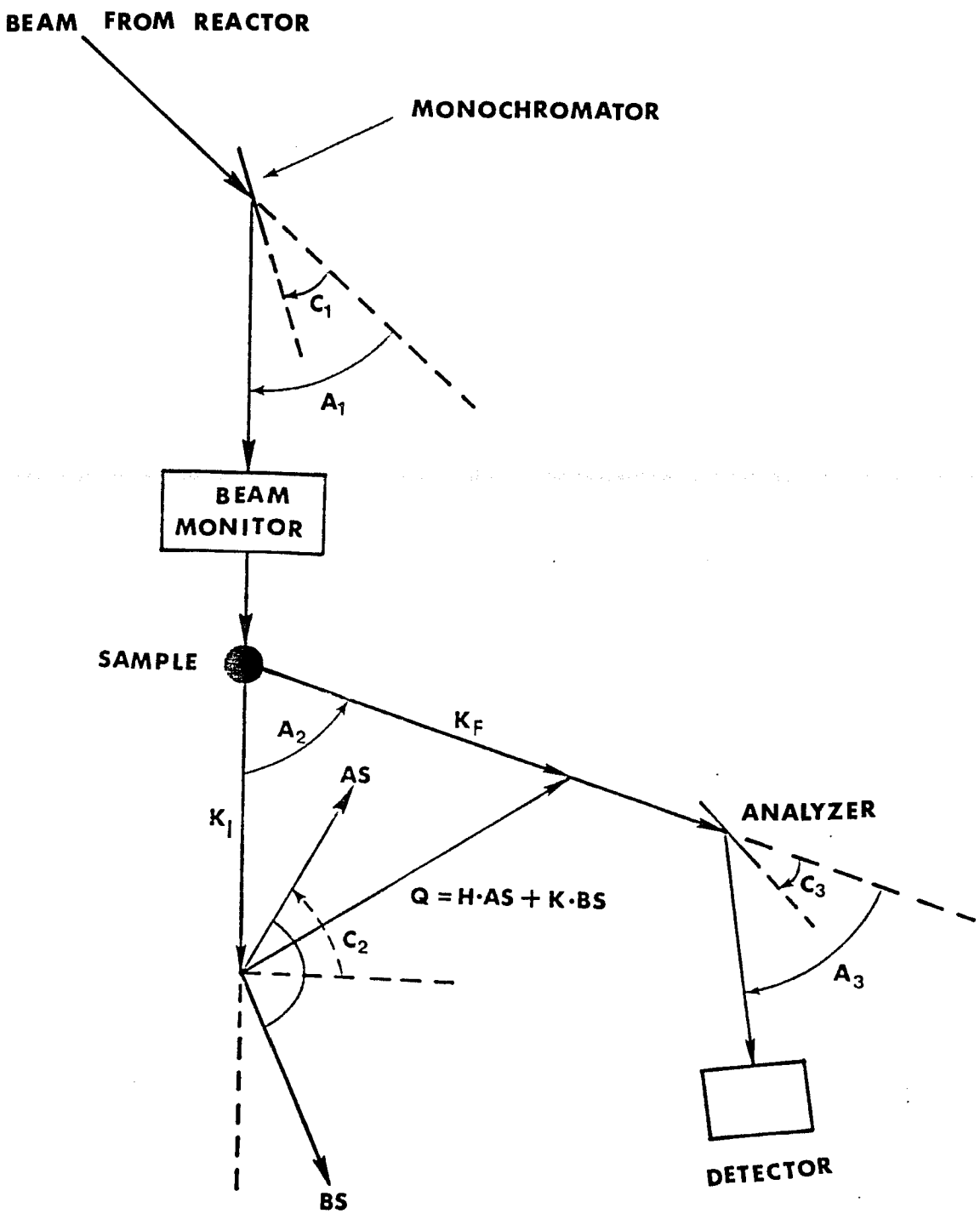
BEAM FROM REACTOR
MONOCHROMATOR
C1
A1
BEAM MONITOR
SAMPLE
A2
KF
AS
KI
ANALYZER
C3
Q = H·AS + K·BS
C2
A3
BS
DETECTOR

E.3

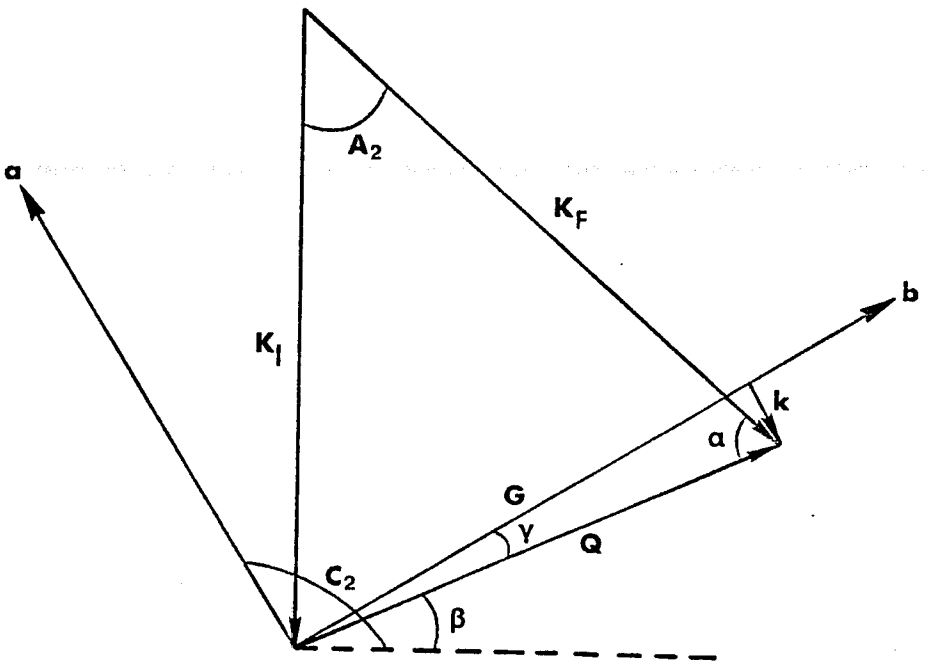

E.4

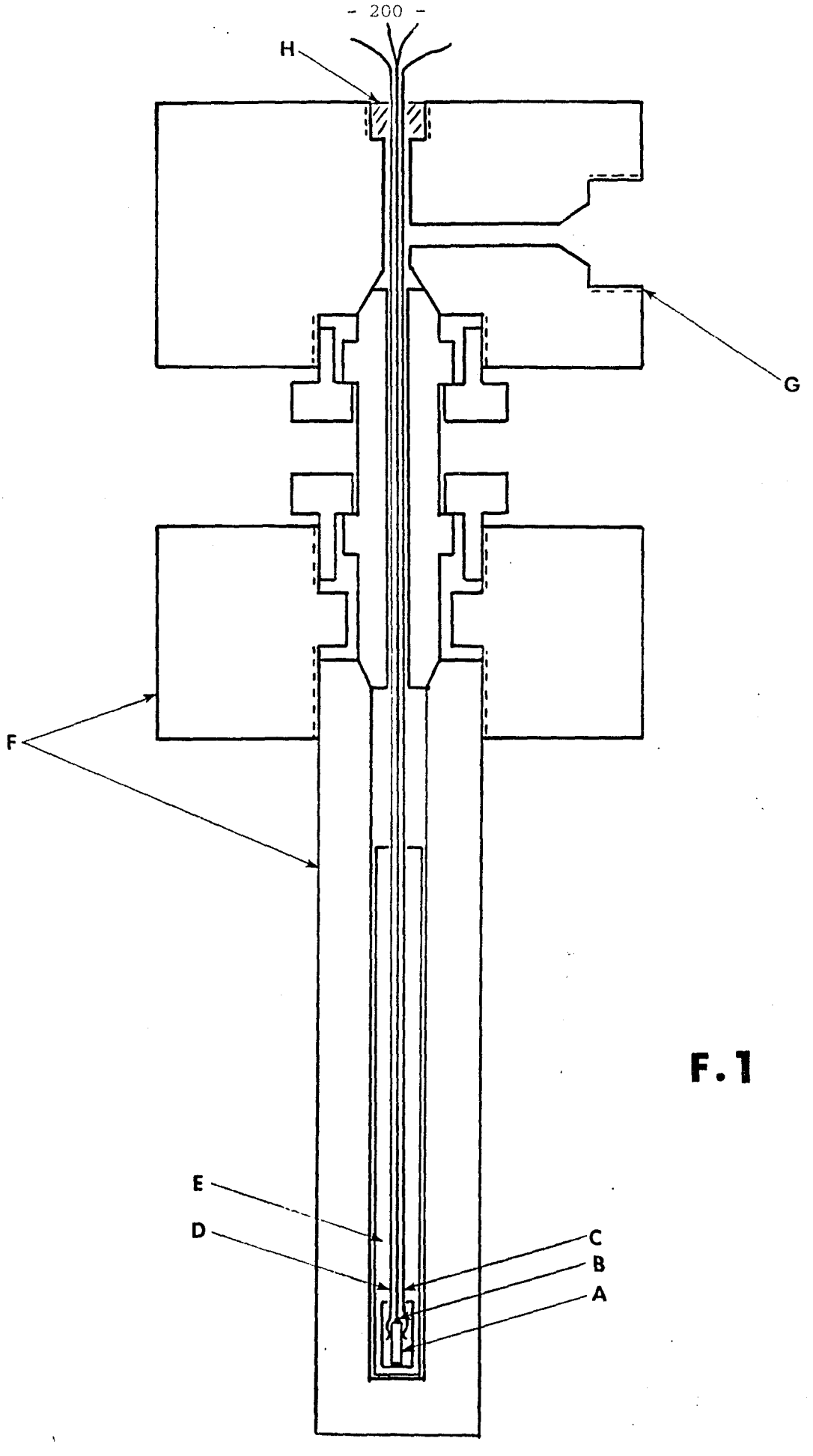

F.1

REFERENCES

1. Y. Ishibashi, Ferroelectrics, **24**, 119 (1980)
2. J. D. Axe, Inst. Phys. C, **64**, 255 (1983)
3. P. M. de Wolff, Acta Cryst., A **30**, 777 (1974)
4. L. D. Landau and E. M. Lifshitz, Statistical Physics, Pergamon Press, London, (1958)
5. R. Blinc, Physics Reports, **79**, 331 (1981)
6. G. Z. Ziegler, Phys. Rev., 38, 1040 (1931)
7. B. Strijk, C. H. MacGillavry, Rec. trav. chim., 62, 705 (1943)
8. B. Strijk, C. H. MacGillavry, Rec. trav. chim., 65, 127 (1946)
9. A. P. Levanyuk, D. G. Sannikov, Sov. Phys. Solid. State, **18** 1122 (1976)
10. A. P. Levanyuk, D. G. Sannikov, Fiz. Trerd. Tela. **18** 1927 (1976)
11. V. Heine, J. D. C. McConnell, Phys. Rev. Lett., **46**, 1092 (1981)
12. J. D. C. McConnell, Am. Mineralogist, 68, 1 (1983)
13. T. Janssen, A. Janner, Ferroelectrics, **24**, 11 (1980)
14. V. Heine, R. M. Lynden-Bell, J. D. C. McConnell, I. R. McDonald, Z. Phys., B **56**, 229 (1984)
15. A. Yamamoto, Phys. Rev., B **31**, 5941 (1985)
16. G. B. Carpenter, Acta. Cryst., **5**, 132, (1952)
17. H. Akao, T. Sasaki, J. Chem. Phys., 23, 2210 (1955)
18. M. R. Truter, Acta. Cryst., **7**, 73 (1954)
19. M. I. Kay, B. C. Frazer, Acta. Cryst., **14**, 56 (1961)
20. M. I. Kay, Ferroelectrics, **4**, 235 (1972)
21. D. Kucharczyk, A. Pietraszko, K. Lukaszewicz, Phys. Stat. Sol., (a)

37, 287 (1976)

22. J. D. Axe, Phys. Rev., **167**, 573 (1968)

23. K. D. Ehrhardt, K. H. Michel, Z. Physk., B **41**, 329 (1981)

24. S. Sawada, S. Nomura, S. Fujii and I. Yoshida, Phys. Rev. Lett., 1, 320 (1958)

25. S. Nomura, J. Phys. Soc. Jpn, **16**, 2240 (1961)

26. S. Sawada, S. Nomura and Y. Asao, ibid **16**, 2207 (1961)

27. Y. Tokugawa, ibid 33, 415 (1972)

28. K. Hamano, ibid **35**, 157 (1973)

29. W. Buchheit, J. Petersson, Solid State Commun., **34**, 649 (1980)

30. K. H. Michel, Phys. Rev., B **24**, 3998 (1981)

31. Y. Sato, K. Gesi, Y. Takagi, J. Phys. Soc. Jpn, **16**, 2172 (1961)

32. E. V. Chisler, M. S. Shur, Phys. Status Solidi, **17**, 173 (1966)

33. H. Betsuyaku, J. Phys. Soc. Jpn., **21**, 187 (1966)

34. S. Suzuki, M. Takagi, ibid **30**, 188 (1971)

35. S. Suzuki, M. Takagi, ibid **32**, 1302 (1972)

36. M. Takagi, H. Murakami and S. Suzuki, Ferroelectrics, **20**, 249 (1978)

37. S. Suzuki, H. Murakami and M. Takagi, J. Phys. Soc. Jpn., **50**, 555 (1981)

38. M. Iwaizumi, S. Kobuta and T. Isobe, Bull. Chem. Soc. Jpn., **44**, 3227 (1971)

39. S. Singh, K. Singh, J. Phys. Soc. Jpn., **36**, 1588 (1974)

40. I. Shibuya, Y. Iwata, N. Koyano, S. Fukui, S. Mitani, M. Tokunaga, ibid **28**, 281 (1970)

41. M. Harada, N. Koyano, S. Meitani, Annu. Rep. Res. Reactor Inst.

Kyoto Univ., 12, 1 (1979)

42. S. Tanisaki, J. Phys. Soc. Jpn., 16, 579 (1961)

43. Y. Yamada, I. Shibuya and S. Hoshino, ibid 18, 1594 (1963)

44. S. Hoshino, H. Motegi, Japan J. Appl. Phys., 6, 708 (1967)

45. H. Bohm, W. Hoffmann, Ferroelectrics, 19, 19 (1978)

46. D. Durand, F. Denoyer, D. Lefur, R. Currat and L. Bernard, J. Physique Lett., 44, L 207 (1983)

47. S. L. Qiu, H. Z. Cummins, S. M. Shapiro, J. C. Steiner, Ferroelectrics, 52, 181 (1983)

48. K. Hamano, J. Phys. Soc. Jpn., 19, 945 (1964)

49. I. Hatta, ibid 38, 1430 (1975)

50. Y. Yamada, Y. Fuji, I. Hatta, ibid 24, 1053 (1968)

51. K. Ema, K. Hamano, I. Hatta, ibid 39, 726 (1975)

52. S. Hoshino, ibid 19, 140 (1964)

53. M. Sakiyama, A. Kimoto, S. Seki, ibid 20, 2180 (1965)

54. R. M. Hazen, L. W. Finger, J. Apll. Phys., 50, 6826 (1979)

55. K. Gesi, K. Ozawa, Y. takagi, J. Phys. Soc. Jpn., 20, 1773 (1965)

56. J. Sakurai, R. A. Cowley, G. Dolling, ibid 28, 1426 (1970)

57. D. Durand, F. Denoyer, M. Lambert, L. Bernard and R. Currat, J. Physique, 43, 149 (1982)

58. D. Durand, These, Universite de Paris-Sud (1982)

D. Durand, F. Denoyer, R. Currat, M. Lambert, Incommensurate Phase In $NaNO_2$, (in: Incommensurate Phase Transition In Dielectric Crystals edited by A. P. Levanyuk and R. Blinc (North Holland - in press)

59. K. Ota, Y. Ishibashi, J. Phys. Soc. Jpn., 29, 1545 (1970)

60. I. Hatta, Y. Shimizu and K. Hamano, ibid 44, 1887 (1978)

61. I. Hatta, M. Hanami and K. Hamano, ibid, **48**, 160 (1980)

62. I. Hatta, ibid, **49**, (suppl. B) 163 (1980)

63. I. Hatta, J. Phys. Soc. Jpn., **53**, 635 (1984)

64. S. Kh. Esayan, V. V. Zhdanova, and V. V. Lemanov, ibid **49**, (Suppl. B) 106 (1980)

65. S. Kh. Esayan, V. V. Lemanov, Sov. Phys. Solid State, 23, 1195 (1981)

66. H. Shimizu, M. Tsukamoto, Y. Ishibashi and M. Umeno, J. Phys. Soc. Jpn., **36**, 498 (1974)

67. T. Yagi, Y. Hidaka and K. Miura, ibid, **48**, 2165 (1980)

68. T. Yagi, Y. Hidaka and K. Miura, ibid, **51**, 3562 (1982)

69. V. S. Gorelik, I. S. Zheludev, M. M. Srishchinskii, Sov. Phys. Crystallogr., **11**, 527 (1967)

70. C. M. Hartwig, E. Wiener-Avnear, S. P. S. Porto, Phys. Rev. B 79 (1972)

71. G. D. Holah, J. Phys. C: Solid St. Phys., **4**, 2197 (1971)

72. G. D. Holah and H. Happ, ibid, **3**, 1807 (1970)

73. W. Buchheit and J. Petersson, Ferroelectrics, **36**, 311 (1981)

74. S. H. Chon, J. Lee, and K. H. Kang, ibid **36**, 297 (1981)

75. T. Yagi, J. Phys. Soc. Jpn., **28**, 321 (1976)

76. T. Oja, R. A. Marino and P. J. Bray, Phys. Lettrs, **26A**, 11 (1967)

77. G. Bonera, A. Rigamonti, Phys. Rev., B **2**, 2784 (1970)

78. R. A. Marino, J. Chem. Phys., **48**, 4833 (1968)

79. P. K. Kadaba, Phys. Stat. Sol., **42**, 855 (1970)

80. H. Betsuyaku, J. Phys. Soc. Jpn., **27**, 1485 (1969)

81. R. Ambrosetti, Phys. Rev., B **15**, 4318 (1977)

82. I. P. Aleksandrova, R. Blinc, Phys. Stat. Sol. (a) **61**, 95 (1980)

83. K. Ito, J. Phys. Soc. Jpn., 34, 138 (1973)

84. K. Inoue, Japan J. Appl. Phys., 9, 152 (1970)

85. K. Inoue, Ferroelectrics, 7, 107 (1973)

86. Y. Asao, I. Yoshida, R. Ando and S. Sawada, J. Phys. Soc. Jpn., 17, 442 (1962).

Y. Takagi, K. Gesi, J. Phys. Soc. Jpn., 22, 979 (1967)

87. M. L. Klein, I. R. McDonald and Y. Ozaki, Phys. Rev. Lett., 48, 1197 (1982)

88. Y. Yamada, Ferroelectrics, 35, 51 (1981)

89. V. Heine, J. Phys. C: Solid State Phys., 17, 1199 (1984)

90. Y. Ishibashi, H. Shiba, J. Phys. Soc. Jpn., 45, 409 (1978)

91. Y. Ishibashi, W. Buchheit and J. Petersson, Solid State Commun., 38, 1277 (1981)

92. K. Ema, K. Hamano and A. P. Levanyuk, J. Phys. Soc. Jpn., to be published

93. P. Bak and von Boehm, Phys. Rev., B 21, 5297 (1980)

94. Y. Yamada, and N. Hamaya, J. Phys. Soc. Jpn., 52, 3466 (1983)

95. W. Selke, P. M. Duxbury, Z. Phys., B 57, 49 (1984)

96. K. H. Michel, Ferroelectrics, 36, 289 (1981)

97. K. H. Michel, E. Courtens, Phys. Rev., B 23, 513 (1981)

98. J. Fivez, K. H. Michel, Z. Phys., B 51, 127 (1983)

99. R. Lynden-Bell, M. L. Klein, I. R. McDonald, Z. Phys., B 54, 325 (1984)

100. R. M. Hornreich, M. Luban and S. Shtrikman, Phys. Rev. Lett., 325, 1678 (1975)

101. R. M. Hornreich, J. Magn. Magn. Mater., 15-18, 387 (1980), and

references therein.

102. C. C. Becerra, Y. Shapira, N. F. Oliveira Jr. and T. S. Chang, Phys. Rev. Lett., 44, 1692 (1980)

103. I. Musevic, B. Zeks, R. Blinc, Th. Rasing and P. Wyder, Phys. Rev. Lett., 48, 192 (1982)

104. A. Levstik, C. Filipic, P. Prelovsek, R. Blinc and L. A. Shuvalov, Phys. Rev. Lett., 54, 1567 (1985)

105. H. Z. Cummins and P. E. Schoen, 1972, Linear Scattering from thermal fluctuations, in: Laser Handbook, eds., F. T. Arecchi and E. O. Schulz-Dubois (North- Holland, Amsterdam) pp 1030

106. J. Randa, Phys. Rev., B 32, 413 (1985)

107. S. Tanisaki, J. Phys. Soc. Jpn., 18, 1181 (1963)

108. Y. Yamada and T. Yamada, ibid, 21, 2167 (1966)

109. K. Gesi, J. Japan, Applied Phys., 4, 818 (1965)

110. Y. Yamada, Ferroelectrics, 35, 51 (1981)

111. R. J. Elliott, Phys. Rev., 124, 346 (1961)

112. S. Redner, H. E. Stanley, J. Phys. C: Solid St. Phys., 10, 4765 (1977)

S. Redner, H. E. Stanley, Phys. Rev. B, 16, 4901 (1977)

113. J. R. Asay, D. L. Lamberson and A. H. Guenther, J. Applied Phys. 40, 1768 (1969)

114. A. Polian and J. M. Besson, M. Grimsditch and H. Vogt, Phys. Rev., 25, 2767 (1982)

115. Exhibit Center, BNL, High Flux Beam Reactor (1981)

116. G. Burns, Introduction to Group Theory With Applications, Acadamic press, New York, (1977)